Thèse pour l'obtention du grade de

Docteur de l'Université Paris-Est

Sciences des Matériaux

présentée par

Mohamed Hassan Khalili

Équipe d'accueil : Multi-Échelle/Navier
École Doctorale : Ecole doctorale Sciences, Ingénierie et Environnement (SIE) n° 531

Titre de la thèse :

Tracking and modelling small motions at grain scale in granular materials under compression by X-Ray microtomography and discrete simulations

Soutenue le 03 Novembre 2016

Composition du jury :

Gaël Combe	*Rapporteur*
Stephen Hall	*Rapporteur*
Hervé Di Benedetto	*Examinateur*
Catherine O'Sullivan	*Examinatrice*
Stéphane Roux	*Président*
Michel Bornert	*Examinateur*
Sébastien Brisard	*Examinateur*
Jean-Noël Roux	*Directeur de thèse*

*Je souhaite dédier particulièrement ce travail
à mon professeur de vie, mon père,
à ma maitresse de primaire et ma raison de vivre, ma mère.*

<div dir="rtl">

إِصبِر عَلَى مَرِّ الجَفَى مِن مُـعَلِمٍ   فَإِن رُسُوبَ العِلمِ في نَفَرَاتِـهِ

وَ مَن لَم يَذُق مَرَّ التَّعَلُّمِ سَاعَةً   تَجَرَّعَ ذَلَّ الجَهلِ طُولَ حَيَاتِهِ[1]

الإمام الشّافعي

</div>

---

[1]Extrait d'un poème arabe de *Imam Al-chafii* (767-820) autour de la quête de la sience, dans lequel il dit (modeste traduction personnelle) qu'il faut être patient dans l'apprentissage, car le vrai échec dans la science est le fait de la fuir. Puis il rajoute que celui qui n'a guerre gouté à l'amertume de l'apprentissage, condamne toute sa vie à l'ignorance.

Remerciements

Depuis que j'ai commencé ma formation d'ingénieur, j'ai été convaincu que la recherche était ma vocation. Je me suis alors fixé l'objectif de faire un doctorat dans les meilleures conditions possibles. Une raison parmi d'autres, m'ayant poussé à ne ménager aucun effort pour être en France et réaliser cette thèse dans le laboratoire Navier aux cotés de chercheurs de calibre international. J'ai rencontré des personnes passionnées par ce qu'elles font, engagées et surtout généreuses. J'étais surtout impressionné par l'ambiance qui régnait au sein du laboratoire, une énergie très positive diffusait dans l'équipe. Ma présence parmi eux me rappelait chaque jour la chance que j'avais de les côtoyer, et de profiter de chaque moment pour la saisir.

Ce voyage est pour moi le début d'une quête de connaissances et de savoir. Il n'aurait pas été simple sans l'aide de mes parents et mes sœurs à qui je dois énormément pour leur attention et affection. Leur soutien moral et financier durant mon parcours m'ont permis, avec la bénédiction du bon Dieu, d'arriver à ce que je suis aujourd'hui.

Mon parcours a été possible avec l'aide et en référence à plusieurs personnes. Allant de mes professeurs qui m'ont fait aimer et donné l'envie de rejoindre ce domaine de recherche, jusqu'à mes superviseurs de thèse qui étaient toujours présents pour moi dans le besoin, pour me motiver et me donner l'exemple à suivre. J'ai eu la chance d'avoir une combinaison de superviseurs de grande qualité, ce qui a transformé le travail sur ma thèse en un grand plaisir. Je les remercie tous, d'abord de m'avoir proposé ce sujet passionnant et fait en sorte d'y aboutir aisément. Ils étaient toujours disponibles pour m'écouter, m'éclairer et me pousser à donner le meilleur de moi-même. Votre professionnalisme, vos qualités humaines, votre sens de partage m'ont marqué sur le plan professionnel et personnel. Je vous en remercie infiniment. Je n'oublierai pas de vous remercier également pour votre assistance dans l'obtention du complément de financement dont j'ai bénéficié. Je remercie du fond du cœur Jean-Noël Roux, mon directeur de thèse et Sébastien Brisard, les deux personnes que j'ai côtoyé le plus durant ce travail. Merci pour le temps que vous m'avez consacré, votre présence permanente et régulière a permis l'avancement de ce travail sans interruption, vous répondiez instantanément à mes questions et me donniez les conseils adéquats qui éclaircissaient mes moments de confusions. Merci également pour votre soutien sur ma décision de rédiger ce manuscrit en anglais, votre aide énorme m'a permis d'y arriver. Par la suite je voudrais remercier Michel Bornert qui, malgré ses responsabilités multiples, a su me consacrer du temps et me faire profiter de sa grande expérience dans le domaine de la corrélation d'image, je le remercie également pour ses réflexions et idées ingénieuses et innovantes qui sont à l'origine de la méthode développée dans ce travail et dont j'ai pu profiter le long de toute ma thèse. De même je remercie Jean-Michel Pereira, pour ses conseils pertinents et indispensables sur toutes les expériences géotechniques que j'ai pu réaliser. À tous mes superviseurs, je vous exprime ici toute ma gratitude, votre présence a rendu mes moments difficiles, faciles à surmonter.

Je n'oublierai pas de remercier également Patrick Aimedieu pour sa disponibilité et les nombreuses journées qu'on a passées ensemble à bricoler et raffiner les installations expérimentales au

mico-tomographe, toujours dans la bonne humeur. Je remercie également Mathieu Vandamme qui n'a pas hésité à m'apporter des remarques et relectures pertinentes sur mes productions scientifiques.

Je tiens à présenter mes remerciements particuliers aux membres du jury qui ont accepté d'examiner ma thèse. Je remercie les deux rapporteurs M. Gaël Combe et M. Stephen Hall qui ont pris la peine de lire en détail ce manuscrit et m'ont fourni des rapports concis et efficaces qui m'ont permis de bien préparer ma soutenance. Je remercie également M. Stéphan Roux le président du jury ainsi que Mme Catherine O'Sullivan et M. Hervé Di Benedetto pour leurs questions pertinentes durant ma soutenance, qui ont soulevé des points intéressants en rapport avec mon travail.

J'ai réalisé cette thèse majoritairement au sein des équipes Multi-échelle et Géotechnique du laboratoire Navier, je ne pourrai clôturer ces remerciements sans en adresser à toutes les personnes et anciens collègues dans ces équipes, l'ensemble des techniciens et l'équipe administrative avec un remerciement particulier à mes collègues du bureau auprès desquels les conditions de travail étaient très conviviales et je dirais même optimales.

Mes amis, ma famille je vous remercie également de m'avoir supporté durant cette phase de ma vie.

Bussy-Saint-Georges, le 21 Décembre 2016.

Abstract

The present work is motivated by the study of creep in granular materials at the microscopic scale.

The first part of this thesis deals with displacement measurements by microtomography. Classical digital image correlation fails to catch time-dependent (possibly fast) phenomena such as short-term creep. A new method named *Discrete Digital Projection Correlation* is developed to overcome this limitation. This method requires very few projections (about 100 times less than classical methods) of the deformed state to perform the correlation and retrieve grain displacements. Therefore, the acquisition time is remarkably reduced, which allows to study time-dependent phenomena. The method is tested on experimental data. While its accuracy compares favorably to that of conventional methods, it only requires acquisition times of a few minutes. The origins of measurement errors are tracked by numerical means, on simulated grain displacements and rotations.

The second part is a numerical simulation study, by the Discrete Element Method (DEM), of oedometric compression in model granular materials, carried out with a simple model material: assemblies of slightly polydisperse spherical beads interacting by Hertz-Mindlin contact elasticity and Coulomb friction. A wide variety of initial states are subject to compression, differing in density, coordination number and fabric anisotropy. Despite apparently almost reversible strains, oedometric compression proves an essentially anelastic and irreversible process, due to friction, with important internal state changes affecting coordination number and anisotropy. Elastic moduli only describe the response to very small stress increments about well equilibrated configurations. The ratio of horizontal stress to vertical stress (or coefficient of earth pressure at rest, commonly investigated in soil mechanics) only remains constant for initially anisotropic assemblies. A simple formula relates it to force and fabric anisotropy parameters, while elastic moduli are mainly sensitive to the latter. Further studies of contact network instabilities and rearrangements should pave the way to numerical investigations of creep behavior.

Keywords : Digital Image Correlation, Discrete Element Method, X-ray tomography, granular materials, full-field measurements, oedometric compression, elastic moduli, creep.

Résumé

Le travail réalisé durant cette thèse a été motivé par l'étude des mécanismes microscopiques à l'origine du fluage dans les matériaux granulaires.

Dans une première partie, on cherche à mesurer les déplacements des grains dans un matériau granulaire par observations en micro-tomographie X. Une telle identification ne peut être efficacement réalisée pour des phénomènes rapides avec les méthodes classiques de corrélation d'images numériques. Une nouvelle méthode nommée *corrélation discrète des projections numériques* qui contourne cette difficulté est développée dans cette thèse. Cette méthode, basée sur la corrélation des projections de tomographie, permet de mesurer les déplacements avec un nombre réduit de projections (100 fois moins que les méthodes classiques), ce qui diminue énormément le temps d'acquisition nécessaire pour la mesure. La méthode, appliquée à des données expérimentales, donne une précision comparable à celles des méthodes classiques tandis que le temps d'acquisition nécessaire est réduit à quelques minutes. Une étude portant sur l'analyse des sources d'erreurs affectant la précision des résultats est également présentée.

Le but de la deuxième partie est de réaliser des simulations numériques pour fournir une caractérisation de l'essai oedométrique. Différents assemblages de billes de verre légèrement poly-disperses interagissant à travers des contacts élastiques de Hertz-Mindlin et frottement de Coulomb ont été utilisés. Ces simulations ont permis d'étudier l'évolution de certains paramètres structuraux du matériau modèle, préparant ainsi le terrain pour de futures études sur le fluage. Il a été particulièrement souligné que les contacts élastiques utilisés dans ces simulations ne reproduisent pas l'irréversibilité des déformations observée dans les expériences sur des sables. Cependant, l'irréversibilité est bien visible sur le nombre de coordination et l'anisotropie. Alors que les paramètres élastiques peuvent exprimer la réponse pour des petits incréments de déformations, la compression oedometrique est belle et bien anélastique, principalement à cause de la mobilisation du frottement. Le rapport entre les contraintes horizontales et verticales (coefficient du sol au repos) n'est particulièrement constant que lorsque l'anisotropie de structure est instaurée dans l'état initial de l'assemblage. Il est par ailleurs relié à l'anisotropie interne de la structure par une formule simple. Finalement, les coefficients du tenseur élastique dépendent principalement du nombre de coordination et son anisotropie est plus liée à l'anisotropie des contacts qu'à celle des forces.

Mots-clés : Corrélation d'Images Numériques, simulations numériques discrètes, micro-tomographie X, matériaux granulaires, mesure de champs, compression oedométrique, modules élastiques, fluage.

Contents

Chapter 1

Introduction and motivations

Contents

This chapter is a general introduction to the studies presented in this doctoral work. This work is motivated by the study of creep in granular materials which is briefly introduced in Sec. 1.1. Afterwards, an experimental program is carried out in Sec. 1.2 to illustrate the types of experiments that we aim to characterize. This experimental campaign introduces the motivations of the experimental and numerical techniques developed during this thesis. Finally, Sec. 1.4 gives an overview of the remaining chapters of this work.

1.1   Introduction

The macroscopic mechanical properties of granular materials are traditionally described and modeled in the realm of soil mechanics [Wood, 1990, Biarez and Hicher, 1993, Mitchell and Soga, 2005] by phenomenological laws. These laws are applied in engineering practice and have benefited, over the last decades, from sophisticated laboratory measurements [Tatsuoka, 2001, di Benedetto et al., 2003].

The increasing strain in granular material under a constant load, also known as creep, is a phenomenon observed at the macroscopic scale. The creep of granular materials is commonly explained by different origins. One potential origin is grains rearrangement [Augustesen et al., 2004, Karimpour and Lade, 2013]. The granular structure might rearrange under a constant load either due to some disturbance occurring on the global structure or because of grains breakage [Leung et al., 1997, Mc-Dowell, 2003] at high stress levels. In both cases, the sample would collapse in order to construct a new structure capable of sustaining the applied load. The reorganization of the grains results in a measurable strain under the constant load. Another potential origin might be some sort of plasticity or damage at the contacts between grains. It has been shown that assemblies of smooth beads exhibit less deformations than assemblies of angular particles [Cavaretta et al., 2010]. This allows thinking that through time grains may undergo surface damages that weaken the contacts and produce additional strain during time.

The logarithmic behavior commonly attributed to creep [Leung et al., 1997, Lade and Liu, 1998, Pestana and Whittle, 1998, Karimpour and Lade, 2013] may be explained by the fact that these potential causes of creep occur less and less with time. For instance, the structure rearrangement results in a more stable structure, which reduces its susceptibility to rearrange.

With such complex behaviors, it is important to access information at the grain scale in order to better understand and characterize the origin of creep. Therefore, during this thesis, we aim to provide efficient tools for studying such phenomena at grain scale. In particular, we dispose of two powerful techniques that allow to access grain scale information. First, micro-tomography allows to acquire 3D images with fine resolution. Therefore, the sample can be observed at the grain level. Furthermore, this technique combined with image correlation enables to track the evolution of granular structures during mechanical tests [Hall et al., 2010]. The second technique is Discrete Element Method, which is used to simulate granular media. With such technique, one can observe the evolution of internal parameters of the structure which are still inaccessible to experiments. Combining the results of these two methods would provide a better understanding of the mechanism involved in such phenomenon.

In the remainder of this chapter, some experiments are performed on sand in order to probe the creep evolution under oedometric compression and point out some interesting facts regarding creep.

1.2 Preliminary experiments

The objective of the experiments presented in this section is to illustrate some features related to the creep experiments using oedometric compression. These experiments are intended to be performed inside local laboratory tomography facility (in-situ experiments). Before conducting such experiment, we performed these tests outside the tomography setup in order to characterize the expected global behavior which will indicate the in-situ experimental conditions.

Laboratory experiments

In this section, we carry out experiments on sand under oedometric compression to measure the creep strain and to determine the experimental conditions to be expected for later experiments inside the tomography facility. These experiments were conducted in the geotechnical team of Navier laboratory, where a classical cylindrical oedometric cell of a diameter $D = 70$ mm and a height $h = 20$ mm (see Fig. 1.2 (1)) was used. The *Oedometric* compression is an axially symmetric process in which one principal strain component ε_1 is increased by applying a vertical stress σ_1, the other strains are maintained at zero ($\varepsilon_2 = \varepsilon_3 = 0$) (see Fig. 1.2 (6)). This test is one of the simplest anisotropic loading processes, which is representative of natural materials under gravity (e.g. sediments consolidating under their weight).

The sample preparation

The specimen used in those experiments is a Hostun sand. This sand, commonly studied in the french community in different fields, comes from Sibelco quarries located at the East of Hostun, a small village of "*département de la Drôme*" (France). Its grains density is about $\rho_s = 2,65$ g $\cdot$ cm^{-3}. The HN31 variant was used in these experiments and sieved to have a grain size distribution narrowed around a mean diameter of 1.2 mm (see Fig. 1.1).

With the intent of using the same specimen for the in-situ test, we chose to have a relatively large grain diameters in order to obtain a good representation of grains in tomographic images. However, to keep an acceptable representativity of the specimen we need to have enough grains in the cell height. We chose a mean diameter of the grains of 1.2 mm which allows to have more than 16 grains in the height of the cell and about 60 in its diameter. With such grain sizes, a tomography resolution of $40\,\mu$m $\cdot$ vox^{-1} provides about 30 voxels in the grain diameter. This resolution also allows to image the whole oedometric sample with one 3D image with 1800x1800x500 voxels, which is a standard image definition on the laboratory CT-device available at Laboratoire Navier.

The preparation of the specimen was inspired from the pluviation (deposition under gravity) technique that allows to prepare samples with homogeneous density. With this technique, the deposition
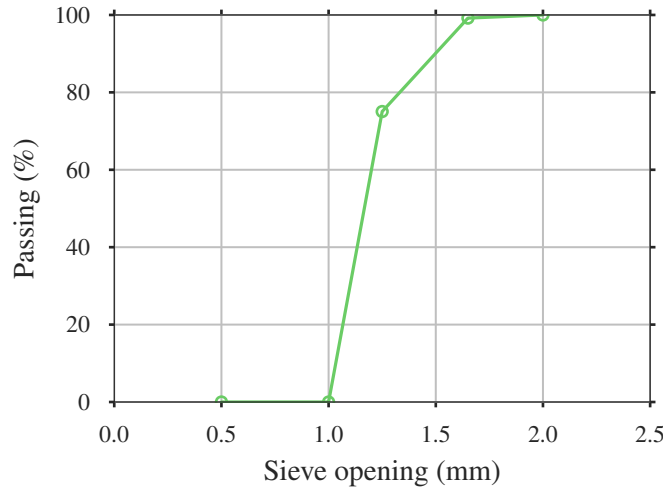
Figure 1.1: Grain size distribution of the Hostun sand (HN31) after sieving.

height is varied with the increase of the specimen height during the grains deposition. The aim is that grains have the same velocity when they reach the specimen surface, regardless of the sample height. The cell used in our case has a small height compared to classical tri-axial test cells. Therefore, in our preparation we did not vary the deposition height. Instead, we used a second sieve to perform a mixing so as to homogenize the sample. The method used for the experiments is detailed in Fig. 1.2 where every step is illustrated.

First, the sand is poured from a height of $H = 20\,\text{cm}$ throughout a sieve of opening size of $10\,\text{mm}$ (step (1) in Fig. 1.2). Once the cell is full (step (2) Fig. 1.2), the second sieve of an opening size of $4\,\text{mm}$ is taken out allowing a second mix of the grains (step (3) Fig. 1.2). Finally, the specimen surface is leveled (step (5) Fig. 1.2), and the load is transmitted to the sample through a metallic stopper (step (6) Fig. 1.2).

At the end of the experiment, the sample is weighted to deduce the initial void ratio using the formula

$$e = \frac{V_{\text{void}}}{V_{\text{solid}}} = \frac{\pi h \rho_{\text{s}} D^2}{4 m_{\text{s}}} - 1, \tag{1.1}$$

where m_{s} is the solid mass (the total mass of grains).

This procedure was used to prepare both wet and dry specimens. At the end of preparation, the wet specimens were saturated. The wetting phase prior to preparation is carried out in order to obtain specimens with higher void ratio [Feng and Yu, 1998].

This method was used on different specimens and provided samples with void ratios of about $e = 0.9$ in the wet preparation, and $e = 0.7$ in the case of dry preparation with fairly good repeatability.
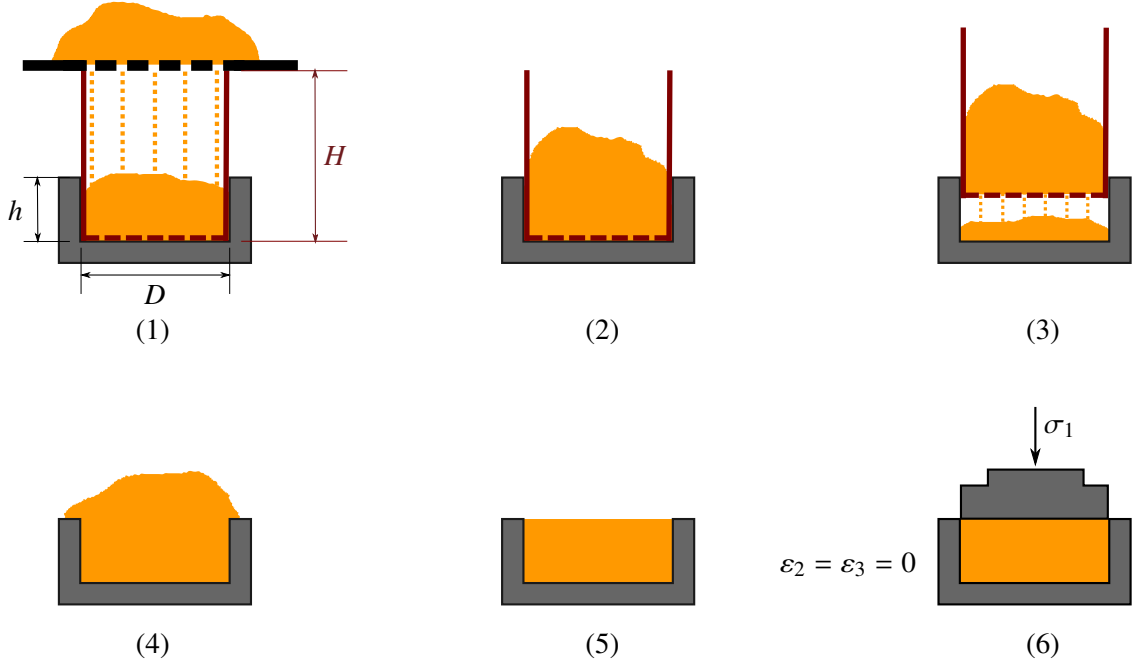
Figure 1.2: Illustration of the procedure used to prepare the samples in the experiments of Sec. 1.2
.

Experimental results

The first result is the difference in the response between dry and saturated specimens. As expected, we observe that the higher instantaneous strain is obtained with the saturated specimen. Consequently, we also observe higher creep strain in the saturated specimen.

The curves in Fig. 1.3 show two different experiments on a saturated and dry sand. A stress $\sigma_1 = 400\,\text{kPa}$ was applied for both samples.

As stated in Sec. 1.1, the creep behavior is commonly modeled as a logarithmic evolution in time. For instance, [Leung et al., 1997] proposed a model where the strain vary with time as:

$$\varepsilon_1 = C \ln t/t_0 \tag{1.2}$$

where t_0 is the time from which creep is measured. C is the creep coefficient, it describes the speed of the creep strain. Measurements of C on the curves presented in Fig. 1.3 gave values of $4 \cdot 10^{-3}\,\%$ for the dry sample and $6.7 \cdot 10^{-3}\,\%$ for the saturated one. In this experiments, the creep time was taken for few hours (16 hours), for which a creep strain of about $0.05\,\%$ for the dry sample and $0.075\,\%$ for the saturated one was obtained. It is shown that looser samples exhibit more creep strain as expected. However, in these experiments the difference between the dry and wet samples is modest. In both cases, these strains are small compared to the instantaneous strains (about 1%). In addition, if we consider the logarithmic behavior and rely on the prediction of Eq. (1.2), after a month of creep only $0.1\,\%$ of strains are expected. In terms of displacement, this value is equivalent to a displacement in order of $20\,\mu\text{m}$, which is only $0.5\,\text{vox}$ for a tomographic resolution of $40\,\mu\text{m} \cdot \text{vox}^{-1}$. Moreover, a large part of this strain occurs at an early stage of the creep phase (more than $30\,\%$ of creep strain is
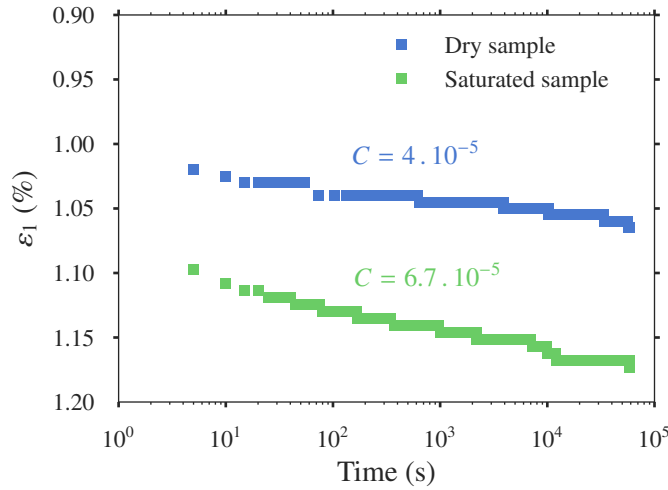
Figure 1.3: Evolution of ε_1 in time, under a constant load of $\sigma_1 = 400\,\text{kPa}$.

measured in the first hour).

Another experiment, where different load levels were applied, showed that with increasing stress level, the observed creep strain increases, as already observed by [Karimpour and Lade, 2013]. Fig. 1.4 shows two different experiments. The first experiment (green curve), shows the sand's behavior when we directly apply a stress $\sigma_1 = 400\,\text{kPa}$. In the second curve (blue curve), the load was applied in increments. At the beginning, a stress $\sigma_1 = 25\,\text{kPa}$ was applied, then the sample was let to evolve under this constant stress. After 15 hours, we increased the stress by $\Delta\sigma_1 = 25\,\text{kPa}$ which makes the overall stress equal to $50\,\text{kPa}$. Then, the sample was let to evolve under constant stress (for 5 hours). We later added $50\,\text{kPa}$, $100\,\text{kPa}$ and $200\,\text{kPa}$ until we got to an overall stress of $400\,\text{kPa}$. The sample was always let to evolve under constant stress between two different incremental steps for 50 to 70 hours. We observe that the presence of creep phases between the incremental stress applications somehow allowed to achieve an overall strain ε_1 twice as large as the one obtained with the direct application of the same overall stress $\sigma_1 = 400\,\text{kPa}$. This larger axial strain in the experiment with the progressive application of the load is primarily due to larger instantaneous strains but also to larger creep strains. Even one can not exclude that these larger instantaneous strains could be due to dynamic effects induced by the application of the incremental loads, another possible explanation is that some complex evolutions of the granular structure that occurred during the creep phases, are inducing instantaneous strains during the next load increment larger than those who would have appeared if the stress had been increased in one step.

Oedometric cell for in-situ experiments

In-situ experiments are conducted inside the tomography facility in order to acquire images and apply digital image correlation to measure the displacements field. In order to perform these experiments, a special oedometric cell was designed to properly achieve the creep experience inside the laboratory
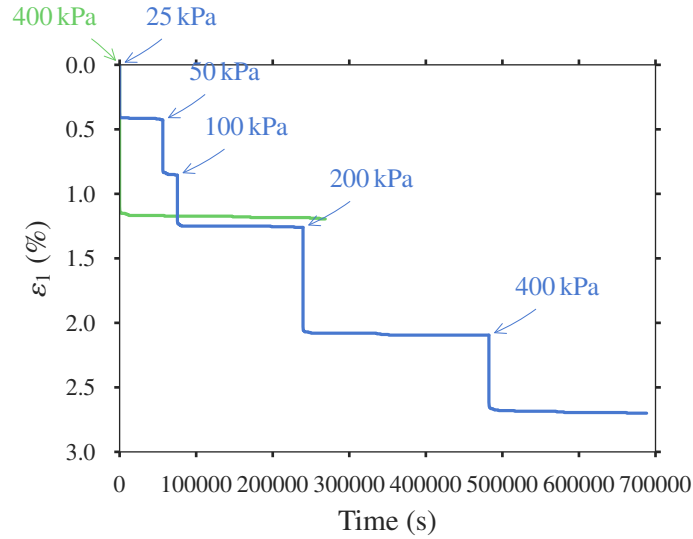
Figure 1.4: Evolution of ε_1 with time, under a constant load of $\sigma_1 = 400$ kPa (green curve) and incremental constant loads (blue curve).

local tomography facility.

This oedometric cell was initially designed during the work of J-F. Bruchon [Bruchon, 2014] to study the mechanical response of sand under oedometric load combined to the effect of imbibition. However, this cell was not perfectly adapted to creep load since the loading device (pneumatic jack) did not allow to maintain a constant load. Therefore, we adapted the cell to use hydraulic jack allowing better pressure control. The hydraulic jack is alimented from a pump which provides a pressure control system that allowed maintaining a constant stress with an accuracy of 0.1 kPa.

Using the new actuator with the cell required adding new features into the cell in order to support the higher stress level and ensure devices safety in case of uncontrolled malfunctioning of the hydraulic jack. In particular, a load cell and a LVDT were used to measure the applied force and the global displacement of the sample. To secure these devices and the tomography setup, some design features were added. Fig. 1.5 shows an image of the cell inside tomography setup where the major parts are indicated.

1.3   Motivation of this work

Creep might be originated from complex and multiple mechanisms. Therefore, some mechanisms at the grain scale need to be addressed with techniques allowing to access the grain scale information of the granular medium. For example, using micro-tomography to acquire images that would allow to track grain movements is a powerful tool. In the experiments presented in this section some important features related to creep were pointed out. However, it was shown that for oedometric compression of sand the observed creep strain is very small which needs a very fine resolution with very accurate measurement techniques allowing subvoxel precision of the displacement. Moreover, a large part
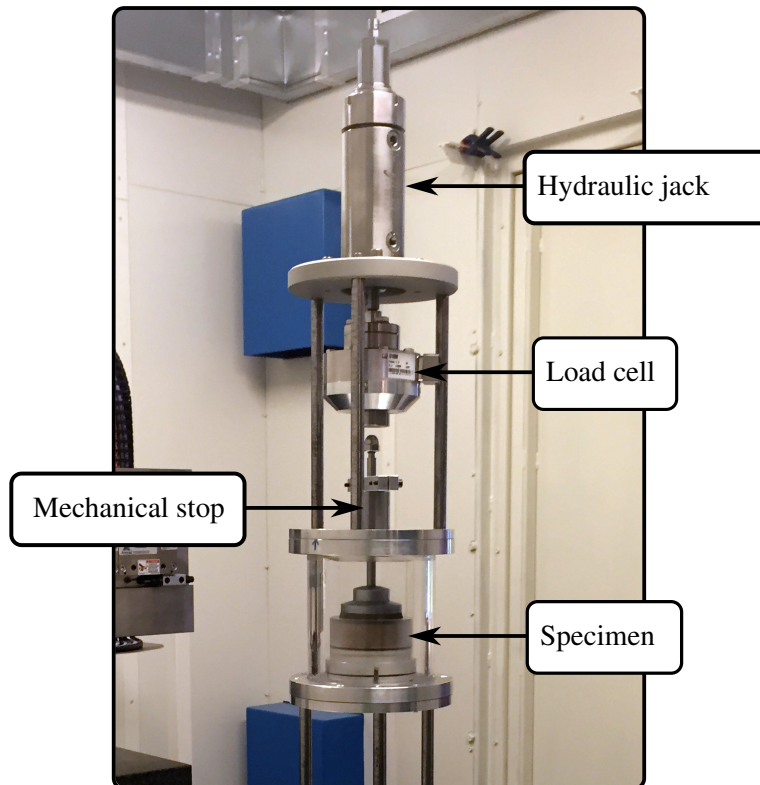
Figure 1.5: Illustration of the oedometric cell designed to carry out in-situ experiments.

of the evolution occurs during the early stage of experiments. Knowing that a tomographic image needs about 1 hour of acquisition time, these short-term evolutions cannot be caught by a complete image acquisition. Therefore, in this doctoral work, we provide a new method to measure the grains displacement with tomography that allows reducing the acquisition time needed to less than few minutes.

Tomography acquisition allows to access multiple grain scale information of the granular medium, and combined with digital image correlation it allows to measure the displacements. However, some structure information is still difficult to retrieve, even with the finest resolutions. For instance, contact detection is complex to establish from tomographic images. Therefore, the coordination number and the contact distributions are not accessible. The force network (the amplitude of the force carried by a grain contact) is even more difficult to measure. Nevertheless, numerical simulations provide readily such information. Accordingly, we propose to study in this work the oedometric compression by the Discrete Element Method in order to characterize this compression in an attempt to relate the internal structure parameters (that are accessible to simulations) to some macroscopic parameters that can be measured from the experiments. For example, the elastic moduli, which can be measured for granular materials in both experiments and simulations, can be related to the internal parameters of the structure. In some studies, the measurement of the elastic parameters was used to characterize the macroscopic creep behavior [Miksic and Alava, 2013].

1.4 Structure of this thesis

As stated in Sec. 1.3, the motivation behind this work is the study of creep in granular materials. In this thesis, a new method for measuring grain displacements using tomography is proposed. This method is more convenient for studying time-resolved phenomena. Moreover, Discrete Element Method is used to model the oedometric compression in the aim of characterizing this mechanical test and providing measurable quantities in order to relate the numeric simulations and the experiments. The results of this work are separated in four chapters as follows:

Chapter 2: The Discrete Digital Projection Correlation method (D-DPC)

Using tomography to track grains displacement in time-resolved phenomena such as creep is limited by the long acquisition time needed to acquire tomographic images. The new method described in this chapter overcomes this limitation. The principle of the method is fully detailed and the method is applied on a validation case. The results of this chapter made the subject of an article submitted to Experimental Mechanics [Khalili et al., a].

Chapter 3: Assessment of errors in D-DPC

This chapter investigates the origins of the errors in the D-DPC method in order to understand them and to provide prospective enhancements of the method accuracy. It is noted that even if the main advantage of the D-DPC method is to obtain an accuracy in the determination of the motions of

individual grains similar to more classical methods with a much shorter acquisition time, another application might be to increase the accuracy of motion quantification using a similar number of projections than classical techniques. This second point of view might be useful to investigate creep mechanisms in the long term, where acquisition time is no longer an issue but accuracy improvement are critical, since strains are very small. It is shown in that chapter that some current limitations of the D-DPC method will not yet allow for such investigations, but routes to go into that directions are provided.

Chapter 4: Characterization of oedometric compression using Discrete Element Method

This chapter reproduces the content of an article submitted to Physical Review E [Khalili et al., c]. In this chapter, the oedometric compression of granular assemblies is modeled using the Discrete Element Method. Both macroscopic and microscopic behaviors are investigated in groups of samples with different internal structure parameters. Characteristics such as density, coordination number, fabric and stress anisotropies are monitored during oedometric loading cycles.

Chapter 5: The elastic parameters and internal state of structures

In this chapter a complementary study to the oedometric compression studied in Chap. 4 is carried out. This chapter contains the content of the companion article of [Khalili et al., c], also submitted to Physical Review E [Khalili et al., b]. In this part, a specific focus is given to the study of the five independent elastic moduli for the samples studied in Chap. 4. These moduli evolutions are investigated against the evolutions of density, coordination number, fabric and force anisotropies.

Chapter 2

The Discrete Digital Projection Correlation method

Contents

In the present work, we aim to perform full-field measurements of mechanical tests of granular materials. These tests are conducted inside the local laboratory tomography facility. The classical volumetric digital image correlation methods are commonly used to achieve such measurements. However, using these methods constitutes a limitation when studying time-resolved phenomena in laboratory tomography setups. In such facilities, a long acquisition time is needed to acquire enough radiographs for an accurate full 3D image reconstruction. The classical methods usually compare the full 3D reconstructions of the reference (undeformed) and current (deformed) states, which is not suitable for studies of time-resolved behaviors, because of the long acquisition time. In the present chapter, we present a new method called *Discrete Digital Projection Correlation* (D-DPC) that overcomes this limitation. In this method, a minimization process allows the correlation to be preformed directly on the tomographic projections.

This chapter describes the principle of the method and some applications. It starts with a brief overview of the available digital image correlation techniques in Sec. 2.1. Then the principle of the new method D-DPC is described in Sec. 2.2. Sec. 2.3 introduces some notations relating to grains kinematics and the projection model. This model allows tomography projections to be simulated with the intent of comparing them to experimental projections in an optimization procedure that constitutes an important phase of the method process. Sec. 2.4 provides an overview of different methods to perform numerical estimation of the Radon transform of a ray from a digital image. This step is crucial for the execution time of the method. Hence, a comparison between algorithms and an algorithm that we propose was necessary to choose the most efficient one. In Sec. 2.5 we study the optimization process and investigate its performances. In Sec. 2.6, 2D synthetic experiments are performed as validation of the technique, while in Sec. 2.7 details on the implementation for the 3D case are provided. Finally, we perform a complete 3D in-situ experiment to discuss and illustrate a real case application of the method.

2.1   Digital Image Correlation

Digital Image Correlation (DIC) is becoming a conventional tool for the investigating of material behaviors. Unlike the typical measurement devices (strain gauges, dial indicators, differential transformers...) that can only measure global values or a value at a specific point, DIC can provide displacements and strains for several points. The principle of DIC relies on having two digital images of the mechanical setup: a reference image (in which every point in the space has a grayscale value) and a deformed (current) state image. The aim is to find the displacement field which transforms the first image into the second one. For this purpose, a correlation coefficient is defined to measure the discrepancy in terms of gray level distributions between the reference image and the deformed one, back convected according to the displacement field. Therefore, the correlation process is to optimize the correlation coefficient between the two states in order to estimate the displacement field. The target displacement field is modeled through some shape function that can be of different orders [Sutton et al., 2009] and that accounts for the displacements in the computation of the correlation

coefficient, assuming conservation of gray levels. This procedure is known as cross-correlation and multiple approaches using this technique have been proposed [Chambon and Crouzil, 2003, Bornert et al., 2004].

The first applications of DIC were restricted to surface measurements and are referred to as 2D-DIC. These techniques can be devided into two major types that differ by the region in which the correlation criterion is optimized. The group that was first introduced is the local correlation techniques also called subset based methods. Their principle is to identify individual sub-regions (subsets) in the reference image. Then, the shape function parameters are individually optimized in the deformed image for every subset. The second group was introduced in the early 2000's and gathers techniques referred to as global approaches. The idea of a global approach is to perform the correlation over the entire ROI (region of interest). The major concern of this type of techniques is the choice of an adequate shape function that will allow an accurate correlation over the entire ROI. Some researchers have proposed the use of Fourier-based kinematics [Wagne et al., 2002, Roux et al., 2002] and later finite-element based functions were proposed. For instance, the Q4-DIC [Besnard et al., 2006] uses four-noded (Q4) elements to discretize the shape function over a regular mesh of the ROI.

In order to reach subpixel measurement resolution, DIC methods make use of interpolation techniques to evaluate the gray levels at subpixel positions. Multiple subpixel interpolations can be used (bilinear, bicubic, splines, Fourier...). The choice of the interpolation technique has to be made carrefully since it can have a strong influence on the uncertainty of measurements [Schreier et al., 2000].

The 2D-DIC methods suffer from limitations related to the out-of-plane motion. For accurate measurements of in-plane strain components, the experiment should guarantee that the imaged surface of the specimen remains planar; otherwise, only in-plane components of the deformation gradient can be determined, and additional assumptions or corrections need to be adopted to evaluate in-plane strain components. To overcome these limitations, 3D-DIC methods that use stereo-vision [Lucas et al., 1981] have been introduced. These techniques allow measuring the 3D motion of planar or curved specimens which allows considering the out-of-plane motion [Sutton et al., 2008] at the price of an accurate calibration of the stereo-vision system. However, even with 3D-DIC, out-of-plane components of strains are still out of reach and the only available measurements are from surface measurements of the material which may not be representative of its three-dimensional behavior. For this reason, it is preferable to use volume images when possible. Micro-tomography can provide such 3D images. Theses volumetric images can be used with Volumetric Digital Image Correlation (V-DIC) which is an extension of the local approach to 3D images introduced by [Bay et al., 1999] in 1999 Also, an extension of Q4-DIC to digital volumes exists [Roux et al., 2008, Rannou et al., 2010] and was named C8-DVC as it uses eight-noded volume elements in the shape function to perform the Digital Volume Correlation.

In this work, we are interested in studying granular materials. When the granular material can be assumed as continuous the V-DIC method can be used on 3D images to measure the apparent dis-

placement of the material. For example, [Bruchon et al., 2013] used V-DIC to investigate the capillary collapse phenomenon in sands. Nevertheless, when the investigation of grain scale phenomena like grain rearrangement is needed, it is no longer possible to consider the granular medium as continuous, and it is more appropriate to retrieve individual grains displacements. For this purpose, discrete methods have been introduced. These methods make the assumption that every grain undergoes a rigid body motion. This assumption is generally true for granular material as long as no breakage occurs. Discrete V-DIC (DV-DIC) [Hall et al., 2010] and the discrete particle tracking approach (ID-Track) [Ando et al., 2012] are two of these techniques. Both techniques are based on an initial segmentation of the granular medium that identifies every individual grain in the reference state. In DV-DIC, a first displacement approximation is made with classical V-DIC where every grain defines a correlation window (subset). Then, using registration algorithms, the six degrees of freedom of every grain are optimized. This procedure was implemented in the CMV-3D program [Bornert et al., 2004]. With this technique a precision about 0.1 voxels in translation and 0.1° in rotation can be obtained as reported in [Pannier et al., 2010] when applied on typical images of sand recorded with a laboratory CT-device, with about 60 voxels in the diameter of the grains. ID-Track uses information about the grain geometry to perform the image matching. A segmentation of the deformed state is also required, in order to pair up every grain in the reference state to its corresponding grain in the deformed state. For each grain in the reference state, an initial search based on its center of mass provides potential corresponding grains in the deformed state (it is assumed that the grain stays within a specified distance of its reference state). Then to identify the exact grain amongst the potential candidates, the grain with the closest volume is chosen. Once the grains are successfully paired up, the centers of masses allow the translations to be determined, and rotations are deduced from the eigenvectors of the inertia tensor for the grains in both states. The authors indicate an expected accuracy of translations under 0.05 voxels while the rotations precision is poor compared to DV-DIC (about 16°) especially for rounded grains (up to 28°). These techniques have been used to understand complex phenomena such as strain localization in granular media. Their applications to triaxial tests showed that grains undergo large rotations within shear bands which may have a thickness of several grains.

In both methods, the full 3D reconstruction of the deformed state is required. Therefore, the time resolution is restricted by the time necessary for a complete scan. The acquisition can be very long, especially in laboratory devices, and hence, prevents from studying time-resolved phenomena. In the remainder of this chapter, we will introduce a new method that aims to overcome this limitation. The method is named Discrete Digital Projection Correlation (D-DPC), as it does not require to reconstruct the deformed state and works directly on its projections. The principle of the method is the subject of the next section.

2.2   Principle of the D-DPC method

As stated in Sec. 2.1 classic image correlation methods demand the full 3D reconstruction of the deformed state. Unluckily, an adequate 3D full reconstruction requires a large number of tomographic

projections, because it involves solving for a large number of unknowns. The unknowns here are the grayscale values in every voxel of the 3D image. For instance, in a detector dimension of L^2 pixels the expected number of image voxels is L^3. Therefore, to reconstruct an accurate image one needs at least L^3 independent measurements which can be given by L projections. In order to reconstruct a volume with $L = 1000$ vox one needs at least 1000 projections. The reconstruction algorithms based on the filtered back-projection might require slightly less projections. For instance, in the local laboratory tomographic setup we, generally, use 1440 projections for 3D images with a typical cross-section of 1800x1800 voxels. With an exposure time of 2s, the scan needs about 1 hour to complete, which is unpractical for measuring fast evolutions. Note that faster acquisition are possible, but at the price of a much higher noise levels in the reconstructed images, which would induce unacceptable errors in the evaluation of the kinematics of the grains. Such limitation is not encountered with Synchrotron tomography where high quality fast acquisitions are possible [Lhuissier et al., 2012, Limodin et al., 2007, Mader et al., 2011]. But these facilities are not as accessible as local laboratory tomography setups. In addition, the width of the synchrotron X-ray beams is often limited (typically less than 20 mm), so that the full investigation of larger samples as those described in Chap. 1 is not possible.

With D-DPC we want to reduce this acquisition time by only taking few projections of the deformed state, which will considerably reduce the scanning time to few minutes or less.

In fact, our main interest is the grain movements inside the sample. These movements constitute a smaller number of unknowns in comparison to the number of unknowns in a full 3D reconstruction. Therefore, in principle, a small number of projections is enough to solve the grain displacements.

This principle was previously employed to reduce the projections needed for accurate image reconstruction, where the unknowns to determine were made smaller than the number of the entire 3D image voxels. For instance, [Sidky et al., 2006] used the prior knowledge of the gradient image sparseness to achieve a reconstruction with fewer data (projections). Because the image gradient is sparse, the total variation of the image can be minimized to compensate for the reduced amount of data available to reconstruct the image.

Another work by [Myers et al., 2015] used this principle to measure fast dynamic evolution in the sample from tomography projections. For example, measuring the dynamic water flow level in a granular structure was made possible by only taking few projections in small time steps. First, the granular structure was determined from a reference reconstruction with a complete tomographic scan. This reconstruction provides a knowledge of the void space, which combined with an adequate modeling of the water flow allowed to only reconstruct the void regions susceptible to receive water. Therefore, the evolutions of water level was determined by steps with few projections.

In our case, we reduce the required data by only considering the grain displacements. However, to directly address this system of unknowns, we must skip the reconstruction phase that needs a larger amount of information. The idea is to reformulate the correlation problem directly on the projections rather than the 3D images. In this way we can use just as many projections as are needed to resolve the grain displacements and reduce the acquisition time. What we are aiming to do, is to use the minimum number of tomography projections to determine the grain rigid body motions. This is

possible because the grain geometry is *a priori* known from the reference state full 3D reconstruction. But, the projections do not depend linearly on the grains displacements as they do with the gray levels of the reconstructed image. For this reason, we will compute the variation of the projections for a trial displacement field and then through a minimization process we will try to find the displacements that provide the same variations as in the projections of the deformed state. To summarize, the reconstructed image of the undeformed state provides a description of grain geometry, from which digital projections are constructed. These projections are then correlated to the projections of the actual state to determine the grain displacements.

Our method can also be presented as a reconstruction technique. Once the kinematics of each grain are determined, the knowledge of grain geometry from the 3D full reconstruction of the reference configuration, can be used to reconstruct the current configuration, if needed.

D-DPC was independently and quasi-simultaneously developed alongside the Projection-based Digital Volume Correlation Procedure (P-DVC) [Leclerc et al., 2015]. This method uses the same principle to measure displacement fields in continua. The reduced system of unknowns in this case is obtained by considering the nodal degrees of freedom of a superimposed mesh. After the reference state full 3D reconstruction was acquired the displacement field sought is decomposed into a suitable kinematic basis (finite element functions like in C8-DVC[Roux et al., 2008]). Then, and since the microstructural details are known from the reference image, digital projections for trial displacement field can be generated and correlated to the available experimental projections. The optimization parameters here are the components of the displacement as expressed by the chosen kinematic basis.

In D-DPC, the optimization parameters are the grain rigid body motions. The vector $\mathbf{q}$ contains these optimization parameters (see Sec. 2.3). Consider that a complete description of the grain geometries is available from the full 3D reconstruction of the sample at its reference state. We acquire a set of projections containing enough information to determine $\mathbf{q}$ at the current state. These experimental projections will be noted $P(\theta, \underline{p})$ for a projection orientation θ and a detector pixel $\underline{p}$. The method is formulated as an inverse problem that consists in determining the current value of $\mathbf{q}$ by minimizing the discrepancy between digital projections $\hat{P}(\theta, \underline{p}; \mathbf{q})$ and experimental projections. In this work, we choose the quadratic difference between the two sets of projections as a cost function

$$\mathrm{F}(\mathbf{q}) = \sum_{\theta, \underline{p}} \left(\hat{P}(\theta, \underline{p}; \mathbf{q}) - P(\theta, \underline{p}) \right)^2 \tag{2.1}$$

and the D-DPC method consists in minimizing this function to obtain the optimal parameters

$$\mathbf{q}_{\text{D-DPC}} = \underset{\mathbf{q}}{\mathrm{Argmin}} \left(\mathrm{F}(\mathbf{q}) \right) \tag{2.2}$$

Fig. 2.2 compares D-DPC to the classical methods in Fig. 2.1. Fig. 2.2 shows that from the full 3D reconstruction (step 2) we can apply a displacement field vector $\mathbf{q}_{\text{trial}}$ as an initial guess of the exact displacement of the grains. This allows to generate the digital projections (step 4) which we compare to the few acquired projections in the deformed state (step 3) to improve the initial guess ($\mathbf{q}_{\text{trial}}$) until the iterations converge to the solution which is the displacements of the grains in the deformed state.
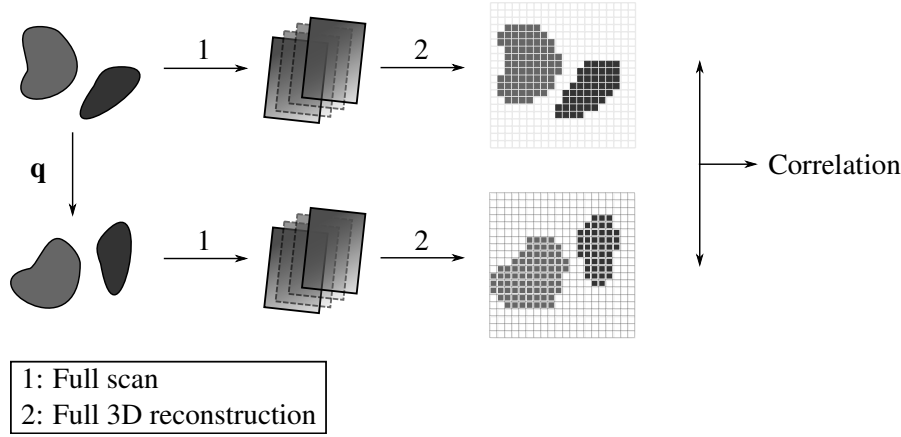
Figure 2.1: Illustration of classical volumetric image correlation techniques. The full 3D reconstructions of both states are required to carry out the correlation.

In the classical methods (see Fig. 2.1), the correlation is made on the 3D full reconstruction of both states.

Computing adequate digital projections that will allow an accurate representation of the tomographic projections is one challenging part of this method. In the next section, we will describe the model used to simulate such projections, which is the forward problem of D-DPC seen as an inverse problem.

2.3   Projection model (forward model)

The projection model of D-DPC simulates digital projections of an assembly of grains for any given set of rigid body motions. This model is based on Beer-Lambert's law that relates the measured intensity to the attenuation of the sample. We assume that every detector pixel is associated with a unique ray. This assumption, which is classically made in algebraic reconstruction algorithms [Kak and Slaney, 1988, Sidky et al., 2006], will be referred to as the *Lumped beam* assumption.

Note that when generating the digital projections, the voxel-based representation of the grains is taken from the initial 3D full reconstruction and is not resampled on a rotated grid. We adopt a *Lagrangian* approach where the rigid body motion is applied to the rays rather than the grains. Hence, the projection is computed in the reference state of the grain as illustrated in Fig. 2.2 (step 4), which prevents loss of accuracy.

For later use, we introduce some notations relating to the tomography setup. The sample is denoted $\mathcal{G}$ and is placed on a rotating stage. Δ denotes its axis of rotation; it is oriented by the unit vector $\underline{e}_\Delta$. The origin O is placed on the rotation axis Δ. With respect to the origin, points are identified with their radius vector.

The sample is illuminated by an X-ray source (parallel or cone-beam), and the resulting projection is measured on a detector $\mathcal{D}$. Each point $\underline{p} \in \mathcal{D}$ of the detector is hit by a unique ray, the direction of which is given by the unit vector $\underline{T}(\underline{p})$, oriented from the source to the detector. We will make the assumption that pixel values returned by the detector correspond to the intensity at the center of
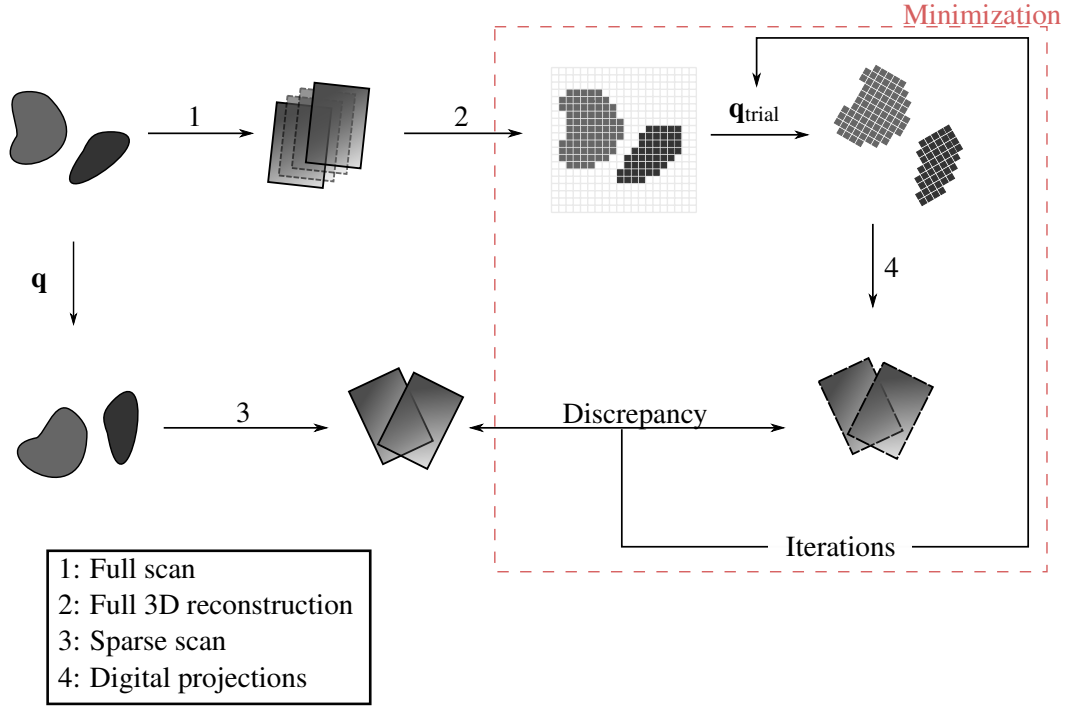
Figure 2.2: Illustration of the D-DPC method. In this method, a minimization process is used to determine the displacements of each grain. A trial displacement field $\mathbf{q}_{\text{trial}}$ is proposed at each iteration based on the comparison of minimal digital and experimental projections. The digital projections are computed from the full 3D reconstruction of the reference state (4).

the pixel; therefore, $\underline{p} \in \mathcal{D}$ will usually refer in the following to the center of a pixel of the detector. For parallel projections, we have $\underline{T}(\underline{p})$ = const. (see Fig. 2.3), while for cone-beam projections (see Fig. 2.4)

$$\underline{T}(\underline{p}) = \frac{\underline{p} - \underline{a}}{\|\underline{p} - \underline{a}\|}, \tag{2.3}$$

where $\underline{a}$ denotes the location of the X-ray point source (apex of the cone).

Note that our method is formulated in an intrinsic way which does *not* require perfect geometries. In particular, it is not assumed that the detector $\mathcal{D}$ is planar or parallel to the axis of rotation Δ of the sample stage. Likewise, it is not assumed that the plane which contains the axis of rotation Δ and the point source $\underline{a}$ is perpendicular to the detector $\mathcal{D}$. However, a "ideal" geometry of the tomography setup will be considered for the applications: for parallel setups, the detector and the axis of rotation of the sample are parallel and the direction of X-rays is perpendicular to the detector, while for cone-beam setups, the axis of rotation of the sample is parallel to the detector, and the plane formed by the point source and the axis of rotation is perpendicular to the detector.

In both cases of ideal geometries, it is convenient to introduce a global frame $(O, \underline{e}_x, \underline{e}_y, \underline{e}_z)$ defined as follows (see also Figs. 2.3 and 2.4). $\underline{e}_z$ is the normal to the detector; it points in the direction of propagation of the X-rays. $\underline{e}_y = \underline{e}_\Delta$ is the (ascending) direction of the axis of rotation. Finally,
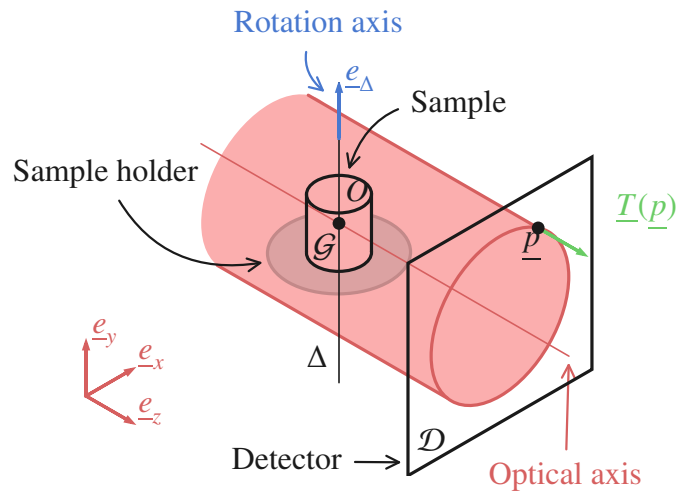
Figure 2.3: Tomography setup for parallel (synchrotron) tomography.
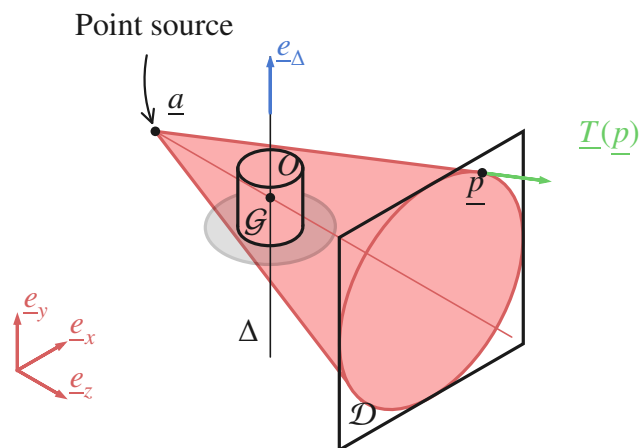

Figure 2.4: Tomography setup for cone-beam (laboratory) tomography.

$\underline{e}_x = \underline{e}_y \times \underline{e}_z$. Besides, for cone-beam setups, the origin O is placed at the intersection between the normal to the detector passing through the point source, and the axis of rotation.

Projection of a single grain

If we consider a unique grain $\mathcal{G}$ scanned in the tomography setup described in 2.1, the Beer-lambert law gives the intensity of a ray measured by a pixel $\underline{p}$ of the detector after it was attenuated by $\mathcal{G}$:

$$I(\underline{p}) = I_0(\underline{p}) \exp\left(-\int \mu\left(\underline{p} + s\underline{T}(\underline{p})\right) ds\right) \tag{2.4}$$

where the map $\underline{x} \in \mathcal{G} \mapsto \mu(\underline{x})$ denotes the grain local linear attenuation coefficient and $I_0(\underline{p})$ the initial intensity of the ray (which might depend on $\underline{p}$). The equation of the ray is described by the arc-length s, the pixel $\underline{p}$ and the direction vector $\underline{T}(\underline{p})$. For what follows we will assimilate the projection on pixel $\underline{p}$ to :

$$\log\left[\frac{I_0}{I}\right](\underline{p}) = \int \mu\left(\underline{p} + s\underline{T}(\underline{p})\right) ds \tag{2.5}$$

This grain undergoes a rigid body motion composed of a translation vector $\underline{u} \in \mathbb{R}^3$ and a rotation denoted by the rotation tensor $\underline{\underline{\Omega}} \in SO(3)$, so that the point initially located at $\underline{X}$ is transported to

$$\underline{x} = \underline{\underline{\Omega}} \cdot \left(\underline{X} - \underline{x}_0\right) + \underline{u} + \underline{x}_0, \tag{2.6}$$

where $\underline{x}_0$ is the center of rotation. Therefore, assuming conservation of the attenuation coefficient during the motion, the projection of the grain at this state reads

$$\log\left[\frac{I_0}{I}\right](\underline{p}) = \int \mu\left(\underline{\underline{\Omega}}^T \cdot \left[\underline{p} + s\underline{T}(\underline{p}) - \underline{u} - \underline{x}_0\right] + \underline{x}_0\right) ds \tag{2.7}$$

Now we will take into account the rotation of the sample stage, the rotation θ about the $\underline{e}_y$ axis (see Figs. 2.3 and 2.4) which corresponds to a rotation tensor $\underline{\underline{R}}_\theta$ the components of which read

$$\underline{\underline{R}}_\theta = \begin{bmatrix} \cos\theta & 0 & \sin\theta \\ 0 & 1 & 0 \\ -\sin\theta & 0 & \cos\theta \end{bmatrix}. \tag{2.8}$$

Composing the rigid body motion of the grain and the rotation of the sample stage, leads to the following formula for the projection at pixel $\underline{p}$ and angle θ of the displaced grain $\mathcal{G}$

$$\log\left(\left[\frac{I_0}{I}\right](\underline{p})\right) = \int \mu\left(\underline{\underline{\Omega}}^T \cdot \left[\underline{\underline{R}}_\theta^T \cdot \left(\underline{p} + s\underline{T}(\underline{p})\right) - \underline{u} - \underline{x}_0\right] + \underline{x}_0\right) ds. \tag{2.9}$$

Extension to assemblies of grains

We now consider an assembly of n grains, where grain i undergoes a rigid body motion defined by the translation $\underline{u}^{(i)}$, the rotation center $\underline{x}_0^{(i)}$ and the rotation tensor $\underline{\underline{\Omega}}^{(i)}$. Assuming that the attenuation coefficient outside the grains is null, the overall attenuation field μ can be written as the sum of the attenuation fields associated with every grain $\mu^{(i)}$. Hence the projection in Eq. (2.9) becomes:

$$\hat{P}(\theta, \underline{p}; \underline{u}^{(1)}, \underline{\underline{\Omega}}^{(1)}, \ldots, \underline{u}^{(n)}, \underline{\underline{\Omega}}^{(n)}) = \sum_i \hat{P}^{(i)}(\theta, \underline{p}; \underline{u}^{(i)}, \underline{\underline{\Omega}}^{(i)}) \tag{2.10}$$

where

$$\hat{P}^{(i)}(\theta, \underline{p}; \underline{u}^{(i)}, \underline{\underline{\Omega}}^{(i)}) = \int \mu^{(i)}\left(\underline{\underline{\Omega}}^{(i)T} \cdot \left[\underline{\underline{R}}_\theta^T \cdot \left(\underline{p} + s\underline{T}(\underline{p})\right) - \underline{u}^{(i)} - \underline{x}_0^{(i)}\right] + \underline{x}_0^{(i)}\right) \mathrm{d}s \tag{2.11}$$

The Eq. (2.10) defines our projection model. This solves the forward model of our method, which is to compute digital projections from a known geometry of a granular medium, for any given set of rigid body motions.

Note that a center of rotation $\underline{x}_0^{(i)}$ chosen far from the grain, will produce artificially large amplitude of translation $\underline{u}^{(i)}$ for the different grains. This issue may inhibit the convergence of the inverse problem considered in this method. To avoid this issue, the center of rotation $\underline{x}_0^{(i)}$ was placed at the center of mass of grain i.

Compact representation of the optimization parameters

For later use in the minimization, we need to parametrize the rotations $\underline{\underline{\Omega}}^{(i)}$. We use Rodrigues' formula [Rodrigues, 1840] to map the rotation vector $\underline{\omega}^{(i)} = \omega^{(i)}\underline{n}^{(i)}$ to the rotation tensor $\underline{\underline{\Omega}}^{(i)}$, where $\omega^{(i)}$ is the angle of rotation and $\underline{n}^{(i)}$ is the axis of rotation ($\|\underline{n}^{(i)}\| = 1$).

$$\underline{\underline{\Omega}} = \underline{\underline{I}} + \frac{\sin \omega}{\omega}\underline{\underline{\omega}} + \frac{1 - \cos \omega}{\omega^2}\underline{\underline{\omega}}^2 = \exp \underline{\underline{\omega}}, \tag{2.12}$$

where $\underline{\underline{\omega}}$ is the skew-symmetric tensor such that $\underline{\underline{\omega}} \cdot \underline{x} = \underline{\omega} \times \underline{x}$ for all $\underline{x} \in \mathbb{R}^3$. It should be noted that this parametrization is not differentiable at some points (namely, $\omega = 2\pi$) [Cardona and Geradin, 1988, Ibrahimbegović et al., 1995], which might cause issues with gradient-based optimization algorithms. An alternative choice would be to use a quaternion description [Hamilton, 1853], which does not suffer from this issue. However, in this work, the expected rotations are relatively small, so that it was not required to consider this corner case.

With this parametrization of rotations, we gather the degrees of freedom (translations and rotations) of all grains in a unique column-vector

$$\mathbf{q} = (\underline{u}^{(1)}, \underline{\omega}^{(1)}, \ldots, \underline{u}^{(n)}, \underline{\omega}^{(n)}). \tag{2.13}$$

The projection model defined by Eqs. (2.10) and (2.11) can then be written

$$\hat{P}(\theta, \underline{p}; \mathbf{q}) = \sum_i \hat{P}^{(i)}(\theta, \underline{p}; \mathbf{q}^{(i)}),$$
(2.14)

where $\mathbf{q}^{(i)} = \mathbf{S}^{(i)} \cdot \mathbf{q}$ and the $6n \times 6$ matrix $\mathbf{S}^{(i)}$ selects the rows in $\mathbf{q}$ corresponding to $\underline{u}^{(i)}$ and $\underline{\omega}^{(i)}$

$$\mathbf{S}^{(i)} = [\underbrace{\mathbf{O}_6, \dots, \mathbf{O}_6}_{i-1 \text{ times}}, \mathbf{I}_6, \underbrace{\mathbf{O}_6, \dots, \mathbf{O}_6}_{n-i \text{ times}}],$$
(2.15)

($\mathbf{O}_6$: 6×6 null matrix; $\mathbf{I}_6$: 6×6 identity matrix).

Discretization

At this stage we have fully resolved the forward problem (step 4 in Fig. 2.2). Our projection model can generate digital projections of the granular medium for any given displacement field. In practical situations, the mapping of the attenuation field at the reference state is only known on a discretized grid of voxels resulting from detector discretization. Therefore attenuation should be written as follows:

$$\mu(\underline{x}) = \sum_{\underline{v}} \mu(\underline{v})\chi(\underline{x} - \underline{v}),$$
(2.16)

where $\underline{v}$ denotes the center of the current voxel and χ is the indicator function of the voxel centered at the origin. The projection formula (2.5) then becomes

$$\sum_{\underline{v}} \mu(\underline{v}) \int \chi\left(\underline{p} - \underline{v} + s\underline{T}(\underline{p})\right) \mathrm{d}s,$$
(2.17)

where the term

$$\int \chi\left(\underline{p} - \underline{v} + s\underline{T}(\underline{p})\right) \mathrm{d}s,$$

is the intersection length of the chord of the voxel centered at $\underline{v}$, supported by the ray $(\underline{p}, \underline{T}(\underline{p}))$. Thus, the value of the projection is the summation of the chord lengths weighted by their attenuation coefficients $\mu(\underline{v})$. This summation is referred to as the radiological path and can be evaluated through several algorithms discussed in the next section.

2.4   Radiological path algorithms

To estimate the radiological path we need a suitable algorithm. The algorithm should be fast so that projections are computed in a reasonable time. The estimation of the digital projections is a repeated frequently during the optimization. Hence, the time needed to evaluate the radiological path is crucial for the optimization speed. For this reason, we test the speed of different algorithms in order to use the fastest for the D-DPC forward model. In what follows and for the sake of simplicity we will only
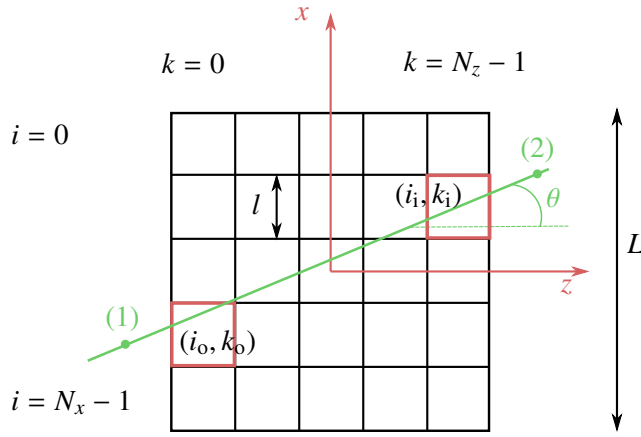
Figure 2.5: A grid representation of a 2D image in the Oxz plan. A ray going through the image is plotted in green, the ray is tilted by θ from the z axis. Points (1) and (2) are chosen in the ray.

describe the different algorithms in their two-dimensional versions. Some implementation details will be given, which requires introduction of some notation to describe 2D images.

A grayscale image is an array in which every element contains a gray level value. These elements are the image pixels. In the 3D case, the volumetric image elements are named voxels. In this work, we are dealing with two types of images, the projections which are 2D images (array of pixels) and the object image which is a 3D image (array of voxels). In the 2D examples, the object is also a 2D image, but we will be referring to its elements as voxels in order to avoid any confusion between the object pixels and the projections pixels.

Fig. 2.5 illustrates a grid representation of the 2D image inside the global reference frame, where i denotes the pixel position along the x axis and k the z axis. The voxels are given a size l which also defines the image resolution. The plane considered is the (Oxz) (see Figs. 2.3, 2.4 and 2.5). We denote by N_x the number of voxels in the x axis and N_z in the z axis such as point $\underline{v}$ is inside the voxel indexed by:

$$i = \frac{N_x - 1}{2} - \left\lfloor \frac{v_x}{l} \right\rfloor, \qquad k = \frac{N_z - 1}{2} + \left\lfloor \frac{v_z}{l} \right\rfloor \tag{2.18}$$

where $\lfloor \cdot \rfloor$ is the floor function.

Naive approach

The first approach that we adopted was to derive a closed-form expression of the intersection length of the ray with the voxel. This expression (and radiological path consequently) depends on geometrical parameters. As is shown in Fig. 2.6 the intersection length of a segment (ray) and a square (voxel) is completely parametrized with two variables r and α. A chord function is defined to express the
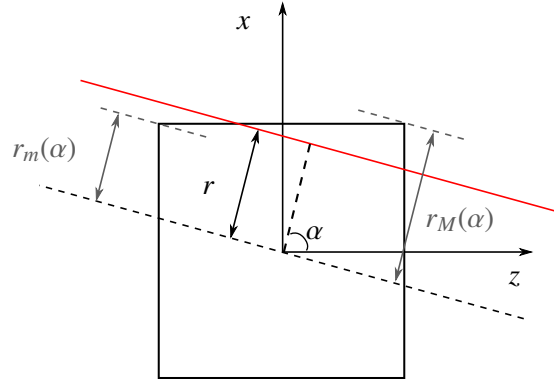
Figure 2.6: Illustration of the parameters used in the chord function in Eq. (2.19)

intersection length between a line and a square as:

$$
C(r, \alpha) = \begin{cases} 0 & \text{if } r > r_{\mathrm{M}}(\alpha) \\ l/\cos\beta(\alpha) & \text{if } r < r_{\mathrm{m}}(\alpha) \\ \dfrac{r_{\mathrm{M}}(\alpha) - r}{\cos\beta(\alpha)\sin\beta(\alpha)} & \text{otherwise} \end{cases} \tag{2.19}
$$

where

$$
r_{\mathrm{M}}(\alpha) = \frac{l}{2}\left(\cos\beta(\alpha) + \sin\beta(\alpha)\right) \tag{2.20}
$$

$$
r_{\mathrm{m}}(\alpha) = \frac{l}{2}\left(\cos\beta(\alpha) - \sin\beta(\alpha)\right) \tag{2.21}
$$

$$
\beta(\alpha) = \frac{\pi}{4} - |\frac{\pi}{4} - \alpha| \tag{2.22}
$$

Notice that in Eq. (2.22) the rotational symmetry of the square by $\frac{\pi}{2}$ was used as were its symmetries with respect to its diagonals.

Now we need to relate the parameters r and α to the tomography setup described before. The following expressions are readily obtained:

$$
r = \|\underline{\underline{\Omega}}^T \cdot \left[\underline{\underline{R}}_\theta^T \cdot \underline{p} - \underline{u} - \underline{x}_0\right] + \underline{x}_0 - \underline{v}\| \tag{2.23}
$$

$$
\alpha = \theta - \omega \tag{2.24}
$$

Because not all the voxels are intersected by the ray, looping over all the voxels is unnecessarily excessive. Therefore, a strategy must be adopted to loop (were possible) only over the voxels where the chord is not null. In practice, we determine geometrically a set of voxels to loop over. If we consider the ray (in green) in Fig. 2.5, the intersected voxels are determined as follow:

1. We determine the entery $(i_\mathrm{i}, k_\mathrm{i})$ and exit $(i_\mathrm{o}, k_\mathrm{o})$ voxels from the orientation θ and the ray position $\underline{p}$ (see Fig. 2.5). Then we determine the maximum number of intersected voxels by line from

the slope of the ray. This number is referred to as the step of voxels.

2. Once these geometric parameters are determined. We simply loop over the image lines by evaluating the chord for a number of voxels equal to the step then go the the next line.

   In the first line, depending on the ray slope, the ray can intersect less than the incremental number of voxels. For this reason, in the first line, we just loop over the voxels until the first null chord value is met then start the algorithm.

This algorithm is for an angle $\alpha \in [0, \pi/2[$. For a $\alpha \in [\pi/2, \pi[$, we can use the same algorithm by applying a rotation of $\pi/2$ to the projected object.

Siddon's algorithm

Siddon's algorithm was developed in 1984 by Robert L. Siddon [Siddon, 1984] in order to provide a faster exact estimation of the radiological path for medical application. The idea behind this algorithm is to consider the CT data as intersections of planes rather than individual voxels (see Fig. 2.7). Indeed, in this presentation, the radiological path is deduced from the intersection of the ray with the planes ($x = $ Cte or $z = $ Cte). The algorithm considers the parametric equation of a ray:

$$\begin{cases} x & = \alpha(x_2 - x_1) + x_1 \\ z & = \alpha(z_2 - z_1) + z_1 \end{cases} \tag{2.25}$$

where (x_I, z_I) are the coordinates of the point (I) ($I = 1$ or 2, see Fig. 2.5). The points are arbitrarily chosen to define the ray equation. The voxels are defined with planes (lines in 2D) intersections, such that the voxel indexed by (i, k) is defined by the planes (see Fig. 2.7):

$$X_i^- = -\frac{N_x - 1}{2} + il \qquad\qquad X_i^+ = -\frac{N_x - 1}{2} + (i + 1)l \tag{2.26}$$

$$Z_k^- = -\frac{N_z - 1}{2} + kl \qquad\qquad Z_k^+ = -\frac{N_z - 1}{2} + (k + 1)l \tag{2.27}$$

The intersections of ray and planes from Eqs. (2.25) and (2.26) provides a set of α_i that are sorted in order to compute the radiological path with the expression:

$$d \sum_i (\alpha_{i+1} - \alpha_i)\mu_i, \tag{2.28}$$

where d is the distance between points (1) and (2) and μ_i is the value of the voxel associated with the difference $\alpha_{i+1} - \alpha_i$. A search of this voxel for every difference $\alpha_{i+1} - \alpha_i$ is necessary to get μ_i. This is done by simply considering the voxel that contains the midpoint defined with:

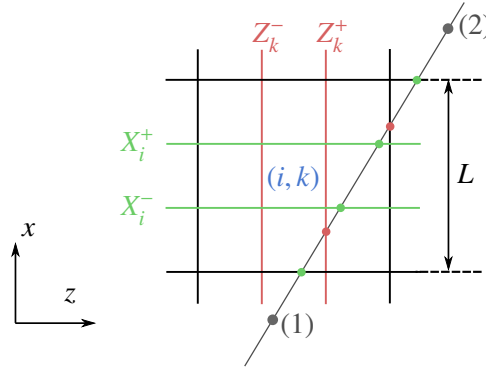$$\alpha = \frac{\alpha_{i+1} + \alpha_i}{2} \tag{2.29}$$

Figure 2.7: Illustration of the image definition by intersecting planes in Siddon's algorithms. The voxel (i, k) is defined from the intersection of the planes X_i^- and X_i^+ with the planes Z_k^- and Z_k^+. A ray defined from points (1) and (2) is drawn and its intersections with X-planes and Z-planes provide the different α's.

Jacobs algorithm

In 1998 Filip Jacobs proposed an improved version of Siddon's algorithm [Jacobs et al., 1998]. Jacobs noticed that the reordering of α_i's and the voxel search are the most time-consuming stages of the algorithm. So he proposed a variation of the algorithm where α's are incrementally estimated after testing a condition rather than computing all of them then sorting them. The condition is as follow: once the first α is determined α is incremented by:

$$\frac{l}{|x_2 - x_1|} \quad \text{or,} \quad \frac{l}{|z_2 - z_1|}$$

depending if we are crossing a x or z plane.

Gao's approach

A recent approach was proposed by Gao in 2012 [Gao, 2012]. This algorithm idea is to consider either columns or lines of voxels to run through, depending on a condition on the ray slope. If $|x_2 - x_1|$ is higher than $|z_2 - z_1|$ than the grid is divided into columns, otherwise, it is divided into lines. With this separation into a group of columns or lines, every element of the group is at most intersected twice by the rays. This allows to treat separately every group element (column or line) which makes this algorithm easily parallelizable.

Comparison of the different algorithms

All four algorithms were implemented in Python on the same machine. Then the different algorithms were used to compute the sinogram of a phantom image (discretized ellipse) with a size 60x60 vox^2 with 360 projections evenly spaced between $0°$ and $180°$. The results are reported in Tab. 2.1.

   The table compares the four different implementations. The first line gives the time to compute the sinogram in seconds. The second line gives the ratio to Siddon's algorithm (the obtained time relative to the time of Siddon's algorithm). The last line provides the same ratio as published by Jacobs

	Naive	Siddon	Jacobs	Gao
Elapsed time (s)	6.25	10.21	3.43	14.37
Ratio to Siddon	0.61	1	0.34	1.4
Author's ratio	-	-	0.13	0.54

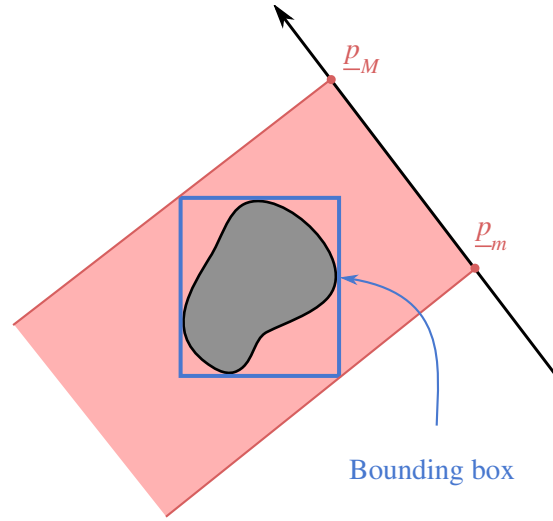Table 2.1: Comparison of different approaches for radiological path computation.

Figure 2.8: Illustration of a grain bounding box and the considered rays.

and Gao. The difference between the obtained ratios with Jacobs and Gao ratios is likely due to the difference in the programming languages used. However, the global trend is preserved and shows that Jacob's version of Siddon's algorithms is the fastest implementation and will be used in this work. The naive approach comes in the second place and provides an analytic expression of the intersection length. This expression is used later in developments related to gradients and can be used for better understanding of phenomenon like singularities in the projection model. The parallelized version of Gao's implementation may provide a better performance but since we will propose a higher-level parallelization of the D-DPC method (see Sec. 2.7) this version was not tested.

In addition to the optimization related to the radiological path computation, another gain can be made by ignoring the rays that do not actually intersect the current grain. For every grain projection, we only loop over the rays actually intersecting this grain. To apply this optimization, we define every grain by its bounding box, and we determine the affected area from the rays intersecting the bounding box corners ($\underline{p}$ between $\underline{p}_m$ and $\underline{p}_M$ in Fig. 2.8). This simple improvement is very important since every grain is treated individually and the typical grain size in a specimen is much smaller, compared to the image size.

2.5 Minimization of the cost function

The minimization of the cost function is a major step in D-DPC and should be conducted carefully in order to guarantee a good estimate of the solution. In this section, we will address some features
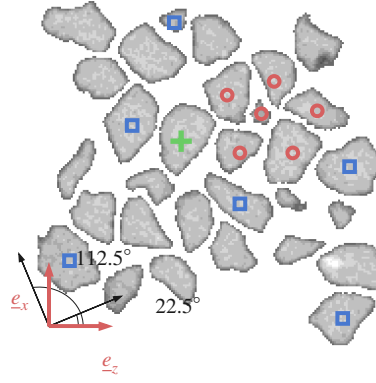
Figure 2.9: Image of the 30 grains considered for the validation of the D-DPC method in Sec. 2.6. The blue squares (resp. red circles) indicate the grains belonging to the "loose" (resp. "dense") set. The typical diameter of the grains is about 30 pix.

of this minimization. As defined earlier in Eq. (2.1), the objective function is the quadratic distance between the real experimental projections and the digital projections generated by means of the model developed in Sec. 2.3. The minimization of this function is known to deliver the maximum likelihood estimate of **q** for data corrupted with Gaussian noise. In the more realistic case of Poisson noise in tomographic projections, a different cost function should be adopted [Shepp and Vardi, 1982, Fessler, 1996]. We use the Levenberg–Marquardt (LM) method [Moré, 1978] to carry out the minimization. The results obtained with methods like LM are sensitive to the chosen initial guess which is discussed in the following section.

Sensitivity to initial guess

The function is expected to meet its minimal value when the discrepancy between the projections $\hat{P}(\theta, \underline{p}; \mathbf{q})$ and $P(\theta, \underline{p})$ is minimal. In order to use LM algorithm to find this minimal value, the initial guess should be chosen in a neighborhood of the solution where the function does not have other local minima. To probe the amplitude of displacements that the method is capable of resolving, we will investigate how the cost function evolves as the displacements diverge from the solution.

First, an insight into the evolution of the function in one dimension is a good start to see how the function behaves around the solution. We consider an assembly of grains in a 2D plan as illustrated in Fig. 2.9. From this assembly we choose the grain marked with a green cross, and submit it to a translation vector expressed as

$$\underline{u}(\alpha) = \alpha \left(\sin \frac{\pi}{3} \underline{e}_x + \cos \frac{\pi}{3} \underline{e}_z \right), \tag{2.30}$$

and a rotation ω. The parameters vector for this unique grain is given by

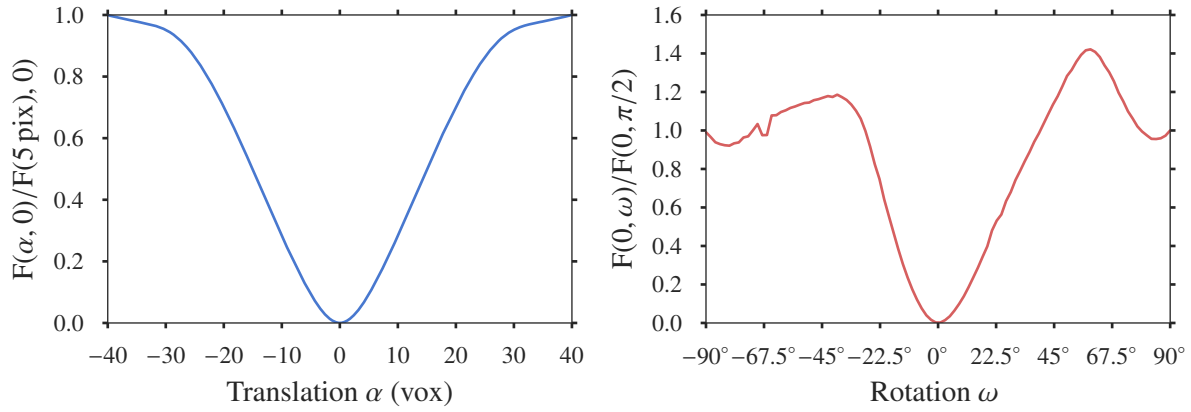$$\mathbf{q} = (\underline{u}(\alpha), \omega) \tag{2.31}$$

Figure 2.10: Cost function evolutions with respect to one dimensional translation in left graph and rotation in right graph.

and hence, the objective function can be written:

$$F(\alpha, \omega) = \sum_{\theta, \underline{p}} \left(\hat{P}(\theta, \underline{p}, \underline{u}(\alpha), \omega) - P(\theta, \underline{p}) \right)^2 \tag{2.32}$$

We will consider two projection orientations ($\theta = 22.5°$ and $\theta = 112.5°$), in which the "experimental" projections are generated by applying the projection model to the initial state of the grain

$$P(\theta, \underline{p}) = \hat{P}(\theta, \underline{p}, \underline{u}(0), 0) \tag{2.33}$$

we set ω to 0, and we vary α from -40 to 40 voxels (the largest diameter of the grain is 37 voxels) then we plot the function $F(\underline{u}(\alpha), 0)$ in the left graph of Fig. 2.10.

We do the reverse to investigate the rotation effect by freezing α and plot the variation of $F(0, \omega)$ for ω between $-90°$ and $90°$ in the right graph of Fig. 2.10.

The figure shows a more regular evolution of the function with translation than rotation and that there are more local minima when we vary the rotation. The positions of these local minima are linked to the grain geometry. The difference between translation and rotation can be explained by the fact that a grain translation produces more variation in the projections than a rotation around the grain center. Of course, this is stated in the case of a unique grain, and we expect that with multiple grains, the translations would also result in lower changes in the projection due to interchanging positions for example.

We observed that the function shape is more irregular with variations of rotation ω than the translation $\underline{u}$. We therefore focus in what follows on the cost function: $\omega \mapsto F(0, \omega)$, where the components of $\underline{u}$ are frozen.

We perform several simulations with different initial guesses $(0, \omega_{\text{init}})$, where ω_{init} takes the values $-90°$, $-45°$, $-22.5°$, $-4.5°$, $4.5°$, $22.5°$, $45°$, $90°$. Then we retrieve the converged values of $\omega_{\text{D-DPC}}$ which are reported in Fig. 2.11. This figure reproduces the right plot of Fig. 2.10 and adds symbols
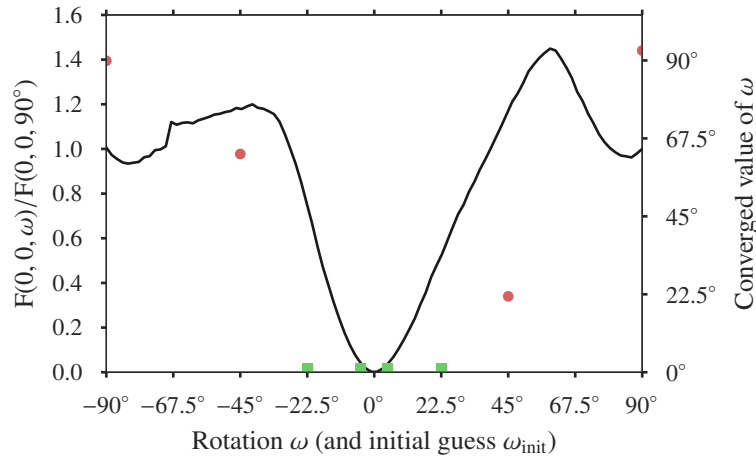
Figure 2.11: Plot of the objective function F versus ω continuous line, left axis).F is not convex for large values of ω, and the initial guess ought to be close enough to the minimum, as illustrated by the symbols (right axis).

that relate the converged value ω_{D-DPC} (right axis) to the corresponding initial guesses ω_{init}. The simulation is successful if the converged value of the rotation is null (up to machine accuracy). In Fig. 2.11, successful simulations correspond to the green squares lying on the x-axis. These results confirm that the initial guess must be close enough to the solution.

It should be noted that we deliberately considered extremely large rotations for the initial guess: true rotations observed in experiments, where measurements are usually made for incremental applications of load, are much smaller [Hall et al., 2010, Ando et al., 2012].

It is observed that successful convergence is obtained for initial guesses of the rotation which are distant from the solution by about 30°, which illustrates the robustness of our method.

To close this section, we mention that the same analysis (not presented here) can be carried out on translations. Our simulations show that convergence to the exact displacement is obtained for initial guesses of the translations which are several voxels distant from the solution. The amplitude of the convergence domain is deemed sufficient for practical applications, especially if the load is applied in small increments.

Variables scaling

When minimizing the objective function we are dealing with the grain rigid body displacements, which are of two natures (translations and rotations), and they have different units (voxels and radians). This leads to different amplitude of variations of the cost function depending on the variable type. In order to have similar effect on the cost function when a step of a given size is applied to any of the components of **q**, a scaling of the variables is required. This procedure is similar to the Jacobi (or diagonal) preconditioner used with iterative linear solvers.

We choose to set all the variables unit to be voxels. Therefore, we define a relative scaling distance d for every grain that converts its rotations into translations. The distance d was taken equal to the

grain size (the longest dimension of the bounding box). This choice gives twice the translation of the most distant point from the grain center. We do not claim that this choice is optimal, and further investigations are to be considered to determine such optimum for d. However, this choice provides a more regular variation of the function for same amplitude of variable variations, as shown by Fig. 2.12. In this figure the map of $F(u, 0, \omega)$ versus u and ω is plotted in the left graph, while the right graph shows the variation of the same function with u and $\tilde{\omega} = d\omega$. Moreover, a gain in the number of iterations during the minimization was observed when using this variables scaling. A simulation with the same grain was run for both cases of Fig. 2.12. The results obtained are averaged on ten individual simulations for every case (with different initial guesses) and show that the variable homogenization reduces the number of iterations from 31 to 25. Even if it is not a dramatic gain, we choose to adopt this variable scaling for the subsequent simulations.
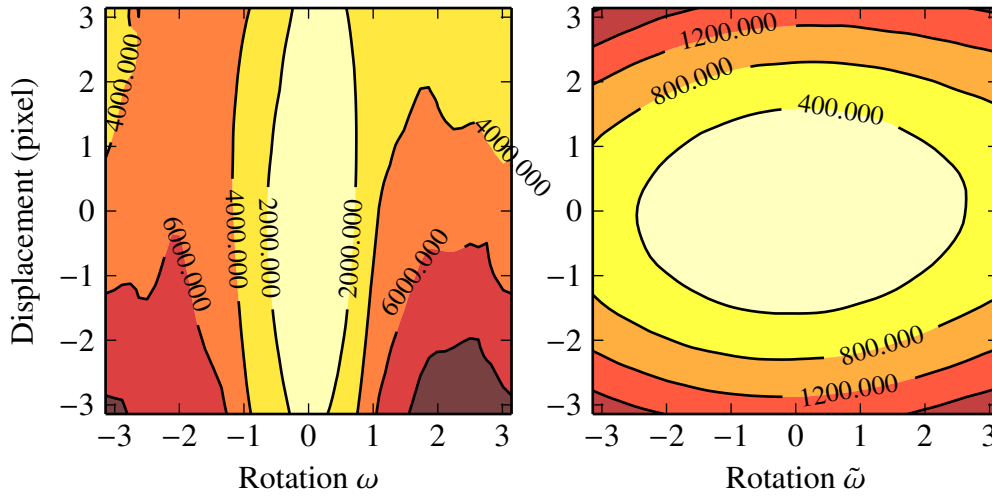

Figure 2.12: (left) Plot of $F(u, 0, \omega)$ versus u and ω. (right) Plot of $F(u, 0, \tilde{\omega}/d)$ versus u and $\tilde{\omega}$. When rotations are scaled, the function variations are more regular for the same variables variations.

Gradient of the function

Levenberg–Marquardt's algorithm makes use of the function gradient to select the search direction. The implementation of the algorithm uses numerical methods to estimate the function gradient, but it is possible to provide gradient when available, in order to speed up the minimization. As we are interested in reducing the execution time of the technique, we will try in this section to provide an efficient evaluation of the gradient of this cost function.

$$\nabla F = \left(\frac{\partial F}{\partial \mathbf{q}^{(i)}} \right)$$

$$= 2 \sum_{\theta, \underline{p}} \left(\frac{\partial \hat{P}(\theta, \underline{p}; \mathbf{q})}{\partial \mathbf{q}^{(i)}} \left(\hat{P}(\theta, \underline{p}; \mathbf{q}) - P(\theta, \underline{p}) \right) \right)$$

This simple derivation shows that the only new quantity to compute is $\dfrac{\partial \hat{P}(\theta, \underline{p}; \mathbf{q})}{\partial \mathbf{q}^{(i)}}$, which only concerns one individual grain, because the projections of a given grain are not affected by the movements of the other grains

$$\frac{\partial \hat{P}^{(j)}(\theta, \underline{p}; \mathbf{q}^{(j)})}{\partial \mathbf{q}^{(i)}} = 0 \quad \text{for } i \neq j. \tag{2.34}$$

$\hat{P}(\theta, \underline{p}; \mathbf{q})$ is just a sum of intersection lengths of voxels and ray, so if we consider the chord function derived in Sec. 2.4, an expression of this function derivatives allows to evaluate the cost function gradient during the radiological path evaluation.

The function gradient can be evaluated at two different levels

The voxel level: At the voxel level we, can estimate the gradient of the function by simply evaluating the gradient of the chord function in Eq. (2.19). This means, that the gradient will be estimated during the loop of the radiological path evaluation. This computation is more adapted when using the naive approach, since the same geometric parameters are used.

The pixel level: We can also evaluate the gradient for every ray. We do not have an analytic expression in this case but a numeric computation by finite difference can be used. Therefore, for each grain, additional estimations of the radiological path, equal to the number of degrees of freedom, are to be evaluated.

Note that the pixel level estimation of the gradient is better than an numeric estimation of the global cost function. With this method, we take advantage of the property in Eq. (2.34) and only evaluate the non null terms of the gradient.

Both levels were tested and gave similar results. However, and contrary to what can be expected, the pixel level method provides faster estimation of the gradient. Even though in the voxel level we can directly evaluate the projection gradient during the radiological path, it is observed that for an image with a small number of voxels (small loops over voxels), the call of mathematical function in the analytical approach is more time consuming than the multiple evaluation of the radiological path in the pixel level method. Hence, the latter is used in D-DPC implementation.

We note that the evaluation of the chord function gradient showed that this function is not everywhere differentiable, as shown in the figure 2.13. From the simulations results, we do not encounter convergence failure due to these singularities. It is also shown in Fig. 2.10 that the objective function maintains a smooth shape in the vicinity of the solution. These observations give us confidence to using a simple minimization algorithm such as Levenberg-Marquardt's. This algorithm is usually designed for convex and differentiable functions, a more rigorous choice would be to use some algorithms for nondifferentiable functions such like subgradient methods [Wolfe, 1975, Polyak, 1977] if the singularities of the chord function caused any convergence failure.
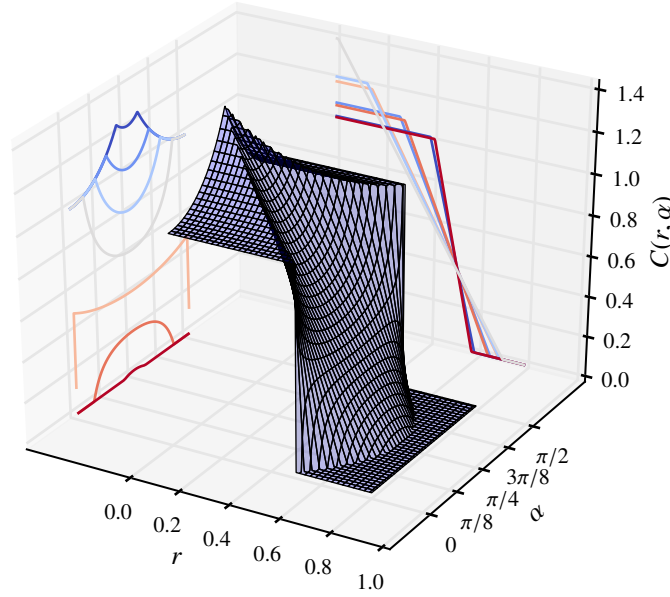
Figure 2.13: 3D plot of the chord function

2.6   2D applications of D-DPC

This section presents various validations of the D-DPC method. We will focus on solving the inverse problem on 2D synthetic examples. The aim of this validation is to provide a test of the method at a level where no experimental imperfection is considered. We consider again the assembly of grains illustrated in Fig. 2.9.

The image gathers 30 grains with different sizes and shapes. Using our projection model we can produce $\hat{P}(\theta, \underline{p}; \mathbf{q})$ for different configurations of the grains. With those projections considered as the "experimental" projections of the deformed state, we can run the minimization of the objective function in Eq. (2.2) to estimate $\mathbf{q}_{\text{D-DPC}}$.

Simulations with individual grains

At first, every grain is considered individually. So we performed 30 simulations where in simulation i only the grain i is considered, and for which we applied a displacement

$$\mathbf{q}_{\text{exact}}^{(i)} = (\underline{u}_i, \omega_i), \tag{2.35}$$

which we expect to retrieve at the end of simulation. For each grain i, the components of the translation vector $\underline{u}_i$ was randomly chosen between -1 voxel and 1 voxel while the rotation ω_i was randomly taken between $-6°$ and $6°$ ($\tilde{\omega}_i$ are in the order of 1 voxel).

For all 30 experiments, we only needed two projections to find exactly the applied displacement, which is the bare minimum. To understand this, consider a parallel projection in the direction $\underline{e}_z$. It is

evident that only the component $\underline{u} \cdot \underline{e}_x$ of the grain translation provides a change into the projection. Therefore, one projection is not enough to determine both components of the translation.

Simulations with groups of grains

We next perform simulations on a group of grains. Three groups that vary by density and number were chosen. As illustrated in Fig. 2.9, the red circles gather a dense group while the blue squares show a looser group. The last group includes all 30 grains.

Small displacements

The first set of simulations is made with the three groups with $\mathbf{q}_{\text{exact}}$ randomly chosen like in Sec. 2.6. Once again, and for only two projections, we find exactly the applied displacements regardless of the chosen group. This result shows that the method is capable of finding the solution regardless of the density and the number of grains. As stated in Sec. 2.5, one may have expected that when multiple grains move closely to each other, the changes in the projection due to their movements may compensate each other and hence that it would be difficult to retrieve their movements with few projections angles. This effect was more likely to appear in dense collections, but in reality no noticeable difference was observed in these simulations.

Larger displacements

We now test the method's convergence when dealing with larger displacements. For this simulation, translations are chosen as follows:

$$u^{(i)} = \alpha x^{(i)}, \tag{2.36}$$
$$w^{(i)} = \beta z^{(i)}, \tag{2.37}$$

with $\alpha = 0.15$ and $\beta = 0.1$; this gives translation amplitudes from 2 to 15 voxels. The rotations are arbitrarily chosen between $-30°$ and $30°$, consistently with the observations in Sec. 2.5 (the scaled rotations $\tilde{\omega}$ are in the order of 10 voxels).

D-DPC fails to find the solution with only two projections unlike in the previous simulations. We quantify the error between the estimated solution $\mathbf{q}_{\text{D-DPC}}$ and the solution $\mathbf{q}_{\text{exact}}$ by the maximal component wise difference between the vectors. Increasing the number of projection to six allows the exact solution to be found. Considering that the initial guess is quite far from the solution, it is very likely that with two and four projections, the optimization algorithm converged to a local minimum. The results of simulations with different numbers of projections are presented in Table. 2.2

2.7   3D implementation

In this section, we will address the 3D case. The difference to the 2D case lies in a geometric complexity because of the third space dimension, but this complexity is easily handled by the projection

Num. proj.	Max. rel. err.
2	26.6
4	2.6
6	$3.26 \; 10^{-13}$

Table 2.2: Maximum component-wise relative error on displacements with the number of projections used.

algorithm as it is fully taken into account by the radiological path algorithm. The other complexity provided by the third dimension is the increase of the number of degrees of freedom to evaluate (by a factor of two) and in the number of image voxels and detector pixels. Much larger information are to be treated which makes the minimization in the 3D case more time consuming. The previous implementation of the algorithm in Python can no longer be efficient and faster implementation are to be considered.

The current implementation already includes *algorithm-level* optimizations. These optimizations are:

- The fast implementation of the radiological path algorithm.

- The optimization of the rays considered for the grain projection regarding its position (bounding box).

Other optimizations are considered in this section. A *compile-level* optimization, is used to speed up the execution time. Then parallelism of the code is used for further improvement.

Compile-level optimization

Python is a very practical language, widely used for scientific computation due to its simplicity and the large number of available scientific packages. The price to pay for Python's comfort is the loss of efficiency. Indeed, because it is a dynamically typed language, its execution is slower compared to compiled languages. To overcome this limitation many solutions were proposed. In the following, we will test Cython on our implementation of the radiological path algorithm in 3D:

Cython is an optimizing compiler for Python (see [Behnel et al., 2011, Smith, 2015]). It generates C code from Python code. Besides, a Cython code based on Python allows to call C functions and declare C types variables to produce more efficient C implementations. With Cython, the computation for one ray is 100 times faster than with the Python implementation. This is shown in Fig. 2.14 where the time needed to compute the radiological path is compared between Python and Cython implementations.

Note that we also tried another option. This one is called Numba; it provides a just in time (JIT) compilation of Python code using the LLVM compiler infrastructure [Oliphant, 2012]. This allows to speed up functions written directly in Python. But we failed to obtain any noticeable improvement.
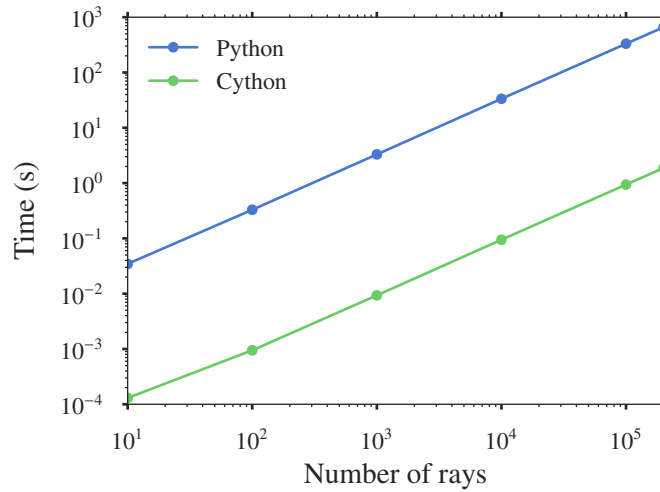
Figure 2.14: Time needed to compute the radiological path with Python vs Cython.

Parallelization

A more relevant speed up is made by parallelizing the objective function evaluation on multiple processes. In every function call, the varying part of the function is the digital projections changing with the parameters of optimization. Fortunately, we can compute every grain projection with no need of other information from other grains (see Eq. (2.10)). Therefore, for every grain, projections can be computed separately on a different process. This parallelization was implemented using the multiprocessing module in the Python standard library. The grains are distributed over processes, and the final projection is evaluated via a MapReduce pattern [McCool et al., 2012].

2.8 Experimental tests

At this stage, we have a suitable implementation to perform a complete experimental test on real tomographic projections. In this section, we will apply D-DPC to real tomographic projections by going through all the steps of the method in a simple experiment.

The full 3D reconstruction of the reference configuration

The filtred backprojection (FBP) is the most commonly used algorithm to reconstruct tomographic images. Thanks to the fast Fourier transform this algorithm is more convenient to reconstruct the large tomographic data. It is also the algorithm implemented in the reconstruction software in use in our local tomography facility. But, a strong assumption is made on the cone angle in the implementation proposed by Feldkamp, Davis and Kress [Feldkamp et al., 1984] and also the discretization is made in Fourier space rather than in the real space. Such assumptions are not made in the projection model. Therefore, when the FBP full 3D reconstructed image is reprojected using our projection model, the digital projections present a large difference with the experimental projections used for the

reconstruction. Therefore, to have a reconstruction that is more consistent with our projection model, we implemented the simultaneous algebraic reconstruction algorithm (SART). In this algorithm an iterative scheme allows the 3D image to be estimated by solving the linear system:

$$\underline{\underline{A}} \cdot \underline{x} = \underline{b} \qquad (2.38)$$

where $\underline{x}$ is a voxel-wise vector representing the object 3D image, $\underline{b}$ is a pixel-wise vector containing the projection value at every pixel for all available orientations. Finally, $\underline{\underline{A}}$ is the projection linear operator which correspond exactly to our projection model with $\mathbf{q} = 0$. The reconstruction is completed when a stopping criterion is met. For instance, we define the relative error

$$\epsilon = \frac{\|\hat{\underline{b}} - \underline{b}\|_2}{\|\underline{b}\|_2} \qquad (2.39)$$

where $\hat{\underline{b}}$ is the evaluation of $\underline{\underline{A}} \cdot \underline{x}$ at every iteration, and we require that ϵ becomes smaller than a prescribed tolerance.

This iterative scheme was efficiently implemented using the Portable Extensible Toolkit for Scientific Computation (PETSc) for language C [Balay et al., 1997, Balay et al., 2015].

Specimen   For this experimental test, we chose a small specimen of limestone gravel from the Boulonnais quarries with a grain mean diameter of 5mm. 15 grains were gathered in a polypropylene recipient (a syringe of 10mm diameter and a height of 30mm) and scanned in our laboratory tomography scanner (see Fig. 2.15).

In the full 3D reconstruction process, the size of the matrix $\underline{\underline{A}}$ can quickly become excessive. In fact, the size of the matrix for a detector of size $N \times N$ and for N_T projections is $N_T \times N^5$. Of course, as the matrix is sparse, we only need a size in the order of $N_T \times (N^2 + 2N^3)$ floating point data to store the non zero terms of the matrix (elements size). For elements of 64bit type (a size of 8 octets), 1440 projections and a total matrix size of 1 To (which corresponds to the internal memory of our most powerful workstation), N should be in an order of 350. For this reason, we choose to use a small area of the detector of $180 \times 280 \, \text{pix}^2$.

Tomographic acquisition of different states   X-ray microtomography experiments were performed at Laboratoire Navier with an Ultratom scanner from RX Solution combining a Hamamatsu L10801 X-ray source (230 kV, 200 W, 5 μm) and a Paxscan Varian 2520V flat-panel imager (1920$\times$1560 pix^2, pixel size 127 μm). All scans were performed at 100 kV and 500 μA, with a frame rate of 2 images per second. In order to increase the signal-to-noise ratio, 40 images were averaged to produce one projection (effective exposure time: 20 s). According to the geometry of the tomography setup, the voxel size was estimated to 0.112 mm $\cdot$ vox^{-1}. Fig. 2.16 shows two orthogonal projections of the sample.

Three full scans (352 radiographs spanning the full 360°) were then performed. For scans 1 and 2, the position of the sample was unchanged (reference configuration), while for scan 3, a 3.5 mm
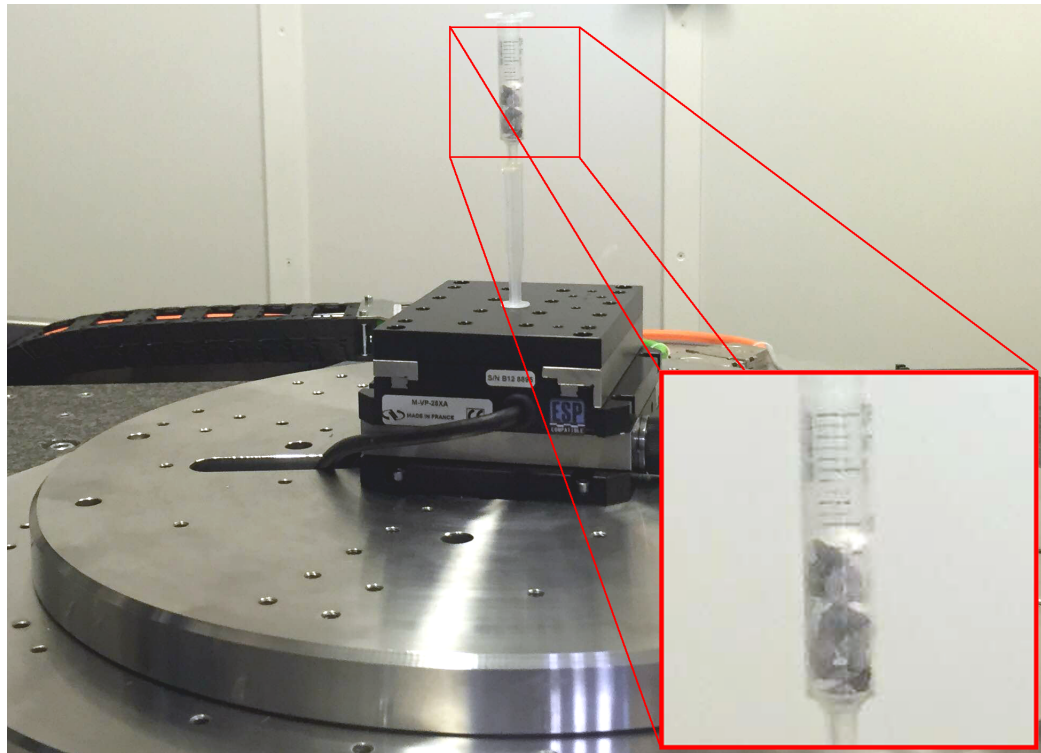
Figure 2.15: The specimen considered in Sec. 2.8. The photograph also shows the sample stage of the tomography setup.
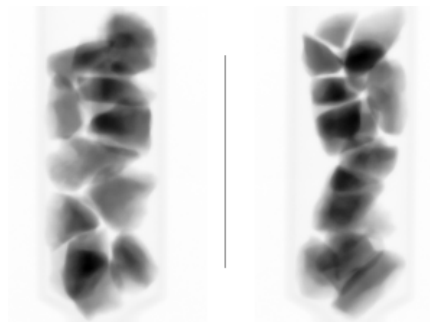

Figure 2.16: Two orthogonal projections of the specimen used for validating the D-DPC experimental test in Sec. 2.8
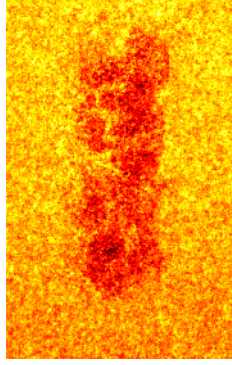
Figure 2.17: Difference between the projection $\theta = 0$ of scan 1 and 2.

translation in the Oxz plane (see Fig. 2.4) was applied to the sample.

Scans 1 and 2 were used to estimate the amplitude of noise in the projections. Since no movement was applied to the sample between these two states, the difference between the projections of these two scans is essentially due to image noise. Fig. 2.17 shows the difference between the projections $\theta = 0°$ of the two states. We evaluate the signal to noise ratio as follow:

$$\text{SNR} = \frac{1}{2}\frac{\|\underline{b}_1 + \underline{b}_2\|_2}{\|\underline{b}_2 - \underline{b}_1\|_2}, \tag{2.40}$$

and found $1/\text{SNR} \simeq 2\,\%$. The noise parameter is then estimated as:

$$\sigma = \frac{1}{2}\frac{\|\underline{b}_2 + \underline{b}_1\|_2}{\text{SNR}}. \tag{2.41}$$

The implementation of the SART algorithm was used to reconstruct the reference state of the specimen. Iterations were stopped when no noticeable improvement of the relative error ϵ was obtained. At the end of the reconstruction $\epsilon = 3\%$, which is consistent with a stopping criterion based on the discrepancy principle [Morozov, 1984], as the noise amplitude in the projection was estimated to 2% in Eq. (2.40). Fig. 2.18 represents two slices (vertical and horizontal) through the reconstructed image.

Grain segmentation

To separately identify each individual grain from the reference image, a segmentation process is needed. The watershed algorithm [Beucher et al., 1992, Beucher and Lantuéjoul, 1979] is a typical procedure based on image topology that allows to segment images. The idea is to identify a seed (water source) for every grain and consider a topography from the image gray levels. Next, the area is flooded from the different water sources (seeds) and interfaces are made when water from different sources met. Usually, the topography image is obtained from the Euclidean distance or a gradient of the image, and the seeds are its local minimum values. Image pre-processing is necessary in order to prevent image over-segmentation (more than a seed by grain) or under-segmentation (no seed in a
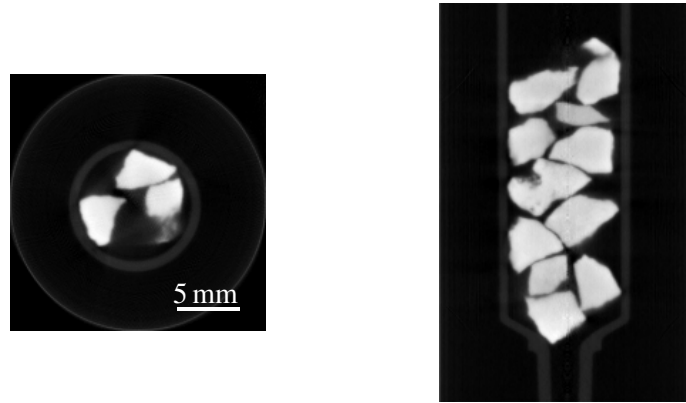
Figure 2.18: (left) Horizontal slice through the reconstructed image of the specimen reference state. (Right) Vertical slice.

grain). For our applications we implemented a succession of image processing operations using the Population framework [Tariel, 2013] on C++ as follow:

1. The image is filtered using anisotropic diffusion [Perona and Malik, 1990] in order to reduce image noise. This filter is known to preserve image details such as lines and edges, which is important in the case of granular media. The filter parameter was manually chosen by the observation of the image noise improvement.

2. A binary version of the image, is obtained by using a standard Otsu thresholding [Otsu, 1975] where only the grains are left (the other features with lower attenuation, like the recipient, are removed from the image).

3. The Euclidean distance map of the binary image is computed [Danielsson, 1980].

4. Seeds are set as the local minima of the distance map after that a dynamic (vertical) filter is applied to merge the close local minima in the distance image and prevent over segmentation. This filter is the geodesic reconstruction [Beucher, 2001] of the image shifted by a certain value by the original image. This value was determined such as every grain contains a unique seed. For large images, a small portion of the image can be considered for determining this value.

5. The watershed algorithm is applied using the seeds and the distance map as a topographic surface.

Fig. 2.19 shows illustrations of every step, applied to an image of Hostan sand.

This procedure was performed to segment the grains in the considered specimen for this experiment and lead to the segmentation presented in Fig. 2.20.

Instability of the projections gray levels

In real tomography acquisition, stability of the source intensity and the detector sensitivity is not guaranteed, hence variations in the projections gray levels can be obtained for the same state. To take
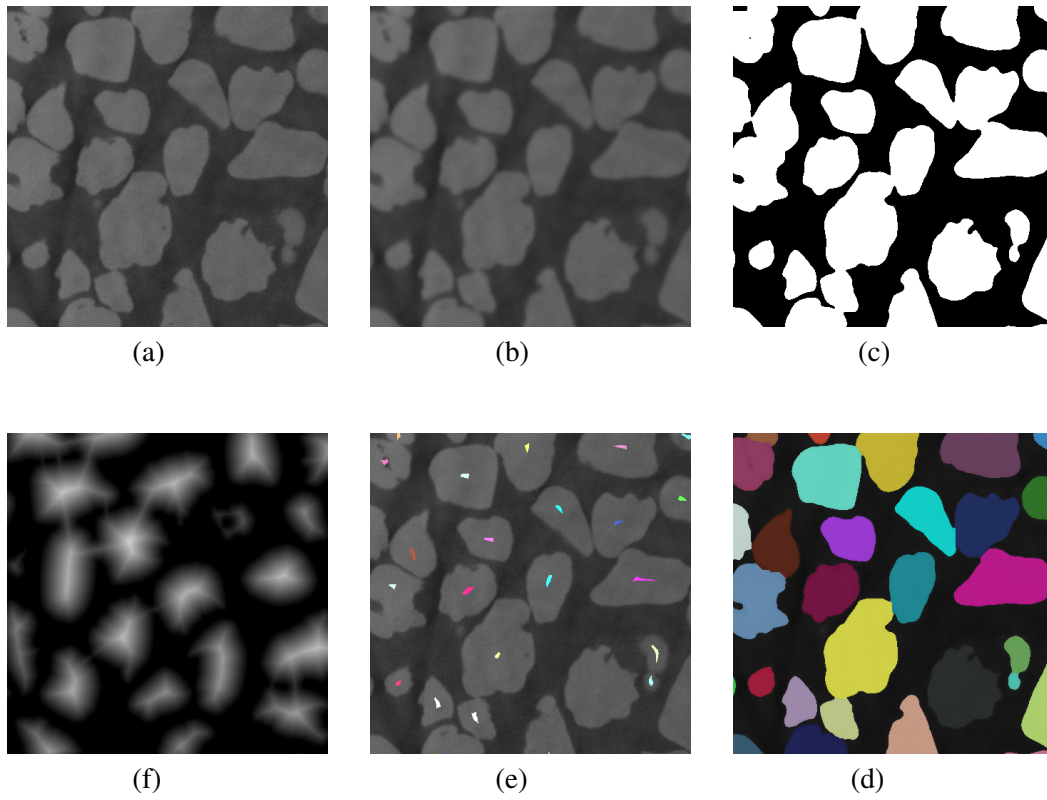
Figure 2.19: Steps followed for grain segmentation. (a) The initial image (b) step 1: *filtered image* (c) step 2: *binarization* (f) step 3: *topological image* (e) step 4: *seeds* (d) step 5: final result after the *watershed* flooding.
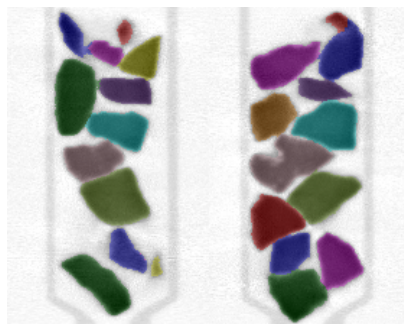

Figure 2.20: Two orthogonal cross-sections through the segmented, reconstructed volume.

into account this variation during the minimization of the cost function we allow an affine variation of the gray levels between the experimental projections and the digital ones. Two parameters a and b were introduced in the expression of the cost function in Eq. (2.1) to allow for such variation

$$F(\mathbf{q}) = \sum_{\theta,\underline{p}} \left(\hat{P}(\theta, \underline{p}; \mathbf{q}) - (aP(\theta, \underline{p}) + b) \right)^2 \tag{2.42}$$

The optimal values of a and b are found respectively for:

$$a_{\text{opt}} = \frac{1}{n_\theta n_p} \frac{\sum_{\theta,\underline{p}} \hat{P}(\theta, \underline{p}; \mathbf{q}) P(\theta, \underline{p}) - \sum_{\theta,\underline{p}} \sum_{\theta',\underline{p}'} \hat{P}(\theta, \underline{p}; \mathbf{q}) P(\theta', \underline{p}')}{\sum_{\theta,\underline{p}} P(\theta, \underline{p})^2 - \sum_{\theta,\underline{p}} \sum_{\theta',\underline{p}'} P(\theta, \underline{p}) P(\theta', \underline{p}')} \tag{2.43}$$

$$b_{\text{opt}} = \frac{1}{n_\theta n_p} \left(\sum_{\theta,\underline{p}} \hat{P}(\theta, \underline{p}; \mathbf{q}) - a \sum_{\theta,\underline{p}} P(\theta, \underline{p}) \right) \tag{2.44}$$

inserting a_{opt} and b_{opt} into Eq. (2.42) provides a more flexible objective function that resemble the Zero mean Normalised Cross-Correlation coefficient [Chambon and Crouzil, 2003, Pan et al., 2009]. However, the estimation of a_{opt} and b_{opt} during the evaluation of $F(\mathbf{q})$ is very costly because of the cross-product summations that it involves. To overcome the cost of the estimation of a_{opt} and b_{opt} we chose to include them as additional optimization parameters for which the relative derivatives of $F(\mathbf{q})$ are readily given by

$$\frac{\partial F(\mathbf{q})}{\partial a} = -2 \sum_{\theta,\underline{p}} P(\theta, \underline{p}) \left(\hat{P}(\theta, \underline{p}; \mathbf{q}) - (aP(\theta, \underline{p}) + b) \right) \tag{2.45}$$

$$\frac{\partial F(\mathbf{q})}{\partial b} = -2 \sum_{\theta,\underline{p}} \left(\hat{P}(\theta, \underline{p}; \mathbf{q}) - (aP(\theta, \underline{p}) + b) \right) \tag{2.46}$$

these gradient expression are much less costly to estimate in comparison with the optimal values of a and b. Therefore, we adopt the second method to take into account the projection variations during minimization. The initial guesses for thoses parameters are naturally chosen as $a_0 = 1$ and $b_0 = 0$.

Measurement of displacements

The segmented 3D reconstruction resulting from Scan 1 was used as a reference configuration for the generation of trial projections within the framework of the D-DPC method.

Application to Scan 2: The specimen is untransformed; therefore, our method should converge to null displacements for all grains. Deviations from this expected result provide an estimate of the accuracy of the D-DPC method.

Application to Scan 3: The specimen was subjected to a 3.5 mm translation in the Oxz plane; therefore, the D-DPC method should converge to the same rigid body motion for all grains. The expected value of this rigid body motion was estimated by means of the standard Volumetric Digital

	X	Y	Z
u [mm]	0.00 (0.04)	0.00 (0.02)	0.00 (0.03)
u [vox]	0.0 (0.3)	0.0 (0.2)	0.01 (0.3)
ω [°]	0.2 (0.7)	−0.2 (0.9)	0.1 (0.9)

Table 2.3: Application of the D-DPC method to Scan 2. The components of the translation u and the rotation ω are averaged over all grains. Figures in parentheses are standard deviations over the grains.

	X	Y	Z
u [mm]	2.76 (0.03)	0.01 (0.04)	−2.12 (0.04)
u [vox]	24.7 (0.3)	0.1 (04.)	−18.9 (0.4)
ω [°]	−0.2 (1.5)	−0.8 (1.9)	0.3 (0.8)

Table 2.4: Application of the D-DPC method to Scan 3. The components of the translation u and the rotation ω are averaged over all grains. Figures in parentheses are standard deviations over the grains.

Image Correlation technique (VDIC) [Lenoir et al., 2007], leading to

$$\mathbf{q}_{\text{VDIC}} = \left(2.78\,\text{mm}, -1.24\ 10^{-3}\,\text{mm}, -2.12\,\text{mm}\right), \tag{2.47}$$

$$\|\mathbf{q}_{\text{VDIC}}\| = 3.503\,\text{mm}. \tag{2.48}$$

Again, deviations from this expected result provide an estimate of the accuracy of the D-DPC method.

In both cases, only four projections (0°, 45°, 90°, 135°) were used to estimate the rigid body motion of each grain. The results are presented in Tables 2.3 (Scan 1) and 2.4 (Scan 2). The measured translations and rotations are averaged over all grains, while the corresponding standard deviation is used as a measure of the method accuracy. For both scans, we found that the accuracy was about 0.01 mm (0.1 vox) for translations and 1° for rotations.

It is again emphasized that only four projections were required to achieve the reported accuracy, despite the fact that the initial guess passed to the optimization algorithm provided purposely a very poor estimate of the true displacements. Indeed, the reference configuration was used as initial guess ($\mathbf{q}_{\text{init}} = 0$). If the initial guess is chosen within 1 vox (translations) and 6° (rotations) of the true displacements, then the accuracy achieved with only two projections (the bare minimum) was similar for translations, and only slightly degraded for rotations. We also note that Leclerc and coauthors [Leclerc et al., 2015] report similar accuracies when using very few projections.

Comparison with DV-DIC and ID-Track

To compare the results of our method with other techniques, we evaluated the motions of grains from scan 1 to scan 3 with two other techniques: ID-Track [Ando et al., 2012] and DV-DIC [Hall et al., 2010].

ID-Track: In order to use this method, the full 3D reconstruction of the deformed state was also segmented. The 15 grains were manually paired up, so the only comparison here is made on the displacements estimation. For every grain, its center of mass in the reference state is computed then

	u_x[vox]	u_y[vox]	u_z[vox]
D-DPC	24.7 (0.3)	0.1 (0.4)	-18.9 (0.4)
DV-DIC[1]	24.6 (1.3)	0.3 (0.5)	-18.9 (1.0)
DV-DIC[2]	24.9 (0.4)	-0.1 (0.5)	-18.9 (0.3)
ID-Track	24.78 (0.04)	-0.01 (0.03)	-18.92 (0.05)

Table 2.5: Result of different methods application to Scan 3. The components of the translation (u_x, u_y, u_z) are averaged over all grains for D-DPC and ID-Track. For DV-DIC the superscript 1 means averaged value over all the grains and the subscript 2 is for an average over the grains with a correlation coefficient under 5%. Figures in parentheses are standard deviations over the grains.

the same is done for its displaced state. Once the centers of masses in both states are known, they are compared to compute the grain translation.

DV-DIC: We use the segmentation of the grains in the reference state, and follow the steps of DV-DIC as implemented in CMV-3D (see [Bornert et al., 2004]).

The results are reported in Tab. 2.5. For DV-DIC two different averaged results are given. The first one is translation components averaged over all the grains. Considering all the grains, the method accuracy is in the order of 1 vox. A second averaging is made over only the grains for which a correlation coefficient under 5% was obtained (0 indicating perfect correlation). Only 7 grains were correlated at this precision while the highest correlation coefficient is about 16%. With the grains successfully correlated the accuracy is comparable with that of D-DPC. However with ID-Track, we obtain a better precision on translations about 0.01 vox. This distinction of ID-Track may be because, due to the fine resolution, a very precise segmentation was obtained in both states which allowed an accurate estimation of the grains center of mass. Moreover, the simple translation in Oxz plan does not produce a noticeable change in the grains discretization (no rotation of the grid). Therefore the grains labels are nearly identical in both states.

2.9 Conclusion

In this chapter we have proposed a new method to capture the movements of grains in granular materials by using X-ray microtomography. This method was called D-DPC for Discrete Digital Projection Correlation, and its main merit is that no reconstruction of the current (deformed) state of the specimen is required. The method only uses the reconstruction of the reference (initial) state and the projections of the current state to retrieve the displacements of grains. Our tests showed that as few as two projections are sufficient to obtain an adequate estimate of the displacements. Reducing the number of projections needed results in a great decrease of the acquisition time, therefore allowing to study time-dependent phenomena such as creep.

The principle and formulation of D-DPC are fully stated in the present chapter. We also presented both synthetic and real-life test cases to validate the method. The experimental tests showed that the accuracy of the method is about 0.1 vox (translations) and 1° (rotations). Although more conventional image processing techniques can achieve more accurate measurements, we believe that this is largely

compensated by the significant gain in acquisition time that our method offers. For further improvement of the method accuracy, many potential ways can be investigated such as refining the projection model and accounting for geometric imperfections of the tomography setup. For this reason, we carry out in the next chapter a detailed assessment of the various sources of errors.

Chapter 3

Assessment of errors in D-DPC

Contents

In the previous chapter, D-DPC was introduced. It is a new method that allows measuring the grain displacements based on tomographic projections. In this chapter, we will address the origins of errors related to D-DPC. This chapter begins with an overview of the methods used in assessment of errors in DIC in Sec. 3.1. Then different types of error sources are investigated and quantified for D-DPC through simple modeling. An assessment of the errors induced by image noise is provided in Sec. 3.2. Then, the errors related to the voxel representation of images are studied in Sec. 3.3. Finally, the effect of the assumptions made in the projection model on the method results is probed in Sec. 3.4.

3.1 Introduction

When using Digital Image Correlation techniques to measure displacement fields from images, one needs an estimation of the method accuracy and the reliability of the measured results. Therefore, it is important to determine and quantify the sources of errors and uncertainties in DIC methods as it has been attempted in several works [Schreier and Sutton, 2002, Roux and Hild, 2006, Wang et al., 2009, Bornert et al., 2009, Pan et al., 2009, Pannier et al., 2010]. In DIC, the error sources can be separated into two groups:

Sources that are extrinsic to the method: these are error sources that are directly linked to the image acquisition process, including the imaging setup and the output images, such as:

- Geometric imperfections of the acquisition device that can produce fake virtual displacements, like the out of plane motion in 2D-DIC and image distortion, or fluctuations of the source and the detector positions in tomography acquisition for 3D-VDIC. These fluctuations may produce a virtual magnification of the objects.

- Change in the acquisition setup, either due to the experimental setup or to instabilities in the output of the imager, as the change in the contrast which may invalidate the assumption of preservation of the gray levels. The evolutions of the object itself during the acquisition of images might also invalidate the latter assumption.

- Intrinsic image noise, which corrupts the acquired images by producing different gray levels for the same state of the object. This error is up to a standard deviation that varies depending on the type of imaging device (from a thousandth of the dynamic range of the sensor for a high tech camera to tenth for a scanning electron microscope (SEM) in fast acquisition mode).

Intrinsic error sources to the method: this group contains the sources which depend on the method formulation, and are generally caused by the DIC algorithm itself or the parameters controlling the implementation. For instance:

- The incapability of the subset shape function in DIC to describe the apparent transformations as it was studied by [Schreier and Sutton, 2002, Bornert et al., 2009]. The shape function allows optimizing a finite number of kinematic parameters which may be insufficient to fit the real displacements.

- The discrete nature of digital images implies the use of interpolation of gray levels to reach sub-pixel or subvoxel precision. This interpolation is known to lead to a systematic error, function of the fractional part of the displacement [Schreier et al., 2000].

In the literature, many approaches have been adopted in view of testing the performance of DIC methods against extrinsic and intrinsic sources of errors. The simplest way to probe the accuracy of a method is to apply it to a real experimental case. In such experiment, the displacements must be known either from results of a reliable experimental technique or by controlling the applied displacements if the experimental setup allows to. This approach takes into account all the prospective sources of errors since it is confronted with real data. However, the application of the displacements should be made with precision at least an order of magnitude better than the accuracy of the tested DIC method. To ensure such property, a very precise mechanical setup is required. In general, the applied displacement is a global rigid body motion, in that way, the local measurements (i.e. from different correlation windows) provide an estimate of the method accuracy from the standard deviations over the local results. This kind of experiment was used to quantify the D-DPC performances in the validation experiment of Sec. 2.8. The standard deviations over the displacements measured for the different grains gave an estimate of the method accuracy in order of 0.1 voxels in translations and about $1°$ in rotations.

Another way to study DIC errors is to numerically transform a reference image by applying a given displacement field. The image is acquired on a real experiment, and hence, it contains all the intrinsic sources of errors. This constitutes an advantage of this approach which has been widely used in several works. For instance, [Hild and Roux, 2006, Roux and Hild, 2006] applied a virtual translation to a real image to evaluate the uncertainties of Q4-DIC method and showed that the displacement uncertainty evolves as a power law with the size of the zone of interest ZOI (the elements size). The authors also provided an expression of the uncertainties due to noise as a function of noise amplitude, ZOI size and the gradient of the tested image gray levels. [Schreier et al., 2000] applied similar approach with the cross-correlation DIC to identify the errors induced by the interpolation phase in the method. The study showed a resulting symmetric S-shape function relating the uncertainty to the sub-pixel fraction of translations. The authors also investigated the error due to the mismatch between the shape functions used in the correlation coefficient and the real transformation in [Schreier and Sutton, 2002]. It has been shown that the error due to the discrepancy between the shape function and the actual displacement is proportional to the first-order term of this discrepancy. A drawback of using this method is that it is required to interpolate the gray level in order to generate displaced images from the acquired image. These interpolations may introduce errors on the measured displacements which do not relate to the DIC method. In the applications cited above, the authors claim that applying the transformation in Fourier space (by making use of the shift theorem) permits to reduce this effect. Strictly speaking, this is true for band-limited images only.

Another approach is to numerically simulate both the reference and the deformed images. In such simulations, one can use available models that mimic the imaging process to generate synthetic images. These models do not need any interpolation of the image gray levels. An additional advantage

of this technique is that it provides a better control of the intrinsic sources of errors to include in images (noise, variations of gray levels...). This approach was used in investigations where a virtual sinusoidal displacement field [Bornert et al., 2009] or a pure translation [Amiot et al., 2013] were applied. The sinusoidal displacement allows varying the spatial frequency of the applied displacement. In [Bornert et al., 2009], it has been shown that three main error regimes exist in DIC results. The first one is obtained when the displacement period is smaller than the subset size. This regime is the most limiting one since the measurement cannot be performed. The second regime is associated with the mismatch of the shape function. This error was shown to increase with increasing subset size. The third regime corresponds to the error obtained when the shape function does accurately fit the actual displacement field. This error increases with the noise level and, contrary to the mismatch error, it decreases when the subset size increases. The second and third regimes have opposite behaviors with respect to the increase of the subset size and hence an optimal size must be determined to reduce the overall error. The study of [Amiot et al., 2013] around the pure translation was applied to multiple packages with different DIC implementations and settings. The authors showed the existence of some generic behaviors common to all different packages. For instance, the existence of the S-shaped systematic error curve, the increase of the random error with image noise and its decrease with the subset size were observed in almost all of the tested DIC implementations.

For the discrete image correlation, a study of the error induced by image noise on the measured displacements is found in [Pannier et al., 2010]. This study presents an adaptation of the model proposed by [Roux and Hild, 2006] to DV-DIC [Hall et al., 2010]. This work provides expressions of the translations and rotations uncertainties as a function of the noise level, gray levels gradient and the grains geometry. In particular, these expressions were analytically evaluated for ideal grain shapes and led to an estimation of errors in the order of 0.003 voxels for translation and 0.02 degrees for rotations for a SNR = 20 and shapes with diameters about 60 voxels. These errors should be taken as lower bounds since only the image noise effect is considered. In the same work, a real overall rigid body motion experiment (similar to the one performed in Sec. 2.8) was carried out and the results gave an overall error of about 0.1 voxels in translations and about 0.1 degrees in rotations.

In the remainder of this chapter, we aim to quantify the errors in D-DPC measurements. For this reason, similar approaches as the one presented before and that are commonly mentioned in the literature will be used. The first approach using real experimental data was already carried out in the previous chapter and provided an estimate of the overall accuracy (0.1 voxels in translation and 1° in rotations, see Sec. 2.8 for experimental details); it does not explain the origins of the errors. In order to understand these origins, a second approach is adopted. Digitally simulated experimental projections from a fully known grains description will be used as experimental projection, like in the synthetic examples in Sec. 2.6 (where both digital and experimental projections were generated through the numerical projection model). Those examples were used as a validation of the method principle. As the aim of these simulations was to validate the method and not to probe its performance, no sources of errors were considered. Indeed, no image noise was added, and the same projection model was used to produce both digital and target projections. Now, in order to explain the origins of the

measurements uncertainties, we should simulate both intrinsic and extrinsic sources of errors in the synthetic experiments. For instance, adding noise into the generated projections allows taking into account the effect of sensor noise on the results. In addition, using a different model to generate the projections allows testing the assumptions made in the projection model described in Sec. 2.3 and its capability to simulate the tomographic projections.

Before carrying out this study, we will present the main sources of error that will be investigated in analogy with the errors observed in DIC. Image noise is a probabilistic phenomenon that is always considered in the assessment of the accuracy of digital image correlation results and will be first addressed in Sec. 3.2. Another potential source of error is image discretization. This error is due to the fact that we compare tomographic projections of a real continuous medium to digital projections of a voxelized representation of the medium. The discretization errors are investigated in Sec. 3.3. The other point that can prevent from reproducing digital projection that accurately fits the experimental ones is the errors related to the projection model. This point is the subject of Sec. 3.4. These two errors in the case of D-DPC can be compared to the errors due to interpolation in the usual DIC methods. In fact, the projections simulated with the projection model developed in Sec. 2.3 can be seen as interpolated projections to approximate the ones we would have if the granular medium geometry was exactly known and the projection model mimics accurately enough the tomographic projections.

Another source of error can be the deviations from the perfect geometry we suppose for the tomography setup. Indeed, we assume no relative motion between the source and the detector and that the rotation axis is fixed. If known, theses fluctuations can be easily introduced in the projection model thanks to the generic formulation of the method. However, these errors are also affecting the full 3D reconstructions, and since no noticeable accuracy loss was observed with classical methods (V-DIC for instance), this point was not investigated.

3.2 The effect of image noise on D-DPC results

Like in every image acquisition apparatus, noise is always present in the output images. In the case of X-ray tomography, the images (the projections) are corrupted with noise due to several random phenomena. The main phenomenon is the number of photons that leave the source which follows a Poisson law. Other phenomena are the number of photons that intersect the object but are not attenuated and those that are not captured by the detector which both follow binomial laws. In the end, in X-ray imaging, the noise distribution is generally approximated as following a Poisson law by neglecting the effect of the other disturbances in the output data. The image noise is quantified by the signal to noise ratio as used before in Eq. (2.40). This ratio describes the ratio of uncertainty in the measured data. To reduce the noise in tomographic projections, two procedures can be used:

- A long exposure time which allows to increase the number of received photons in the detector and the signal to noise ratio, within the saturation limit of the detector.

- Averaging over multiple images for the same projections which allows reducing the noise variance in the averaged image by a factor of $\sqrt{N}$, where N is the number of averaged images.

The two procedures are generally combined in order to produce images with reduced noise. In the case of our test in Sec. 2.8 a SNR = 50 was found with a frame rate of 2 images per second and projections averaged over 40 images (see Fig. 2.17).

In order to illustrate how this probabilistic noise affects the results of D-DPC, let us recall that the aim of the method is to find the displacements as a vector $\mathbf{q}$ supposed to be the minimizer of a given cost function $F(\mathbf{q})$. If we consider the evolution of the function with respect to a one-dimensional translation we obtain the plot given in Fig. 2.10 left. We consider now a noise variable $N(\theta, \underline{p})$ for every pixel $\underline{p}$ and orientation angle θ that we add to projections. As defined in Sec. 2.3, the projections are the logarithm of the calibrated radiographs. A more realistic consideration of noise, as random variables added to radiographs is discussed later in Sec. 3.2. We define a new cost function with noisy experimental projections by using the noise variables as follows:

$$F^N(\mathbf{q}) = \sum_{\theta, \underline{p}} \left[\hat{P}(\theta, \underline{p}; \mathbf{q}) - \left(P(\theta, \underline{p}) + N(\theta, \underline{p}) \right) \right]^2 \tag{3.1}$$

Adding noise induces a statistical error in the determination of the displacements of the grains. Indeed, there is no reason why the objective function F^N, defined in Eq. (3.1), should reach its minimum at the same point as the objective function F, defined in Eq. (2.1). This is illustrated in Fig. 3.1 where F and F^N are plotted against a grain translation u. The noisy objective function presented in the figure is an average of ten functions computed with different noise realizations. A Gaussian distribution $\mathcal{N}(0, \sigma^2)$ was used to generate the $N(\theta, \underline{p})$, with a deliberately small signal to noise ratio such that

$$\max_{\underline{p}} P(\theta, \underline{p}) = 5\sigma$$

We can evaluate the mean and variance of this function as follows:

$$E[F^N(\mathbf{q})] = \sum_{\theta, \underline{p}} E[N(\theta, \underline{p})^2] - 2 E[N] \sum_{\theta, \underline{p}} \left[\hat{P}(\theta, \underline{p}; \mathbf{q}) - P(\theta, \underline{p}) \right] + \sum_{\theta, \underline{p}} \left[\hat{P}(\theta, \underline{p}; \mathbf{q}) - P(\theta, \underline{p}) \right]^2$$

$$= n_\theta n_p \sigma^2 + F(\mathbf{q}) \qquad \text{(because } E[N] = 0) \tag{3.2}$$

$$\text{var}\left(F^N(\mathbf{q}) \right) = \text{var}\left(\sum_{\theta, \underline{p}} N(\theta, \underline{p})^2 - 2N(\theta, \underline{p}) \left[\hat{P}(\theta, \underline{p}; \mathbf{q}) - P(\theta, \underline{p}) \right] \right)$$

$$= n_\theta n_p \, \text{var}(N^2) + 4\sigma^2 F(\mathbf{q}) - 4 \, \text{cov}(N^2, N) \sum_{\theta, \underline{p}} \left[\hat{P}(\theta, \underline{p}; \mathbf{q}) - P(\theta, \underline{p}) \right] \tag{3.3}$$

where n_θ and n_p are respectively the number of orientations and pixels. In the parallel beam case, the integration of the intensity over the detector represents the attenuation of the overall specimen. Therefore, this integration does not change with grains motion and we can write:

$$\int_{-\infty}^{+\infty} \int_{-\infty}^{+\infty} \hat{P}(\theta, x\underline{e}_x + y\underline{e}_y; \mathbf{q}) \mathrm{d}x \mathrm{d}y = \int_{-\infty}^{+\infty} \int_{-\infty}^{+\infty} P(\theta, x\underline{e}_x + y\underline{e}_y) \mathrm{d}x \mathrm{d}y, \tag{3.4}$$
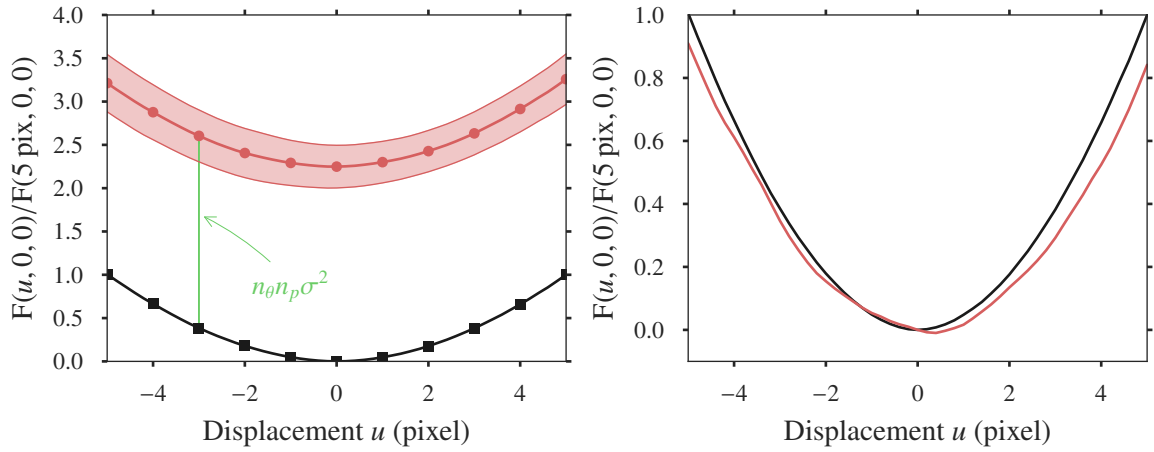
Figure 3.1: Influence of noise on the objective function: (Left) The black curve (square symbols) is the objective function. The red curve (disk symbols) is the average over ten realizations of the noisy objective function while the red thinner curves represent the standard deviation around the mean objective function. (Right) In red the averaged noisy objective function minus its minimum value to be compared with the objective function in black.

In the cone beam case, a difference is expected due to the projection geometry but we assume that it is small enough to be neglected compared to F($\mathbf{q}$). Accordingly, the sum over the pixels of the detector in the last term of Eq. (3.3) can be approximated by an integral and be neglected according to (3.4). As a result, the variance is approximated by:

$$\text{var}\left(\text{F}^N(\mathbf{q})\right) = n_\theta n_p \, \text{var}(N^2) + 4\sigma^2 \, \text{F}(\mathbf{q}) \tag{3.5}$$

We found that the mean of the noisy objective function (Eq.(3.1)) is equal to the noiseless function plus a constant term, while the variance depends on $\mathbf{q}$. This explains that the difference between the two functions in Fig. 3.1 is not constant along the horizontal axis which causes the shift in the global minimum (see Fig. 3.1, right).

An estimation of the noise-induced error can be obtained by Monte-Carlo simulations. When running simulations with noisy projections, we obtain, as expected, an error on the results. This error gets higher when the level of noise σ increases. It is also observed that the error diminishes when the number of projections used increases. A residual error remains even for the highest numbers of projections. The results of these simulations are reported in Fig. 3.2 by the square marks.

The value of the noise induced error depends on two types of parameters: the SNR which is linked to the imaging device imperfection, and the geometry parameters which include the object shape and size, the number of projections and the orientations of projections. Like in other DIC methods, the error increases with the image noise level. When increasing the number of projections, the error decreases (see Fig. 3.2) in a similar way to what it does with the subset size in DIC when there is no shape function mismatch [Amiot et al., 2013]. In the next section, we will present how to estimate this error from these parameters.

Estimation of error due to image noise

We want to evaluate the error induced by projection image noise in the estimated solution. Considering noise in the experimental projections, we write:

$$\mathbf{q} = \mathbf{q}^\star + \delta\mathbf{q}$$

where $\delta\mathbf{q}$ is the noise induced error between the optimization estimated solution $\mathbf{q}$ and the real solution $\mathbf{q}^\star$. Assuming $\delta\mathbf{q}$ is small compared to $\mathbf{q}^\star$ we can study the behavior of the objective function by linearizing the function expression. This linearization is an adaptation of the model developed in [Roux and Hild, 2006, Pannier et al., 2010] to our cost function.

We recall the form of the objective function with noise presence in experimental projections, with $P(\theta, \underline{p}) = \hat{P}(\theta, \underline{p}; \mathbf{q}^\star)$ (assuming that the digital projection of the medium at the solution is a good approximation of the experimental projections),

$$F^N(\mathbf{q}) = \sum_{\theta, \underline{p}} \left[\hat{P}(\theta, \underline{p}; \mathbf{q}) - \left(\hat{P}(\theta, \underline{p}; \mathbf{q}^\star) + N(\theta, \underline{p}) \right) \right]^2 \tag{3.6}$$

In the neighborhood of $\mathbf{q}^\star$ we can write:

$$\hat{P}(\theta, \underline{p}; \mathbf{q}) = \hat{P}(\theta, \underline{p}; \mathbf{q}^\star) + \delta\mathbf{q}^T \cdot \frac{\partial \hat{P}}{\partial \mathbf{q}} \left(\theta, \underline{p}; \mathbf{q}^\star \right) \tag{3.7}$$

Plugging Eq. (3.7) into Eq. (3.6), and expressing that $\mathbf{q} = \mathbf{q}^\star + \delta\mathbf{q}$ is a critical point of the noisy objective function, we find

$$\mathbf{M} \cdot \delta\mathbf{q} = \mathbf{b}^N \tag{3.8}$$

with :

$$\mathbf{M} = \sum_{\theta, \underline{p}} \frac{\partial \hat{P}}{\partial \mathbf{q}} \left(\theta, \underline{p}; \mathbf{q}^\star \right) \cdot \frac{\partial \hat{P}^T}{\partial \mathbf{q}} \left(\theta, \underline{p}; \mathbf{q}^\star \right) \tag{3.9a}$$

$$\mathbf{b}^N = \sum_{\theta, \underline{p}} N(\theta, \underline{p}) \frac{\partial \hat{P}}{\partial \mathbf{q}} \left(\theta, \underline{p}; \mathbf{q}^\star \right) \tag{3.9b}$$

Hence, and using the independence of the random realizations of noise on the pixels of the sensor $N(\theta, \underline{p})$, we can compute the expected value and variance of the noise induced error $\delta\mathbf{q}$

$$E[\delta\mathbf{q}] = \mathbf{M}^{-1} \cdot E[\mathbf{b}^N] = 0 \tag{3.10a}$$

$$\text{var}(\delta\mathbf{q}) = E[\delta\mathbf{q} \cdot \delta\mathbf{q}^T] = \mathbf{M}^{-1}\sigma^2 \tag{3.10b}$$

The matrix $\mathbf{M}$ varies as a function of the number and angles of projections used and also the geometry of grains, expressed by the gradient of the projections. The inverse of this matrix characterizes how

these parameters influence noise on the results and in particular the beneficial effect of increasing the number of projections.

An important property of the matrix $\mathbf{M}$ can be deduced from the independence of grains projections from the other grains displacements. From Eqs. (2.14) and (3.9a)

$$
\begin{aligned}
\mathbf{M} &= \sum_{\theta,\underline{p}} \frac{\partial \hat{P}}{\partial \mathbf{q}} \left(\theta, \underline{p}; \mathbf{q}^\star\right) \cdot \frac{\partial \hat{P}}{\partial \mathbf{q}}^T \left(\theta, \underline{p}; \mathbf{q}^\star\right) \\
&= \sum_{\theta,\underline{p}} \sum_i \frac{\partial \hat{P}^{(i)}}{\partial \mathbf{q}} \left(\theta, \underline{p}; \mathbf{S}^{(i)}\mathbf{q}^\star\right) \cdot \sum_j \frac{\partial \hat{P}^{(j)}}{\partial \mathbf{q}}^T \left(\theta, \underline{p}; \mathbf{S}^{(j)}\mathbf{q}^\star\right) \\
&= \sum_{\theta,\underline{p}} \sum_{i,j} \frac{\partial \hat{P}^{(i)}}{\partial \mathbf{q}^{(i)}} \left(\theta, \underline{p}; \mathbf{S}^{(i)}\mathbf{q}^\star\right) \cdot \mathbf{S}^{(i)} \cdot \mathbf{S}^{(j)} \cdot \frac{\partial \hat{P}^{(j)}}{\partial \mathbf{q}^{(j)}}^T \left(\theta, \underline{p}; \mathbf{S}^{(j)}\mathbf{q}^\star\right) \\
&= \sum_i \sum_{\theta,\underline{p}} \frac{\partial \hat{P}^{(i)}}{\partial \mathbf{q}^{(i)}} \cdot \frac{\partial \hat{P}^{(i)}}{\partial \mathbf{q}^{(i)}}^T \left(\theta, \underline{p}; \mathbf{S}^{(i)}\mathbf{q}^\star\right) \cdot \mathbf{S}^{(i)}
\end{aligned} \tag{3.11}
$$

The last simplification in the expression of $\mathbf{M}$ is due to the fact that $\mathbf{S}^{(i)} \cdot \mathbf{S}^{(j)} = \mathbf{O}_6$ if $i \neq j$. Introducing

$$
\mathbf{M}^{(i)} = \sum_{\theta,\underline{p}} \frac{\partial \hat{P}^{(i)}}{\partial \mathbf{q}^{(i)}} \cdot \frac{\partial \hat{P}^{(i)}}{\partial \mathbf{q}^{(i)}}^T \left(\theta, \underline{p}; \mathbf{S}^{(i)}\mathbf{q}^\star\right) \cdot \mathbf{S}^{(i)} \tag{3.12}
$$

we get:

$$
\mathbf{M} = \begin{bmatrix}
\mathbf{M}^{(1)} & 0 & \cdots & \cdots & 0 \\
0 & \mathbf{M}^{(2)} & 0 & \cdots & \vdots \\
\vdots & 0 & \ddots & & \vdots \\
\vdots & & & \ddots & 0 \\
0 & \cdots & \cdots & 0 & \mathbf{M}^{(n)}
\end{bmatrix} \tag{3.13}
$$

Every matrix $\mathbf{M}^{(i)}$ depends only on the variations of the projections produced by the motion of grain i. Expression (3.13) shows that the matrix $\mathbf{M}$ is block diagonal and that there is no coupling between two different grain displacements. This means that when it comes to estimating the noise induced error on a grain displacements, the estimated value is the same whether the grain is alone or within a granular medium. This result holds provided similar imaging conditions are used. In practice, these may however change, in particular because of the saturation limits and the dynamic range of the sensor.

As suggested by (3.13) we can study the noise effect individually for every grain. In this part, we will compute the component of the matrix $\mathbf{M}$ for a particular grain in two different ways:
As shown by the definition (3.12) of $\mathbf{M}^{(i)}$, a numerical estimation (by finite differences) of the projec-

tion gradient through the projection model developed in Sec. 2.3 allows to estimate the matrix **M**. Direct Monte-Carlo approach allows to estimate the covariance matrix var(δ**q**) for a given noise level σ. Then we can deduce the components of **M** from Eq. (3.10b).

The chosen grain has an elliptic shape of size 14x30 vox^2, and two projections were considered with angles of orientation $\theta = 0°$ and $90°$. Below, we provide results that compare both model evaluations of **M** and Monte-Carlo simulations for the same grain. The model evaluation is noted **M**$_{model}$ and the simulation estimation **M**$_N$ with N the number of realizations used. Also, standard deviations of the noise error computed by means of the model are reported in Fig. 3.2 by the black dots.
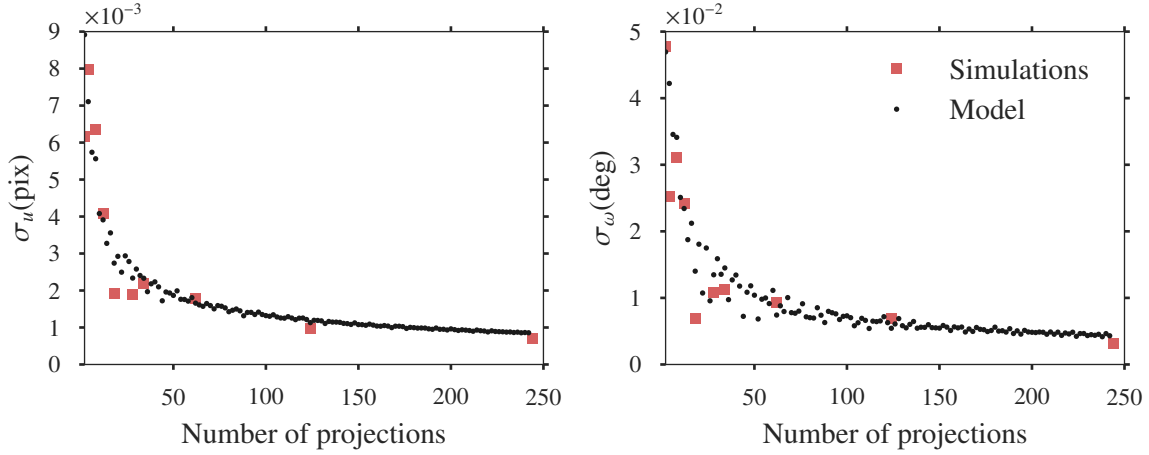

Figure 3.2: Noise error evolution as a function of the projections number for one grain: The squares link the number of projections used to the standard deviation of the obtained error. The standard deviations are computed from ten realizations. The black dots are the estimated noise error using the model developed in 3.2.

$$\mathbf{M}_{model} = \begin{bmatrix} 2.49 \ 10^{-3} & 1.24 \ 10^{-3} & -4.56 \ 10^{-15} \\ 1.24 \ 10^{-3} & 4.97 \ 10^{-3} & -1.32 \ 10^{-14} \\ -4.56 \ 10^{-15} & -1.32 \ 10^{-14} & 9.73 \ 10^{-6} \end{bmatrix} \quad (3.14a)$$

$$\mathbf{M}_{10} = \begin{bmatrix} 2.18 \ 10^{-3} & 1.68 \ 10^{-3} & 7.23 \ 10^{-5} \\ 1.68 \ 10^{-3} & 3.72 \ 10^{-3} & 6.47 \ 10^{-5} \\ 7.23 \ 10^{-5} & 6.47 \ 10^{-5} & 6.02 \ 10^{-6} \end{bmatrix} \quad (3.14b)$$

$$\mathbf{M}_{100} = \begin{bmatrix} 2.88 \ 10^{-3} & 1.69 \ 10^{-3} & 1.22 \ 10^{-5} \\ 1.69 \ 10^{-3} & 5.0 \ 10^{-3} & 1.74 \ 10^{-5} \\ 1.22 \ 10^{-5} & 1.74 \ 10^{-5} & 8.99 \ 10^{-6} \end{bmatrix} \quad (3.14c)$$

The results prove adequacy between the model estimation and the simulation errors. In the case of two projections, the simulations results were computed from 10 then 100 realizations and showed that ten simulations are sufficient to properly determine the noise error standard deviation; thus, only

ten simulations were used for the higher numbers of projections in Fig. 3.2.

Another estimation of the matrix **M** is made by analytical computation of the matrix components for the ellipse shape. This estimation gave the following result

$$\mathbf{M}_{\text{ana}} = \begin{bmatrix} 2.46 \ 10^{-3} & 1.77 \ 10^{-3} & 0 \\ 1.77 \ 10^{-3} & 6.0 \ 10^{-3} & 0 \\ 0 & 0 & 3.84 \ 10^{-6} \end{bmatrix} \tag{3.15}$$

In addition to the adequacy with the previous results, the analytical expression showed that the vanishing covariances are due to the particular symmetric geometry of the ellipse (the vanishing covariances were not caught accurately by the Monte-Carlo simulations). Moreover, in the case of a unique projection orientation, the matrix expression is singular which shows again, that with a unique projection the translations can not be both determined. Also for the particular case of circle shape the rotation component vanishes which shows that, as expected, the rotation cannot be determined in that case.

This estimation model constitutes a powerful tool for the tuning of the method. It allows having a prior value of the expected noise error. We can choose the number of projections and their orientations, then improve the noise level depending on the desired accuracy. Inversely, for a given noise level, we can estimate the number of projections needed to achieve the desired accuracy. For instance, in a real experiment, we can numerically evaluate the matrix $\mathbf{M}^{-1}$. Then, for the desired error level, that we express as a covariance matrix $\text{var}(\delta\mathbf{q})$, we can adjust the noise parameter and the number of projections using Eq. (3.10b).

Realistic model of tomographic noise

The noise in tomography projections as stated in Sec. 3.2 does not follow a Gaussian distribution. A local study by A. Gaye (see Appendix A of [Gaye, 2015]) of the noise in our tomography sensor, inspired from [Wang et al., 2010], shows, as expected, that the noise is not uniform but depends on the number of received photons and nearly follows a Poisson law. The dependence on the photon number is translated in the sensor output by a dependence on the gray levels. This study resulted in an expression of the noise parameter dependence on the pixel gray level of the local tomography detector given by the following function:

$$\sigma(G(\underline{p})) = \sqrt{0.6G(\underline{p}) - 2230} + 3.66 \tag{3.16}$$

where $G(\underline{p})$ is the gray level given by the pixel $\underline{p}$ of the detector for the orientation angle. In order to perform simulations with more realistic radiographs (corrupted with realistic noise rather than Gaussian noise), we use this function to generate them as:

$$G^N(\underline{p}) = G(\underline{p}) + N(\underline{p}) \tag{3.17}$$

where $N(\underline{p})$ are individually sampled from a centered normal distribution of standard deviation $\sigma(G(\underline{p}))$, in respect with Eq. (3.16). The choice of the normal distribution here is not to be confused with the

Gaussian noise used in the model of Sec. 3.2. This choice is to provide independent variables to use in Eq. (3.17).

We consider the grain chosen in the simulations of Sec. 2.5 (grain marked with green cross in Fig. 2.9). Our aim is ot generate projections of this grain corrupted with realistic noise.

By using Beer-Lambert's law written as

$$G(\underline{p}) = G_0 \exp\left(-\rho P(\underline{p})\right), \tag{3.18}$$

we can transform the projections $P(\underline{p})$ of the grain into radiographs gray levels $G(\underline{p})$ by writing:

$$\begin{cases} G_{\min} = G_0 \exp\left(-\rho P_{\max}\right) \\ G_{\max} = G_0 \exp\left(-\rho P_{\min}\right) = G_0 \end{cases} \Rightarrow \rho = -\log\left(\frac{G_{\min}}{G_{\max}}\right)/P_{\max} \tag{3.19}$$

$G_{\max}$ and $G_{\min}$ are the maximal and minimal values of the detector response in the study that provided Eq. (3.16). In this example, $P_{\min}$ is null (i.e not all the rays are attenuated). If not, $P_{\min}$ should be taken into account in the expression of Eq. (3.19).

Once we have the radiographs $G(\underline{p})$ of the grain, we use Eq. (3.18) to corrupt them with noise and then we get the noisy projections as

$$P^N(\underline{p}) = -\log\left(\frac{G^N(\underline{p})}{G_{\max}}\right)/\rho \tag{3.20}$$

We will now compare simulations made with projections corrupted with Gaussian noise, and others with realistic noise. It is no longer possible to compare the results of the matrix $\mathbf{M}$ because we have no such expression for the realistic noise. Therefore, we compare here the covariance matrix $\mathrm{var}(\delta\mathbf{q})$. For a relevant comparison we set σ of the Gaussian noise model to the maximal value of $\sigma(P(\underline{p}))$, which was estimated by producing multiple realizations of $P^N(\underline{p})$ (see Fig. 3.3).

Realistic noise model			Gaussian noise model		
$1.86\ 10^{-5}$	$2.02\ 10^{-6}$	$-1.37\ 10^{-6}$	$1.84\ 10^{-4}$	$9.25\ 10^{-5}$	$5.88\ 10^{-6}$
$2.02\ 10^{-6}$	$5.88\ 10^{-5}$	$-2.94\ 10^{-7}$	$9.25\ 10^{-5}$	$1.59\ 10^{-4}$	$-2.59\ 10^{-7}$
$-1.37\ 10^{-6}$	$-2.94\ 10^{-7}$	$1.99\ 10^{-7}$	$5.88\ 10^{-6}$	$-2.59\ 10^{-7}$	$8.25\ 10^{-7}$

Table 3.1: Covariance matrix comparison between realistic noise model and the Gaussian one

Results from simulations are reported in Tab. 3.1, and show that the error estimated with the Gaussian noise model is higher than the error found with the realistic noise model as expected from the choice of the standard deviation of the Gaussian noise, which induces an overestimation of the realistic noise. Therefore, the estimation model is still applicable as it provides an upper bound of the expected error.
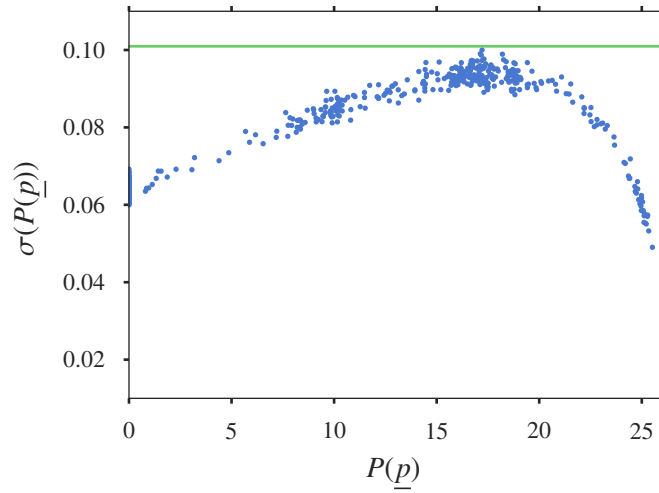
Figure 3.3: The blue points are the plot of standard-deviation of $\sigma(P(\underline{p}))$ estimated from 1000 realizations of $P^N(\underline{p})$ as given by Eq. (3.20). The green line indicate the chosen value for σ of the Gaussian noise model

Application to the experiment of Sec. 2.8

We can now estimate the noise effect on the results obtained in the test of Sec. 2.8. As it was demonstrated in Sec. 3.2, no coupling is found between different grains displacement when we estimate the errors induced by noise. Therefore, we treat every grain individually by calculating the matrix $\mathbf{M}^{(i)}$ at the reference state, then, inverting the matrix and multiplying by the noise variance σ^2 provides the estimated covariance matrix of the noise induced errors on the grain displacements. σ was estimated from the SNR value and Eq. (2.41).

Table 3.2 gathers the obtained standard deviations of all the grains. Expected errors are in the order of 0.001 voxels for translations and 0.1° for rotations.

The error amplitude expected from noise is way smaller than the method resolution that we get in the experiment of Sec. 2.8 (0.1 voxels and 1°). In the previous section, we saw that the fact of considering a Gaussian noise model overestimates the errors from a realistic noise model. Therefore, this estimation allows concluding that noise corruption is not the major source of error in the measured results.

The results obtained here are in the same order as the analytical error evaluations reported by [Pannier et al., 2010] for D-VDIC where quite similar SNR, and grains size and shapes were used.

3.3   Discretization: effect of the voxel representation.

The grain's representation as a voxelized image cannot provide an exact description of its geometry, therefore we cannot reproduce exactly its projections. For instance, let us consider an ellipse shaped

Grain number	u_x(vox)	u_y(vox)	u_z(vox)	$\omega_x(°)$	$\omega_y(°)$	$\omega_z(°)$
1	$9.84 \ 10^{-3}$	$2.14 \ 10^{-3}$	$6.08 \ 10^{-3}$	$1.46 \ 10^{-1}$	$4.32 \ 10^{-1}$	$1.11 \ 10^{-1}$
2	$6.4 \ 10^{-3}$	$1.55 \ 10^{-3}$	$5.74 \ 10^{-3}$	$5.89 \ 10^{-2}$	$2.06 \ 10^{-1}$	$8.36 \ 10^{-2}$
3	$1.01 \ 10^{-2}$	$1.87 \ 10^{-3}$	$4.33 \ 10^{-3}$	$1.4 \ 10^{-1}$	$2.35 \ 10^{-1}$	$6.92 \ 10^{-2}$
4	$6.99 \ 10^{-3}$	$1.82 \ 10^{-3}$	$6.27 \ 10^{-3}$	$8.57 \ 10^{-2}$	$2.84 \ 10^{-1}$	$6.72 \ 10^{-2}$
5	$7.09 \ 10^{-3}$	$2.4 \ 10^{-3}$	$4.37 \ 10^{-3}$	$1.17 \ 10^{-1}$	$2.81 \ 10^{-1}$	$1.29 \ 10^{-1}$
6	$9.17 \ 10^{-3}$	$1.8 \ 10^{-3}$	$6.88 \ 10^{-3}$	$9.14 \ 10^{-2}$	$2.71 \ 10^{-1}$	$5.83 \ 10^{-2}$
7	$5.49 \ 10^{-3}$	$2.67 \ 10^{-3}$	$6.64 \ 10^{-3}$	$1.42 \ 10^{-1}$	$3.78 \ 10^{-1}$	$1.48 \ 10^{-1}$
8	$5.08 \ 10^{-3}$	$1.83 \ 10^{-3}$	$4.16 \ 10^{-3}$	$9.55 \ 10^{-2}$	$2.54 \ 10^{-1}$	$8.29 \ 10^{-2}$
9	$6.66 \ 10^{-3}$	$1.77 \ 10^{-3}$	$4.8 \ 10^{-3}$	$9.87 \ 10^{-2}$	$1.76 \ 10^{-1}$	$6.35 \ 10^{-2}$
10	$5.4 \ 10^{-3}$	$1.99 \ 10^{-3}$	$4.63 \ 10^{-3}$	$8.21 \ 10^{-2}$	$2.24 \ 10^{-1}$	$7.27 \ 10^{-2}$
11	$5.45 \ 10^{-3}$	$2.43 \ 10^{-3}$	$7.33 \ 10^{-3}$	$9.15 \ 10^{-2}$	$2.4 \ 10^{-1}$	$1.25 \ 10^{-1}$
12	$6.08 \ 10^{-3}$	$2.71 \ 10^{-3}$	$7.31 \ 10^{-3}$	$1.39 \ 10^{-1}$	$2.79 \ 10^{-1}$	$1.74 \ 10^{-1}$
13	$5.02 \ 10^{-3}$	$2.78 \ 10^{-3}$	$8.05 \ 10^{-3}$	$1.01 \ 10^{-1}$	$2.09 \ 10^{-1}$	$1.55 \ 10^{-1}$
14	$9.24 \ 10^{-3}$	$4.68 \ 10^{-3}$	$8.25 \ 10^{-3}$	$2.93 \ 10^{-1}$	$3.02 \ 10^{-1}$	$2.66 \ 10^{-1}$
15	$5.85 \ 10^{-3}$	$2.35 \ 10^{-3}$	$5.4 \ 10^{-3}$	$9.17 \ 10^{-2}$	$2.34 \ 10^{-1}$	$1.11 \ 10^{-1}$
Mean	$6.93 \ 10^{-3}$	$2.32 \ 10^{-3}$	$6.02 \ 10^{-3}$	$1.18 \ 10^{-1}$	$2.67 \ 10^{-1}$	$1.14 \ 10^{-1}$

Table 3.2: Estimated standard-deviations
on displacements components of all the grains in the experiment of Sec. 2.8. The values are
estimated with the noise model developed in Sec. 3.2.

object. Its projection reads

$$
\begin{cases}
\dfrac{2ab}{R(\alpha)} \sqrt{1 - \left(\dfrac{r}{R(\alpha)}\right)^2} & \text{if } |r| \le R(\alpha) \\
0 & \text{otherwise}
\end{cases}
\tag{3.21}
$$

$$
R(\alpha) = \sqrt{a^2 \cos^2(\alpha) + b^2 \sin^2(\alpha)}
$$

where a and b are the semi-axes (see Fig. 3.4).

For an ellipse with $a = 16$ vox and $b = 12$ vox, Fig. 3.5 shows two sinograms. The first one is computed with the radiological path algorithm presented in Sec. 2.4 from a discretized image of the
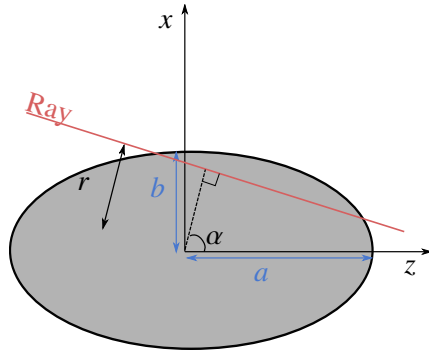

Figure 3.4: Illustration of an ellipse shape with semi-axis a and b in the tomography setup plane (Oxz). The parameters r and α allow to estimate the intersection between a ray and the ellipse as given by Eq. (3.21).
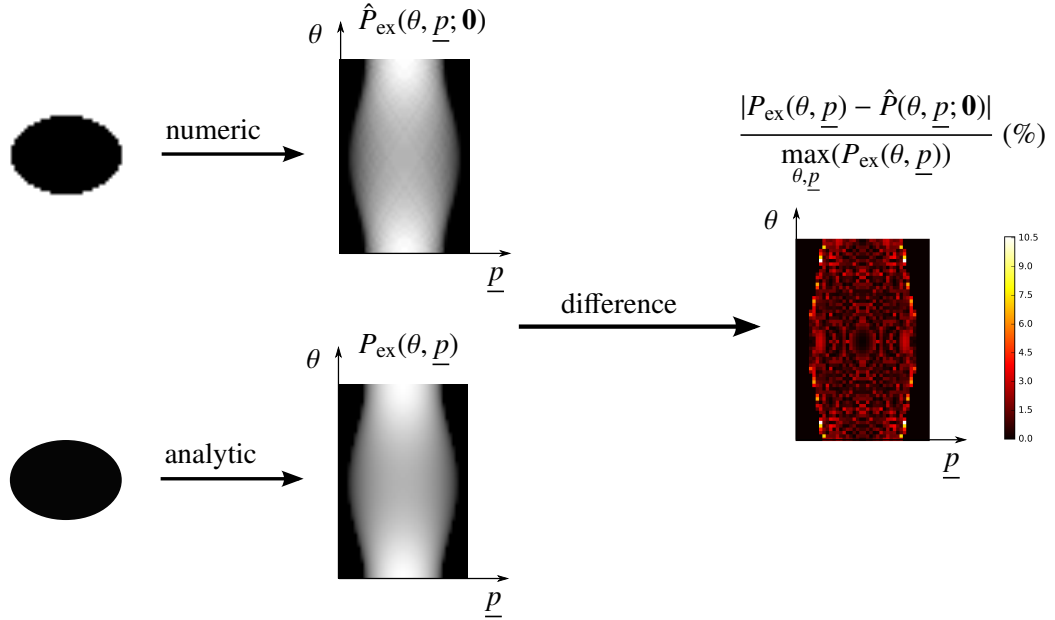
Figure 3.5: Sinograms computed from analytic and discrete description of an ellipse. The ellipse semi-axes are $a = 16$ vox and $b = 12$ vox, $\epsilon = 2.5\%$.

ellipse. This image is generated from the ellipse equation, such as, if the voxel center is inside the ellipse, then the voxel gray level is maximal ($\mu = 1$) otherwise it gets the minimal value ($\mu = 0$). The second sinogram is computed with Eq. (3.21). The difference between the sinograms is also shown in the figure; the errors are localized on the border which indicates that they are due to the discretization of the ellipse, especially at the borders.

To quantify this error we define a relative error as follow:

$$\epsilon = \left[\frac{\sum_{\theta, \underline{p}} \left(P_{\text{ex}}(\theta, \underline{p}) - \hat{P}(\theta, \underline{p}; \mathbf{0}) \right)^2}{\sum_{\theta, \underline{p}} P_{\text{ex}}(\theta, \underline{p})^2} \right]^{1/2} \tag{3.22}$$

where $P_{\text{ex}}(\theta, \underline{p})$ are exact sinograms computed from the closed-form expression and $\hat{P}(\theta, \underline{p}, \mathbf{0})$ sinograms from the discretized image. ϵ in this example is about 2.5%. We investigate how this error evolves with increasing image resolution. For that, we consider a discretized ellipse of minor semi-axis $b = a/2$ (a being the major semi-axis) and compute ϵ for different values of a/l (l being the voxel size). Fig. 3.6 represents the evolution of ϵ as a function of a/l. We used 120 projections angles evenly spaced over $[0°, 180°[$. The projection angles were maintained constant for relevant comparison. The figure shows that the error decreases when increasing the resolution of the image, which confirms that the obtained error is due to discretization.

It should be noted that this example is penalizing for the comparison. In fact, the transition from the ellipse to void is very harsh; we directly go from completely white voxels to completely black voxels, which amplifies the discretization effect. This type of discretization is going to be referred to as the sharp discretization. In real tomographic images, the partial volume effect [Hutton and Osiecki, 1998] results in a gradual change of the gray levels. In order to take this effect into account
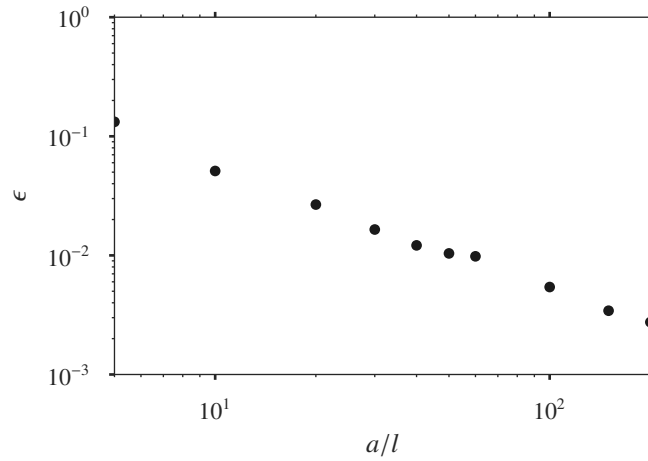
Figure 3.6: The evolution of the error ϵ defined in Eq. (3.22) with image resolution.
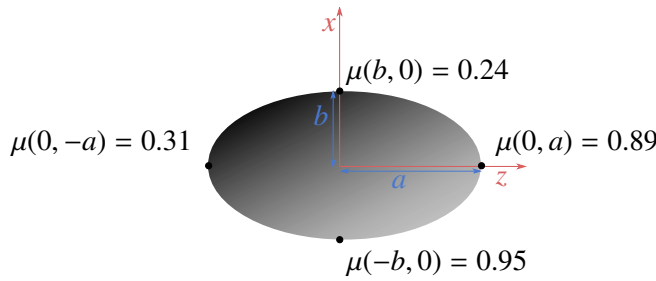

Figure 3.7: Illustration of the linear variation of grey levels given by Eq. (3.23)

in the evaluation of the error, we consider a new discretization of the ellipse, where this time, the edges are softly diminished. In this case, the voxel gray level is proportional to the ellipse volume fraction that it contains. We assume that the partial volume, equivalent to the arithmetic mean of attenuations, is representative of the partial volume effect. In fact, there is no obvious reason why the full 3D reconstruction would result in an arithmetic mean of the attenuations in border voxels. However, this choice was made just as an approximate representation of the smoothed gray levels in the object borders. In practice, we obtain such discretization by binning a higher resolution of the sharp discretization (every voxel is averaged here over 10x10 voxels). This discretization will be referred to as the smooth discretization.

We also considered an heterogeneous ellipse to see how the inside heterogeneity contributes to this effect. We chose a linear variation of gray levels inside the ellipse. The linear variation allows having a closed form expression of the heterogeneous ellipse projections. This variation of the attenuation inside the ellipse is given by (see Fig. 3.7):

$$\mu(x, z) = -\frac{5}{7a}x + \frac{2}{7a}z + \frac{3}{5} \tag{3.23}$$

The same evaluations of ϵ is made for the different discretizations, and results are reported in
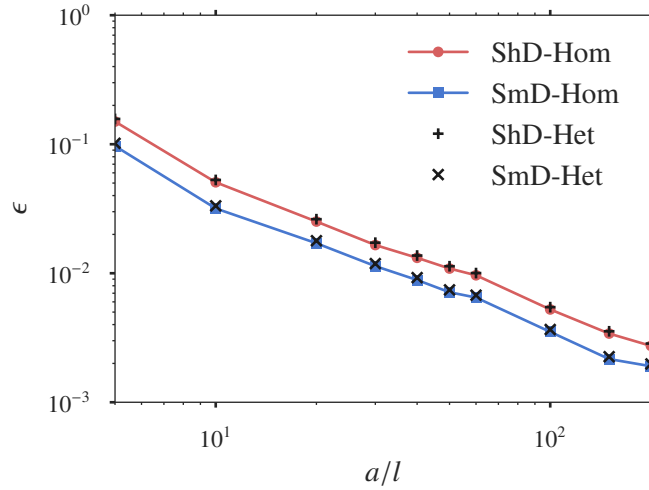
Figure 3.8: The evolution of the error ϵ defined in Eq. (3.22) with image resolution. ShD stands for Sharp Discretization and SmD for Smooth Discretization, while Hom or Het is for homogeneous or heterogeneous ellipse.

Fig. 3.8. The figure shows an improvement of the error when the edge discretization is gradual. This improvement is independent of the resolution, as the two curves of different discretization remain at same distance regardless of the value of a/l. This means that the smooth discretization does not improve the convergence rate of $\epsilon(a/l)$ to zero. The other aspect that the figure shows is the difference between the homogeneous and heterogeneous ellipses. No noticeable difference in the error is observed between the homogeneous and heterogeneous cases. Despite a very small increase of the error in the heterogeneous case, the points of the curves almost coincide. For the linear variation of gray levels considered in this example, the results allow concluding that the heterogeneity contribution to discretization errors are negligible in comparison to the initial discretization error.

Some D-DPC simulations were performed with these discretized ellipses to observe the impact of this error on the estimated displacements. In these simulations, we applied to the ellipse a motion

$$\mathbf{q}_{\text{exact}} = (-0.037a, 0.48a, -4°), \tag{3.24}$$

then we computed its analytic projection using the closed-form expression. We run simulations, where the analytic projections are used as the target projections $P(\theta, \underline{p})$ while the projections $\hat{P}(\theta, \underline{p}; \mathbf{q})$ (see Eq. (2.1)) were simulated with the projection model from the sharp discretization of the ellipse.

To generate digital projections from the polyginal discretization, a simple adaptation of the radiological path algorithm is needed. Fig. 3.9 shows the different segments to estimate for a border voxel in the usual and polygonal discretization. The ray is represented in red, and the aimed ray segment is plotted in a thicker width. Assuming that the line describing the object border is defined by a point and a normal vector $\underline{n}$, and that the object surface is oriented such that the normal vector is outgoing from the object. Instead of computing the chord from $\alpha_2 - \alpha_1$, $|\alpha_2 - \alpha_i|$ should be considred, where
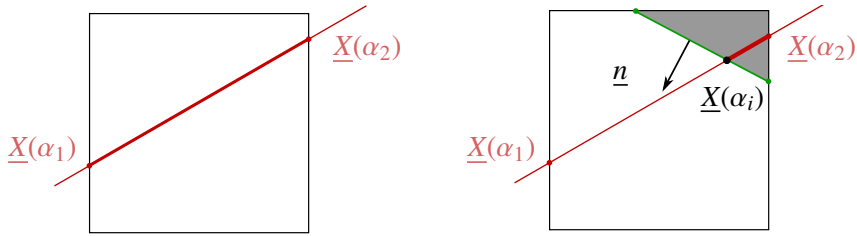
Figure 3.9: Illustration of the adaptation added to Siddon's algorithm in order to take account for the polygonal discretization at border voxels.

	$a/l = 10$	$a/l = 100$
2 projections	$\left(4.9\ 10^{-3}\,a, 5.4\ 10^{-3}\,a, 0.45°\right)$	$\left(2.7\ 10^{-4}\,a, 2.6\ 10^{-4}\,a, 0.06°\right)$
4 projections	$\left(3.8\ 10^{-3}\,a, 5.4\ 10^{-3}\,a, 0.43°\right)$	$\left(9.6\ 10^{-5}\,a, 1.6\ 10^{-4}\,a, 0.05°\right)$
12 projections	$\left(4.3\ 10^{-3}\,a, 5.6\ 10^{-3}\,a, 0.68°\right)$	$\left(1.19\ 10^{-4}\,a, 1.07\ 10^{-4}\,a, 0.003°\right)$

Table 3.3: Errors obtained in simulations of a discretized ellipse displaced by $\mathbf{q}_{\text{exact}} = (-0.037a, 0.48a, -4°)$. The experimental projections are computed from the closed-form expression in Eq. (3.21). The table reports results for different values of a/l and numbers of projections.

α_i is computed from the intersection of the ray and the borderline. In practice we evaluate α_i from the intersection, and we consider $|\alpha_2 - \alpha_i|$ or $|\alpha_i - \alpha_1|$ depending on the sign of $\underline{n} \cdot (\underline{X}_2 - \underline{X}_1)$. This modification is only recquired for the border voxels.

In a first simulation two projections of angles $\theta = 0°$ and $90°$ were used. The results of the simulation are presented in the first line of Tab. 3.3. From this experiment we can see that the increase of resolution provides a better accuracy on the measure of translations. We went from a precision in the order of $10^{-3}a$ to a precision in the order of $10^{-4}a$ on the measure by going from a resolution of $0.1a$ per voxel to $0.01a$ per voxel. The precision on translation is coherent with the increase in the resolution fineness, but in terms of voxels the subvoxel accuracy remains the same (namely 0.01 voxels).

Regarding the rotations, we also observe a better accuracy in the same order of magnitude than the increase of resolution. If we choose a particular adequate distance, we can convert the rotation errors into translation errors and once again the subvoxel accuracy would stay independent of the resolution.

We now consider more projections (4 and 12 projections evenly spaced in $[0°, 180°[$) to compensate for the information loss due to discretization by additional angles of projections. It is observed in Tab. 3.3 that the increase of projections angles does not provide a noticeable improvement in precision, unless maybe for rotations as we can see in the case of $a/l = 100$ with 12 projections. More similar simulations are performed with other discretization methods and provide complementary results in the following section.

An enhanced image discretization: Polygonal discretization

In this section, we will adopt a different discretization approach to see how the improvement of the discretization enhances the method. This approach, permits a better description of the objects borders.
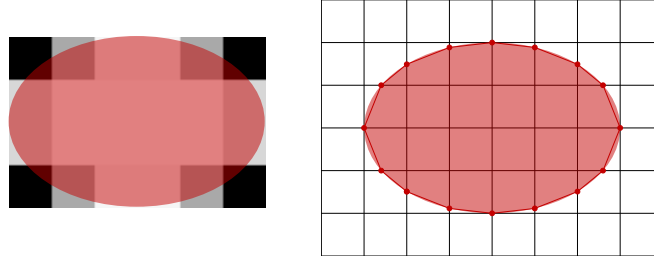
Figure 3.10: Illustration of the new discritization introduced in Sec. 3.3 in comparison with a smooth discretization of an ellipse.
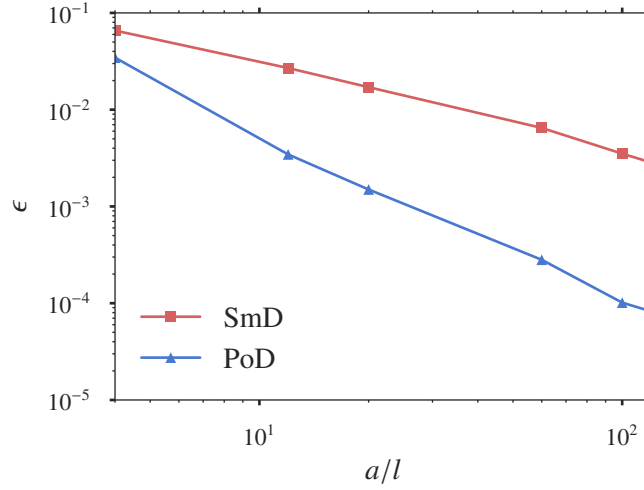

Figure 3.11: Evolution of ϵ as defined in Sec. 3.3 with the resolution a/l for an ellipse with smooth discretization in red and the polygon discretization in blue.

As shown by Fig. 3.10 the shape is discretized as a polygon instead of a group of voxels. The inside of the polygon is still voxelized, but its boundaries are defined by segments. This discretization will be referred to as polygonal discretization.

Let us assume that this kind of polygonal discretization is available. With this new discretization, for the same a/l the error ϵ is considerably smaller compared to the other discretizations. Moreover, when increasing the resolution a/l the error ϵ decreases faster. We can see in Fig. 3.11 a comparison of the evolution of ϵ in the case of regular smooth discretization of an ellipse and the case of the polygonal discretization.

To test the effect of this improvement of ϵ on D-DPC method, we conduct simulations like earlier in this section (Sec. 3.3). We consider the same ellipse with semi-major axis a and semi-minor axis $a/2$. We apply a displacement

$$\mathbf{q}_{\text{exact}} = (u_s, v_s, \omega_s), \tag{3.25}$$

and compute the analytic projections of this ellipse at this state. Then we run the simulation with two
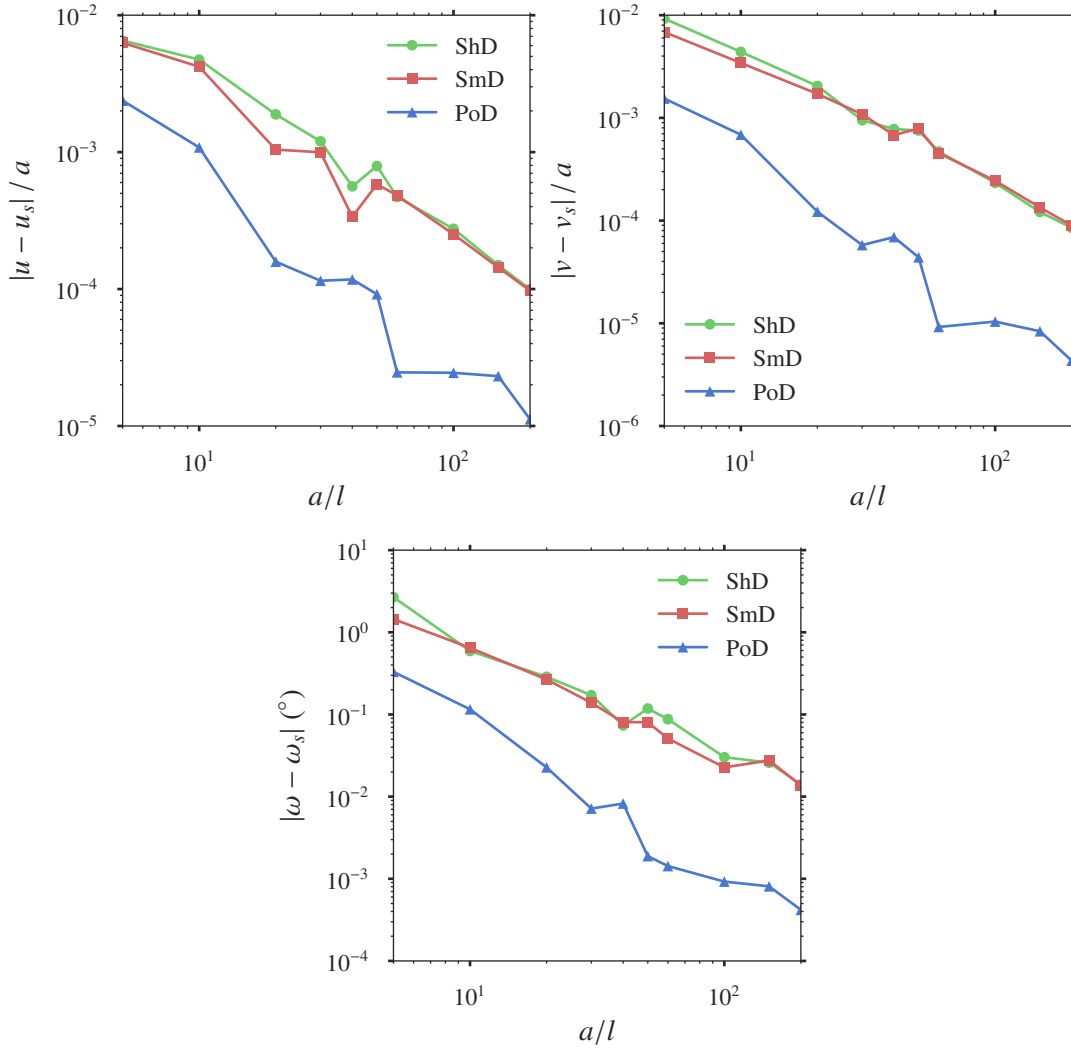
Figure 3.12: Plots of the evolution of errors on the components of $\mathbf{q}_{\text{D-DPC}}$ for sharp discretization (green), smooth discretization (red) and polygonal discretization (blue).

digital projections computed from sharp, smooth and polygonal discretizations of the ellipse. The projections were taken at angles $\theta = 0°$ and $90°$. u_s and v_s were randomly chosen between -1 and 1 voxels and ω between $-6°$ and $6°$. Fig. 3.12 shows results averaged over 10 realizations of $\mathbf{q}_{\text{exact}}$. In the figure, we see that with the polygonal discretization, the simulation errors decreases at the starting resolution with about an order of magnitude for both translations and rotations. Moreover, with increasing resolution fineness the error decreases faster in the polygonal discretization. The curves slopes in the log-log scale are about 1.5 in translation and 2 in rotation for polygonal discretization against 1 and 1.4 in the other discretizations.

These simulations prove that considering a more precise representation of the granular medium can provide a better accuracy when using D-DPC.
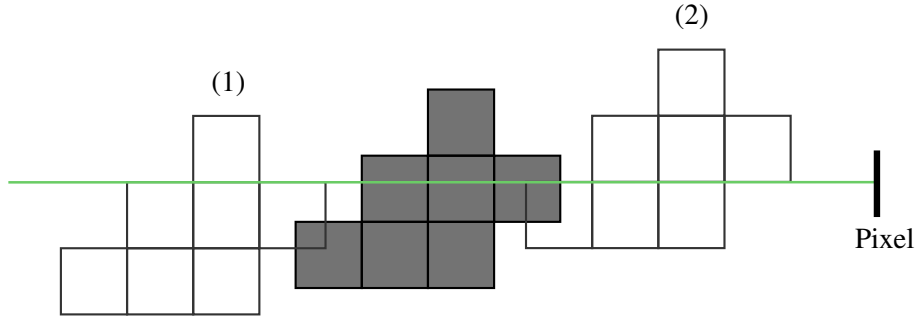
Figure 3.13: Illustration of the case where the image grid and the detector are parallel. The green ray is a ray from a parallel beam projection parallel to the grid. With the lumped beam assumption, a movement of the discretized grain perpendicular to the ray and smaller than one pixel (from state (1) to (2)) does not induce any change in the ray attenuation.
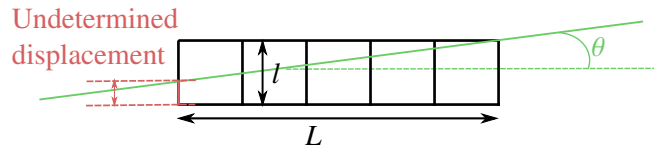

Figure 3.14: The undertemined translation due to the lumped beam assumption. The red distance is the translation of the object that does not provide a change in the ray attenuation.

The lumped beam assumption

The assumption of lumped beam was made in the projection model (Sec. 2.3). It states that every detector pixel receives a unique ray associated with its center. As we said before, this assumption is common in algebraic reconstruction algorithms as a good approximation of the ray integration on the detector pixels. The problem is, in some scenarios, a unique ray by pixel is not sufficient to change the pixel value for a small displacement of the grain. This occurs when the ray intersects the same grain voxels, even if the grain moves. The worst case is in a parallel beam projection. In the parallel beam case, detector pixels and image voxels have the same size. Therefore, when the image grid and the detector grid are parallel, and the rays direction is also parallel to the grid, a movement smaller than the pixel size has no effect on the projections. This problem is illustrated in Fig. 3.13, where the green line describes a ray in parallel beam setup. The movement of the discretized object from state (1) to state (2) does not affect the attenuation of the ray. In this case, the displacement that cannot be determined is in the order of the pixel size.

This problem is compensated when taking more than one projection, except for the direction $\underline{e}_y$ (the rotation axis) for which the object discretization is always parallel to the detector despite the orientation angle. Moreover, the projections which are not in the parallel direction also suffer from this problem with a minimum undetermined displacement that can be estimated by (see Fig. 3.14):

$$l - L\tan(\theta), \quad \text{as long as} \quad L \leq \frac{l}{\tan(\theta)} \tag{3.26}$$

This issue should be considered for every grain and not the overall image, because every grain is individually projected. If we consider a grain with a discretization grid parallel to detector and a

diameter of 40 voxels we need to use projections with $\tan(|\theta|) \geq \frac{1}{40}$ which is about 1.5°. Moreover, the grains are in different rotation states. Therefore, to guarantee at least one projection that does not suffer from this error, we should have at least two projections with a $\Delta\theta$ of at least 3° and less than 87°.

For the cone-beam projections case, the rays have different directions for the same projection angle. Therefore, this limitation does not occur, but a similar effect with reduced amplitude is to be expected. This effect is expected to be more critical as much as the voxel size gets closer to the pixel size (optical magnification closer to 1).

3.4 Projection model errors

The projection model as described in Sec. 2.3 makes use of the lumped beam assumption . We showed in Sec. 3.3 that because of the object discretization, this assumption leads to an intrinsic error of the method. Another error related to this assumption is also expected with the projection model. In fact, every detector pixel receives a beam of rays and the intensity measured by the pixel is actually an integrated intensity over the beam. Moreover, according to Beer-Lambert's law an integration over intensity is an integration of the exponential of the attenuation coefficients. More rigorously Eq. (2.4) should be corrected to take into account the pixel size h and read:

$$I(\underline{p}) = I_0(\underline{p}) \int_{-h/2}^{h/2} \int_{-h/2}^{h/2} \exp\left(-\int \mu\left(\underline{p} + x\underline{e}_x + y\underline{e}_y + s\underline{T}(\underline{p} + x\underline{e}_x + y\underline{e}_y)\right) ds\right) dxdy \tag{3.27}$$

In this section, we will investigate the errors induced by the approximation of Eq. (3.27) by Eq. (2.4) in the projection model. This question will be investigated by means of a simplified model, first in 2D and then in 3D.

A simplified case to study the model errors

We will consider an ellipse in the 2D case inside a tomography setup as illustrated in Fig. 3.15. In this figure, we represent the ellipse and the detector pixels. The detector is composed of n_p pixels of size h and referenced by the axis $\underline{e}_x$.

The ellipse center is displaced in the $\underline{e}_x$ direction by u. For a point $x\underline{e}_x$ of the detector the measured intensity is denoted $I_u(x)$ which can be precisely given through a closed form expression. Every physical pixel of the detector is indexed by an integer k such that the points of the pixel k are in the domain $]kh, (k+1)h]$ for $k = -n_p/2 \ldots (n_p/2 - 1)$.

Gray level functions

We denote by the gray level function, the value returned by the sensor pixel k. This value, depends on the assumption made about the sensor discretization. The ellipse position u is also a parameter for this function hence, the function is noted $G(k, u)$.
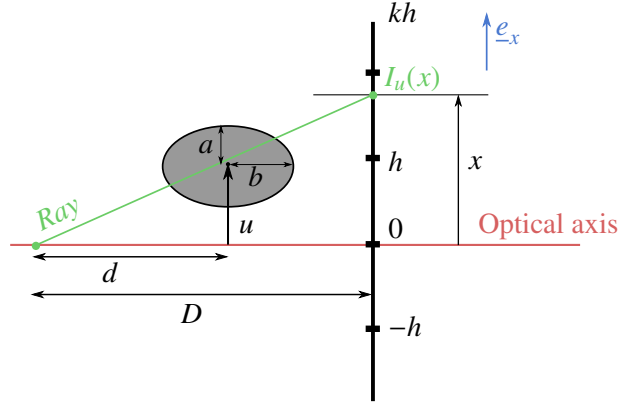
Figure 3.15: Illustration of the simplified case chosen to study the model assumptions effect on D-DPC accuracy in Sec. 3.4.

If we consider the integration over the rays of the beam received by the pixel k, then the value should be written:

$$G_{IB}(k, u) = \frac{1}{h} \int_{kh}^{(k+1)h} I_u(x)\mathrm{d}x \tag{3.28}$$

where IB is for "integrated beam" assumption. In the case of the "lumped beam" assumption (LB), the grey level value is given by:

$$G_{LB}(k, u) = I_u((k + \frac{1}{2})h) \tag{3.29}$$

In D-DPC, we make use of the lumped beam assumption in the projection model. If we consider that G_{IB} is representative of the true detector response (tomographic projections) and that G_{LB} represents the digital projections generated with the projection model (Sec. 2.3), a comparison of these two different detector responses (Eqs. (3.28) and (3.29)), will provide an estimation of the error made with this assumption. In order to carry out the comparison a geometry of the system must be chosen. The same geometry as in the test of Sec. 2.8 is considered to reproduce the experimental conditions:

- Pixel size: $h = 1\,\mathrm{pix} = 127\,\mu\mathrm{m}$

- Object to source distance: $d = 138.546\,\mathrm{cm}$

- Source to detector distance: $D = 156.704\,\mathrm{cm}$

and the ellipse size is taken in the order of the grains size in the experiment with:

$$a = 10\,\mathrm{vox} \tag{3.30}$$
$$b = 15\,\mathrm{vox} \tag{3.31}$$

where vox is the voxel size given by :

$$l = 1\,\mathrm{vox} = \frac{d}{D} \times h = 112\,\mu\mathrm{m} \tag{3.32}$$
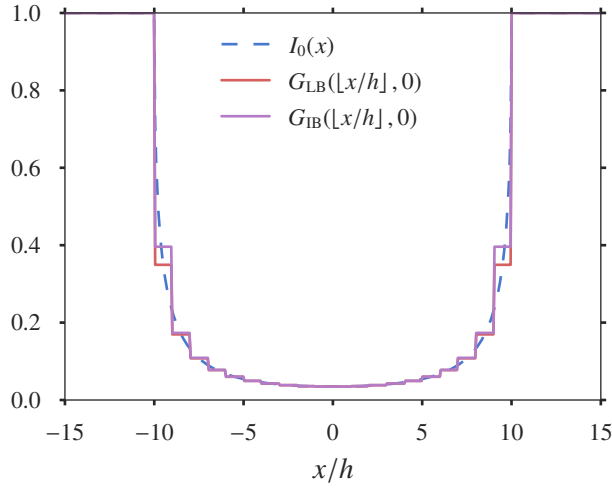
Figure 3.16: The evolution of measured intensity on the detector for the ellipse in Fig. 3.15. Discretized values following Eq. (3.29) and (3.28) are also plotted.

The functions $I_0(x)$, $G_{IB}(k, 0)$ and $G_{LB}(k, 0)$ are plotted in Fig. 3.16, where k is computed as the floor function of x by h

$$k = \lfloor x/h \rfloor \tag{3.33}$$

The figure shows the difference between the different sensor discretizations. A maximal difference between G_{LB} and G_{IB} is observed at the edges of the projected grain (pixels $k = 10$ and $k = -10$) and it is about 12%. Similar difference is to be expected between the digital and tomographic projections when using the lumped beam assumption in the projection model. Therefore, regarding this discrepancy, it is interesting to investigate its effect on the minimization process of the method.

The effect of the lumped beam assumption on the cost function

To evaluate the effect of the discrepancy due to the lumped beam assumption on the cost function, a functional that gives a different cost function depending on the model assumption is defined

$$\mathcal{F}[G](\delta u, u) = \sum_k \left(\log G(k, \delta u + u) - \log G_{IB}(k, u) \right)^2, \tag{3.34}$$

where δu is a small increment of u. In order that the minimization leads to the solution, this cost function should ideally find its minimum for $\delta u = 0$.

For instance, $\mathcal{F}[G_{LB}]$ compares G_{LB} to G_{IB}. This comparaison is similar to D-DPC cost function because the lumped beam assumption is made in the projection model, while G_{IB} is representative of the experimental projections that physically take account of the integration over the beam rays.

We plot both $\mathcal{F}[G_{IB}]$ and $\mathcal{F}[G_{LB}]$ for different values of u from 0 to 0.5 vox. The results are reported in Fig. 3.17. The left graph of the figure shows the curves for $\mathcal{F}[G_{IB}]$ where the integration
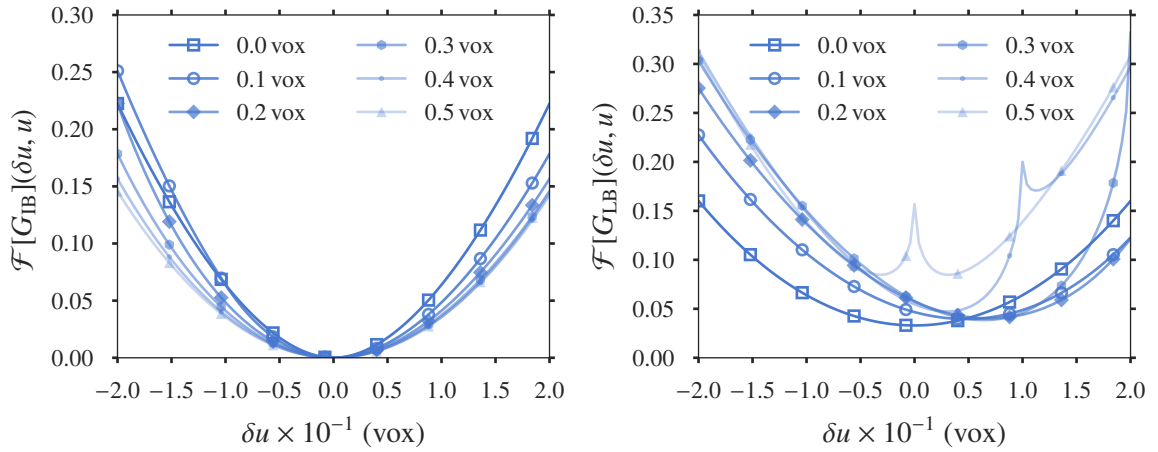
Figure 3.17: Plot of $\mathcal{F}[G](\delta u, u)$ (see Eq. (3.34)) for G_{LB} at left graph and G_{IB} in the right one, as a function of δu for different values of u.

over the ray beams is considered in both digital and experimental projections. For this case, as expected, the function always meets its minimum for $\delta u = 0$ and the minimum value is null.

In the right graph, for $u = 0$ vox the function $\mathcal{F}[G_{\text{LB}}]$ meets its minimum for $\delta u = 0$, but its value is not null because of the difference between G_{LB} and G_{IB}. Moreover, for other values of u the minimum is no longer met at $\delta u = 0$. Thus, the function minimum will not provide the correct estimate of displacement. The error reaches values in the order of 0.1 vox for u values between 0.3 and 0.4 vox.

This shows that errors in the order of 0.1 voxel can be expected in the results only due to the model adopted for projection. Note that in this example the ellipse geometry is entirely known in both digital and experimental projections and only the detector discretization was considered.

These results suggest the existence of a systematic error function of the fractional part of the grain displacement. This error can be quantified as the minimizer value of $\mathcal{F}[G_{\text{LB}}]$

$$\delta u_{\min}(u) = \underset{\delta u}{\text{argmin}} \left(\mathcal{F}[G_{\text{LB}}](\delta u, u) \right). \tag{3.35}$$

Fig. 3.18 shows that this systematic error is a periodic error with 1 voxel as period. The error evolves with respect to u taken from 0 to 5 voxels. A zoom of the graph for values of u smaller than 1 voxels shows that in a half voxel the error increase from zero for $u = 0$ vox to 0.075 vox for $u = 0.22$ vox, then it starts decreasing until -0.025 vox at half of the voxel ($u = 0.5$ vox) where it becomes discontinuous and changes sign. The second half is symmetric to the first one. This symmetry recalls the known S-shaped curve of the error induced by subvoxel interpolation in DIC [Schreier et al., 2000].

The discontinuity of the error encountered for $u = 0.5$ vox is explained by the discontinuity of $G_{\text{LB}}(k, u)$ at the border voxels ($k = 10$ and $k = -10$) with respect to the variations of u as shown in Fig. 3.19 with comparison to $G_{\text{IB}}(k, u)$. In particular, a plot of the function $G_{\text{LB}}(10, u) + G_{\text{LB}}(-10, u)$
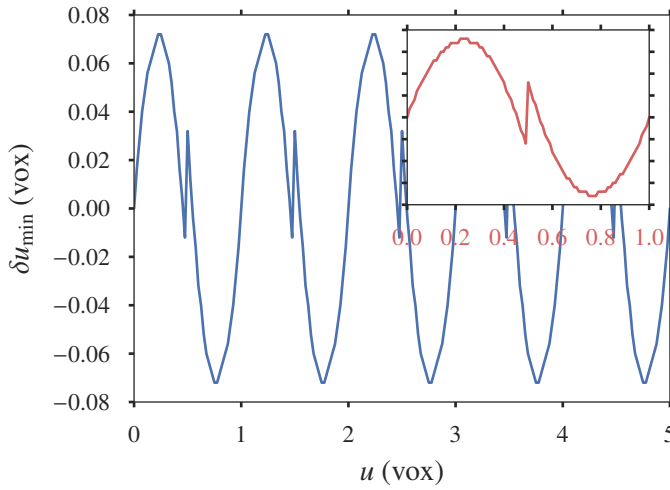
Figure 3.18: Evolution of $v_{\min}$ (see Eq. (3.35)) as a function of u.

as a function of u illustrates the discontinuity resulting at $u = 0.5$ vox in this example (see Fig. 3.20). This discontinuity is also at origin of the discontinuities observed on the curves of Fig. 3.17 (right). These discontinuities are observed for $u + \delta u = 0.5$vox, and induce local minima to appear on the cost function.

Extension to 3D

In this section, we provide an extension to 3D of the simplified case introduced in Sec. 3.4. For now, an ellipsoid is used instead of the ellipse and can move in the x and y directions. We also solve the expression of the measured intensity for a given projection orientation θ, so we can also investigate the effect of the multiple projection angles on the errors.

In a similar way as for the 2D case we define the intensity function $I_{u,v}(x, y)$ which gives the measured intensity on a continuous detector for the ellipsoid displaced by u in x direction and v in y direction. We also define the various 3D gray level functions as

$$G_{\text{IB}}(k_x, k_y, u, v) = \frac{1}{h^2} \int_{k_x h}^{(k_x+1)h} \int_{k_y h}^{(k_y+1)h} I_{u,v}(x, y) \mathrm{d}x\mathrm{d}y \tag{3.36}$$

$$G_{\text{LB}}(k_x, k_y, u, v) = I_{u,v}((k_x + \frac{1}{2})h, (k_y + \frac{1}{2})h) \tag{3.37}$$

With the same geometry parameters, and taking the third ellipsoid semi-axis $c = 12$ vox we have plotted in Fig. 3.21 in the left graph a two-dimensional plot of the function $I_{0,0}(x, y)$. This function is smooth and represents a projection of the ellipsoid at orientation angle $\theta = 0°$. Of course, this representation of the projection does not consider the detector discretization. Like in the 2D case, we can consider the detector discretization either by taking into account the integration over the beam for every pixel as stated in Eq. (3.27) which leads to the function G_{IB}, or by using the lumped beam
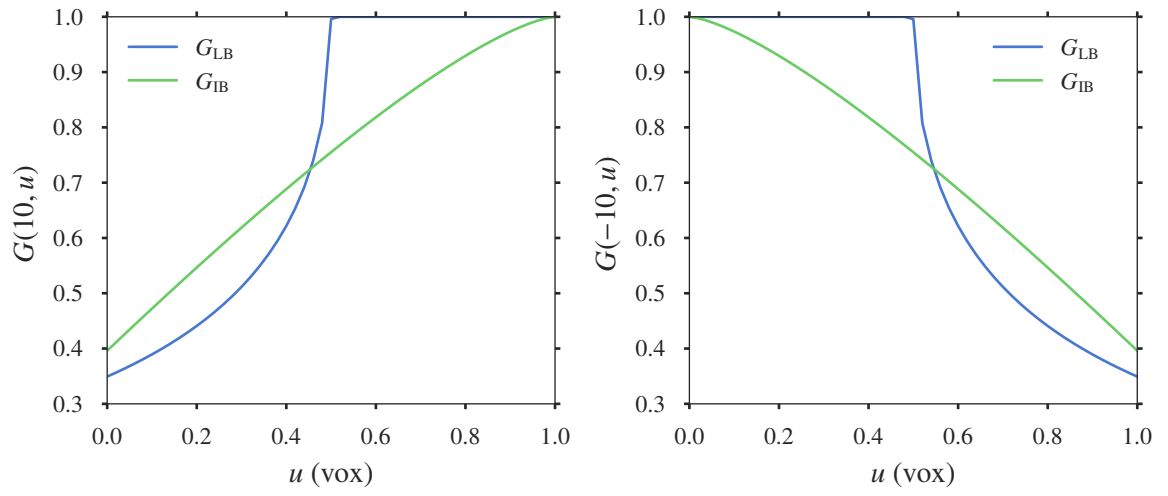
Figure 3.19: Plot of $G_{\mathrm{IB}}(k, u)$ and $G_{\mathrm{LB}}(k, u)$ as a function of u for (Left) $k = 10$ and (right) $k = -10$.
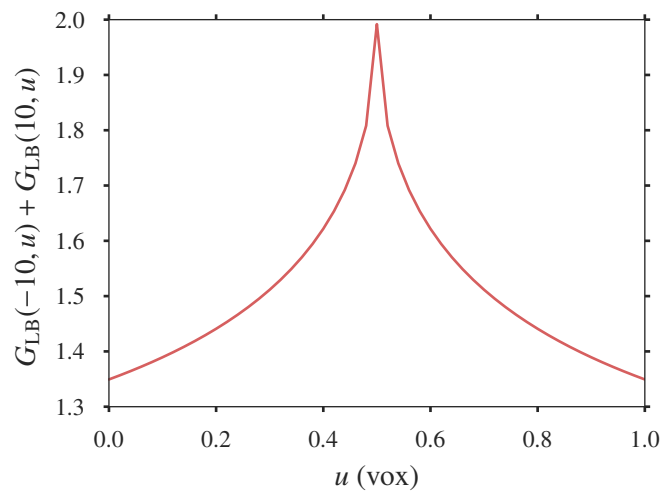

Figure 3.20: Plot of $G_{\mathrm{LB}}(10, u) + G_{\mathrm{LB}}(-10, u)$ as a function of u.
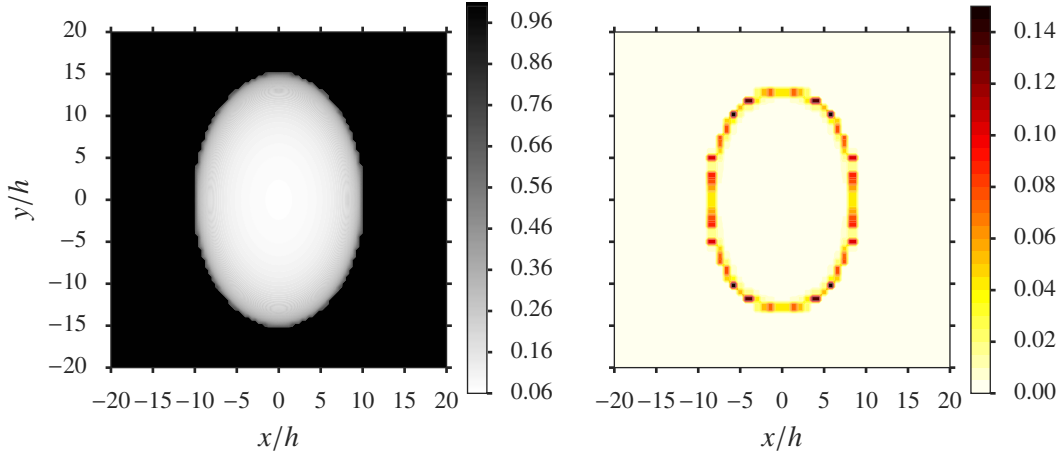
Figure 3.21: A two dimensional plot of the function $I_{0,0}(x, y)$ in the left graph. The right graph is the difference between model discretization of the detector and more realistic discretization taking account for the in-pixel integration of the intensities $|G(\lfloor x/h \rfloor, \lfloor y/h \rfloor, 0, 0) - G_{\mathrm{IB}}(\lfloor x/h \rfloor, \lfloor y/h \rfloor, 0, 0)|$.

assumption as for the projection model and use the G_{LB} function. The difference between projections obtained with this two types of discretization is represented in the same Fig. 3.21 at the right graph. As expected, the errors are concentrated at the borders of the projected ellipsoid.

We can now conduct the same analysis as in the 2D case, by redefining the functional in Eq. (3.34) to take into account the second dimension of the detector and the summation over the different projections orientations

$$\mathcal{F}[G](\delta u, \delta v, u, v) = \sum_{\theta} \sum_{k_x, k_y} \left(\log G(k_x, k_y, \delta u + u, \delta v + v, \theta) - \log G_{\mathrm{IB}}(k_x, k_y, u, v, \theta) \right)^2 \qquad (3.38)$$

We consider 4 projections with orientations $0°, 45°, 90°$ and $135°$, and we carry out the same analysis as in Sec. 3.4 for the 3D case. We consider a one-dimensional translation r such as $u = r \sin(\pi/3)$ and $v = r \cos(\pi/3)$ and define

$$\mathcal{F}_r[G](\delta r, r) = \mathcal{F}[G]\left(\delta r \sin \frac{\pi}{3}, \delta r \cos \frac{\pi}{3}, r \sin \frac{\pi}{3}, r \cos \frac{\pi}{3}\right) \qquad (3.39)$$

The evolutions of $\mathcal{F}_r[G_{\mathrm{LB}}]$ are reported in Fig. 3.22. We observe again that for $r = 0$ the minimum of $\mathcal{F}_r[G_{\mathrm{LB}}]$ is met in the right place (i.e $\delta r = 0$). When we increase r we obtain different values of δr at the minimum of $\mathcal{F}_r[G_{\mathrm{LB}}]$. This values are smaller than the values found in the 2D case, but they remain in the same order of magnitude (about 0.02 vox). Moreover, in this case, the variations of the objective function are less smooth, and several local minima have appeared. The existence of these local minima may constitute a serious limitation in the minimization process of D-DPC.

To see the effects of the lumped beam assumption on rotations, we carry out the same analysis but this time for a rotation variable ω. We consider the rotation around the axis $\underline{e}_y$ which coincides with
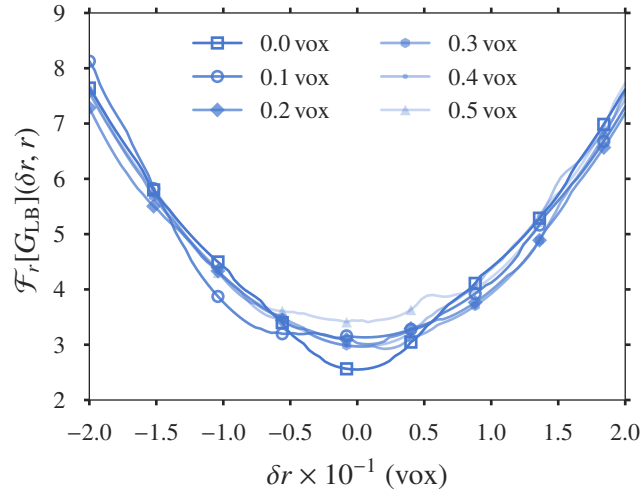
Figure 3.22: Plot of $\mathcal{F}_r[G_{\text{LB}}](\delta r, r)$ (see Eq. (3.39)). The evolution is as a function of δr for different values of r.

the stage rotation when $u = v = 0$, so we redefine $\mathcal{F}_\omega[G]$ as:

$$\mathcal{F}_\omega[G](\delta\omega, \omega) = \sum_\theta \sum_{k_x, k_y} \left(\log G(k_x, k_y, 0, 0, \theta - (\omega + \delta\omega)) - \log G_{\text{IB}}(k_x, k_y, 0, 0, \theta - \omega) \right)^2 \qquad (3.40)$$

With the same projections as before, and with $\omega = 6°$, we obtain the cost function evolution in Fig. 3.23. In a similar way to the translation case, we observe a minimum of the cost function which does not coincide with $\delta\omega = 0$. The minimum is met for $\delta\omega_{\text{min}} = 0.2°$. And again local minima have appeared in a small domain from $-2°$ to $2°$ around the solution.

The results obtained in this section, extend our conclusions to the 3D case. Both translation and rotation results are affected by the discrepancy observed between the gray levels obtained with the lumped beam assumption and those obtained when the intensity is integrated over the pixel size. These errors are in the order of 0.02 voxels and 0.2°. Moreover, local minima appear in the vicinity of the global minimum which may disturb further the estimated solution with the minimization process.

Approximation of the integration over the ray beam

In this section, we will see how approximating the ray beam integration in the projection model would allow reducing the errors. A trapezoidal approximation is considered. This integration is very costly and the projection time is as much higher as the number of integration points by pixel. Besides, as it was stated in Eq. (3.27) the integration is made over the intensities which are the exponential of the projections (radon transform).

To illustrate the advantage of considering the integration over the beam, we will consider the worst case where the lumped beam assumption is made and the intensities are computed from a discretized
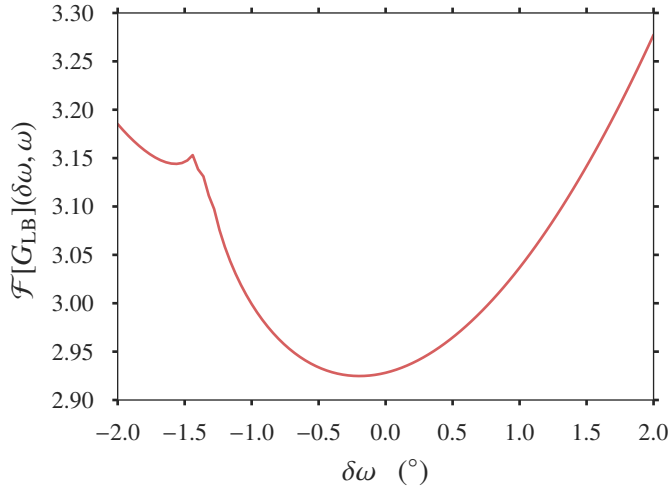
Figure 3.23: Plot of $\mathcal{F}_\omega[G_{LB}](\delta\omega, \omega)$ (see Eq. (3.40)), as a function of $\delta\omega$ for $\omega = 6°$.

ellipse with same dimensions a and b and voxel size l. We go back to the 2D case, where $I_u^d(x)$ denotes this intensity and G_{LB}^d the gray level given by projecting a discretized grain with the lumped beam assumption.

$$G_{LB}^d(k, u) = I_u^d((k + \frac{1}{2})h) \tag{3.41}$$

The green curve in Fig. 3.24 is the plot of $\mathcal{F}[G_{LB}^d](\delta u, u)$. Because we only consider a unique projection $\theta = 0°$ (the grain grid is parallel to the detector) in this example, the cost function is made of steps, which illustrates the undetermined displacement discussed in Sec. 3.3. This function is compared to the smooth $\mathcal{F}[G_{IB}](\delta u, u)$ given by the black curve.

We consider now the function G_n, which is a trapezoidal approximation of the intensity integration on the pixel over n points

$$G_n(k, u) = \frac{1}{4n}\left(I_u^d(kh) + 2\sum_{i}^{2n-1} I_u^d((k + \frac{i}{2n})h) + I_u^d((k + 1)h)\right) \quad \text{for } n > 0 \tag{3.42}$$

Fig. 3.24 shows a comparison between the different cost functions. The figure shows how the integration allows overcoming the limitation due to the lumped beam assumption by providing a better approximation of $\mathcal{F}[G_{IB}]$. The steps size decreases as the number of integration points increase. The error is divided by $2n$, which indicates that an integration with $n = 5$ is needed to achieve an improvement of an order of magnitude. In addition, the integration is made on the intensities, which requires estimating the exponential of the projections for every integration point. This provides and additional cost for the function evaluation, especially for the gradient of the function.
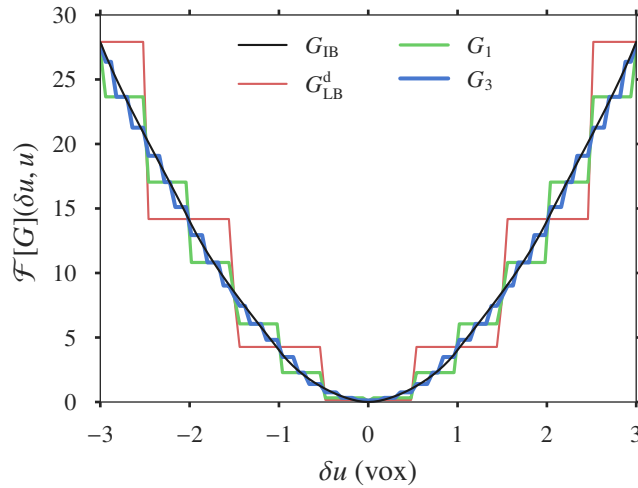
Figure 3.24: Plot of $\mathcal{F}[G](\delta u, u)$ For different intensity computations. The black line is for the intensity G_{IB}. The red line is for G_{LB}^{d} that takes into account the object discretization. The other curves are for G_n with $n = 1$ for the green curve and $n = 3$ for the blue one.

3.5 Discussion and conclusions

We studied different sources of errors related to D-DPC applications. The analysis of the effect of image noise in tomographic projections led to a model that estimates the expected errors. When this model was applied to the experiment of Sec. 2.8, we obtained results in the order of 0.001 voxels for translations and 0.1° for rotations, with a SNR value of 50. These results are in agreement with the analytical error estimates reported by [Pannier et al., 2010]. This shows that even with very few projections, our method has similar sensitivity to noise than the classical methods which require the recording of a whole sinogram. The values obtained for the noise effect do however not explain the accuracy obtained in the experiment and other sources of errors must be investigated.

Two additional sources of errors were studied. The first one is the voxel representation of the grains geometry, and the second one is the discrepancy in the projections caused by the lumped beam assumption. While these two factors are strongly correlated when the digital projections are generated, we tried to separate their effects by considering synthetic experiments where the grain geometry is perfectly controlled. These analyses showed that the errors due to discretization do not depend on the image resolution. Indeed when displacements are expressed in voxels, the precision maintains the same regardless of the resolution. For translations, this error is estimated in the order of 0.01 voxels. For rotations, the error goes from 0.1° for $a/l = 10$ to 0.01° for $a/l = 100$, with a as a characteristic length of the grain size and l is the voxel size.

The lumped beam assumption induces errors of about 0.02 voxels (translations) and 0.2° (rotations). Also, local minima of the cost function appear, which may disturb more the estimation of the solution and might explain the actual errors observed in a simple real experiment with uniform motion.

Another error linked to this assumption is that it produces an uncertainty on the measurement, just because in some cases a unique ray by pixel is not sufficient to catch the change in the projection produced by a small movement of the grain. The worst case, is the parallel beam projection for the $\underline{e}_y$ direction, for which the uncertainty is about one voxel.

The lumped beam assumption is commonly used in the full 3D reconstruction algorithms. Therefore, this discrepancy between the projection model and the response of the detector may also affect theses reconstructions. In particular, if such uncertainties are obtained on the geometry, comparing the full 3D reconstructions of different states is also subjected to such loss of accuracy.

The sources of errors investigated here provide an amount of material regarding improvements that can be considered to enhance the accuracy of the D-DPC method, which will be left for future developments.

Chapter 4

Characterization of oedometric compression using Discrete Element Method

Contents

In this work, we used the Discrete Element Method to model granular assemblies behavior subjected to *Oedometric* compression. The aim of this study is to characterize this type of mechanical test by understanding the macroscopic behavior of model granular material. We investigate the influence of the preparation process on the microstructure and stresses in the initial state. Such characteristics as density, coordination number, fabric and stress anisotropies will be monitored in oedometric loading cycles. This chapter is structured as follows. Sec. 4.1 introduces the main features studied in this chapter with an overview of related works found in the literature. Then, the model material and simulations procedure are described in Sec. 4.2. The different numerical packing methods and the resulting initial states under low stress are presented in Sec. 4.3. Results on the oedometric compression of the different initial states are reported in Sec. 4.4, both for the macroscopic behavior and the evolution of internal variables and microstructure. Sec. 4.5 discusses the mechanical response with reference to elasticity, frictional dissipation and contact network instabilities. Sec. 4.6 then investigates the effects of unloading and compression cycles. Sec. 4.7 finally sums up and discusses the results. We note that the results presented in this chapter are the subject of the article [Khalili et al., c] submitted for review.

4.1 Introduction

Beyond phenomenological description, investigations of the mechanics of granular materials in connection with their microscopic structural and rheophysical features are now being pursued throughout a significantly wider, multidisciplinary research community [Herrmann et al., 1998, Nakagawa and Luding, 2009, Goddard et al., 2010], ranging from geotechnical engineering to condensed matter physics. To this end, particle-level numerical simulations, analogous to molecular dynamics, and often referred to as "discrete element modeling" (DEM) for granular materials [Radjaï and Dubois, 2011, O'Sullivan, 2011], provide extremely valuable information. Such approaches have successfully been employed to investigate grain-level origins of such important aspects of granular mechanics as dilatancy properties by which dense and loose configurations differ in their small strain response [Thornton, 2000, Radjaï et al., 2004, Suiker and Fleck, 2004], the role of grain shape or such features as rolling resistance and angularity [Azéma et al., 2013, Saint-Cyr et al., 2012, Estrada et al., 2011, Azéma et al., 2012] in the development of internal friction. An important concept, the "critical state" – an attractor state under monotonically growing strains, as in homogeneous quasistatic shear flow, which does not depend on initial conditions – has been characterized and its properties related to micromechanical aspects [Radjaï et al., 2004, Rothenburg and Kruyt, 2004, Radjaï et al., 2012, Kruyt and Rothenburg, 2014].

Unlike such steady states, the configurations and the mechanical response of granular materials under small and moderate strains are sensitive to the initial material structure. In addition to their density, initial states are characterized in terms of structural anisotropy, whose importance has long been recognized in experiments [Oda, 1972, Arthur and Menzies, 1972, Lam and Tatsuoka, 1988, Benahmed et al., 2004, Atman et al., 2005, Khidas and Jia, 2010], and more recently investigated by numerical means [Silbert et al., 2002, Combe and Roux, 2011, Atman et al., 2014]. Coordination

numbers (i.e., average numbers of force-carrying contacts per grain) have also been observed to vary, independently of density. As coordination numbers are mostly inaccessible to experiment, these observations were carried out in numerical studies [Agnolin and Roux, 2007a, Magnanimo et al., 2008, Song et al., 2008], although some indirect comparisons with laboratory observations, through elastic moduli, were also proposed [Agnolin and Roux, 2007c]. Compressive loads, in which stress intensities, rather than stress directions, are varied, are crucially influenced by contact deformability and elasticity. Isotropic compression [Makse et al., 2000, Agnolin and Roux, 2007b] of isotropically assembled model granular materials is apparently a simple process, in which the contact network gets enriched due to a recruitement process closing gaps between neighboring grains. This simplicity is partly deceptive, though: upon unloading, while only a very small strain irreversibility is observed, the contact network may undergo profound changes; specifically, the final coordination number under low pressure may be much smaller than its initial value, before the compression cycle. Simple prediction schemes based on the assumption of homogeneous strain prove unable to capture such changes in contact number [Agnolin and Roux, 2007b].

The present work is a numerical study of oedometric compression of a model material made of elastic-frictional spherical beads, investigating how material anisotropy, either initially present or acquired in the compression, couples to stresses and strains. We shall systematically refer to ε_1, σ_1 as *axial* stress and strain, and to $\varepsilon_2 = \varepsilon_3$ and $\sigma_2 = \sigma_3$ as the *lateral* or *transverse* strains and stresses, respectively. Extending previous studies of isotropically assembled and compressed materials [Agnolin and Roux, 2007a, Magnanimo et al., 2008], a special attention is paid to the various possible initial states, which differ in density, coordination number and anisotropy, and their influence on the subsequent material response under load. As in a number of recent experimental and numerical studies [Khidas and Jia, 2010, Cavaretta et al., 2010, Lee et al., 2013, Lopera Perez et al., 2015, Gu et al., 2015], the ratio K_0 of lateral to axial stresses, which results from both the initial state and the effects of the subsequent compression, is monitored, and related to internal anisotropy. The effects of unloading and compression cycles are explored, both macroscopically (strains, density, K_0) and microscopically (contact network and fabric). Elastic moduli are investigated in order to assess the nonelastic, irreversible nature of compression response. Elastic moduli are also measurable characteristics apt to probe material microstructure and anisotropy, but this aspect is dealt with in next chapter.

4.2   Numerical model

Based on the integration of the equations of motion for solid objects, involving linear and angular momentum, masses and moments of inertia, the DEM simulations exploited here are a standard tool in granular micromechanics, as used in many articles [Thornton, 2000, Silbert et al., 2002, Suiker and Fleck, 2004] and described in more comprehensive treatises [Radjaï and Dubois, 2011]. We therefore dispense below with a full presentation of all relevant equations, by referring adequately to previous published work in which very similar models were implemented [Agnolin and Roux, 2007a, Peyneau and Roux, 2008b]. Nevertheless, we need to fix notations, introduce relevant control parameters, and

provide a sufficient definition of the numerical procedure.

Model material

We consider assemblies of spherical beads, interacting in their contacts through contact elasticity and Coulomb friction. The beads are slightly polydisperse, with diameter D distributed according to the following probability density function:

$$p(D) = \frac{2D_1^2 D_2^2}{(D_2^2 - D_1^2)} \frac{1}{D^3} \quad (D_1 \leq D \leq D_2), \tag{4.1}$$

which ensures a uniform distribution by volume between minimum value D_1 and maximum value $D_2 = 1.2 \times D_1$.

For contact elasticity, the same simplified version of the Hertz-Mindlin model [Johnson, 1985] is adopted as in Ref. [Agnolin and Roux, 2007a], suitably adapted to a polydisperse bead collection. Specifically, considering two beads i and j, with respective centers at points $\mathbf{r}_i$ and $\mathbf{r}_j$ and radii R_i and R_j, and introducing notation $h_{ij} = \|\mathbf{r}_j - \mathbf{r}_i\| - R_i - R_j$, the normal force transmitted F_{ij}^N in their contact vanishes for $h_{ij} > 0$ (distant bead surfaces) and depends otherwise on deflection $-h_{ij} >\geq 0$ as follows. Introducing the Young modulus E and the Poisson ratio ν of the solid material the beads are made of, and using notation $\tilde{E}$ for $E/(1 - \nu^2)$, one has

$$F_{ij}^N = \frac{\tilde{E} \sqrt{d_{ij}}}{3} |h_{ij}|^{3/2} \tag{4.2}$$

in which $d_{ij} = \dfrac{4R_i R_j}{R_i + R_j}$ is an effective diameter combining surface curvatures in the contact region. Due to Eq. 4.2 the normal stiffness expressing the response to small variations of deflection in the contact varies with deflection $|h_{ij}|$ or contact force F_{ij} as

$$K_{ij}^N = \frac{\tilde{E} \sqrt{d_{ij}}}{2} |h_{ij}|^{1/2} = \frac{3^{1/3}}{2} \tilde{E}^{2/3} d_{ij}^{1/3} \left(F_{ij}^N\right)^{1/3}. \tag{4.3}$$

The tangential elastic force $\mathbf{F}_{ij}^T$, as in [Agnolin and Roux, 2007a], relates to the relative tangential displacement in the contact, $\delta \mathbf{u}_{ij}^T$, involving a (deflection-dependent) tangential stiffness coefficient K^T assumed proportional to K^N:

$$d\mathbf{F}_{ij}^T = K_{ij}^T \, d\left(\delta \mathbf{u}_{ij}^T\right), \text{ with } K_{ij}^T = \frac{2 - 2\nu}{2 - \nu} K_{ij}^N. \tag{4.4}$$

Tangential stiffness K^T has to be suitably adapted (rescaled) whenever the normal elastic force decreases, in order to avoid spurious elastic energy creation [Elata and Berryman, 1996, Agnolin and Roux, 2007a].

The Coulomb condition enforces inequality $\|\mathbf{F}_{ij}^T\| \leq \mu F_{ij}^N$, with the friction coefficient μ set to 0.3 in the present study. It is taken into account by suitably projecting $\mathbf{F}_{ij}^T$ onto the circle of radius μF_{ij}^N in the tangential plane, after applying incremental relation (4.4), whenever necessary. Normal

and tangential contact force components also follow the general motion of the grain pair in order to ensure the objectivity of the model [Kuhn and Chang, 2006, Agnolin and Roux, 2007a].

While we use the elastic properties of glass, $E = 70$ GPa and $\nu = 0.3$ in our simulations, results, if suitably expressed in dimensionless form, exactly apply to all materials sharing the same dimensionless characteristics μ and ν. (Moreover, Poisson ratio ν only mildly affects elastic properties [Agnolin and Roux, 2007c], while material properties do not vary fast with the friction coefficient in the range $0.2 \leq \mu \leq 0.4$ [Fazekas et al., 2007, Lemaître et al., 2009]).

Finally a normal viscous force is added to the elastic-frictional one, in order to ease the approach to mechanical equilibrium under static loads. The same model as in Refs. [Agnolin and Roux, 2007a, Peyneau and Roux, 2008a] is used, with a damping constant choice corresponding to a velocity-independent, very low coefficient of restitution in binary collisions.

Boundary and loading conditions

We consider cuboidal samples, periodic in all three directions. We denote as L_1, L_2, L_3 the dimensions of the simulation cell parallel to the three axes of coordinates, to which correspond basis unit vectors $\mathbf{e}_1$, $\mathbf{e}_2$, $\mathbf{e}_3$. In oedometric compression, L_2 and L_3 are kept fixed, while L_1 varies, either enforcing the value of strain rate $\dot{\varepsilon}_1 = -\dot{L}_1/L_1$, or requesting the system to reach an equilibrium configuration under a given level of the corresponding normal stress in direction 1, σ_1.

In the stress-controlled case, L_1, the cell size in direction 1, satisfies an equation of motion such that it slowly increases or decreases, according to the sign of the difference between requested and measured values of σ_1 [Agnolin and Roux, 2007a, Peyneau and Roux, 2008a, Peyneau and Roux, 2008b]. Both strain rate controlled and stress-controlled simulations are carried out in such conditions that inertial effects remain small, by enforcing small enough strain rates $\dot{\varepsilon}$. Inertial effects are controlled by requesting the *inertial number I* [Roux and Chevoir, 2011] to remain very small. I is defined in terms of the mass m_1 of a grain of diameter D_1 and characteristic stress σ_1 as

$$I = \dot{\varepsilon} \sqrt{\frac{m_1}{D_1 \sigma_1}}. \tag{4.5}$$

We request I not to exceed $I^{\max} = 10^{-3}$ in the preparation stage, as a granular gas is gradually compressed to form the initial solid configuration. In the subsequent strain-rate controlled, quasistatic oedometric compression, we set $\dot{\varepsilon}$ to a smaller value, corresponding to $I = 10^{-5}$; upon unloading (as σ_1 and ε_1 decrease), even smaller strain rates are imposed, corresponding to $I = 10^{-6}$.

As in [Agnolin and Roux, 2007a, Peyneau and Roux, 2008b], the effect of global strains is equally felt by the grains throughout the sample, upon decomposing their motion into a fluctuating, periodic part and an affine contribution; and, in the stress-controlled case, the equation for cell dimensions L_α involves an acceleration term proportional to the difference between the requested value of stress $\sigma_{\alpha\alpha}$ and the currently measured one, using the following classical formula for stress components

$$\sigma_{\alpha\beta} = \frac{1}{V} \left[\sum_{i=1}^{N} m_i v_i^\alpha v_i^\beta + \sum_{1 \leq i < j \leq N} F_{ij}^\alpha r_{ij}^\beta \right]. \tag{4.6}$$

Eq. 4.6 expresses stress components as a kinetic term involving masses m_i and velocities $\mathbf{v}_i$ of all N grains i within sample volume V, added to a sum over pairs of interacting grains i, j transmitting force $\mathbf{F}_{ij}$ (from i to j) in their contact, $\mathbf{r}_{ij}$ denoting the "branch vector" pointing from the center of i to the center of j.

Although the present study focusses on oedometric compression, in which only L_1 varies, while L_2 and L_3 are fixed, we are also interested in the consequences of the procedure by which the initial solid configuration is assembled by compression from a loose configuration (a 'granular gas'), and we consider both oedometrically and isotropically compressed initial configurations under stress $\sigma_{\alpha\beta} = P\delta_{\alpha\beta}$, as in Refs. [Agnolin and Roux, 2007a, Peyneau and Roux, 2008b], all three L_α's being simultaneously reduced in the isotropic case. Isotropic compression is, however, only applied to granular gases at the assembling stage. The resulting granular packs are then subjected to oedometric loading paths.

4.3   Sample preparation, initial states

Motivation

Although widely recognized as crucially important for small strain mechanical response of granular materials, the assembling processes by which granular packs are prepared in a solid state are relatively seldom investigated, either experimentally [Lam and Tatsuoka, 1988, Rad and Tumay, 1987, Benahmed et al., 2004, Atman et al., 2005] or numerically [Emam et al., 2005, Combe and Roux, 2011]. One serious difficulty in the numerical modeling of such processes is the dependence [Silbert et al., 2002, Roux and Combe, 2011] of the final microstructure (density, coordination number) on dynamical dissipation parameters (such as restitution coefficients) which are not well known, and for which modeling choices are often guided by computational convenience as much as by physical realism.

We chose here to implement idealized assembling models, with the objective of obtaining a variety of initial structures representative of a wide range of *possible* material states. Although admittedly not conforming to laboratory procedures, those numerical preparation methods can be argued to exhibit some of the basic features resulting from such procedures as vibration or gravity deposition. Their main advantage is the possibility of varying, through rather wide intervals, the basic state variables: solid fraction Φ, coordination number z, and anisotropy in contact orientations. We also record the proportion of *rattlers* (i.e., grains that do not carry any force, in the absence of gravity), denoted as x_0, and other data pertaining to interneighbor distances and force networks.

Numerical assembling process and stress control

In practice, all configurations are obtained on compressing a loose configuration ($\Phi \simeq 0.45$, no intergranular contact, no kinetic energy) to equilibrium under low initial stress σ_0. Specifically, one requests $\sigma_1 = \sigma_0$ for oedometric compression, or $\sigma_1 = \sigma_2 = \sigma_3 = \sigma_0$ for isotropic compression. We use $\sigma_0 = 10$ kPa, assuming the particles are glass beads. This stress level is expressed in dimensionless form using a stiffness parameter κ, defined, as in [Agnolin and Roux, 2007a, Peyneau and Roux,

2008b, Roux and Chevoir, 2011], by

$$\kappa = \left(\frac{\tilde{E}}{\sigma_1}\right)^{2/3}. \tag{4.7}$$

With glass beads ($\tilde{E} \simeq 77$ GPa), $\sigma_0 = 10$ kPa corresponds to $\kappa_0 \simeq 39000$. Definition (4.7) is such that the typical ratio of contact deflection ($-h_{ij}$ in Eq. 4.2) to grain diameter is of order κ^{-1} [Agnolin and Roux, 2007a].

Defining $F_1 = \sigma_1 D_1^2$ as the relevant force scale, we request, as a practical equilibrium condition, all forces to balance on each grain within tolerance $10^{-4} F_1$, all torques to balance within tolerance $10^{-4} F_1 D_1$, while the kinetic energy per grain should not exceed $10^{-8} F_1 D_1$ and controlled stress components should be measured equal to their set values, within relative error 10^{-4}.

Different initial packing states

The assembling procedure is designed such that these configurations equilibrated under $\sigma_1 = \sigma_1$ in the oedometric case, or $\sigma_1 = \sigma_2 = \sigma_3 = \sigma_1$ in the isotropic case, vary in density and in coordination number. We thus obtain 6 different initial states, as described below. Their properties are listed in Table 4.1.

Maximally dense states with high coordination number. In order to maximize density, as in [Agnolin and Roux, 2007a], we set the friction coefficient μ to zero in the assembling stage. In the isotropic case, this results in the random close packing state (RCP), as often investigated in the literature [O'Hern et al., 2003, Donev et al., 2005, Agnolin and Roux, 2007a, Peyneau and Roux, 2008b] for monodisperse spherical beads. The results obtained here are almost not affected by the slight polydispersity, as the solid fraction averages to 0.638 with 4000 beads, hardly larger than the value 0.637 reported on applying the same treatment with the same number of grains in the monodisperse case [Agnolin and Roux, 2007a]. In the rigid limit, the coordination number of non-rattler grains, $z^* = z/(1 - x_0)$ approaches the isostatic value of 6 in the limit of rigid grains ($\kappa \to \infty$), while x_0 remains quite small. We refer to this initial state as **DHi** for **D**ense, **H**igh coordination number, **i**sotropically compressed in the assembling stage.

Using oedometric, rather than isotropic, compression to reach an equilibrated configuration with $\sigma_1 = \sigma_1$, still without intergranular friction, we obtain the **DHo** state (**D**ense, **H**igh coordination number, **o**edometrically assembled). Their properties are similar to DHi, save for a slight anisotropy, evidenced in the observed value $K_0 \simeq 0.94$ of the ratio of transverse to axial stress. As studied in Ref. [Peyneau and Roux, 2008b], frictionless bead assemblies may transmit anisotropic stresses, but the corresponding states (dubbed "anisotropic random close packing states" in [Peyneau and Roux, 2008b]) share the same density and coordination numbers as the isotropic ones.

Maximally dense packing with low coordination number. In order to mimic laboratory procedures in which dense configurations are obtained through agitation or vibration, and to obtain pre-

	LLo	LLi	DHo	DHi	DLo	DLi
Φ	0.584	0.589	0.639	0.638	0.634	0.637
z	4.22	4.14	5.98	5.99	4.06	4.17
$z^\star$	4.63	4.63	6.07	6.07	4.54	4.65
$x_0(\%)$	8.8	10.3	1.5	1.3	10.4	10.37
K_0	0.72	1	0.94	1	0.51	1

Table 4.1: Solid fraction Φ, coordination numbers of all grains, z, and of nonrattler ones, z^*, rattler fraction x_0, and stress ratio K_0 for the initial states, according to preparation procedure. $K_0 = 1$ in all isotropically assembled states (denoted as "XYi"). Values averaged over 3 configurations of $N = 4000$ grains (sample to sample differences lie below given accuracy level, except for x_0).

sumably more realistic values of coordination numbers, a very small isotropic dilation is applied to DHi configurations (multiplying bead center coordinates by 1.001), so that all contacts open; the system is then subjected (after a mixing step as in [Agnolin and Roux, 2007a]) to an isotropic compression, with the final value $\mu = 0.3$ of the friction coefficient (the one used in the subsequent study of the solid, quasistatic response), until an equilibrium state is obtained. The solid fraction is close to the initial RCP value, but the coordination number is now about 4, with a large rattler fraction. This final state is referred to as **DLi** (**D**ense, **L**ow coordination, **i**sotropically assembled. The same procedure may also be applied, with an oedometric final compression stage (with $\mu = 0.3$). We note, in that case, that the mixing stage is not necessary to obtain a small final coordination number. We denote the final state as **DLo** (**D**ense, **L**ow coordination, **o**edometrically assembled. Interestingly, this DLo state exhibits a rather large preparation-induced stress anisotropy, with $K_0 \simeq 0.51$.

Looser states.   States obtained on directly compressing the loose "granular gas" configurations ($\Phi = 0.45$), with the final value $\mu = 0.3$ of the intergranular friction coefficient (and condition $I \leq I^{\max} = 10^{-3}$), are low coordination states with many rattlers, but looser than DHi or DHo, with solid fractions between 0.58 and 0.59. Depending on whether they are isotropically or oedometrically assembled, we refer to these initial static configurations as **LLi** or **LLo**, in accordance with previous notation conventions (**L**oose, **L**ow coordination, **i**sotropically or **o**edometrically assembled). K_0, in the LLo case, shows a significant level of stress anisotropy, but smaller than for DLo. Although rather loose, the LLo state is likely not the loosest possible structure of a rigid bead assembly with $\mu = 0.3$. Different procedures, possibly involving capillary cohesion in an initial stage [Than et al., 2016], could result in lower solid fractions.

All 6 initial states of Tab. 4.1 were prepared for 3 different samples of 4000 grains, over which recorded measurements are averaged. One additional system with 13500 grains was assembled in the DLo state, in order to check for the absence of size effects. Data pertaining to this larger sample are labelled "DLo+" on some figures below.

Other characteristics of initial states.

The possibility to obtain a low coordination number z for a solid fraction Φ nearly equal to its maximum (random close packing) value was first pointed out in previous studies of isotropic packings [Ag-

nolin and Roux, 2007a][1]. It is generalized here to anisotropic packings DLo. Apart from the data listed in Tab. 4.1, initial states might also be characterized in terms of force distribution, friction mobilization and neighbor distance statistics. Some of these properties are studied in Sec. 4.4, in which state variable evolutions under oedometric compression are studied.

Although grains should tend to have more close neighbors in denser systems, arbitrarily small displacements suffice to open contacts in the rigid limit ($\kappa \rightarrow \infty$), whence the possibility of widely different z values. It is instructive to explore at which scale neighbor distance statistics are correlated to contact statistics. Fig. 4.1 shows, for different initial states, plots of growing function $z(h)$, defined
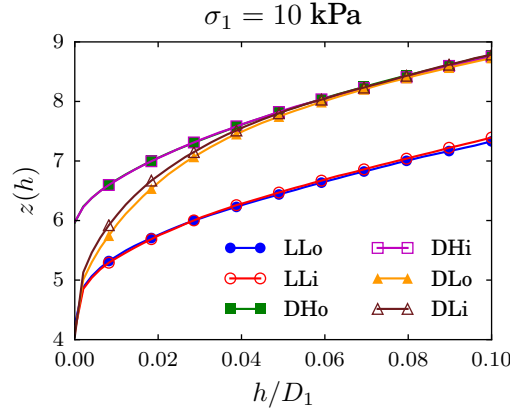

Figure 4.1: h-dependent coordination number $z(h)$ for the different initial states.

as the number of neighbor grains separated by a gap lower or equal to distance h, and such that $z(0) = z$. As in the isotropic, monodisperse sphere packings of Ref. [Agnolin and Roux, 2007a], $z(h)$ functions take larger values in denser systems, except for small values of h (say, $h \leq 0.05D_1$) as the value of the contact coordination number is approached. Thus, direct observations of bead packs by microtomography techniques [Aste et al., 2005] should be able to resolve distances of order $D_1/100$ to provide information on coordination numbers. In Ref. [Agnolin and Roux, 2007a], it is also shown that the treatment of rattlers (which would tend to rely on neighboring grains underneath in the presence of gravity) might significantly affect function $z(h)$ at small distance. In view of the close similarity with the results obtained in isotropic systems, the structure of (orientation averaged) pairs correlations is not pursued further in the present paper, which focusses more on anisotropy.

4.4 Oedometric compression

We now report on the observed material evolution in oedometric compression. Once the details of the numerical loading procedure are specified in Sec. 4.4, the variation of the simplest, scalar state variables is monitored and discussed in Sec. 4.4. Observations of stress anisotropy, as expressed by

---

[1]Save for the small grain size polydispersity, states DHi, DLi, LLi are identical to the states respectively denoted as A, C and D in Ref. [Agnolin and Roux, 2007a], dealing with monodisperse bead assemblies.

coefficient K_0, are then reported and compared to literature results (Sec. 4.4). The anisotropy of force networks, as investigated in Sec. 4.4, is directly related to K_0, as shown in Sec. 4.4.

Loading process.

In order to dispel all possible confusion, let us first insist that the main object of the present study is oedometric compression of the chosen model material with intergranular friction coefficient $\mu = 0.3$. All samples of 4000 grains in all six initial states, even though some of them were prepared, as described above in Sec. 4.3, without friction, and/or by isotropic, rather than oedometric, compression of a granular gas, are subjected to quasi-static oedometric compression, for which μ is set to 0.3.

We apply a strain-rate controlled loading program [maintaining small values of I (Eq. 4.5), see Sec. 4.2]. Intermediate configurations are recorded when σ_1 reaches, for glass beads, values 31.62 kPa, 100 kPa, 316.2 kPa, 1 MPa, 3.162 MPa, 10 MPa, 31.62 MPa (increasing as a geometric progression, with factor $\sqrt{10}$), corresponding to κ decreasing (by constant factor $10^{1/3}$) from 39000 at 10 kPa down to 181 at 31.62 MPa. Each of those intermediate configurations is subjected to equilibration under constant σ_1 – using the same numerical tolerance on equilibrium criteria as stated in Sec. 4.3. This equilibration step is carried out in order to record accurate characterizations of contact networks. It results in a very small "creep" strain increment (typically of order 10^{-5} for dense states, up to 10^{-4} in looser systems), in which z increases by a small amount (from 0.5 to about 3.5 %, the highest increases corresponding to the less coordinated states) [2]. In the following, state variables are, unless specified otherwise, measured in equilibrated configurations.

Evolution of scalar state variables

Density

Solid fractions for the different initial states are plotted versus σ_1 or κ^{-1} in Fig. 4.2. Two different sets of curves are obtained, pertaining to initially dense and initially loose systems. Quite unsurprisingly, the density increase with applied stress is of the same order as κ^{-1}, characterizing contact deflections, and tends to be larger in looser systems. The influence of the initial coordination number seems quite secondary, only noticeable, on the figure, for DLi and LLi systems under low stress. Note the DLo+ data points, showing the same behavior in a larger sample (N=13500 grains) – save for a very small systematic density increase, compatible with the slight size dependence (proportional to $N^{-1/2}$) recorded for the RCP density in [O'Hern et al., 2003, Agnolin and Roux, 2007a].

A comparison with similar isotropic compression results [Agnolin and Roux, 2007b] reveals a density increase of the same order, but, as one should expect, somewhat smaller under axial stress σ_1 than under isotropic stress $P = \sigma_3 = \sigma_2 = \sigma_1$. Thus dense systems reach solid fractions of about 0.658 under isotropic stress $P = 31.6$ MPa [Agnolin and Roux, 2007b] while oedometrically compressed dense samples (DHo or DLo) do not exceed solid fraction 0.654. Axial strain ε_1, on the

---

[2]This small numerical creep phenomenon, which stops once the system reaches equilibrium, should not be confused with creep observed in the laboratory.
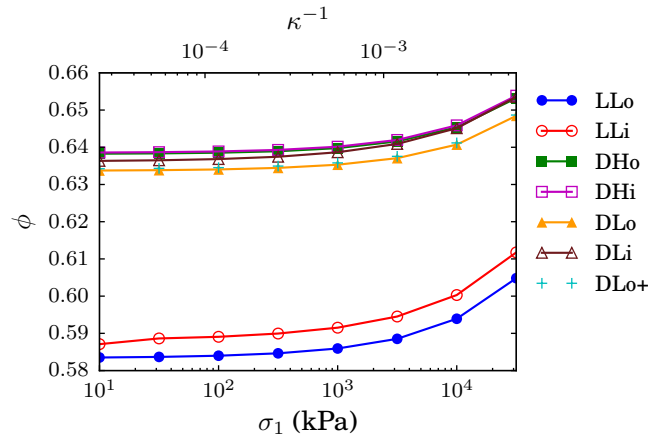
Figure 4.2: Evolution of solid fraction Φ with axial stress σ_1 in oedometric compression for different initial states.

other hand, is larger in the oedometric compression case, as it accounts for the whole density change $\Delta\Phi$, rather than $\Delta\Phi/3$ in isotropic compression.

Coordination number and rattler fraction

The coordination number, z, as shown in Fig. 4.3, exhibits a slightly more unexpected variation under growing stress: while it gradually increases with σ_1 in low coordinated states, whatever their density, it tends to decrease in a first stage if initially high (in DHi and DHo systems). Note the absence of
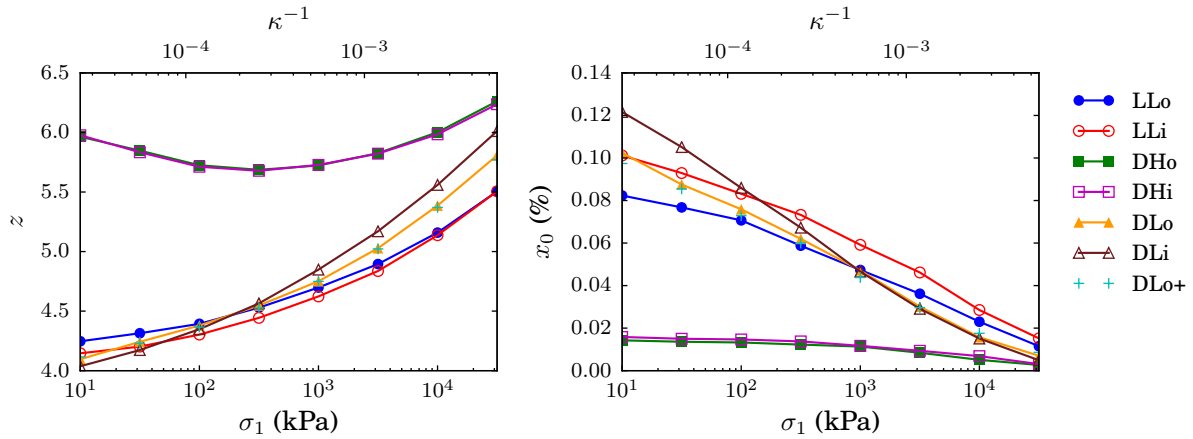
Figure 4.3: Coordination number z and rattler fraction x_0 versus vertical stress σ_1 along oedometric loading path for the different sample preparations.

sample size dependence: results for N=13500 and N=4000 grains are identical. The rattler fraction, on the other hand, steadily decreases in compression for all initial states. The nonmonotonic variation of z, if initially high, is a first clue that the oedometric compression is not always as simple and

predictible as might be expected on assuming homogeneous shrinking of distances along the axial direction. Such a uniform strain assumption necessarily predicts coordination number z to increase. It would tend to explain, nevertheless, the faster increase of z in DL systems than in LL ones: the creation of new contacts in compression is achieved sooner in more densely packed structures. Quite detailed tests of the homogeneous shrinking assumption were carried out for isotropic compression in Ref. [Agnolin and Roux, 2007b], revealing fairly correct predictions of coordination number increases under compression: within 20-30% of the measured values in low coordination number systems. (Yet the homogeneous strain assumption proved unable to capture the evolution of coordination numbers on unloading – see Sec. 4.6). As for Φ, changes in z under compression prove smaller in the present oedometric case than in the isotropic compressions of Ref. [Agnolin and Roux, 2007b], with maximum values of z below 6.5 (for DHi-DHo), in range 5.8–6 (DLi-DLo states), or below 5.5 (Li-Lo states), as opposed to, respectively, $\simeq 6.8$, $\simeq 6.6$ and 5.9 under isotropic load with the same value of σ_1.

The results of Fig. 4.3 also signal the enduring effects of initial anisotropy: the differences between systems DLi and DLo do not tend to vanish, even after the applied stress increased by more than 3 orders of magnitude.

Force distribution

From (4.6), in equilibrium, the average normal force $\langle F^N \rangle$ in the contacts is readily related to the pressure $P = (\sigma_1 + \sigma_2 + \sigma_3)/3$, as

$$\langle F^N \rangle = \frac{\pi \langle D^3 \rangle P}{z \Phi \langle D \rangle}. \tag{4.8}$$

This formula, involving the first and third moments of the diameter distribution, assumes a decorrelation between normal force intensity F^N_{ij} and intercenter distance $R_i + R_j$ in contacts i, j, which is satisfied in good approximation (the maximum relative error is 1.4 %, for the highest stress level). The evolution of the normal force distribution in compression is well characterized on normalizing forces by $\langle F^N \rangle$. The probability distribution of $f = F^N / \langle F^N \rangle$ was observed in the isotropic case [Agnolin and Roux, 2007b] to concentrate on a narrower interval about its average as compression proceeds, the faster the better coordinated the system. In the present case of oedometric compression, this effect is still present, although considerably smaller. Fig. 4.4 shows the p.d.f. of f for different stresses σ_1 for initial state DLo, and exhibits little change, except for large forces. The shape of force distributions may be characterized [Agnolin and Roux, 2007b] with reduced moments

$$Z(\alpha) = \frac{\langle (F^N)^\alpha \rangle}{\langle F^N \rangle^\alpha} \tag{4.9}$$

As shown in Fig. 4.5 (Left), the reduced second moment $Z(2)$ decreases quite slowly (except for the initial evolution of high z states, likely correlated with the nonmonotonic variation of z) as a function of σ_1. Similarly, $Z(1/3)$ (Fig. 4.5 (Right)), which from Eqs. (4.3) and (4.8) relates the average contact stiffness to $P^{1/3}$ [Agnolin and Roux, 2007b] hardly changes in oedometric compression: for
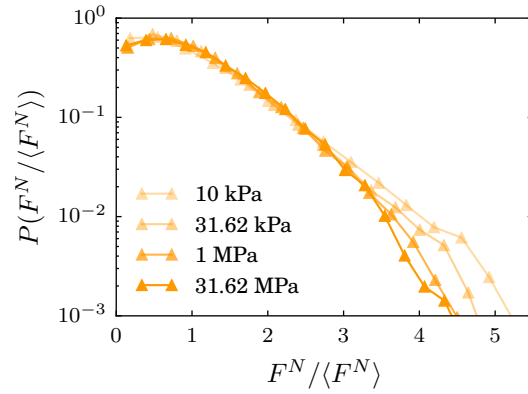
Figure 4.4: Probability density function of $f = \dfrac{F^N}{\langle F^N \rangle}$ in oedometric compression of initial state DLo, for different axial stress levels.
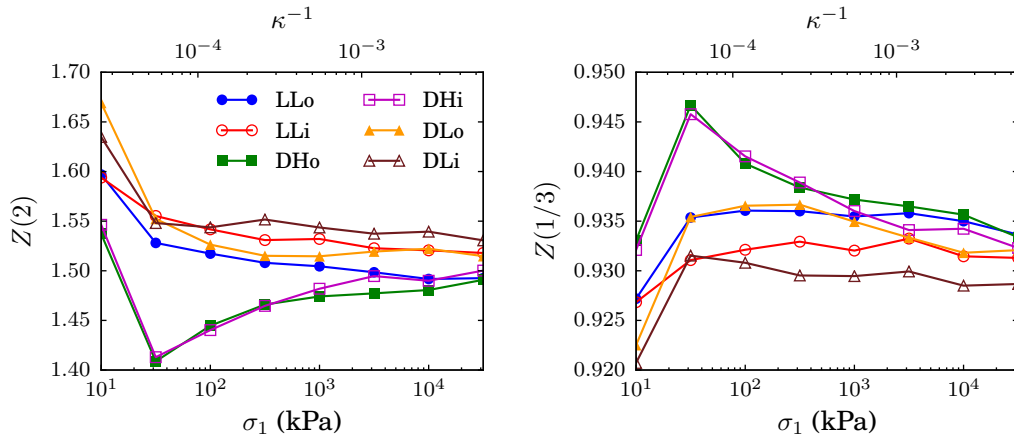

Figure 4.5: Evolution of reduced second moment of normal contact forces, $Z(\alpha)$ (Eq. 4.9) in oedometric compression. (Left) $Z(2)$. (Right) $Z(1/3)$.

all systems, it stays between 0.92 and 0.95. Unlike the isotropic compression studied in [Agnolin and Roux, 2007b] for similar stress levels, the oedometric compression does not cause strong changes in force distributions.

Stress ratio K_0

Traditionally, coefficient K_0 (termed "coefficient of earth pressure at rest") is regarded as a basic characteristic of material response under oedometric load, and expected to remain constant as axial stress σ_1 increases (in a horizontal, homogeneous sand layer under its weight, both vertical and horizontal stresses thus increase proportionally to depth). However, some preparation techniques reportedly produce initial state dependent K_0, which might also vary with σ_1 – thus raising the question of the conditions in which K_0 might indeed be regarded as a constant ratio [Okuchi and Tatsuoka, 1984, Lee et al., 2013, Gao and Wang, 2014]. The availability of the six widely different initial states, in the present study, provides an opportunity to investigate this issue.

Results

The variations of K_0 along the oedometric loading path are displayed in Fig. 4.6, in which isotropically assembled initial states are distinguished from oedometrically assembled ones, on separate plots. Systems that are first assembled by isotropic compression only gain stress anisotropy in the course of the subsequent oedometric compression, and thus exhibit K_0 values decreasing from 1, faster for a higher density, and faster for a larger coordination number. Thus K_0, in the DHi case, reaches values slightly above 0.6 at $\sigma_1 = 1$ MPa (or $\kappa^{-1} \simeq 6.10^{-4}$), and hardly changes under larger axial stress. K_0, in DLi systems (dense with low initial coordination) and LLi (loose) ones, steadily decreases as functions of σ_1, without approaching an asymptotic value, even under quite high stress levels (tens of MPa). Among the three different oedometrically assembled initial states, the dense, highly
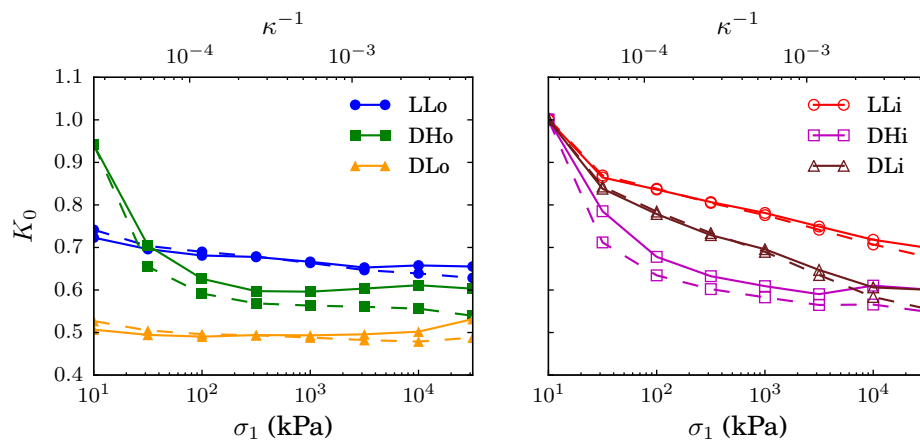

Figure 4.6: K_0 versus axial stress σ_1 in oedometric compression (dots joined by solid lines, as specified in legend). Dots joined by dashed lines: predictions of Eq. 4.17 (see Sec. 4.4). Left graph: oedometrically assembled systems ("XYo"). Right graph: isotropically assembled ones ("XYi").

coordinated one, DHo, is in a nearly isotropic stress state ($K_0 = 0.94$) and close (see Tab. 4.1) to fully isotropic state DHi. Consequently, the behavior of K_0 is quite similar in oedometric compression for DHo and DHi. However, the looser anisotropic initial state (LLo), and the dense, yet poorly coordinated one (DLo), both exhibit quite different K_0 evolutions in oedometric compression, with a remarkably constant value ($\simeq 0.5$) for DLo, and a very slowly decreasing one for LLo (if a smaller interval of σ_1 is considered, $K_0 \simeq 0.7$ might be considered constant, as a good approximation, for LLo as well). Constant K_0 values are thus observed in situations for which the anisotropy of the assembling process is similar to that of the subsequent quasistatic oedometric loading history.

Comparison to experimental and numerical literature

Okochi and Tatsuoka [Okuchi and Tatsuoka, 1984] published a detailed experimental study of factors affecting K_0 values measured in a reference, well characterized sand, subjected to many different initial treatments in the preparation stage, including a first compression (which is not oedometric as lateral strains are not set to zero), up to a relatively small stress level (about 20 kPa), in which σ_2/σ_1 is kept constant by separately controlling axial and lateral stresses (in a triaxial cell). In the subsequent oedometric compression to higher stress values, they observed lower values of K_0 in denser systems, and, a decrease of K_0 for increasing σ_1, from an initial isotropic state of stress. Interestingly, K_0 converges to an asymptotic value (close to 0.5) as σ_1 increases to about 200 kPa. This asymptotic value does not appear to depend on the initial stress ratio applied in the first compression. The numerical results appear to be in qualitative agreement with these observations, except that, in the numerical case, a limiting, high stress value of K_0 is not approached as soon as σ_1 is merely multiplied by 10. The experimental setup of [Okuchi and Tatsuoka, 1984] does not, however, enable the simpler procedure which consists in, first, depositing the sample under gravity, and then applying an exactly one-dimensional compression (zero lateral strain). Carried out in an oedometer, equipped with tactile pressure sensors to record lateral stresses, rather than a triaxial cell, the measurements of Gao and Wang [Gao and Wang, 2014] allow for such a simpler procedure to be applied. Using air pluviation (i.e., deposition under gravity, under controlled conditions) to assemble the solid sample, these authors observed a constant K_0 in the subsequent oedometric compression. Thus, regarding the oedometric assembling procedure, defining initial states LLo and DLo (Tab. 4.1), as roughly similar to pluviation, it should be noted that simulations agree with laboratory observations in this respect: K_0 remains constant for assembling procedures resembling one-dimensional compression[3]

The experiments of Lee *et al.* [Lee et al., 2013] also reveal a roughly constant K_0 when the tested granular materials (assembled by some unspecified process) are first oedometrically compressed from 16 to 115 kPa. Tested materials include glass beads prepared at intermediate solid fractions : $\Phi \simeq 0.603$, for which $K_0 \simeq 0.55$, and $\Phi \simeq 0.614$, for which $K_0 \simeq 0.51$ – values with which (despite possible different contact friction coefficients) our numerical results for dense system DHo approximately agrees.

---

[3]The experiments of [Gao and Wang, 2014] are complex, involving creep periods of several days, during which K_0 increases, but K_0 reverts to its previous value as standard oedometric compression is resumed. Creep phenomena are not studied here.

The experimental study of Khidas and Jia [Khidas and Jia, 2010], carried out on glass beads in oedometric conditions, considers two different initial densities ($\Phi \simeq 0.605$ and $\Phi \simeq 0.643$), and aims at a characterization of anisotropic elastic properties. Values of K_0 are noted, though corresponding to a secondary compression process, after a first compression cycle – which we shall briefly discuss in Sec. 4.6.

On the numerical side, two recent publications are particularly relevant for comparisons with the present study, Refs. [Lopera Perez et al., 2015, Gu et al., 2015]. Both Lopera Perez *et al.* [Lopera Perez et al., 2015] and Gu *et al.* [Gu et al., 2015] consider spherical grains, with the polydispersity of the Toyoura sand particles of Ref. [Okuchi and Tatsuoka, 1984], and prepare samples by varying the friction coefficient, in the initial assembling stage by isotropic compression, from zero to its actual value used in quasistatic compression: $\mu = 0.5$ in [Gu et al., 2015] ($0.600 \leq \Phi \leq 0.629$), $\mu = 0.25$ in [Lopera Perez et al., 2015]($0.600 \leq \Phi \leq 0.648$). Those initial states thus interpolate between DHi and LLi. Investigated stress ranges in these studies are narrower than in our case, extending from 25 to 1250 kPa in [Lopera Perez et al., 2015] (where particles with elastic properties of glass beads are also simulated), and from about 130 to 1040 kPa in [Gu et al., 2015] (once stresses are rescaled in order to compare systems of equal stiffness level κ). Gu *et al.* also prepared samples by direct oedometric compression (similar to a series of systems interpolating between DHo and LLo).

Our results for isotropically compressed systems for DHi and LLi agree semi-quantitatively with those of [Lopera Perez et al., 2015, Gu et al., 2015] for K_0 values and trends, but the decrease of K_0 values for growing σ_1 is notably slower in our case. Similarly, our observations contradict those made by Gu *et al.* as regards the difference between LLi and LLo. These authors obtain roughly constant (σ_1-independent) K_0 values for oedometrically assembled systems, and find that K_0 in isotropically assembled systems approaches this value as soon as σ_1 increases by a factor of 10 or 20, while, in the present study, K_0 values for LLi and LLo still differ after a thousandfold increase of σ_1. One possible explanation for these discrepancies is that we could approach the quasistatic limit in compression with better accuracy: the rate of compression, as measured by the inertial number, is 250 times as small in our simulations as in [Lopera Perez et al., 2015] (while its value is left unspecified in [Gu et al., 2015]). Neither one of those two groups studied initial states of different coordination numbers for the same density, and thus our DLi and DLo results are, to our knowledge, entirely new. (Coordination numbers are not specified in [Lopera Perez et al., 2015]; values of z^* specified in [Gu et al., 2015] in the looser samples approximately agree with our LLi or LLo results for the same value of κ; Gu *et al.* do not prepare systems as dense as our "DXy" ones).

Anisotropy

We now characterize anisotropy appearing in oedometrically compressed systems, both in the contact network, in the correlations between neighboring grains, and in force intensity and friction mobilization.

Contact and neighbor pair anisotropy

As a result of oedometric compression, the distribution of the orientation of unit normal vectors in contacts, on the unit sphere, ceases to be isotropic, although it remains rotationally symmetric about the compression direction (referred to as the axial direction and denoted "1" throughout the chapter). Defining angle θ between direction 1 and that of normal unit vector $\mathbf{n}$, with $0 \leq \theta \leq \pi$, the orientation distribution (or *fabric*) anisotropy is conveniently expressed by the probability density function (p. d. f.) of $\cos \theta = n_1$ over interval $-1 \leq n_1 \leq 1$, $p(n_1)$. By construction, it is an even function ($\mathbf{n}$ and $-\mathbf{n}$ are equivalent), constant with value $1/2$ in an isotropic system. $p(n_1)$ might be expanded in the series of Legendre polynomials, with only terms of even order. Truncating the series after the term of order 4, one has:

$$p(n_1) = 1 + A_2\left(3n_1^2 - 1\right) + A_4\left(35n_1^4 - 30n_1^2 + 3\right), \tag{4.10}$$

in which coefficients are related to moments of the distribution: thus coefficient, A_2, given by

$$A_2 = \frac{15}{4}\left(\langle n_1^2 \rangle - \frac{1}{3}\right) = \frac{15}{4} \int_{-1}^{1} p(n_1) n_1^2 dn_1 - \frac{5}{4}, \tag{4.11}$$

is directly related to the difference between the second moment and its isotropic value, for which we introduce the notation

$$\tilde{c}_2 = \langle n_1^2 \rangle - \frac{1}{3}. \tag{4.12}$$

Fig. 4.7 shows that expansion (4.10) truncated at order 2 is already quite a good representation of the
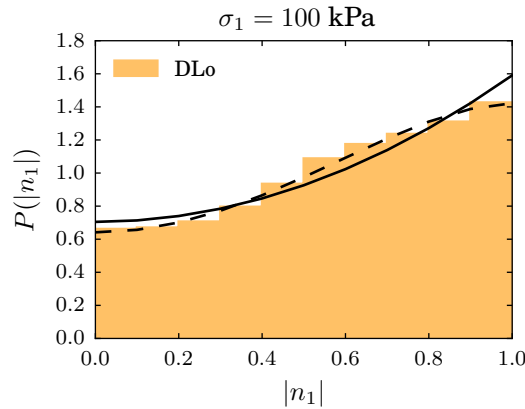
Figure 4.7: Anisotropy of contact orientations: histogram of $|n_1|$ values in system DLo at $\sigma_1 = 100$ kPa, a,d its representation with expansion (4.10), truncated after order 2 (solid line) or order 4 (dashed line).

p. d. f. of $|n_1|$ [i.e., $P(|n_1|) = 2p(n_1)$], and that adding the term of order 4 achieves an excellent fit.

As σ_1 increases in oedometric compression, $\tilde{c}_2$ evolves, for the 6 different investigated states, as displayed in Fig. 4.8. Isotropic packings, as well as nearly isotropic DHo ones, progressively acquire

Figure 4.8: Anisotropy parameter $\tilde{c}_2$, versus σ_1 or κ^{-1}, for all six different initial states.

an anisotropic structure under growing oedometric load, faster in dense systems than in the LLi case: from the results of Fig. 4.3, contact networks u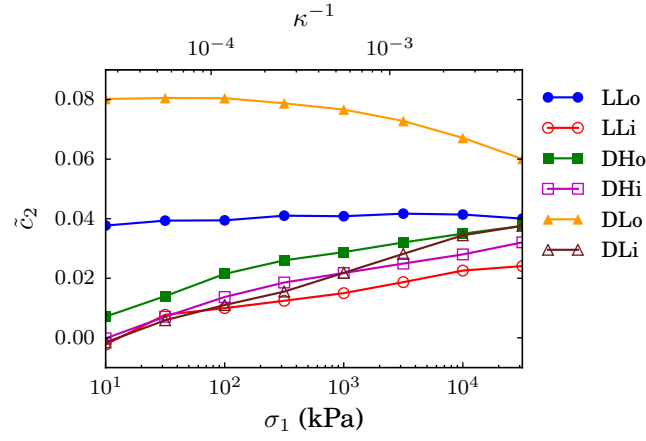ndergo more changes for higher densities. Under large stress, the level of fabric anisotropy of initially isotropic systems is comparable to its value in the LLo case, which is roughly stress-independent ($\tilde{c}_2 \simeq 0.04$). The larger value of $\tilde{c}_2$ in the most anisotropic system, DLo, decreases slightly for the larger stress levels. The high coordination numbers reached at large σ_1 in dense systems (Fig. 4.3) precludes very large fabric anisotropies, as many neighbors in contact with the same central grain, by steric exclusion, tend to be more isotropically distributed at its periphery [Radjaï and Roux, 2004].

It is worth investigating over which distance scale the distribution of neighboring grains is similarly anisotropic. To this end, Fig. 4.9 plots function $\tilde{c}_2(h)$ obtained on extending the definition of $\tilde{c}_2$ (its value for $h = 0$) to the orientation of normal vectors joining neighbors at distance below h, both in the initial states, and under a high stress level. While the strong anisotropy of the DLo state,
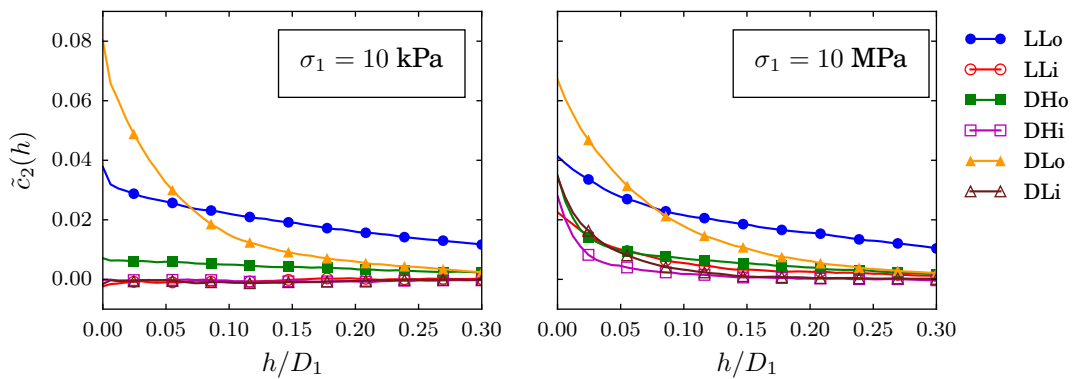

Figure 4.9: Anisotropy of orientation of pair of near neighbors as expressed by h-dependent coefficient $\tilde{c}_2(h)$. Left graph: $\sigma_1 = 10$ kPa (or $\kappa \simeq 39000$, initial states). Right graph: $\sigma_1 = 10$ MPa ($\kappa \simeq 390$).

and the moderate ones observed under stress in DHo and initially isotropic ones, tend to vanish at distances reaching 0.05 to $0.1D_1$, the distribution of neighbor pairs in the LLo case is still notably anisotropic over a much larger range of interparticle gaps, extending to about $0.2D_1$. The anisotropic structure of loose systems, resulting from the assembling process, should be easier to detect with microtomography techniques.

Angular distribution of normal force amplitudes.

Contact force values tend to reflect stress anisotropy, resulting both from one-dimensional loading and from the initial packing process (for oedometrically assembled states). Classifying contacts by the orientation of normal vector **n**, some classes tend to carry larger forces than others. We denote as $\mathcal{F}(\mathbf{n})$ the average normal force amplitude for contacts with normal direction **n**, normalized by the global average $\langle F^N \rangle$, such that its integral over the unit sphere, Σ, weighed by the orientation distribution $p(\mathbf{n})$, satisfies

$$\int_{\Sigma} p(\mathbf{n})\mathcal{F}(\mathbf{n})d^2\mathbf{n} = 1. \tag{4.13}$$

Similarly to $p(\mathbf{n})$, $\mathcal{F}$, a function of $|n_1|$, may be expanded in a series of Legendre polynomials. We define

$$\tilde{f}_2 = \frac{1}{4\pi}\int_{\Sigma}\mathcal{F}(|n_1|)n_1^2 d^2\mathbf{n} - \frac{1}{3}, \tag{4.14}$$

which vanishes in isotropic systems. Fig. 4.10 shows the evolution of $\tilde{f}_2$ in oedometric compression. Under compression, the force anisotropy parameter $\tilde{f}_2$ steadily increases in all studied systems. This
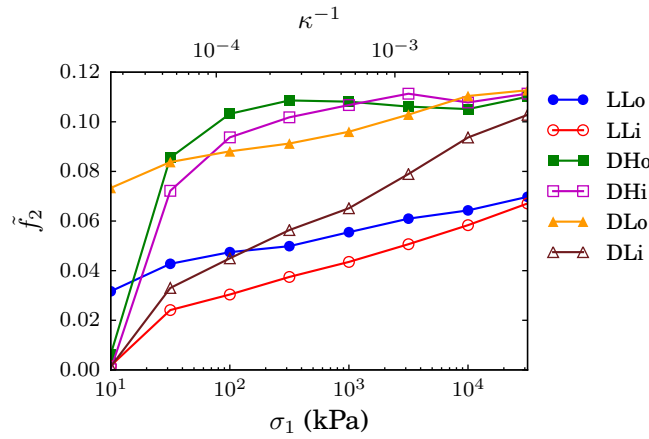
Figure 4.10: Force anisotropy parameter $\tilde{f}_2$, versus σ_1 or κ^{-1}, for all six different initial states.

increase is strikingly fast in initially isotropic states, especially those with a large coordination number. Unlike fabric, which requires changes in the contacts (presumably related to finite strains), force anisotropy might change quickly by redistributing the forces within the existing network. Such redis-

tributions are easier in better coordinated ones, whereas force values are more strongly constrained by the network geometry in poorly coordinated states with relatively low force indeterminacy.

Estimation of K_0 from anisotropy parameters

Relating stresses to fabric and force anisotropy parameters is quite a standard, well-known procedure in granular micromechanics [Peyneau and Roux, 2008b, Azéma and Radjaï, 2014, Khamseh et al., 2015], which was, in particular, successfully applied to oedometric compression in the recent numerical studies discussed in Sec. 4.4 [Lopera Perez et al., 2015, Gu et al., 2015]. We use it here, in a particularly simple form, to relate K_0 to anisotropy parameters $\tilde{c}_2$ and $\tilde{f}_2$, and to discuss the roles of both kinds of anisotropies. To obtain the desired approximative relation, we ignore the (negligible) contribution of tangential forces to normal stresses σ_1 and $\sigma_2 = \sigma_3$, we truncate to second order the expansions of $p(\mathbf{n})$ and $\mathcal{F}(\mathbf{n})$, and neglect the products of anisotropic coefficients $\tilde{c}_2$ and $\tilde{f}_2$ (those small coefficients are dealt with to first order [4]). The normal force contribution to principal stresses, given ($\alpha = 1, 2, 3$) by:

$$\sigma_\alpha = \frac{3z\Phi\langle F^N\rangle\langle D\rangle}{\pi\langle D^3\rangle} \int_\Sigma p(\mathbf{n})\mathcal{F}(\mathbf{n}))(n_\alpha)^2 d^2\mathbf{n}, \tag{4.15}$$

becomes,

$$\sigma_\alpha \simeq \frac{3z\Phi\langle F^N\rangle\langle D\rangle}{\pi\langle D^3\rangle} \left[\langle n_\alpha^2\rangle + f_2^{(\alpha)} - \frac{1}{3}\right], \tag{4.16}$$

using the notation

$$f_2^{(\alpha)} = \int_\Sigma n_\alpha^2 \mathcal{F}(\mathbf{n}) d^2\mathbf{n}.$$

Knowing that $\langle n_2^2\rangle = \langle n_3^2\rangle = \frac{1}{2}(1 - \langle n_1^2\rangle)$, one may finally estimate K_0 as:

$$K_0 = \frac{\sigma_{22}}{\sigma_{11}} \simeq \frac{2 - 3(\tilde{c}_2 + \tilde{f}_2)}{2 + 3(\tilde{c}_2 + \tilde{f}_2)}. \tag{4.17}$$

This estimate of K_0 agrees quite well with measured values (see Fig. 4.6).

Thus anisotropy parameters $\tilde{c}_2$ and $\tilde{f}_2$ appear combined into the sum $\tilde{c}_2 + \tilde{f}_2$, and their relative effect is appreciated on comparing their values, as plotted in Figs. 4.8 and 4.10. Force anisotropy is clearly the dominant effect in stress anisotropy (expressed by ratio K_0, deviating from 1) in isotropically prepared systems, except for the loose initial state under high stress. In oedometrically assembled ones, with initial fabric anisotropy, both effects, of fabric and force anisotropies, are of the same order, except in the case of DHo, with its very small initial value of $\tilde{c}_2$.

---

[4]It is consistent with this order of approximation to replace $p(\mathbf{n})$ by 1 under the integral in normalization relation (4.13)

4.5   Elasticity and friction

We now investigate the nature of stress-strain response in oedometric compression, discussing the role of elastic and frictional response.

Oedometric compression and elastic response

Elastic moduli in the six anisotropic states subjected to oedometric compression in the present study will be studied specifically in next chapter, in which their connection to density, coordination number, fabric and force anisotropies will be investigated in detail. The issue we wish to address here first is whether and how the quasistatic stress-strain or stress-density curves (Fig. 4.2) recorded under oedometric load relate to elastic response.

Measurement of elastic moduli

An elastic response, in granular materials, is measured when small stress and strain increments about a prestressed, equilibrated configuration, are related in a reversible way, associated with an elastic potential energy. Elastic moduli may then be measured either statically, with adequate devices apt to capture very small strains, or deduced from sound wave velocities in granular materials [Shibuya et al., 1992, Hicher, 1996, Hoque and Tatsuoka, 1998, Kuwano and Jardine, 2002, Duttine et al., 2007, Khidas and Jia, 2010]. An elastic response is only observed for small strain intervals, and should in fact be viewed as an approximation, as dissipation mechanisms are always present (in particular, solid friction) and preclude the general definition of an elastic energy. The relative amount of dissipation decreases as the size of the probed strain interval approaches zero, and it is often observed, for usual conditions in which granular materials are probed, that an elastic model is satisfactory for strain increments not exceeding some upper bound of order 10^{-6} or 10^{-5}. For that reason, teh material behavior is best characterized as "quasielastic" in that limited range. In Ref. [Agnolin and Roux, 2007c], a numerical study of elastic properties of isotropic spherical bead assemblies, carried out with the same model material as the present one (except for the small polydispersity, absent in [Agnolin and Roux, 2007c]), very similar observations were made as in the experimental literature as to the amplitude of the "quasielastic" domain. In simulations, an elastic model is considered for well-equilibrated configurations, in which the contact structure behaves just like a network of linear elastic springs. One may then build the stiffness matrix (also known as the "dynamical matrix") for this network, with stiffness parameters K^N and K^T as determined by Eqns. 4.3 and 4.4, by the procedure explained in Ref. [Agnolin and Roux, 2007c], where details are provided about the necessary approximations to obtain an elastic response. The elastic moduli are then obtained by solving appropriate systems of linear equations, for the small (linear and angular) displacements of all the grains associated with global strains and stresses. We refer to [Agnolin and Roux, 2007c] and to the next chapter for details about the stiffness matrix and its treatment. In the present case, we obtain all independent five elastic moduli appropriate for a transversely isotropic material (as in [Kuwano and Jardine, 2002, Peyneau and Roux, 2008b, Khidas and Jia, 2010]). Specializing to diagonal matrix components, the relation

between stress increment $\Delta\underline{\underline{\sigma}}$ and strain increment $\Delta\underline{\underline{\varepsilon}}$ reads:

$$\begin{pmatrix} \Delta\sigma_1 \\ \Delta\sigma_2 \\ \Delta\sigma_3 \end{pmatrix} = \begin{pmatrix} C_{11} & C_{12} & C_{12} \\ C_{12} & C_{22} & C_{23} \\ C_{12} & C_{23} & C_{22} \end{pmatrix} \cdot \begin{pmatrix} \Delta\varepsilon_1 \\ \Delta\varepsilon_2 \\ \Delta\varepsilon_3 \end{pmatrix}, \tag{4.18}$$

with a symmetric positive definite matrix of elastic moduli $C_{\alpha\beta}$, $1 \le \alpha, \beta \le 3$, abiding by the rotational invariance about axis 1. Postponing a more complete study of the (transversely anisotropic) tensor of elastic moduli in oedometric compression to next chapter (in which shear moduli are also measured), we focus here on moduli C_{11} and C_{12}, which express the response to varying axial strain ε_1. Those moduli increase with σ_1 in the compression, mainly due to the contact law. In view of Eqns. 4.3 and 4.4, moduli tend to scale as $\sigma_1^{1/3}$. As in the isotropic case [Agnolin and Roux, 2007c], they are primarily sensitive to coordination numbers, with values in poorly coordinated dense systems DLo and DLi close to the ones observed in loose systems.

Stress increments and elasticity

Note that the assumption of elastic response underlying relation (4.18) implies that sliding contacts are absent or have negligible effects, and that the contact network is stable. This may of course be checked by confronting the predictions of (4.18) to a complete DEM computation, in which a steadily, very slowly growing strain is applied, and the effects of friction and of network rearrangements are taken into account. Such a comparison, carried out in the isotropic case [Agnolin and Roux, 2007c], showed the elastic response and the complete computation to coincide for small enough strain or stress intervals, in good agreement with laboratory results.

In the present study, a growing strain ε_1 is imposed in the axial direction, and the elastic response of an equilibrium configuration to a small increment $\Delta\varepsilon_1$ should be:

$$\begin{aligned} \Delta\sigma_1 &= C_{11}\Delta\varepsilon_1 \\ \Delta\sigma_2 &= \Delta\sigma_3 = C_{12}\Delta\varepsilon_1. \end{aligned} \tag{4.19}$$

Fig. 4.11 compares the predictions of (4.19) for $\Delta\sigma_1$, with modulus C_{11} identified from the stiffness matrix (thereby assuming an elastic behavior in all contacts), to the full DEM-computed mechanical response to small σ_1 increments, in one DLo and one DHo systems, equilibrated for different intermediate values of σ_1 along the oedometric curve. The elastic modulus correctly describes the iÄnitial slope and the first data points recorded on the curve (while the strain increment is of order 10^{-6} or 10^{-5}), and then the material response turns softer.

A similar comparison is made for $\Delta\sigma_2$ in Fig. 4.12, showing similar small strain and stress intervals for which the lateral stress increments abides by the elastic prediction, using modulus C_{12}. This time, the material gets *stiffer* as it departs from the elastic response.

The results on the 6 different systems (one sample of each type) for the amplitude of the strain interval for which the quasi-elastic model applies are gathered in Fig. 4.13. The convention was
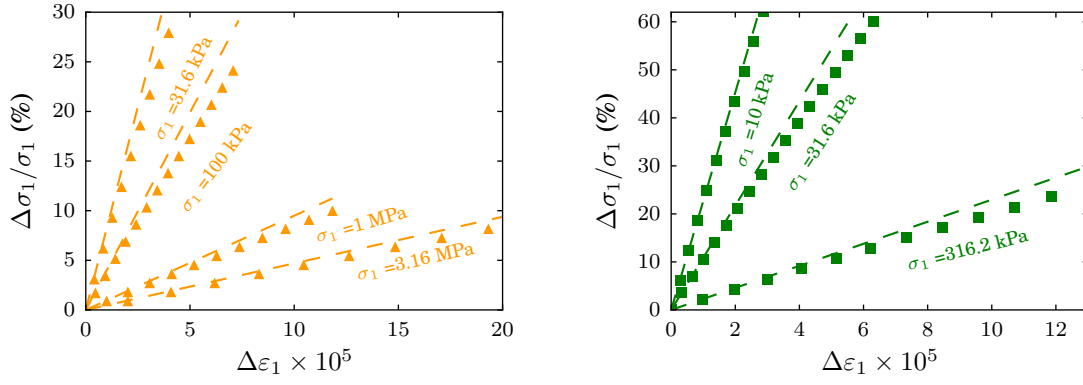
Figure 4.11: Ratio of stress increments $\Delta\sigma_1$ to initial stress σ_1, versus strain increment $\Delta\varepsilon_1$. Dots: DEM results, after system equilibrates under application of growing $\Delta\sigma_1$. Dotted lines: elastic prediction (slope C_{11}/σ_1). Data recorded for different σ_1 values as indicated, in one DLo sample (top graph) and a DHo one (bottom graph).
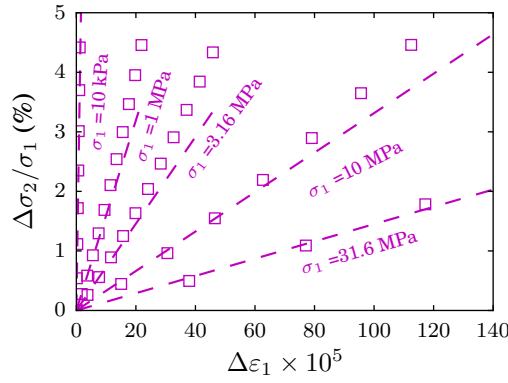

Figure 4.12: Ratio of stress increments $\Delta\sigma_2$ to initial stress σ_1, versus strain increment $\Delta\varepsilon_1$. Dots: DEM results, after system equilibrates under application of growing $\Delta\sigma_1$. Dotted lines: elastic prediction (slope C_{12}/σ_1). Data recorded for different σ_1 values as indicated, in one DHi sample

adopted here that the elastic response is correct as long as the relative error made on predicting stress increments with Eq. 4.19 remains below 5%. As noted earlier in isotropic systems[Agnolin and Roux, 2007c], this quasi-elastic range, expressed as a strain interval, is of the same order as observed in experiments. It tends to be larger in better coordinated systems: DHo, DHi, and also DLo and DLi once z has significantly increased under compression (Fig. 4.3). It also increases with σ_1, roughly proportionally to $\sigma_1^{2/3}$. This exponent [Agnolin and Roux, 2007c] may be regarded as a reflection of a roughly σ_1-independent quasielastic range, if expressed in terms of relative stress increase $\Delta\sigma_1/\sigma_1$. As moduli tend to scale as $\sigma_1^{1/3}$, a constant $\Delta\sigma_1/\sigma_1$ translates into the observed scaling $\sigma^{2/3}$ for strain increments.
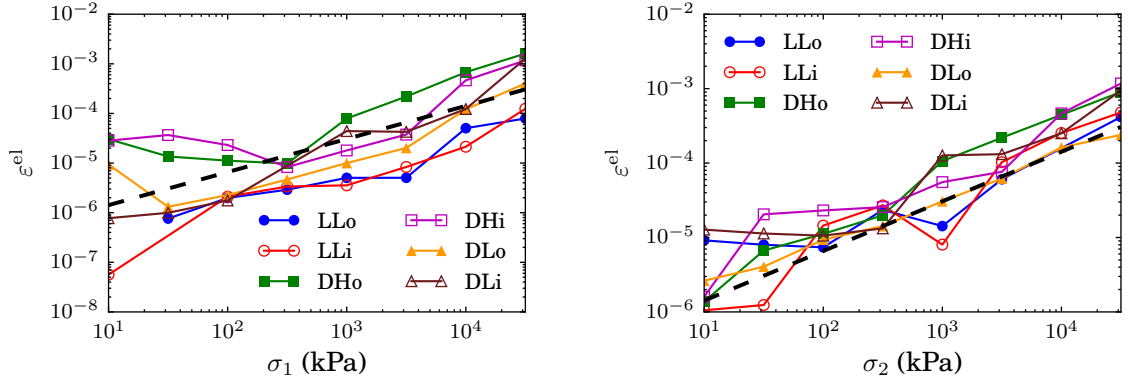
Figure 4.13: Quasielastic range, defined as ε_1 interval for which (4.19) holds with 5%, versus equilibrium stress in probed system. Top graph: axial stress response ($\Delta\sigma_1$). Bottom graph: lateral stress response ($\Delta\sigma_2$). Dashed lines have slopes 2/3.

K_0 and elasticity.

Should stress variations with axial stress ε_1 satisfy elastic behavior and relations (4.19), then stress ratio K_0 should be related to elastic moduli. Specifically, defining an "incremental" stress ratio $K'_0 = \Delta\sigma_2/\Delta\sigma_1$, as in Ref. [Gu et al., 2015], K'_0 should be equal to C_{12}/C_{11}. However, as already apparent in Figs. 4.11 and 4.12, stress increments differ from the predictions of the tangential quasielastic behavior and, consequently, coefficient K_0 and ratio C_{12}/C_{11} vary independently, as visualized in Fig. 4.14. This figure makes it clear that both quantities are quite different, with much lower values of
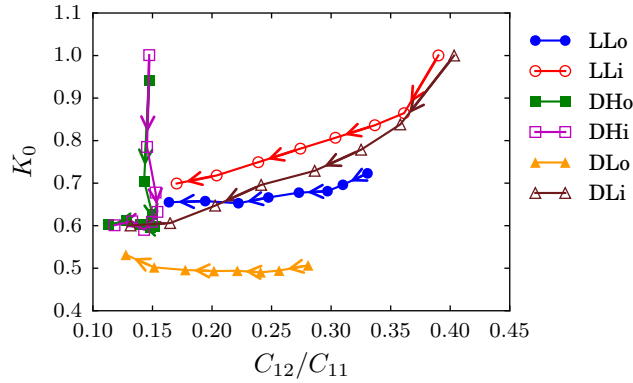
Figure 4.14: Plot of K_0 versus C_{12}/C_{11}. Data points correspond to all six prepared initial states, as indicated in the legend, and pertain to the different equilibrated configurations along the oedometric compression curve.

C_{12}/C_{11}. As remarked before in connection with Fig. 4.13, modulus C_{11} overestimates the variation of axial stress, $\Delta\sigma_1$ with ε_1, while C_{12} underestimates the variation of lateral stress, $\Delta\sigma_2$. Both effects entail that C_{12}/C_{11} is smaller than $K_0 = \Delta\sigma_2/\Delta\sigma_1$. Furthermore, ratio C_{12}/C_{11} is nearly constant in systems DHi and DHo, while K_0 changes to a large extent. The opposite is true for the four other

states, in which C_{12}/C_{11} changes much more than K_0. Elastic moduli, in general, are thus quite uncorrelated to K_0.

These remarks raise the question of the status and validity of simulated experiments in which elastic moduli are measured, as in the case of the results shown in Figs. 4.11 and 4.12. One may wonder how one can observe, e.g., a constant stress ratio K_0 along the quasistatic compression curve, on the one hand; and a different ratio of stress increments, $\Delta\sigma_2/\Delta\sigma_1 = C_{12}/C_{11}$ for small probes applied to any intermediate equilibrium state along the curve, on the other hand. The solution to this conundrum is provided by the very small "numerical creep" phenomenon observed when well equilibrated contact networks are obtained along the primary, strain rate controlled compression curve (Sec.4.4). As the system evolves towards a well equilibrated configuration (which is necessary to build a nonsingular stiffness matrix), it is observed that the population of contacts with full friction mobilization (i.e., for which the Coulomb inequality is satisfied as an equality, $\|\mathbf{F}^T\| = \mu F^N$), disappears. Instead, a number of contacts carry force values barely inside the Coulomb cone (typically, $\|\mathbf{F}^T\|/\mu F^N > 0.95$). This is enough to allow for a small interval of strains within which the elastic model, assuming friction is irrelevant, applies as a good approximation.

It should be recalled that experimental measurements of elastic moduli by static means, along a stress-strain curve, are often carried out in a similar way [Duttine et al., 2007, Ezaoui and di Benedetto, 2009]: first equilibrated under static stresses, samples are subjected to small oscillatory probes; while the first cycles tend to cause small amounts of strain to accumulate, the subsequent ones are reproducible and quasielastic. Upon resuming the compression curve (most usually a triaxial compression test) at fixed strain rate, the initial slope of the stress-strain curve coincides with the elastic modulus.

Another way to observe an elastic response is to reverse the loading direction [Agnolin and Roux, 2007c].

Anelasticity being largely due to friction mobilization, reversing the sign of strain rate $\dot{\varepsilon}_1$ tends to cause tangential relative displacements to change sign, thereby bringing back contact forces inside the Coulomb cone. Consequently, upon gradually applying a *negative* $\dot{\varepsilon}_1$ (with due caution, keeping accelerations very small), the obtained stress-strain curve exhibits a quasi-elastic range which is larger than in the forward direction (typically by one order of magnitude). Moreover, unpon unloading this quasielastic response interval is observed even without waiting for the small creep strain leading to full equilibration to occur.

Like in experiments, on resuming the strain rate controlled compression after a static elastic probe, the evolution of stresses versus ε_1 in our numerical oedometric tests tends to return to the previous (nonelastic) behavior. Fig. 4.15 is a plot of stress increment $\Delta\sigma_2$ versus $\Delta\sigma_1$ following an elastic probe applied to an equilibrium configuration. The slope of this plot coincides with C_{12}/C_{11} for small stress increments, and gradually approaches K_0 for larger ones. (K_0 coincides with ratio $\Delta\sigma_2/\Delta\sigma_1$ along the oedometric compression curve since it is constant in good approximation for initial states DLo.)
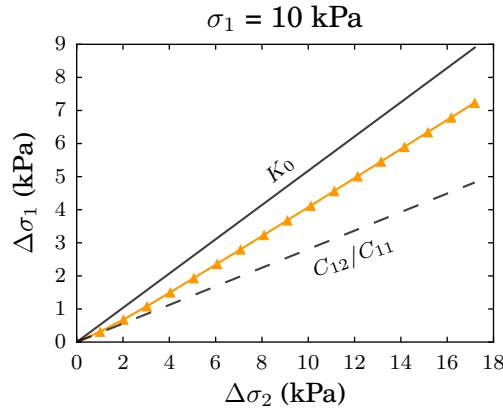
Figure 4.15: $\Delta\sigma_2$ versus $\Delta\sigma_1$ in sample DLo at $\sigma_1 = 10$ kPa, on resuming compression after equilibration under $\sigma_1 = 10$ kPa. Dots show DEM data, solid line has slope K_0, dashed line has slope C_{12}/C_{11}.

Role of friction in oedometric compression

Incremental response

Results of Figs. 4.14 and 4.15 make it obvious that oedometric compression curves are not ruled by the quasielastic behavior evidenced for small stress or strain increments about a prestressed, well-equilibrated configuration. Departures from this elastic regime (as investigated previously in the isotropic case [Agnolin and Roux, 2007a]) are due to frictional forces and, possibly, to contact network instabilities. As visualized in Fig. 4.16, the elastic response coincides, on resuming the oedometric compression from an intermediate (equilibrated) configuration, with that of a fixed contact network in which no contact creation occurs (although some of the existing contacts may open), and frictional sliding is forbidden (setting μ to an infinite value). We also investigated the response of
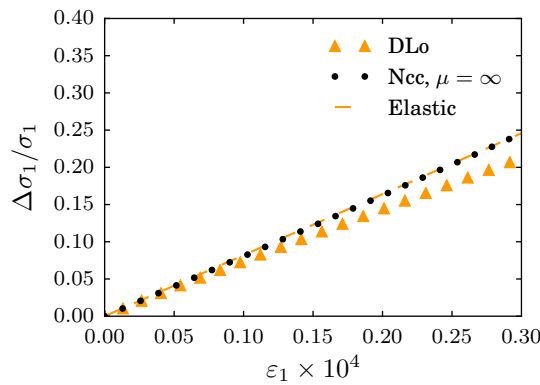

Figure 4.16: Oedometric loading curves from equilibrium state under $\sigma_1 = 31.6$ kPa in a DLo sample. "Ncc, $\mu = \infty$" labels simulations carried out without creation of any new contact, and infinite friction (no sliding). The linear elastic response of the initial contact network is shown as dashed straight line.

fixed contact networks (forbidding contact creation), and observed them not to differ from the full response on the scale of Fig. 4.16. The gradual departure from the elastic response is thus mainly due to frictional sliding.

Friction mobilization

Contact sliding is thus the major cause of the nonelastic nature of the mechanical response in oedometric compression. How the sliding (or full friction mobilization) status of a contact correlates to its orientation is shown in Figs. 4.17 and 4.18 below. Fig. 4.17, a plot of average friction mobiliza-
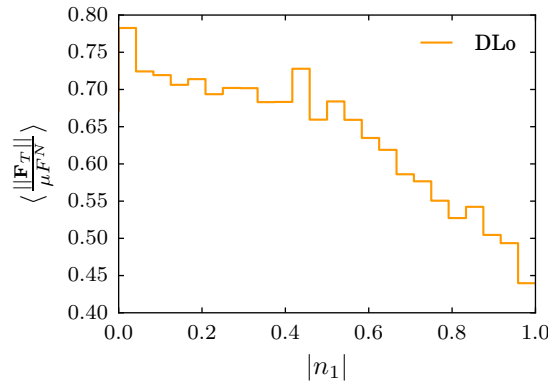

Figure 4.17: Average level of friction mobilization, $\langle \frac{\|\mathbf{F}^T\|}{\mu F^N} \rangle$, in contacts sharing common normal orientation $\mathbf{n}$, versus $|n_1|$, in state DLo under $\sigma_1 = 91$ kPa.

tion versus $|n_1|$ in contacts sharing normal unit vector $\mathbf{n}$, shows a significantly greater proximity to the sliding limit, on average, near $n_1 = 0$, i.e. for nearly transversely oriented normals, close to the plane of directions 2 and 3. Fig. 4.18, recording measurements carried out during controlled strain rate oedometric compression, shows moreover that the proportion of exactly sliding contacts, or even almost sliding ones (with $\frac{\|\mathbf{F}^T\|}{\mu F^N}$ close to 1), reaches its maximum for directions almost orthogonal to the axial direction.

This angular variation of friction mobilization might seem surprising, as, from the macroscopic strain field, one does not expect any tangential displacement in the contacts oriented in the transverse plane. The assumption of uniform strain might however provide some insight. Let us write the relative displacement at the contact between grains i and j, $\delta\mathbf{u}_{ij}$, as

$$\delta\dot{\mathbf{u}}_{ij} = \underline{\dot{\varepsilon}} \cdot \mathbf{r}_{ij} = (R_i + R_j)\underline{\dot{\varepsilon}} \cdot \mathbf{n}_{ij},$$

the dot denoting a derivative with respect to time. Given the uniaxial strain tensor $\underline{\varepsilon} = \varepsilon_1 \mathbf{e}_1 \otimes \mathbf{e}_1$, the
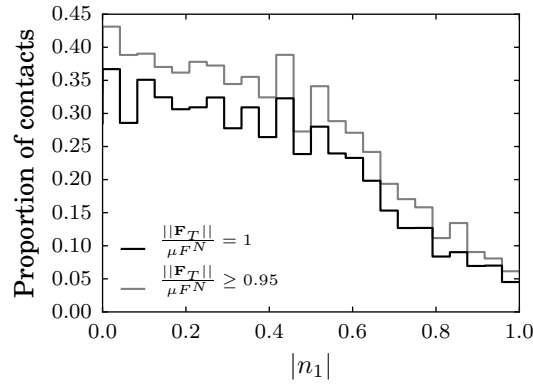
Figure 4.18: Proportion of contacts for which friction mobilization $\frac{\|\mathbf{F}^T\|}{\mu F^N}$ is equal to 1 or exceeds threshold 0.95 in contacts sharing common normal orientation $\mathbf{n}$, versus $|n_1|$, in state DLo under $\sigma_1 = 91$ kPa (these data correspond to one intermediate state in the course of strain-rate-controlled compression).

normal and tangential components of $\delta\dot{\mathbf{u}}_{ij}$ read

$$\delta\dot{u}_{ij}^N = (R_i + R_j)\dot{\varepsilon}_1(n_{ij}^{(1)})^2$$
$$\delta\dot{\mathbf{u}}_{ij}^T = (R_i + R_j)\dot{\varepsilon}_1 n_{ij}^{(1)}(\mathbf{e}_1 - n_{ij}^{(1)}\mathbf{n}_{ij}). \tag{4.20}$$

Thus the corresponding elastic force component derivatives are such that their normal component vanishes faster than their tangential one as $n_{ij}^{(1)}$ approaches zero. Contacts with nearly transverse normal directions thus tend to carry tangential forces varying faster than the normal ones, and are thus likely to reach the Coulomb sliding condition more easily.

Discussion

To summarize our observations, we have checked that quasi-elasticity, characterizing the response of a contact network in which friction mobilization might be neglected, only applies to well-equilibrated configurations (in which full friction mobilization is lost), or to the beginning of an unloading stress-strain curve. Anelasticity is further related to lack of reversibility in unloading in Sec. 4.6. On the compression curve, strains are associated to some frictional sliding, distributed among all directions of normal vector $\mathbf{n}$ but occurring more frequently for those close to the transverse plane. Frictional sliding reduces the apparent stiffness of the material. Unlike material deformation under deviatoric load [Roux and Combe, 2002], the anelastic response under oedometric compression does not appear to involve large scale internal rearrangements and failure of contact networks.

Yet, K_0, the stress ratio, is often related to global failure conditions. First, the ratio of principal stresses cannot exceed an upper bound R_p related to the internal friction angle φ as

$$R_p = \frac{1 + \sin\varphi}{1 - \sin\varphi}, \tag{4.21}$$

thereby setting a lower bound $R_a = 1/R_p$ to the possible value of K_0 (R_p and R_a are referred to as the *passive* and *active* principal stress ratios, in the context of retaining wall engineering). φ (or, equivalently, R_p) is most usually, in simulations as well as in experiments, measured in triaxial compression, which consists in compressing in direction 1 while maintaining stresses $\sigma_2 = \sigma_3$ constant, which involves lateral expansion. In spherical grain assemblies with intergranular friction coefficient $\mu = 0.3$, R_p, which depends on the initial state, does not exceed 2.5 [Roux and Combe, 2010]. Thus K_0 should exceed $0.4 = 1/R_p$, which from Fig. 4.14 is always larger than C_{12}/C_{11}: the compression could not be elastic.

A second way in which K_0 is often linked to internal friction is through the Jaky relation:

$$K_0 = 1 - \sin\varphi, \tag{4.22}$$

which many experimental [Okuchi and Tatsuoka, 1984, Lee et al., 2013, Gao and Wang, 2014] and numerical [Lopera Perez et al., 2015] works attempted to check, with varying success. We did not systematically test relation 4.22 – which is somewhat problematic as K_0 is not constant in general (and would require a nonambiguous definition of φ as well). However, let us note that in state DLo for which K_0 remains, in good approximation, constant as σ_1 increases, (4.22) would yield $\varphi \simeq 30°$, which is notably larger than the values recorded for the internal friction angle in spherical bead assemblies [Roux and Combe, 2010].

4.6   Unloading and compression cycles.

One major issue in oedometric compression is reversibility. It is often assumed that the compression is a plastic, irreversible process. Unloading, on the other hand – i.e., reversing the sign of $\dot{\varepsilon}_1$ or decreasing σ_1 after it has increased to some maximum value, σ_1^p – is often regarded as elastic. Strain (or density), varies less. As the initial value of σ_1 is retrieved, the system has not recovered its initial density, an irreversible density increase is observed. Then, upon reloading, the same "elastic" stress-strain path is retraced as in the previous unloading branch, until σ_1^p, the *preconsolidation stress* is attained. Any further stress increase beyond σ_1^p results in an additional plastic response, with a faster increase of ε_1. Such is the classical behavior of sands and other soils in oedometric compression, as described in treatises [Mitchell and Soga, 2005] and textbooks [Biarez and Hicher, 1993].

Density and coordination

To ease comparisons with the literature, in this section we describe density changes in terms of the void ratio e, defined as

$$e = -1 + \frac{1}{\Phi}. \tag{4.23}$$

Fig. 4.19 displays the variations of void ratio e in the oedometric compression cycle, in which the compression described in Sec. 4.4 is followed by a decompression, with the procedure described in

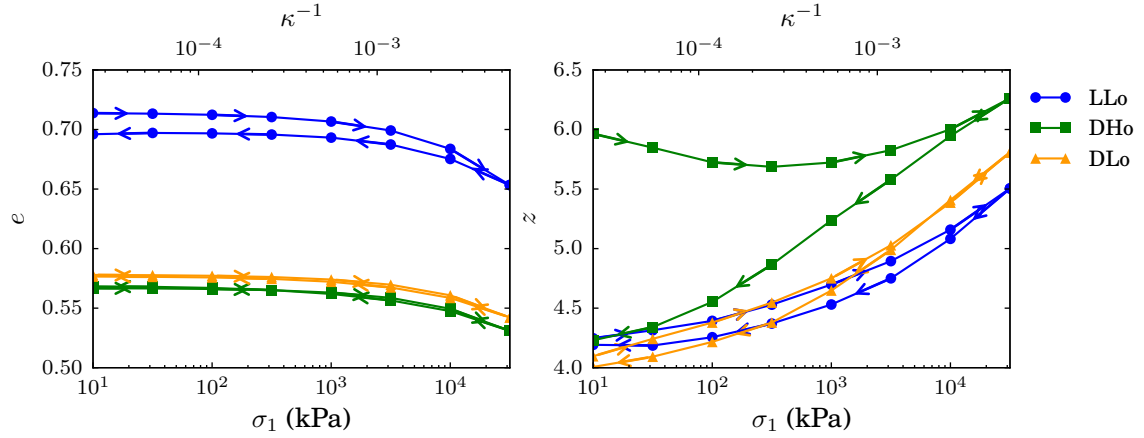Sec. 4.2, down to the lowest stress level $\sigma_1 = 10$ kPa. The void ratio change (Fig. 4.19, upper graph)

Figure 4.19: Void ratio e (top) and coordination number z (bottom) versus σ_1 in oedometric compression cycle.

is almost reversible, especially in dense systems – an observation which strikingly differs from the classically reported behavior of sands (see, e.g., [Sanzeni et al., 2012]). In fact, similar irreversible density increases under oedometric loads as in laboratory experiments on sands were to our knowledge never retrieved in DEM simulations in which grains interact merely by elasticity and Coulomb friction in their contacts. *Cohesive* DEM models, on the other hand, do exhibit large irreversible density increases under isotropic [Gilabert et al., 2008, Than et al., 2016] or oedometric [Kadau et al., 2003] loads, and behave similarly to laboratory powders, clays or sands, with the preconsolidation stress ruling the onset of further plastic compaction. Cohesionless systems, as dealt with in simulations, appear to lack some modeling ingredient to exhibit similar plasticity in compression as sands, most likely some form of plasticity or damage at the contact scale. This interpretation is confirmed by the experimental observations reported in Ref. [Cavaretta et al., 2010]: assemblies of smooth beads, in oedometric compression, deform much less than assemblies of angular, irregular shaped particles, unless the beads break under very high stress. Contacts through small asperities tend to exhibit breakage or damage under lower stresses.

In the present numerical study, small irreversible strain changes are nevertheless observed. The lack of reversibility is also, as amply demonstrated in Sec. 4.5, evidenced by the departure from elastic response in compression. Table 4.2 compares the total axial strain, in compression and decompression, with an elastic strain, evaluated as

$$\varepsilon_1^{\text{el}} = \int_{\sigma_1^{\text{min}}}^{\sigma_1^{\text{max}}} \frac{\mathrm{d}\sigma_1}{C_{11}(\sigma_1)} \tag{4.24}$$

The values of C_{11} have to be interpolated for all values of σ_1 along the loading curve to evaluate the elastic strain according to (4.24). It is of the same order as the measured strain, but with a relative difference of order one.

The compression cycle is most conspicuously irreversible as regards the internal microstructure

	$\varepsilon_1^{\text{el}}$	$\varepsilon_1^{\text{ld}}$	$\varepsilon_1^{\text{uld}}$
Lo	1.72 %	3.54 %	2.58 %
DHo	1.27 %	2.28 %	2.38 %
DLo	1.38 %	2.22 %	2.14 %

Table 4.2: Total strains computed from elastic moduli ($\varepsilon_1^{\text{el}}$) and measured in simulations along loading ($\varepsilon_1^{\text{ld}}$) and unloading ($\varepsilon_1^{\text{uld}}$) paths .

of the system. Thus the coordination number (Fig. 4.19, lower graph), if initially large (as in DHo systems) decreases to values nearly as low as in poorly coordinated initial states, either dense (DLo) or loose (LLo). This behavior is quite similar to the one reported in isotropic compression [Agnolin and Roux, 2007b].

This decrease of coordination number after unloading also occurs for smaller compression cycles (smaller maximum axial stress). Fig. 4.20 thus shows, both on the void ratio and on the coordination
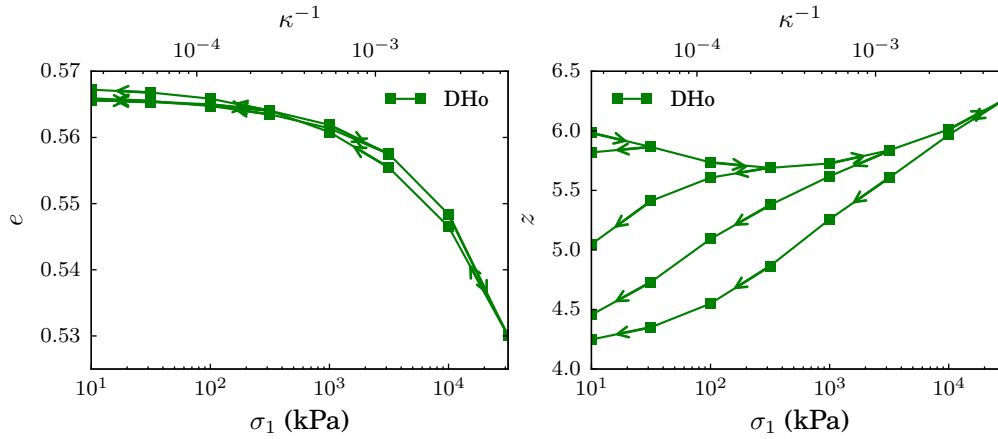
Figure 4.20: Void ratio e (left) and coordination number z (right) versus σ_1 in oedometric compression cycle on one DHo sample.

number, the effect of unloading from σ_1 values of 31.62 kPa, 316.2 kPa, and 3.162 MPa on the primary compression curve, in addition to the maximum stress 31.6 MPa. All compression cycles produce a decrease in z once σ_1 returns to its initial low value, the larger the wider the covered stress interval.

The first graph in Fig. 4.20, with a void ratio scale appropriate for DHo states, shows small density changes after a stress loop. Although in some cases the final density is *smaller* than the initial one (see also Tab. 4.2), the work done in the stress loop, as evaluated by the (algebraic) area under the stress-strain curve, is of course positive, signaling energy dissipation (this is discussed in [Agnolin and Roux, 2007b] in the case of isotropic compression).

K_0 and anisotropies

In unloading, a plot of K_0 versus σ_1, as shown in Fig. 4.21, first signals a gradual decrease in stress anisotropy, with K_0 increasing towards 1. In initially isotropic systems, as well as for DHo (only marginally anisotropic), the transverse directions become major principal stress directions and K_0 takes values larger than 1 (up to about 1.6 in the DHi case). DLo states, however, after a moderate decrease of K_0, keep direction 1 as the principal stress direction (and so do LLo ones). Loose states
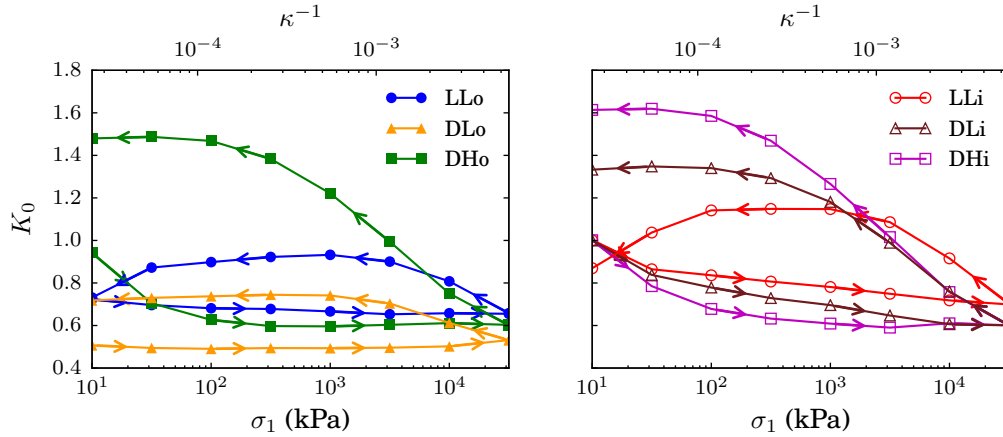

Figure 4.21: K_0 versus σ_1 in oedometric compression cycle.

tend to lose their stress anisotropy for the lower stress values in decompression, which might partly be due to some instability as the load is decreased onto fragile networks.

Since formula (4.17) still provides a good prediction of K_0 values on the unloading branch of the cycle, the different in evolutions of K_0 upon decompressing might be ascribed to different variations of anisotropy parameters $\tilde{c}_2$ and $\tilde{f}_2$: $\tilde{c}_2$ changes, which request changes in the contact network, are slower than changes of $\tilde{f}_2$, which are obtained on simply redistributing forces. Fig. 4.22 shows that fast increases of K_0 in decompression correspond to quickly evolving force anisotropy parameters $\tilde{f}_2$ in systems DHi, DLi, LLi and DHo.

Elastic moduli

Fig. 4.23 shows the variation of elastic moduli C_{11} and C_{12} in the compression cycle. As announced, moduli are roughly proportional to $\sigma_1^{1/3}$, with, possibly a somewhat faster increase in compression associated with changes in coordination number, and some effects of fabric and force anisotropies.

The evolution of elastic moduli during unloading phases reveals their dependence on the coordination number and anisotropy, rather than density. The evolution of C_{11} in system DHo in loading and unloading parallels that of its coordination number z (se Fig. 4.19). While C_{11} values on the compression branch is significantly larger for DHo systems than for DLo or LLo ones, this difference vanishes, just like the coordination number difference, upon returning to the initial stress down the decompression branch. The final value of C_{11}, after the loading cycle, is even lower for DHo than
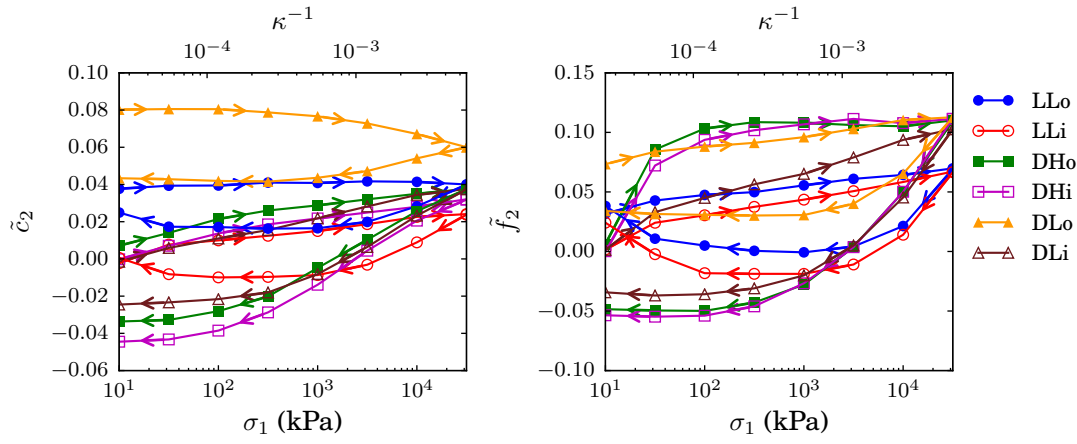
Figure 4.22: $\tilde{c}_2$ and $\tilde{f}_2$ versus σ_1 in oedometric compression cycle.

for LLo, despite the higher density – a difference to be attributed to the different anisotropies shown in Fig. 4.22. Compared to coordination numbers or fabric anisotropies, elastic moduli are easier to
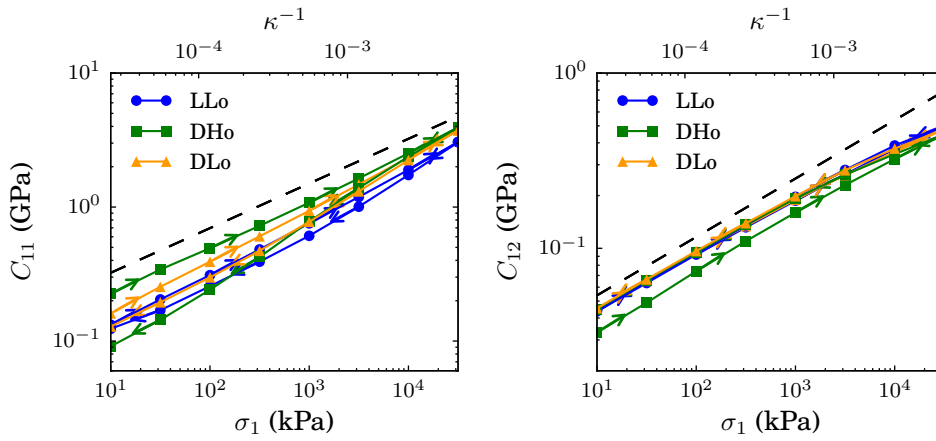
Figure 4.23: C_{11} and C_{12} versus σ_1, in loading cycle. Black dashed line has slope 1/3.

measure in the laboratory, and some of our observations could thus be checked.

Further compression cycles.

Under varying axial stress σ_1, oedometrically compressed granular materials thus undergo complex, irreversible evolutions, and one should in principle investigate the effects of arbitrary load histories, in which σ_1 may be increased or decreased, over any sequence of load intervals. We report here on a (limited) investigation of the effects of repeating the same compression cycle in systems DHo and DLo.

It is interesting to see whether the compression cycle is retraced upon compressing again: one may

wonder to what extent the memory of the initial state survives repeated cycles, and whether systems sharing the same initial density will tend to approach a common limit state. Fig 4.24 shows that the slight density difference between DLo and DHo does not appear to gradually vanish under repeated compression cycles. Meanwhile, the coordination number of the DHo state, after its strong decrease in the first cycle, oscillates in the following ones between values that remain somewhat larger than the ones observed in the initially poorly coordinated system DLo. Although the difference of coordination
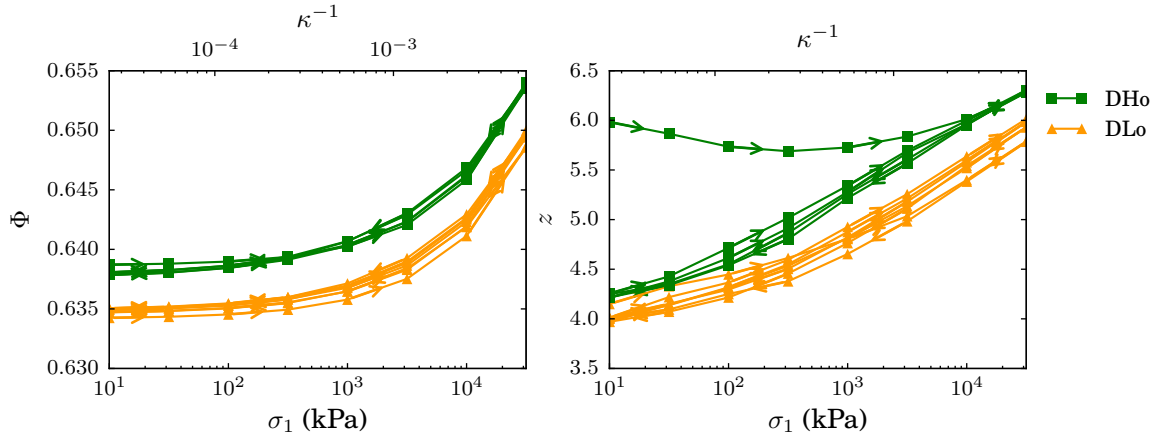
Figure 4.24: Solid fraction Φ (left) and coordination number z (right) versus σ_1 in oedometric compression cycles, with three unloading and reloading steps after the first compression to maximum value of axial stress.

number between DHo and DLo is greatly reduced after the first cycle, the stress anisotropy of the final states is then quite different, as noted previously (see Fig. 4.21), with $K_0 > 1.4$ for DHo, and $K_0 < 0.8$ for DLo. This difference in the evolution of the principal stress ratio, as shown in Fig. 4.25, does not
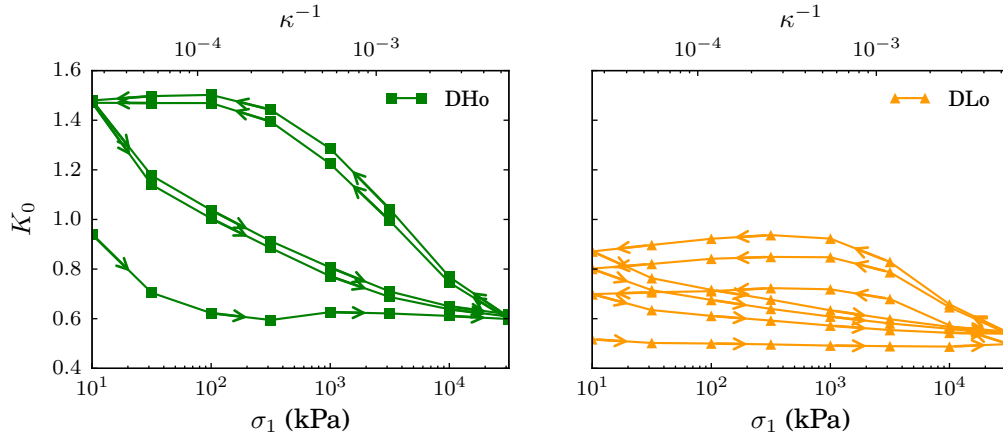
Figure 4.25: K_0 versus axial stress σ_1 in cycles of Fig. 4.24.

tend to disappear under repeated cycles: while K_0 in DHo systems oscillates between about 0.6 at large σ_1 and nearly 1.5 under low stress, it oscillates below 1 for DL0, with a systematic increasing

tendency. Thus, under repeated decompression and recompression steps, systems DLo and DHo still behave differently: while the DHo state seems to approach a limit cycle, with the same values of Φ, z and K_0, the observation of K_0 values for DLo reveals a gradual evolution towards gradually less anisotropic, and possibly denser states.

4.7   Conclusions

We now summarize and comment our observations, suggesting a few perspectives to the present study.

We carried out systematic numerical simulations of quasistatic oedometric compression of model granular materials, in which contact mechanics does not involve other ingredients than (suitably simplified) Hertz-Mindlin elasticity and Coulomb friction (with friction coefficient $\mu = 0.3$). The material is first assembled in initial states varying in density, coordination number (which might be large or small, depending on preparation, in dense systems, as in isotropic grain assemblies [Agnolin and Roux, 2007a, Magnanimo et al., 2008, Song et al., 2008]), and anisotropy. In the compression cycle, axial stress σ_1 varies by a factor larger than 3000, corresponding, for glass beads, to the range $10\,\text{kPa} \le \sigma_1 \le 31.6\,\text{MPa}$. The observed behaviors prove somewhat more complicated than superficial observations would seem to indicate, with nontrivial initial state dependence and anelastic reponse.

Although the strain response (or the change in solid fraction) under growing axial stress seems nearly reversible, the internal state of the material does evolve irreve

rsibility, as apparent in the variations of coordination numbers and anisotropy parameters. Compared to the behavior of sands as described in the geomechanics literature, the stress-strain irreversibility (usually described as a plastic response) is much smaller, a difference we attribute to the absence of plasticity or damage in the implemented contact model. Just like in isotropic compression [Agnolin and Roux, 2007b], coordination numbers tend to decrease in a compression cycle, once the initial stress value is retrieved, the more the larger the maximum stress value in compression. The stress anisotropy, as expressed by ratio K_0, is in general not constant, although it varies little with σ_1 in some systems assembled under similar one-dimensional compressions of granular gases, except in the case of a high coordination number, possibly unrealistically large, as pobtained on suppressing friction in the assembling stage. We expect gravity-deposited systems, in conditions ensuring homogeneous density and microstructure, to behave similarly. Stress ratio $K_0 = \sigma_2/\sigma_1$ is correctly predicted, in all configurations along the loading or unloading curves, by a formula involving the leading order anisotropic terms in Legendre polynomial expansions of normal vector-dependent contact densities and average normal force value distributions over the unit sphere. It should thus be possible to predict the mechanical response and the internal material evolution if the evolution of axial strain ε_1 could be related to anisotropy parameters.

This latter task seems however arduous, given the complex non-elastic strain response of the material. Elastic moduli, although measurable upon applying small load increments onto well-equilibrated configurations along the compression path, do not correctly predict the slope of the oedometric compression curve, or the stress ratio, K_0. This conclusion might seem paradoxical, since the compression curve is supposed to be quasistatic, i.e., consisting of a continuous sequence of equilibrium states.

We attribute this apparent contradiction to the subtle role of the very small creep step preceding, in numerical simulations as well as in the laboratory, the static measurement of elastic properties. In simulations this creep stems from the small distance to equilibrium of transient configurations along a strain-rate controlled loading path. This distance decreases as the strain rate, expressed in dimensionless form by inertial number I, decreases. As well equilibrated, static states are obtained with good accuracy, such that the stiffness matrix of the contact network is well behaved, friction mobilization is lost, and for a small, non-vanishing stress increment, it is a good approximation to assume all contacts to behave elastically. In the laboratory, although strain rates are considerably smaller, and intermediate configurations are likely closer to equilibrium, some creep also takes place, possibly caused by other phenomena at contact scale, with similar results that quasielastic relations between small stress and strain increments might be subsequently measured. Creep phenomena, as observed in real laboratory materials, in general, would deserve more detailed investigations, although the elucidation of their origin is likely to involve little known micromechanical ingredients at the contact scale.

The elastic properties being easier to measure than fabric variables and coordination numbers, we provide in the next chapter a more detailed study of the relations of all five independent moduli in the transversely anisotropic configurations obtained by oedometric compression to microstructural variables. A comparison of elastic moduli in numerical and experimental works should help understanding which type of numerical preparation scenario produces initial states closer to experimental ones.

Although strains predicted by the elastic response are of the same order of magnitude as observed strains, the difference is important, and strongly affects the value of stress ratio K_0. The anelastic response is mainly due to friction mobilization, which, although distributed over all contact orientations, surprisingly affects the most the contacts with normal direction close to the transverse plane. Contact network instabilities, avoided thanks to new contact creations, do not seem to play an important part. Detailed, strictly quasistatic analyses [Roux and Combe, 2002, McNamara and Herrmann, 2006, Welker and McNamara, 2009, Roux and Combe, 2011] of elastic-frictional response of contact networks to oedometric loads could be carried out to relate microscopic frictional sliding to macroscopic behavior.

Another remarkable result of the present numerical study is the persistent effect of the assembling process and the resulting initial state characteristics: the difference, e.g., between high coordination and low coordination dense systems is not lost after several compression cycles. Our numerical results, as regards the evolution of K_0, differs somewhat from experimental observations, which sometimes report a quicker convergence to a common value of this stress ratio for different initial states. This is likely due, like irreversibility, to the absence of contact-level plasticity or damage in the numerical model. Some features of assemblies of nonspherical, rough or angular grains as probed in oedometric compression of sands might need to be modeled – with the same identification difficulties as for creep – if the effects of growing stress intensity are to be quantitatively described.

Chapter 5

Elastic moduli and anisotropic structural states

Contents

In this chapter, we specifically focus on studying the elastic moduli in the six states previously subjected to oedometric compression in Chap. 4. The connection of these moduli to density, coordination number, fabric and force anisotropies is investigated. After a brief introduction of this chapter objectives in Sec. 5.1. The method by which elastic properties are measured for each equilibrated configuration (Sec. 5.2) is recalled. Then we present the evolution of all 5 independent elastic moduli in the transversely isotropic states along the compression curves in Sec. 5.3, correlate them to state variables (Sec. 5.5), discuss the performance of simple predictive schemes (Sec. 5.5), confront our observations to experiments and previous numerical works (Sec.5.4), before presenting a brief conclusion (Sec. 5.6).

5.1   Introduction

This chapter deals with the macroscopic mechanical properties of a model granular material in anisotropic structural and stress states, as investigated by discrete numerical simulation. The previous chapter (Chap. 4), studied stress-strain relations and described how state variables evolve in oedometric compression. Sec. 4.6 clearly shows that the strain-stress relation in oedometric compression or compression cycles is not elastic, but that elastic moduli express stress-strain response in very small probes superimposed on previously well-equilibrated intermediate states, provided a very small creep phase during configuration stabilization has suppressed friction mobilization. The chapter, thus does not investigate the quasi-elastic response domain any further. Rather, its objective is to investigate how elastic moduli are related to microstructural features of the same anisotropic granular packings, and could be measured to infer useful information on such variables as coordination number and fabric. The elastic properties of anisotropic granular materials have quite often been studied experimentally, with sands [Chen et al., 1988a, Chen et al., 1988b, Hardin and Blandford, 1989, Shibuya et al., 1992, Hoque and Tatsuoka, 1998, Kuwano and Jardine, 2002, Geoffroy et al., 2003, Duttine et al., 2007, Ezaoui and di Benedetto, 2009] or glass beads [Kuwano and Jardine, 2002, Khidas and Jia, 2010], and recently addressed in simulations as well [Peyneau and Roux, 2008b, La Ragione and Magnanimo, 2012a, La Ragione and Magnanimo, 2012b] . We exploit here the variety of initial material states subject to oedometric compression histories as studied in Chap. 4 to compare the tensor of elastic moduli to this literature, and to test modeling schemes.

5.2   Computation methods

Stiffness matrices and elastic moduli

Elastic moduli express the relations between small stress increments $\Delta\sigma$ and small strains $\underline{\varepsilon}$, assuming the contact network, in equilibrium, behaves like a network of elastic springs, with stiffnesses K_N and K_T varying from contact to contact according to relations 4.3 and 4.4.

As our numerical results are obtained with systems enclosed in periodic cuboidal cells, displacements considered in elastic problems (implicitly assumed small) are conveniently parametrized, for

all grains i with position $\mathbf{r}_i$ in the simulation cell, as

$$\mathbf{u}_i = \tilde{\mathbf{u}}_i - \underline{\underline{\varepsilon}} \cdot \mathbf{r}_i, \tag{5.1}$$

where $\tilde{\mathbf{u}}_i$'s are fluctuating, periodic displacements, while the second, affine term represents the effect of global strain $\underline{\underline{\varepsilon}}$, a symmetric tensor (the minus sign results from our convention of positive compressive strains). Supplementing the displacements of the N particle centers, $(\mathbf{u}_i)_{(1 \leq i \leq N)}$ with their (small) rotations $\underline{\theta}_i$, this results in $N_f = 6N + 6$ degrees of freedom, which we gather in a single displacement vector $\mathbf{U} = (\tilde{\mathbf{U}}, \underline{\underline{\varepsilon}})$, the coordinates of ($\tilde{\mathbf{U}}$ comprising all those of $(\tilde{\mathbf{u}}_i, \underline{\theta}_i)_{1 \leq i \leq N}$. The conjugate load, denoted as $\mathbf{F}^{\text{ext}}$, contains all components of external forces $\mathbf{F}^{\text{ext}}$ and torques $\mathbf{\Gamma}^{\text{ext}}$ applied to the grains as well as the 6 independent components of external stress $\underline{\underline{\sigma}}$, such that

$$\sigma_{\alpha\beta} = \frac{1}{\Omega} \sum_{i<j} F_{ij}^{(\alpha)} r_{ij}^{(\beta)}. \tag{5.2}$$

In (5.2), $r_{ij}^{(\beta)}$ denotes the coordinate β of the vector joining the centers of grain i to the center of the nearest image, by the group of translations associated to the periodic boundary conditions, of its contacting neighbor j, and Ω is the cell volume. On probing elastic properties, small stress increments $\Delta\underline{\underline{\sigma}}$ and contact force increments $\Delta\mathbf{F}_{ij}$ are considered, related by (5.2).

The small displacements associated with a load *increment* $\Delta\mathbf{F}^{\text{ext}}$ should satisfy (to first order in $\mathbf{U}$)

$$\Delta\mathbf{F}^{\text{ext}} = \underline{\underline{\mathbf{K}}} \cdot \mathbf{U}, \tag{5.3}$$

(5.3) is a statement of the system of N_f linear equations one has to solve to find the N_f unknowns contained in vector $\mathbf{U}$ and determine the linear elastic response about a prestressed equilibrium configuration. It involves the $N_f \times N_f$ symmetric, positive definite *stiffness matrix* $\underline{\underline{\mathbf{K}}}$. More details on the structure of matrix $\underline{\underline{\mathbf{K}}}$, as discussed in Ref. [Agnolin and Roux, 2007c], are provided in Appendix A.

Specifically, one wishes to find the 5 independent moduli corresponding to the transversely isotropic granular systems under oedometric compression along axis 1. Those are defined by the following macroscopic relation between stress increments and small strains about an equilibrium prestressed state:

$$\begin{bmatrix} \Delta\sigma_{11} \\ \Delta\sigma_{22} \\ \Delta\sigma_{33} \\ \Delta\sigma_{23} \\ \Delta\sigma_{31} \\ \Delta\sigma_{12} \end{bmatrix} = \begin{bmatrix} C_{11} & C_{12} & C_{12} & 0 & 0 & 0 \\ C_{12} & C_{22} & C_{23} & 0 & 0 & 0 \\ C_{12} & C_{23} & C_{22} & 0 & 0 & 0 \\ 0 & 0 & 0 & 2C_{44} & 0 & 0 \\ 0 & 0 & 0 & 0 & 2C_{55} & 0 \\ 0 & 0 & 0 & 0 & 0 & 2C_{55} \end{bmatrix} \cdot \begin{bmatrix} \varepsilon_{11} \\ \varepsilon_{22} \\ \varepsilon_{33} \\ \varepsilon_{23} \\ \varepsilon_{31} \\ \varepsilon_{12} \end{bmatrix} \tag{5.4}$$

We thus use a notation in which $\Delta\underline{\underline{\sigma}}$ and $\underline{\underline{\varepsilon}}$ appear as 6-dimensional vectors, and the elastic moduli are gathered in a second-rank tensor which we denote as $\underline{\underline{\mathbf{C}}}$, with the usual Voigt convention, i.e., C_{11} for

C_{1111}, etc...

Symmetries about all three planes of coordinates and isotropy within the transverse plane (2,3) require some moduli to coincide, as already written in (5.4) (e.g., $C_{66} = C_{55}$), others to vanish (e.g., $C_{14} = 0$), and the following relation to hold:

$$C_{22} - C_{23} = 2C_{44}. \tag{5.5}$$

(5.5) expresses the identity of shear response along all directions within the transverse plane.

To obtain $\underline{\underline{C}}$ from the numerical data, one may solve linear system (5.3) with appropriate values for the right-hand side load vector, e.g., setting all its coordinates to zero except for one component of $\Delta\underline{\sigma}$. This yields one line of the inverse of tensor $\underline{\underline{C}}$. One may also directly determine the elements of $\underline{\underline{C}}$ on imposing appropriate values of $\underline{\varepsilon}$, rather than imposing $\Delta\underline{\sigma}$. To do so, one exploits the block structure of matrix $\underline{\underline{K}}$, writing

$$\underline{\underline{K}} = \begin{bmatrix} \tilde{\underline{\underline{K}}} & {}^T\underline{\underline{L}} \\ \underline{\underline{L}} & \underline{\underline{k}} \end{bmatrix}, \tag{5.6}$$

with a $6N{\times}6N$ matrix $\tilde{\underline{\underline{K}}}$ associated to particle displacements and rotations, a $6{\times}6$ matrix $\underline{\underline{k}}$ associated with global degrees of freedom, while the nondiagonal block, $\underline{\underline{L}}$, of dimension $6{\times}6N$, couples stresses to grain displacements and rotations. Stress increments are related to imposed strains as

$$\Delta\underline{\sigma} = \underline{\underline{L}} \cdot \tilde{U} + \underline{\underline{k}} \cdot \underline{\varepsilon},$$

with $\tilde{U}$ satisfying

$$\tilde{\underline{\underline{K}}} \cdot \tilde{U} = - {}^T\underline{\underline{L}} \cdot \underline{\varepsilon},$$

so that the measured elastic moduli are given by

$$\underline{\underline{C}} = \underline{\underline{k}} - \underline{\underline{L}} \cdot \tilde{\underline{\underline{K}}}^{-1} \cdot {}^T\underline{\underline{L}}. \tag{5.7}$$

Both methods yield the same results within numerical accuracy.

It should be recalled that the very existence of an elastic response involving symmetric matrix $\underline{\underline{K}}$ requires several approximation steps, which are discussed, e.g., in Ref. [Agnolin and Roux, 2007c]. The present chapter deals with elastic moduli as identified through the stiffness matrix approach. In Chap. 4, it was explicitly checked that this expresses the material response to small stress increments about well equilibrated configurations with very good accuracy. A dynamical simulation with all ingredients of intergranular interactions produces, for small stress increments and small strains, yields the same results as the elastic stiffness matrix approach.

Averaged formula of contact stiffness

Elastic moduli, expressing the macroscopic stiffness of a spring network, should tend to vary proportionally to the density of contacts and to the average contact stiffness. The density of contacts can be conveniently written as

$$\frac{N_c}{\Omega} = \frac{3z\Phi}{\pi\langle D^3\rangle}.$$ (5.8)

The average stiffness, as written previously in the isotropic, monodisperse case of Ref. [Agnolin and Roux, 2007c], can be related to the average normal contact force $\langle F_N\rangle$. Assuming no correlation between forces and grain diameters, $\langle F_N\rangle$ relates to the average pressure $P = \text{tr}\underline{\underline{\sigma}}/3$ as

$$\langle F_N\rangle = \frac{\pi P\langle D^3\rangle}{z\Phi\langle D\rangle}.$$ (5.9)

From (5.9) and (4.3), the average normal stiffness is giving as (still overlooking correlations between forces and radii)

$$\langle K_N\rangle = \frac{\pi^{1/3}Z(1/3)}{2(z\Phi)^{1/3}} \frac{\langle D^3\rangle^{1/3}\langle\tilde{d}^{1/3}\rangle}{\langle D\rangle^{1/3}} \tilde{E}^{2/3}P^{1/3},$$ (5.10)

where we introduce the notation $\tilde{d}$ for d_{ij} as outlined in (4.2) and define

$$Z(1/3) = \frac{\langle F_N^{1/3}\rangle}{\langle F_N\rangle^{1/3}}.$$ (5.11)

The small level of polydispersity implies that all characteristic diameters are close to the average $\langle D\rangle = \frac{2D_1 D_2}{D_1+D_2}$: thus $\langle D^3\rangle^{1/3} \simeq 1.003 \times \langle D\rangle$, while $\langle\tilde{d}^{1/3}\rangle \simeq 1.0006 \times \langle D\rangle^{1/3}$. The ratio $Z(1/3)$, which is a characteristic of the force distribution, varies little between samples and along the loading paths, remaining between 0.92 and 0.945. We directly checked that prediction (5.10) is correct to within 1%.

One expects a dependence of moduli on $z\Phi$, which might, in a naive approach assuming proportionality to the contact density, be proportional to $(z\Phi)^{2/3}$ [Khidas and Jia, 2010]; and a variation with stress as a power law, as $P^{1/3} \propto \sigma_1^{1/3}(1 + 2K_0)^{1/3}$. Since z varies more (from nearly 4 to about 6.2 between different states and according to the stress level) than Φ (confined between 0.58 and 0.65), one should observe, like in the isotropic systems studied in Refs. [Agnolin and Roux, 2007c, Magnanimo et al., 2008], that macroscopic moduli classify the different granular packings by their coordination rather than their density.

Anisotropy should influence the tensor of elastic moduli both through contact orientations – the geometry of the elastic network is not isotropic, with more bonds oriented nearly parallel to axial direction 1 than near the transverse plane – and through contact stiffnesses – the bonds being oriented near the axial direction bear larger forces and, due to formula 4.3, are consequently stiffer. To a large extent, these effects are respectively encoded in coefficients $\tilde{c}_2$ and $\tilde{f}_2$. Unlike the stress ratio

K_0, which is directly related to fabric and angular force distribution, whence relation 4.17, elastic moduli are not expressed by such explicit formulae, and we thus have to correlate them to anisotropy parameters. We also test, in Sec. 5.5, the performance of approximate expressions predicting the moduli, which could be used to directly relate them to anisotropy parameters, if sufficiently accurate.

Our study covers a rather wide variety of equilibrium states, in which the coordination number varies from 4 to 6, stress ratio K_0 from 0.5 to 1.6 and $\tilde{c}_2$ reaches 0.08. This should ease comparisons with laboratory observations, as experimentally probed material states are likely to fall within the range of numerically investigated ones. This should also provide more stringent tests to theoretical attempts at predicting some of the elastic properties of spherical bead packs [La Ragione and Magnanimo, 2012a, La Ragione and Magnanimo, 2012b].

5.3   Elastic moduli

Representativity and symmetry.

For each of the six system types and each value of axial stress σ_1, results are averaged over the 3 statistically similar samples of 4000 spherical grains obtained with the preparation and oedometric compression procedures described in Chap. 4. Sample-to-sample differences are typically of order 5 % for poorly coordinated systems, in which fluctuations tend to be he largest, and decrease to 1 % for large coordination numbers.

The full 6×6 matrix $\underline{\mathbf{C}}$ as defined by (5.4) is obtained, line by line, using relation 5.7 and imposing independently the value of each one of the six coordinates of $\underline{\varepsilon}$, while setting the others to zero. The 6×6 matrix is exactly symmetric (within numerical precision).

The *material symmetries*, i.e., transverse isotropy, imposing the matrix to depend on 5 independent coefficients as written in Eqs. 5.4–5.5 (with, e.g., $C_{14} = 0$, $C_{33} = C_{22}$, etc.) are satisfied to the extent that the sample set is statistically representative. In our case, we observe that relative differences between coefficients that should be equal (such as C_{55} and C_{66}) do not exceed 2–3% in the worst cases (those, again, of low coordination systems).

To improve the accuracy and representative nature of the results, averages are taken over all equivalent moduli or moduli combinations: thus C_{66} is dealt with as an independent measurement of C_{55}, and C_{13} as another measurement of C_{12}.

Stress dependence

Longitudinal moduli

The dependence of the longitudinal moduli C_{11} and C_{22} on the axial stress σ_1 in oedometric loading (leaving aside, for now, the moduli observed in the decreasing axial stress branch of the cycle) are shown in Fig. 5.1 for all 6 studied systems, on doubly logarithmic plots. As observed previously in isotropic systems [Agnolin and Roux, 2007c], moduli are systematically larger in better coordinated systems, and increase with confining stress σ_1, roughly as a power law, with an exponent slightly
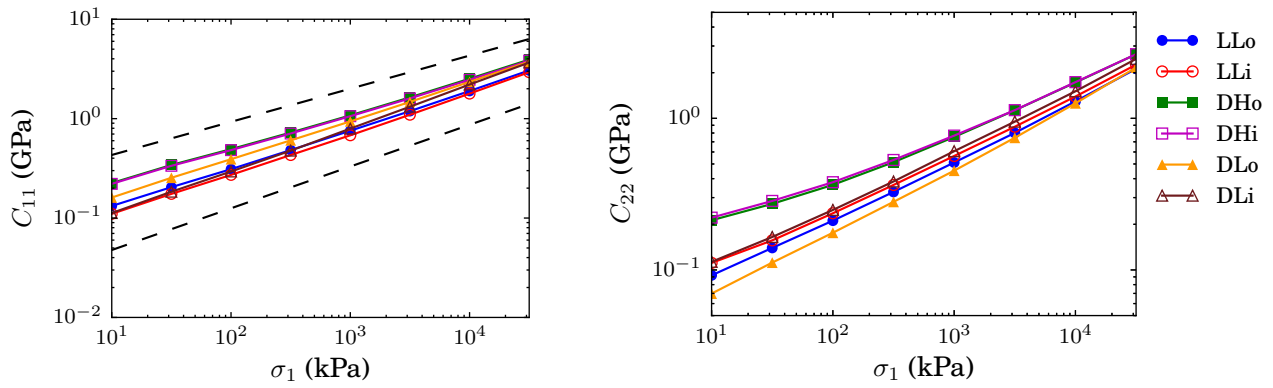
Figure 5.1: Longitudinal moduli: (left) C_{11} and (right) C_{22} versus σ_1 in systems DHo, DLo, LLo, DHi, DLi, and LLi. Dashed lines in plot (left) have slopes 1/3 and 0.42.

larger than the value 1/3 that results from a naive averaging of the Hertz law. A fit of the C_{11} data by a power law,

$$C_{11} \propto \sigma_1^{\alpha_1} \tag{5.12}$$

yield exponents α_1, in range 0.4-0.46, depending on the system and, actually, on the stress range over which the power law is identified (there is no reason to expect an exact power law over the wide σ_1 range investigated here). The observation of an exponent $\alpha > 1/3$ is, in part, due to the increase of coordination number under compression, as new contacts are created between approaching grains. Thus, Fig. 5.1 shows that the moduli increase faster in systems DLo and DLi, in which the large density and the low initial coordination number entail the most significant increase in z, from nearly 4 to about 5.5 in the compression to the largest σ_1 value. In Fig. 5.1(left) the slope, on the logarithmic plot, of the C_{11} versus σ_1 in DHi and DHo systems appears to decrease in some interval (comprising the first 4 or 5 data points), which is to be related to the slight *decrease* of the coordination number in that range (see Chap. 4). Plots of C_{22} (Fig. 5.1(right)) are farther from straight lines on the logarithmic scale, but a plot versus $\sigma_2 = K_0\sigma_1$ (Fig. 5.2) shows that C_{22} is slightly better represented as a power law of lateral stress σ_2:

$$C_{22} \propto \sigma_2^{\alpha_2} \tag{5.13}$$

 This scaling of longitudinal moduli (or of longitudinal elastic wave velocities) along principal stress directions with the stress component in the same direction is reported in experimental studies on sands and spherical bead packs [Hoque and Tatsuoka, 1998, Khidas and Jia, 2010].

Shear moduli

Shear moduli, as shown in Fig. 5.3, exhibit similar stress dependences, approximately varying as power laws of σ_1, with exponents somewhat larger than 1/3, approaching 1/2 in low coordination
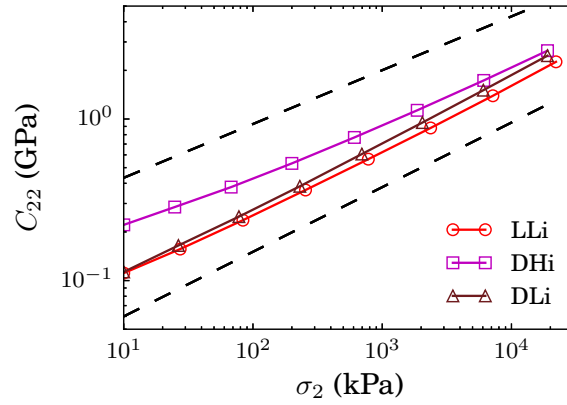
Figure 5.2: C_{22}, in DHi, DLi and LLi systems (same data as in Fig. 5.1(right)) versus σ_2. Straight line slopes are 1/3 and 0.4.
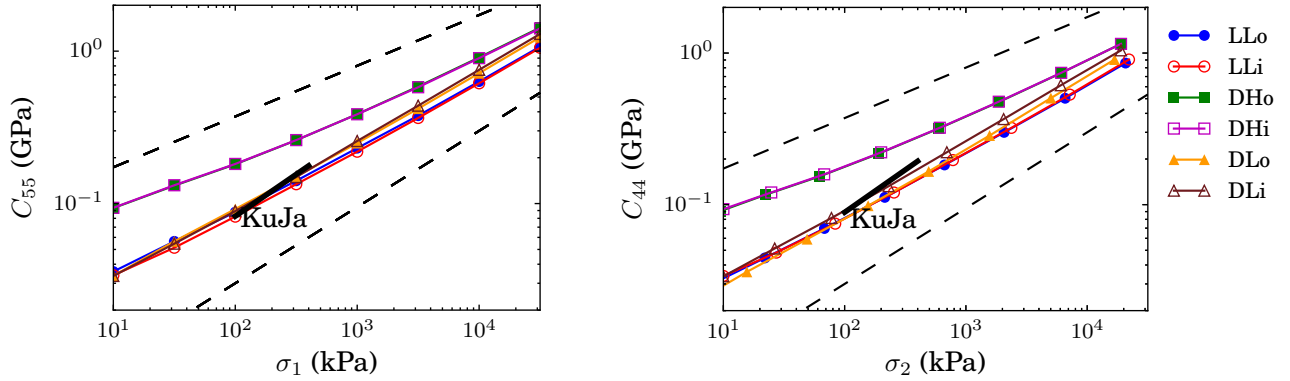
Figure 5.3: Shear moduli: (left) C_{55} versus σ_1 and (right) C_{44} versus σ_2. In both graphs upper and lower straight lines have slopes 1/3 and 1/2. Comparison with experimental data of Kuwano and Jardine [Kuwano and Jardine, 2002] (shown as thick straight lines marked "KuJa") to be discussed in Sec. 5.4.

systems. According to the literature on sands [Duttine et al., 2007], it could be more appropriate to express C_{44}, the shear modulus in the transverse plane, as a power law function of σ_2, the isotropic stress in this plane, while C_{55}, associated to shear within planes containing the axial direction, should scale as a power of $\sqrt{\sigma_1 \sigma_2}$. While our data, for which stress components do not vary independently, do not enable accurate tests of those predictions, a plot of shear modulus C_{44} versus σ_2, on a doubly logarithmic scale, does appear straighter than versus σ_1.

Off-diagonal moduli

C_{12} and C_{23}, coupling stresses in one direction to normal strains in orthogonal directions, vary with σ_1 somewhat similarly to diagonal elements of the elastic tensor, as shown in Fig. 5.4. However, it should be noted that those moduli, opposite to diagonal terms of tensor $\underline{\underline{C}}$, tend to be *smaller* in

Figure 5.4: Modulus C_{12} versus σ_1. Dashed line has slope $1/3$.

systems with large coordination numbers, and that their growth with axial stress is *slower* than power law $\sigma_1^{1/3}$.

Anisotropy of elastic moduli

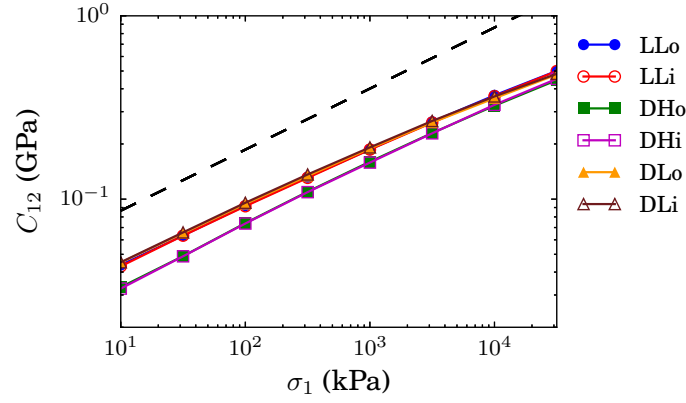The data of Fig. 5.1 also reveal the effects of anisotropy in the moduli: at low σ_1, close to the initial states, C_{22} is smaller for DLo than for DLi, while C_{11} is larger. DLo and DLi have very nearly the same density and coordination number. They differ by their fabric and stress anisotropy, initially absent for DLi. Anisotropy makes DLo-type samples stiffer in direction 1, hence a larger C_{11} than in isotropic systems DLi, while the depleted population of contacts oriented in the transverse directions, as well as their smaller stiffness entail smaller C_{22} values. Similar differences are visible between LLo and LLi. Fig. 5.5 shows that the ratio of longitudinal moduli in the axial and in transversal directions reaches values larger than 2 in DLo states and about 1.4 in LLo ones, while it increases from 1 in initially isotropic systems as elastic anisotropy reflects the growing stress and microstructural anisotropies. Anisotropy is also reflected by the shear moduli, which are larger when the shear plane contains the major principal stress direction 1 thus ratio C_{55}/C_{44} is larger in more anisotropic systems, reaching nearly 1.6 in the DLo sample series, and about 1.25 for LLo systems, as shown in Fig. 5.6, with values in initially isotropic packings following a similar trend as for the longitudinal moduli (Fig. 5.5).

Remarkably, some moduli are not sensitive to stress and fabric anisotropy. This is the case for shear modulus C_{55}, shown in Fig. 5.3, as well as modulus C_{12}, plotted in Fig. 5.4 (but C_{44} and C_{23} do exhibit anisotropy effects). The bulk modulus, expressing the response of average stress P to the volumetric strain of an isotropic strain tensor, $\underline{\underline{\varepsilon}} = \dfrac{\delta}{3}\underline{\underline{\mathbf{1}}}$, as $\Delta P = B\delta$, is given by

$$B = \frac{C_{11} + 2C_{22} + 4C_{12} + 2C_{23}}{9}. \tag{5.14}$$

A plot of B versus average pressure $P = (\sigma_1 + 2\sigma_2)/3$ does not distinguish material states accord-
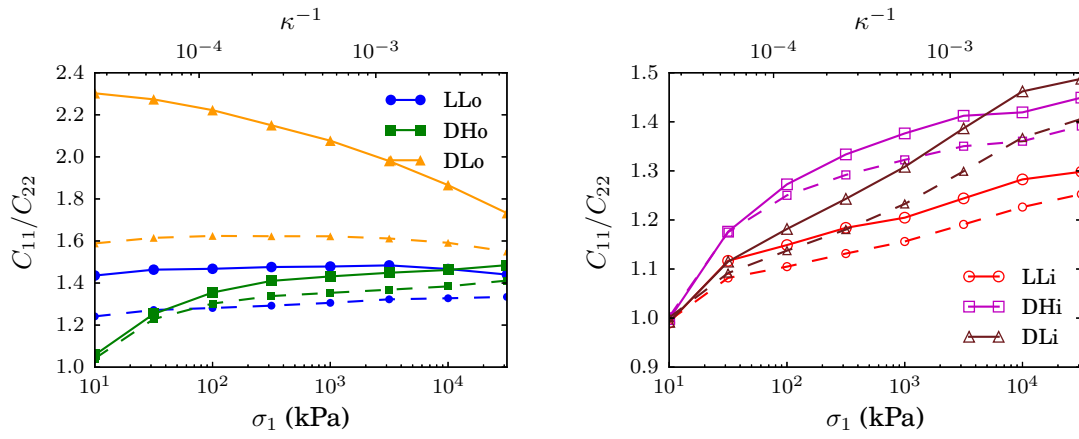
Figure 5.5: C_{11}/C_{22} versus σ_1 or κ^{-1} in initially anisotropic (left) or isotropic (right) sample series. Dashed lines depict the prediction of the Voigt approximation to be discussed in Sec. 5.5.

ing to their anisotropy. As shown in Fig. 5.7, it simply distinguishes large (DHi, DHo) from small (DLi, DLo, LLi, LLo) coordination numbers. Accordingly, data corresponding to isotropic compressions [Agnolin and Roux, 2007c], very nearly coincide with the present oedometric compression results.

5.4   Comparisons with experimental and numerical literature

The six different system series subjected to oedometric compression were chosen with the objective of exploring a rather wide variety of initial states, with large differences in density, coordination number and anisotropy. This should ease comparisons with different available experimental and numerical results, and enable tests of existing theoretical models or empirical descriptions of stress and internal state dependences of anisotropic elastic tensors. Theoretical attempts to relate moduli to microscopic state variables are tested in Sec.5.5. The present section first confronts our results to available numerical and experimental data.

Experiments on sands

Most experiments carried out on granular materials in geomechanics laboratories use devices in which stresses, rather than strains, are imposed. Thus, in the classical triaxial compression test, σ_1 and ε_1 are slowly increased, while lateral stress $\sigma_2 = \sigma_3$ is maintained constant (as opposed to strains $\varepsilon_2 = \varepsilon_3 = 0$ in oedometric compression), and lateral strain $\varepsilon_2 = \varepsilon_3$ is measured.

Consequently, quasistatic measurements of small strains provide direct access to the tensor of elastic compliances, the inverse of the tensor of elastic moduli, $\underline{\underline{M}} = \underline{\underline{C}}^{-1}$. Denoting as $\underline{\underline{\tilde{C}}}$ and $\underline{\underline{\tilde{M}}}$ the upper left blocks, of dimension 3×3, in $\underline{\underline{C}}$ and $\underline{\underline{M}}$, the corresponding compliances are usually written
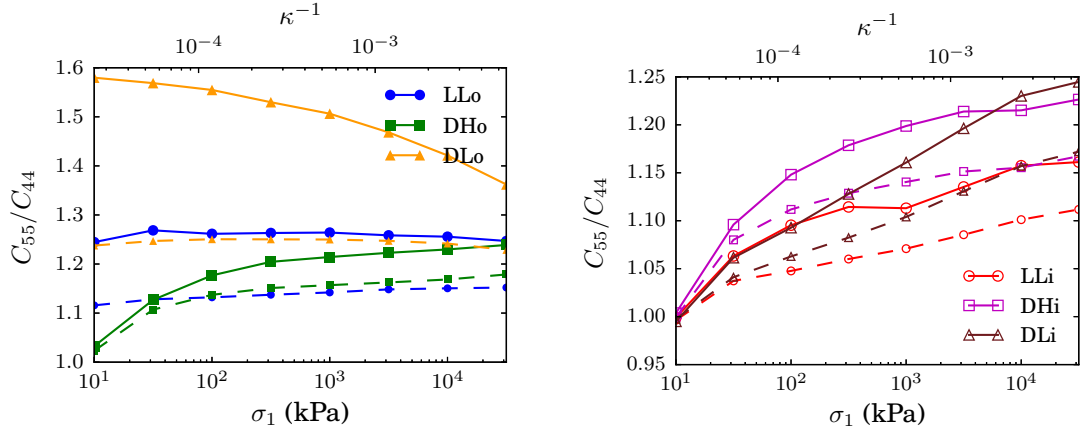
Figure 5.6: C_{55}/C_{44} versus σ_1 or κ^{-1} in initially anisotropic (left) or isotropic (right) sample series. Dashed lines: Voigt approximation (Sec. 5.5).
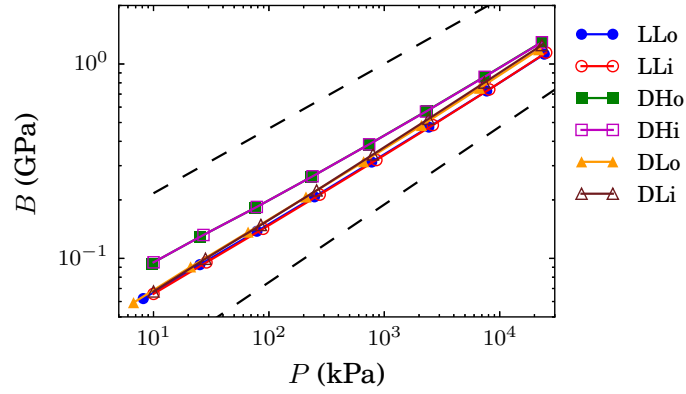
Figure 5.7: Bulk modulus B versus average stress P. Dashed line slopes: 1/3 (top) and 0.4 (bottom).

in terms of Young moduli E_1, E_2 and Poisson ratios ν_{12}, ν_{23} as

$$\underline{\underline{\tilde{\mathbf{M}}}} = \begin{bmatrix} \dfrac{1}{E_1} & \dfrac{-\nu_{12}}{E_1} & \dfrac{-\nu_{12}}{E_1} \\ \dfrac{-\nu_{12}}{E_1} & \dfrac{1}{E_2} & \dfrac{-\nu_{23}}{E_2} \\ \dfrac{-\nu_{12}}{E_1} & \dfrac{-\nu_{23}}{E_2} & \dfrac{1}{E_2} \end{bmatrix} \tag{5.15}$$

Empirical formulae have been proposed to relate those compliances to material state and stresses [Duttine et al., 2007]. They often involve a certain function $f(e)$ of void ratio $e = -1 + 1/\Phi$ [Hardin and Blandford, 1989], in which the contact network properties are summed up. The correspondence between Young moduli and stress along the same direction was clearly established [Hoque and Tat-

suoka, 1998], and expressed as power laws with a single exponent, as

$$E_1 = f(e)\sigma_1^m \quad \text{independently of } \sigma_2;$$
$$E_2 = f(e)\sigma_2^m \quad \text{independently of } \sigma_1.$$

(5.16)

Note that experiments on sands usually record considerably larger elastic anisotropy under anisotropic stresses (E_1/E_2 reaching 2) implying that the sole effect of fabric anisotropy, as created by the assembling process in isotropically compressed packs, should be smaller (causing, typically, ratios E_1/E_2 between 0.9 and 1.1) [Ezaoui and di Benedetto, 2009]. Such pure fabric effects are ignored in simple relations (5.16).

A unique factor $f(e)$ ignores fabric anisotropy, and assumes that, for a given material, the contact network density is determined by the packing density, which is contradicted by the numerical observation of systems of equal density but different coordination numbers, in the present study as well as in previous numerical investigations of isotropic bead assemblies [Agnolin and Roux, 2007a, Magnanimo et al., 2008, Song et al., 2008].

Ref. [Duttine et al., 2007] proposes a 3-parameter fit of elastic tensors applicable to transversely isotropic granular systems, according to which the values of Poisson ratio ν_{23} should be stress independent, while ν_{12} should be proportional to $1 + K_o^m$. Poisson ratios ν_{12} and ν_{23} of all six numerical sample series of the present study, under oedometric compression, are shown in Fig. 5.8. Both ν_{12}
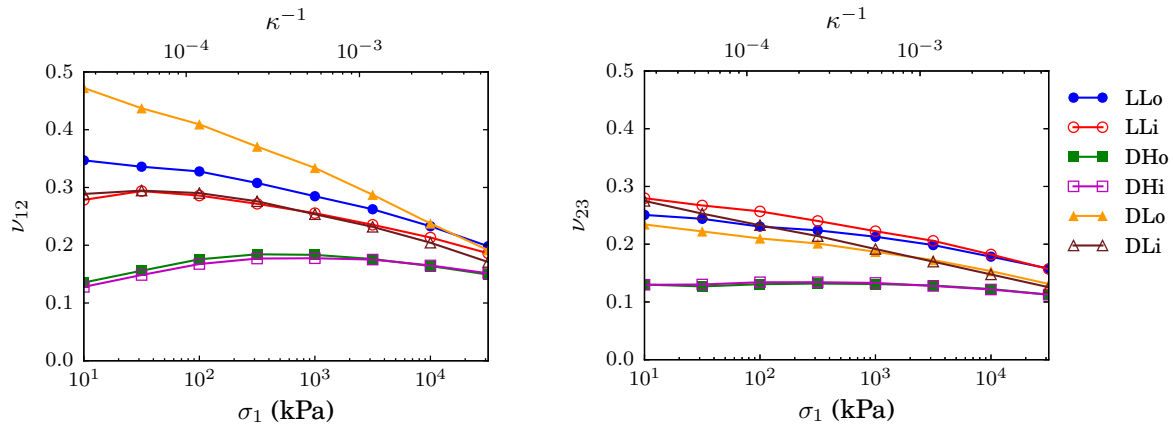
Figure 5.8: Poisson ratios (left) ν_{12} and (right) ν_{22} versus σ_1 or κ^{-1}.

and ν_{23} vary with σ_1 in the present numerical study, especially in poorly coordinated systems (as in the isotropic case [Agnolin and Roux, 2007c]), even in those systems (DLo, LLo) for which K_0 is approximately constant in oedometric compression. It should be recalled, though, that most experimental studies do not explore such a wide confining stress range as the present set of numerical results.

Experiments on bead packs

Young moduli E_1 and E_2, as obtained in our numerical simulations, expressing response to uniaxial *stress* variations in direction 1 or in the transverse plane, exhibit axial stress dependence along the oedometric loading path quite similar to those of longitudinal moduli. They can be directly confronted to the measurements published by Kuwano and Jardine [Kuwano and Jardine, 2002] on glass bead samples: see Fig. 5.9. Those authors report results of of bead samples initially assembled in rather loose ($\Phi \simeq 0.59$), anisotropic states, under isotropic pressures ranging from $P = 100$ to $P = 400$ kPa. While the loading history is different, similar trends are to be expected, from relation (5.16). Fur-
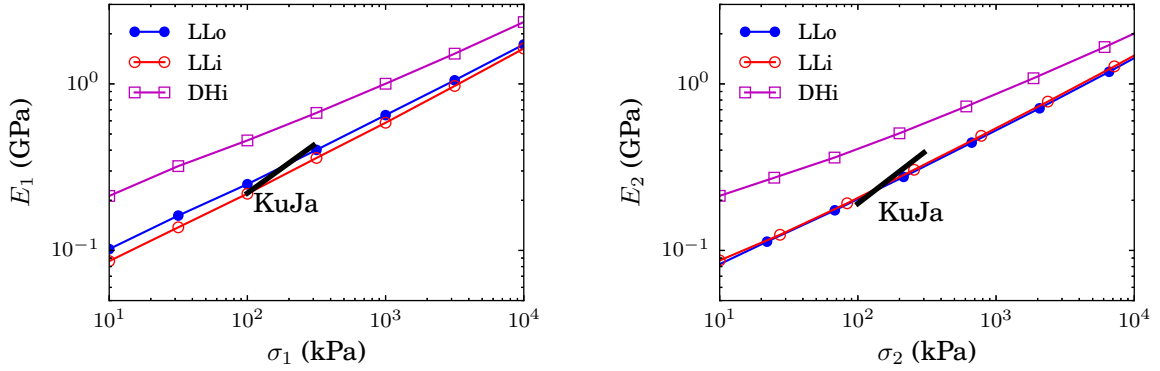
Figure 5.9: Young moduli: (left) E_1 versus σ_1, and (right) E_2 versus σ_2. Results of Ref. [Kuwano and Jardine, 2002] are shown as thick lines marked "KuJa".

thermore, our results (anticipating on Sec. 5.5) indicate that *fabric* anisotropy, which is present in those experimental results, is the most important source of elastic anisotropy in our range of states and parameters.

Fig. 5.9 shows good agreement between those experimental results and the numerical ones obtained in loose systems (or, more precisely, in poorly coordinated systems, which all share similar values of moduli), as regards the absolute values of Young moduli in the available stress range. Both data sets also show a power law increase of moduli with stress, as in (5.16), with some exponent m exceeding 1/3. The value of m fitted to the experimental points in [Kuwano and Jardine, 2002] (0.61 for E_1 and 0.64 for E_2) is however larger than the one observed in simulations (about 0.42). Ratios E_1/E_2 vary between 1.2 and 1.15 in those experiments, similar to their values in sample series LLi in the same stress range, while we observe values near 1.4 in sample series LLo (which would be more appropriate as a model for the experiment). As to shear moduli, as shown in Fig. 5.3, a good agreement is also to be noted between their values in poorly coordinated numerical systems and in the experiments of Kuwano and Jardine, although the experimental moduli also tend to increase a little faster with stress (with exponent 0.55, as opposed to slightly below 0.5 in simulations) and differ in terms of anisotropy ($C_{44} > C_{55}$ is reported in [Kuwano and Jardine, 2002], instead of the opposite inequality in the numerical results).

Another way to obtain elastic moduli is through ultrasonic (or seismic) waves. In a transversely

isotropic material, still denoting with index 1 the direction of the axis of rotational symmetry, longitudinal waves (or P waves) and transverse ones (or S waves) propagate in axial or in tranverse directions at velocities given by:

$$
V_P^{(1)} = \sqrt{\frac{C_{11}}{\rho^*}}; \qquad V_P^{(2)} = \sqrt{\frac{C_{22}}{\rho^*}}
$$
$$
V_S^{(1)} = \sqrt{\frac{C_{55}}{\rho^*}}; \qquad V_S^{(2)} = \sqrt{\frac{C_{44}}{\rho^*}}
$$

(5.17)

In (5.17), index P or S indicates the nature of the wave and index 1 or 2 its propagation direction, while ρ^* is the mass density of the granular material. Khidas and Jia [Khidas and Jia, 2010] measured all four velocities written in (5.17) in oedometrically compressed glass bead assemblies. They used two different modes of preparation, resulting in different densities, $\Phi \simeq 0.605$ and $\Phi \simeq 0.642$, and sound velocities were recorded for 100 kPa$\leq \sigma_1 \leq$ 900 kPa. In both states the stress dependence of sound velocities were fitted, for axial stresses between 300 and 900 kPa, as a power law with exponent 1/6, corresponding to moduli increasing as $\sigma_1^{1/3}$. Sound velocities corresponding to the numerical results of the present study can be obtained on using relations (5.17), with ρ^* deduced from the mass density of glass, $\rho \simeq 2.5 \times 10^{-3}$kg.m^{-3}, as $\rho^* = \rho\Phi(1 - x_0)$ (the rattlers do not belong to the elastic network in which waves are propagated). Comparisons between sound velocities obtained in numerical results and reported by Khidas and Jia are shown in Figs. 5.10 and 5.11.

Figure 5.10: (left) Velocity of longitudinal sound waves propagating in axial direction, V_P^1, normalized by $\sigma_1^{1/6}$, versus σ_1; and (right) velocity of longitudinal sound waves propagating in transverse directions, V_P^2, normalized by $\sigma_2^{1/6}$, versus σ_2. Results by Khidas and Jia [Khidas and Jia, 2010] are shown as thick lines marked "KhJi" for the two different experimental packings.

Obviously, those experimental results resemble the numerical ones obtained with highly coordinated states DHi or DHo, in two respects: the large value of wave velocities and the apparent proportionality to $\sigma_1^{1/3}$. In the other sample series, Fig. 5.10 and Fig. 5.11 (which only considers the looser laboratory samples, with the better quality power law fit) clearly show that a power law fit would yield a notably
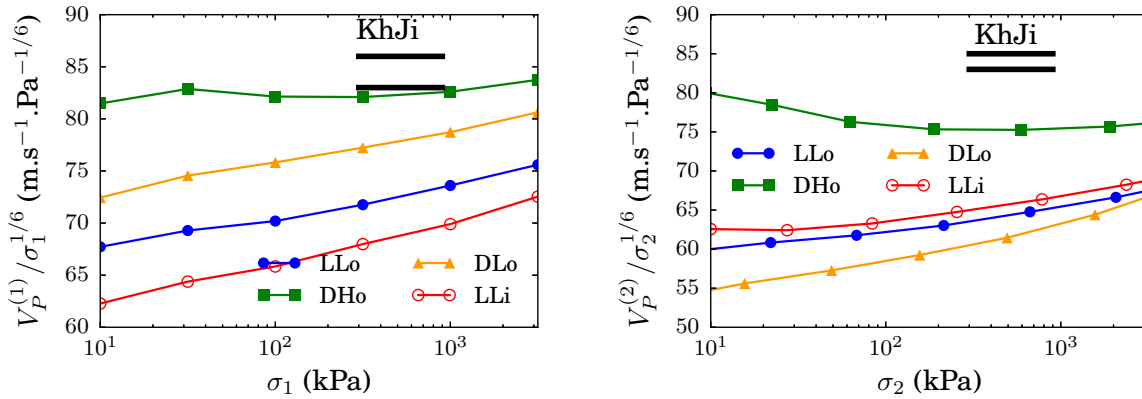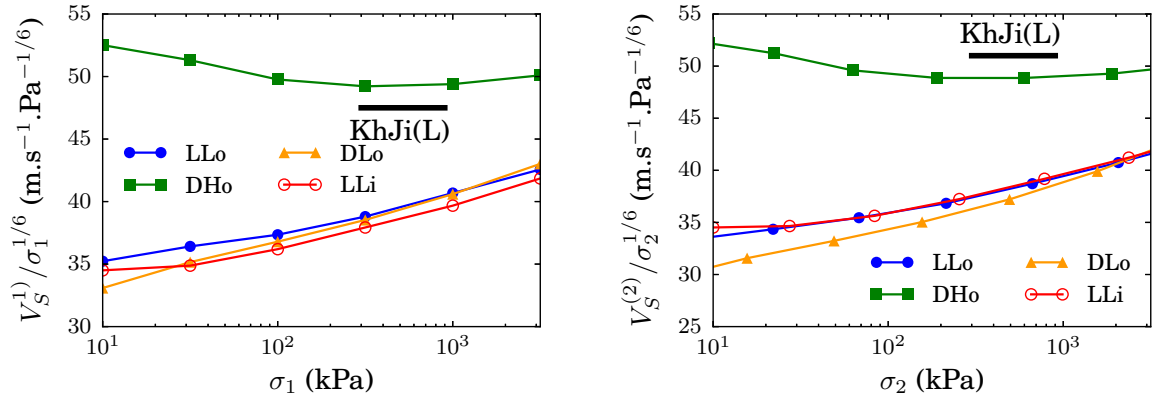
Figure 5.11: (left) Velocity of transverse sound waves propagating in axial direction, V_S^1, normalized by $\sigma_1^{1/6}$, versus σ_1; and (right) velocity of transverse sound waves propagating in transverse directions, V_S^2, normalized by $\sigma_2^{1/6}$, versus σ_2. Results by Khidas and Jia [Khidas and Jia, 2010] are shown as thick lines marked "KhJi(L)" for their looser type of packing.

larger exponent. The level of stiffness probed by the wave speed measurement in the looser state investigated by Khidas and Jia seems somewhat surprising. The discrepancy between numerical and experimental results could be due, in part, to the observed decrease of coordination number in DLi and DLo systems between the first equilibrium stress 10 kPa at assembling stage and the experimental stress range ~ 100 kPa. On directly compressing agitated grains (the initial granular gas) under larger σ_1, it is likely that slightly better coordinated contact networks could be observed above 100 kPa. Anyway, the comparison implies that granular samples with internal states similar to our dense, well coordinated numerical samples of types DH are observed in the laboratory. One may also note that the level of elastic anisotropy recorded in this experimental study, as expressed by ratios C_{11}/C_{22} (reaching up to 1.4 in denser systems, about 1.25 in looser ones) and C_{55}/C_{44} (with a maximum value near 1.15 for both sample types) are compatible with the numerical results on systems DHo for σ_1 in the same stress range, as shown in Figs. 5.5 and 5.6. Khidas and Jia mainly attribute the anisotropy of elastic properties to the anisotropy of stresses. The vertical to horizontal stress ratios measured in their experiments reach 2.5 in the looser investigated state, and exceeds 3.2 in the denser one – which seems very large in an an assembly of elastic-frictional beads. There are other questions arising in relating the results of Ref. [Khidas and Jia, 2010] to micromechanics, in particular in relation to the experimental control of the stress state. Some influence of the lateral walls on stress homogeneity might be suspected, given the aspect ratio of the samples, and the apparent influence of a prior stress cycle (up to 400 kPa) on the results. Furthermore, the transversely isotropic symmetry appears not exactly satisfied, since a significant difference is observed between shear moduli C_{55} and C_{66}. In view of those difficulties of interpretation of the experiments, we did not strive to improve the quantitative agreement with such laboratory results, which should be deemed already satisfactory for dense systems with large coordination numbers.

Numerical results on anisotropic bead packs

Our results should be compared to those obtained by La Ragione and Magnanimo, who carried out simulations on anisotropic glass bead assemblies and proposed some schemes to predict elastic anisotropy. One study [La Ragione and Magnanimo, 2012a] considers different systems prepared with anisotropic fabric, with a large density and coordination numbers varying from 4.9 to 5.6 (intermediate between DLo and DHo in this respect), under *isotropic* compression, keeping deviator stress to zero. Fabric anisotropy parameter $\tilde{c}_2$ stays constant as isotropic compression proceeds (from 50 to 500 kPa) and varies from sample to sample between a small value 0.02, while z varies from 4.9 to 5.6. In the second study [La Ragione and Magnanimo, 2012b] a dense system with isotropic fabric (corresponding to our DHi state) is subjected to triaxial compression up to a principal stress ratio of 1.4, and its elastic moduli recorded a different stages of growing stress deviator. Those two papers thus address separately either the influence of stress anisotropy, or that of fabric anisotropy, on elastic moduli. Our results from oedometric compression inevitably mix up both effects. However, we were able to cover a significantly wider range of state parameters (see Sec. 4.3). The main objective of Refs. [La Ragione and Magnanimo, 2012a, La Ragione and Magnanimo, 2012b] is to suggest the use of the Voigt approximation for microscopic strains and moduli to predict the anisotropy of moduli. Our numerical results enable a test of this approach in more demanding conditions than the ones explored by La Ragione and Jenkins. The performance of Voigt estimates is investigated in Sec. 5.5 below.

5.5   Elastic moduli and internal state variables

We now strive to establish relations between the anisotropic tensor of elastic moduli and the internal state variables characterizing granular samples under oedometric compression, first by testing available theoretical approaches (Sec. 5.5), then by resorting to simple "experimental" tests and correlations (Sec. 5.5).

Predictive schemes

Voigt approximation

The simplest estimate for the elastic moduli is the Voigt approximation, also referred to as "effective medium theory" (EMT), in which an affine field of particle displacements is assumed, as determined by the macroscopic strain [Walton, 1987, Makse et al., 1999, Jenkins et al., 2005, Agnolin and Roux, 2007c, Khidas and Jia, 2010]. This amounts to ignoring the non-affine contribution to displacements in Eq. 5.1, and discarding the second term in the right-hand-side of relation 5.7, writing, with the notation introduced in (5.6),

$$\underline{\underline{C}} = \underline{\underline{k}}. \tag{5.18}$$

To write the Voigt estimates (denoted with superscript V) for the 5 moduli of expression (5.4), we introduce notations $f_N = F_N/\langle F_N \rangle$ for the normal contact force divided by its average, $\alpha_T = K^T/K^N = (2 - 2\nu)/(2 - \nu)$ (see Eq. 4.4) for the ratio of tangential to normal contact stiffnesses, and $\tilde{D}$ for a certain averaged diameter such that (see Eq. 4.2)

$$\tilde{D}^{7/3} = \langle \frac{1}{4}(D_i + D_j)^2 d_{ij}^{1/3} \rangle. \tag{5.19}$$

With the chosen diameter distribution one has $\tilde{D} \simeq 1.23$. We also introduce a certain factor C_0, proportional to the contact density and to a typical normal contact stiffness:

$$C_0 = \frac{3^{4/3}}{2\pi^{2/3}} \frac{(z\Phi)^{2/3} \tilde{D}^{7/3}}{\langle D^3 \rangle^{2/3} \langle D \rangle^{1/3}} \tilde{E}^{2/3} P^{1/3}, \tag{5.20}$$

and define useful averages over all contacts, involving any coordinates α, β of unit normal vector $\mathbf{n}$:

$$\mathcal{A}_\alpha = \langle f_N^{1/3} n_\alpha^2 \rangle; \quad \mathcal{B}_{\alpha\beta} = \langle f_N^{1/3} n_\alpha^2 n_\beta^2 \rangle. \tag{5.21}$$

Voigt estimates of elastic moduli are then written as: (no summation over repeated indices)

$$C_{\alpha\alpha} = C_0 \left[(1 - \alpha_T)\mathcal{B}_{\alpha\alpha} + \alpha_T \mathcal{A}_\alpha \right] \quad (1 \leq \alpha \leq 3) \tag{5.22}$$

$$C_{\alpha\beta} = C_0(1 - \alpha_T)\mathcal{B}_{\alpha\beta} \quad (1 \leq \alpha < \beta \leq 3) \tag{5.23}$$

$$C_{44} = C_0 \left[(1 - \alpha_T)\mathcal{B}_{23} + \frac{1}{2}\alpha_T \mathcal{A}_3 \right] \tag{5.24}$$

Beyond the simplest form of Voigt approximation, estimates of moduli should be improved [Jenkins and La Ragione, 2001, Gay and da Silveira, 2004, Agnolin and Roux, 2007c] on imposing a suitably chosen common spin to all particles. This spin vanishes whenever the strain tensor commutes with the fabric tensor $\underline{\mathbf{F}}$ (defined by $F_{\alpha\beta} = \langle n_\alpha n_\beta \rangle$). In the present case this spin effect is only present for shear modulus C_{55}, and results in a modified formula

$$C_{55} = C_0 \left[(1 - \alpha_T)\mathcal{B}_{12} + \alpha_T \frac{\mathcal{A}_1 \mathcal{A}_2}{\mathcal{A}_1 + \mathcal{A}_2} \right] \tag{5.25}$$

These expressions of estimated moduli rely on decoupling averages over diameters on the one hand, and over forces and fabric (which remain coupled), on the other hand. For formula (5.10), we could check that this does not entail any significant loss of accuracy. However, one should avoid decoupling averages written in (5.21), as forces and fabric are correlated: contacts oriented near the axial direction are more numerous, and also tend to carry larger forces, whence the inequality

$$\langle f_N^{1/3} n_\alpha^2 \rangle > \langle f_N^{1/3} \rangle \langle n_\alpha^2 \rangle, \tag{5.26}$$

for which we could check the members to differ typically by 10 to 20%. Assuming equality in (5.26) and decoupling averages in (5.21) accordingly would reduce the values of estimated moduli, and thus accidentally improve the predictions of longitudinal and shear moduli, which are too large – an

improvement based on a fortuitous compensation of errors.

A more accurate treatment of averages defined by (5.21) is possible in terms of expansions of angular distributions of contacts and of $f_N^{1/3}$ in Legendre polynomials, leading to some formula for Voigt-estimated moduli, analogous to expression (4.17) of stress ratio K_0. We did not however, deem such a treatment justified, given the poor accuracy of the Voigt scheme to estimate moduli.

As noted in a number of previous studies [Makse et al., 1999, Agnolin and Roux, 2007c, La Ragione and Magnanimo, 2012a] the Voigt approximation is quite inaccurate, and largely overestimates, in particular, shear moduli. It fails particularly badly in poorly coordinated systems, in which the fluctuating (or "non-affine") part of the displacement field contributes the most. This correlation between the inaccuracy of the Voigt estimates and the coordination number is made very conspicuous in plots of ratios of estimates to true moduli shown in Fig. 5.12. Only in well coordinated systems, due to a
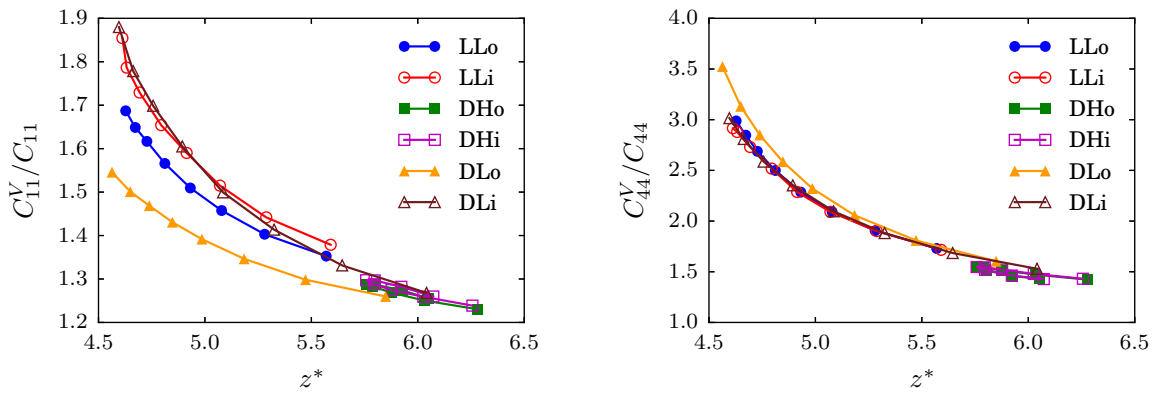
Figure 5.12: Ratios of Voigt estimates to true moduli C_{11} (left) and C_{44} (right) versus rattler-corrected coordination number z^*.

specific preparation (for DHi and DHo) or to the effect of a large stress in a dense sample (as in DLo, DLi), is the prediction of longitudinal moduli, shown in Fig. 5.12(left), reasonably accurate. As to shear moduli, Fig. 5.12(right) makes it clear that they are always severely overestimated.

Another basic inadequacy of the Voigt scheme is its poor treatment of moduli C_{12} and C_{23} coupling normal stresses and strains along different axes. In view of expression (5.23), proportional to $1 - \alpha_T$, estimates C_{12}^V and C_{23}^V are considerably too small, which, correlatively, leads to predictions of Poisson ratios below 0.05, much smaller than their true values shown in Fig. 5.8. Unlike individual elements of matrix $\underline{\underline{C}}$, the Voigt estimate of the bulk modulus, as defined in Eq. 5.14, proves surprisingly accurate. Just as in isotropic bead packs [Agnolin and Roux, 2007c], the Voigt estimate B^V of the bulk modulus is in excess, but reasonably accurate (with ratios B^V/B between 1 and 1.15), in the present anisotropic systems in all sample series, as apparent in Fig. 5.13. This good performance of the Voigt prediction for B, given its expression (5.14), results form the underestimation of C_{12} and C_{23} compensating the overestimation of C_{11} and C_{22}. Note that, on combining Eqs. 5.14, written for

Figure 5.13: Ratio of Voigt estimate to measured value of bulk modulus in all sample series, versus σ_1, in oedometric compression.

Voigt estimates of moduli, and 5.21, a simpler expression of B^V emerges,

$$
\begin{aligned}
B^V &= \frac{C_0}{3} Z(1/3) \\
&= \frac{1}{2} \frac{\tilde{D}^{7/3} Z(1/3)}{\langle D^3 \rangle^{2/3} \langle D \rangle^{1/3}} \left(\frac{z \Phi \tilde{E}}{3\pi} \right)^{2/3} P^{1/3},
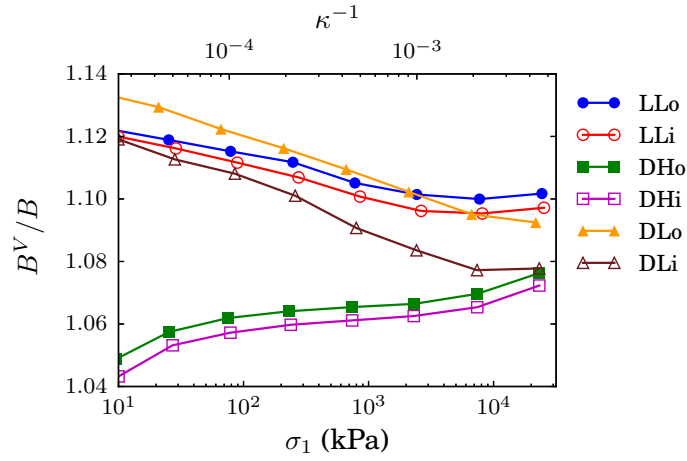\end{aligned}
\tag{5.27}
$$

which is independent of fabric anisotropy, and coincides (save for the slight polydispersity effect) with the estimate written in the isotropic, monodisperse case [Agnolin and Roux, 2007c]. The observation (see Fig. 5.7) that the variation of B with P is the same as in isotropically compressed systems, for which B^V is a good estimate of B, explains the success of the Voigt approximation for B in the present anisotropic ones.

While the Voigt scheme or EMT does not provide accurate predictions for elastic moduli values, it has been suggested by La Ragione and Magnanimo [La Ragione and Magnanimo, 2012a, La Ragione and Magnanimo, 2012b] that it could describe anisotropy effects. More precisely those authors concluded that EMT could satisfactorily predict the ratios of moduli between anisotropic systems and reference, isotropic ones. This would imply correct Voigt estimates of ratios C_{11}/C_{22} and C_{55}/C_{44}. Those ratios, though, as shown in Figs. 5.5 and 5.6, are only correctly predicted for longitudinal moduli in moderately anisotropic systems: samples of types DHi, DLi, LLi, and DHo, under moderate axial stress σ_1, before fabric and stress anisotropy increase due to oedometric compression. Likewise the Voigt approach is only reasonably accurate for ratio C_{55}/C_{44} as long as it does not exceed 1.1. Our results therefore contradict, in part, the conclusions of Refs. [La Ragione and Magnanimo, 2012a, La Ragione and Magnanimo, 2012b], which is likely due to our investigation of larger domains of state parameters, as noted in Sec. 5.4.

The reasons why the Voigt approach, although it naturally incorporates the influence of stress-dependent average contact stiffness and contact density, badly fails (except for B), particularly in

poorly coordinated systems, were discussed in Ref. [Agnolin and Roux, 2007c], and related to the properties of granular contact networks with small force indeterminacy. In particular the faster than predicted variations of shear moduli with stress, or, correlatively, the variations, faster than the expected $z^{2/3}$, of the ratio plotted in Fig. 5.12, were attributed to the tendency of moduli to vanish [Wyart, 2006] as the limit of vanishing force indeterminacy, occurring at $z^* = 4$ (with a small correction due to 2-coordinated grains), is approached. While the absence of force indeterminacy is spontaneously achieved for frictionless grain packs in the limit of large stiffness level κ [Roux, 2000, Silbert et al., 2002, O'Hern et al., 2003, Agnolin and Roux, 2007a], it is usually not closely approached in the presence of friction, except on setting the friction coefficient to infinity (or a very large value) [Zhang and Makse, 2005, Agnolin and Roux, 2007a]. However, anomalously low shear moduli are observed for the smallest z^* values [Somfai et al., 2007, Agnolin and Roux, 2007c], which increase faster than expected from Voigt estimates as compression entails small increase of coordination numbers. In the present study of anisotropic granular packs, similar trends are visible in Fig. 5.3, with a faster variation of shear moduli in poorly coordinated systems, and in Fig. 5.12, where the strong increase of C_{44}^V/C_{44} for decreasing z^* might signal an incipient divergence near $z^* = 4$. The only non-anomalous modulus is poorly coordinated systems with vanishing force indeterminacy is the one expressing the response to a stress increment proportional to the preexisting stress, whence a dominant eigenvalue in the elastic moduli tensor (which is equal to the bulk modulus in isotropic conditions). This is explicitly shown and exploited in Ref. [Peyneau and Roux, 2008b] for transversely isotropic assemblies of nearly rigid, frictionless beads. In such extreme situations of vanishing force indeterminacy, ratios of moduli C_{11}, C_{22}, C_{23}, C_{12} are all directly related to stress ratio K_0, which is not the case for our data in the least coordinated systems (as observed in). The larger values of off-diagonal elements C_{12}, C_{23} in those cases might be seen as the approach

Reuss approximation for a specific load increment

The particular compliance S_P expressing the material elastic response to a stress increment $\Delta\underline{\underline{\sigma}}$ proportional to $\underline{\underline{\sigma}}$, might be evaluated via the Reuss estimate, as defined in Refs. [Agnolin and Roux, 2007c, Peyneau and Roux, 2008b]. The Reuss approach is based on an evaluation (in excess) of the elastic energy written as a function of force increments. With $\Delta\underline{\underline{\sigma}} = \delta \times \underline{\underline{\sigma}}$, this elastic energy is given, at the global scale, by

$$\Delta W = \Omega \frac{S_P \delta^2}{2} \underline{\underline{\sigma}} : \underline{\underline{\sigma}}, \tag{5.28}$$

with, introducing principal stress ratio K_0 and compliance matrix elements:

$$S_P = \frac{1}{E_1} - \frac{4\nu_{12} K_0}{E_1} + \frac{2(1 - \nu_{23})K_0^2}{E_2}. \tag{5.29}$$

The Reuss estimate is based on trial force increments $\Delta \mathbf{F}_{ij} = \delta \mathbf{F}_{ij}$ in all contacts i-j, and reads [Agnolin and Roux, 2007c, Peyneau and Roux, 2008b]

$$S_P^R = 2 \left(\frac{3\pi}{z\Phi} \right)^{2/3} \frac{\langle D^3 \rangle^{2/3} \langle \hat{D}^{-1/3} \rangle}{\langle D \rangle^{5/3}} \frac{\tilde{Z}(5/3)}{\tilde{E}^{2/3} P^{1/3}} \tag{5.30}$$

Factor $\tilde{Z}(5/3)$ is defined from the force distribution and the friction mobilization as in [Agnolin and Roux, 2007c]:

$$\tilde{Z}(5/3) = \frac{\langle F_N^{5/3}(1 + \frac{r_T^2}{\alpha_T}) \rangle}{\langle F_N \rangle^{5/3}} \tag{5.31}$$

(r_T denoting, in each contact, the ratio $\|F_T\|/F_N$) and its values remain between 1.26 and 1.38 for the whole data set. In (5.30) we also introduced notation $\hat{D}^{-1/3}$ for the average of $d_{ij}^{-1/3}$. Compliance
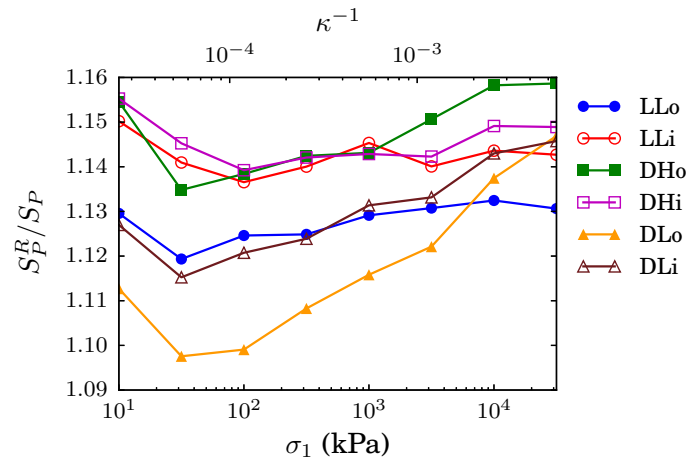
Figure 5.14: Ratio of Reuss estimate of proportional load increment compliance, defined in (5.29), to its measured value in all sample series, versus σ_1.

S_P is better approached by its estimate S_P^R for poorly coordinated systems, since with little force indeterminacy the trial force increments used in the Reuss approximation become closer to the real ones. Remarkably [Agnolin and Roux, 2007c], $(S_P^R)^{-1}$ and B^V (Eq. 5.27) only differ by factors of order 1, related to polydispersity and force distribution. The Reuss estimate of S_P is accurate with a relative error below 16%, as shown in Fig. 5.14. In isotropic systems ($K_0 = 1$), upper bound S_P^V to $S_P = 1/B$ provides a lower bound to bulk modulus: $B \geq 1/S_P^R$. For anisotropic systems, estimates B^V for B and S_P^R for S_P are in general the only available quantitatively accurate predictions.

More sophisticated estimation schemes, in which fluctuations about the main strain field are dealt with self-consistently, have been developed for isotropic packings [La Ragione and Jenkins, 2007] (and corresponding ideas, or generalizations thereof, tested by numerical means [Kruyt, 2014]) with some partial success for shear moduli in well-coordinated systems [Agnolin and Roux, 2007c].

Correlation of elastic, force and fabric anisotropies

For lack of available predictive schemes adequately relating elastic moduli to material state variables such as coordination number and fabric anisotropy over the range of material states explored in our study, we resort to systematic investigations of correlations between the anisotropy of elastic moduli and fabric and force anisotropy parameters $\tilde{c}_2$ and $\tilde{f}_2$ (see Eqs. (4.12) and (4.14)). In Hertz law, the contact stiffness depends on the normal force which makes the dependence of the elastic moduli coupled between force and fabric anisotropies. This coupling is visible in the averaged expressions provided by the EMT approximation (Eqs. (5.21) to (5.25)). In the case of linear contact law, the contact stiffness K_N^L is constant. Hence, the moduli are expected to depend only on the fabric anisotropy. As consequence of a constant contact stiffness, the approximations given by Eq. (5.22) become

$$C_{\alpha\alpha}^{LV} = C_0^{'} \left[(1 - \alpha_T)\mathcal{B}_{\alpha\alpha}^{'} + \alpha_T \mathcal{A}_{\alpha}^{'} \right] \quad (1 \le \alpha \le 3) \tag{5.32}$$

with

$$C_0^{'} = \frac{3z\Phi}{\pi\langle D^3\rangle}\langle D^2\rangle K_N^L \quad \text{and} \quad \mathcal{A}_{\alpha}^{'} = \langle n_{\alpha}^2\rangle; \quad \mathcal{B}_{\alpha\beta}^{'} = \langle n_{\alpha}^2 n_{\beta}^2\rangle. \tag{5.33}$$

By analogy, similar expression can be derived of the other elastic moduli.

    Eqs. (5.32) and (5.33) suggests comparing the evolution of $C_{\alpha\beta}^L/K_N^L$ as a function of $z\Phi$ to eliminate the influence of other parameters than fabric, and only observe the effect of the latter. Therefore, we define reduced moduli for both Hertzian and linear contacts cases by the expressions:

$$c_{\alpha\beta} = \frac{C_{\alpha\beta}\langle D\rangle}{\langle K_N\rangle} \quad \text{and} \quad c_{\alpha\beta}^L = \frac{C_{\alpha\beta}^L\langle D\rangle}{K_N^L}, \tag{5.34}$$

where we multiplied by $\langle D\rangle$ to provide an adimensional parameter.

    The longitudinal reduced moduli, regardless of the contact law, exhibit similar dependence with $z\Phi$ as shown by Fig. 5.15. Despite if computed with Hertzian or linear contacts, the effect of the structural anisotropy is clearly visible as the sample with higher anisotropy parameters shows the highest modulus c_{11}, and reversely, the lowest modulus c_{22}. This trend is conserved for the moduli c_{11}^L and c_{22}^L which might indicate that the effect of force anisotropy (expected to matter less in the linear contact case) is smaller compared to the fabric anisotropy influence.

    As stress increases during the compression, both $\tilde{f}_2$ and $\tilde{c}_2$ increase, unless for the DLo state (for which $\tilde{c}_2$ tends to decrease at highest stress levels) and for LLo where $\tilde{c}_2$ is almost constant. No effect of this inverted trend of $\tilde{c}_2$ was observed on the evolution of moduli neither for Hertzian nor linear case. In DLo state, contrary to K_0 which maintains constant as $\tilde{c}_2$ and $\tilde{f}_2$ exhibit inverted trends, the ratio C_{11}/C_{22} varies during the loading phase. We compare the variations of this ratio to $\tilde{c}_2$ and $\tilde{f}_2$ in Fig. 5.16. The difference between the highest and lowest values of $\tilde{c}_2$ are comparable during loading and unloading, while $\tilde{f}_2$ double its variation. In the other hand, the ratio C_{11}/C_{22} variation in unloading is almost half the loading variation, which is comparable to $\tilde{f}_2$ variation. Such observation may lead into thinking that the elastic anisotropy is more controlled by force anisotropy. However, the
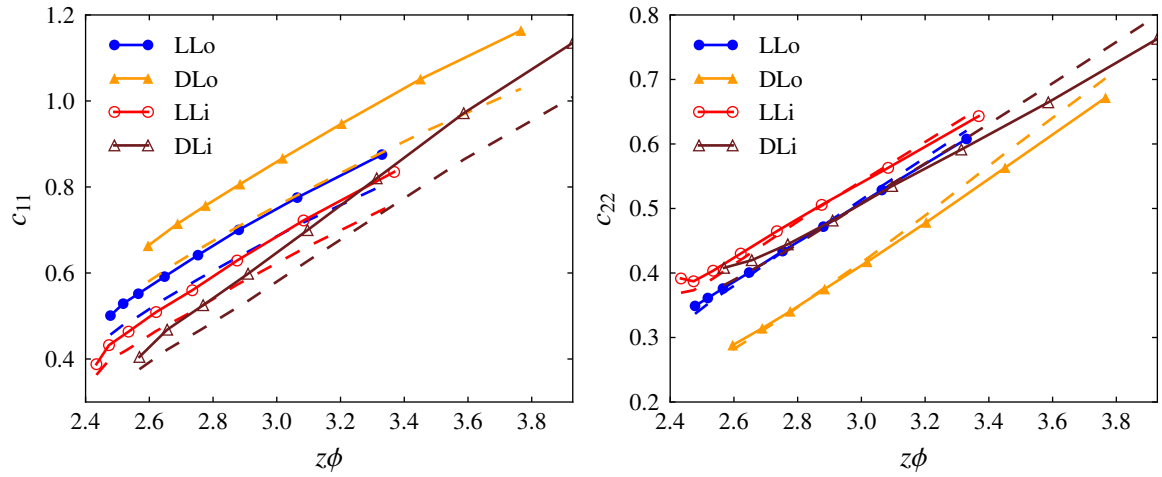
Figure 5.15: Evolution of the reduced moduli c_{11} and c_{22} with $z\Phi$. (left) Moduli computed with Hertz contacts, (right) moduli computed with linear contacts (c_{11}^{L} and c_{22}^{L}).

same analysis for LLo state shows that the ratio C_{11}/C_{22} is almost constant when $\tilde{c}_2$ is constant, while $\tilde{f}_2$ varies by the same order as in DLo state (about 0.04). Considering both cases, we tend to conclude that fabric anisotropy influences more the elastic anisotropy, but for high levels of anisotropy, in which the predominance of fabric anisotropy effect over the force anisotropy tends to decrease.

The statement that fabric anisotropy has more impact on elastic anisotropy is confirmed by the results of Fig. 5.17(left). Moduli from all different states during compression cycles are presented on this figure, where $\tilde{f}_2$ values are reported on vertical axis and $\tilde{c}_2$ on the horizontal one. The colors, giving the values of the ratio C_{11}/C_{22}, show a more clear gradient in the direction of $\tilde{c}_2$ variations than $\tilde{f}_2$, unless for the highest anisotropy states. Same observations are made for C_{44}/C_{55} as shown in Fig. 5.17(right).

5.6   Conclusions

Constructing the stiffness matrix of the equilibrated configurations obtained from oedometric compression of different initial states allows to measure the five independent elastic moduli of these transversely isotropic assemblies. First these elastic moduli were confronted to experimental data from literature, providing fairly good agreements. Thanks to the variety in the initial state structural parameters (density, coordination number, stress and fabric anisotropy), with the large domain of the applied stress variations, our results cover different experimental studies. In particular, the simulations reproduced the power law evolution of elastic and Young moduli, with exponents slightly different from those measured in experiments and was shown to agree with the model proposed by [Hoque and Tatsuoka, 1998]. However, it should be noted that the authors claim that the fitting parameters are only dependent of the void ratio, while simulations clearly show that the moduli are more dependent on coordination numbers than density. Results of moduli measured from experiments on
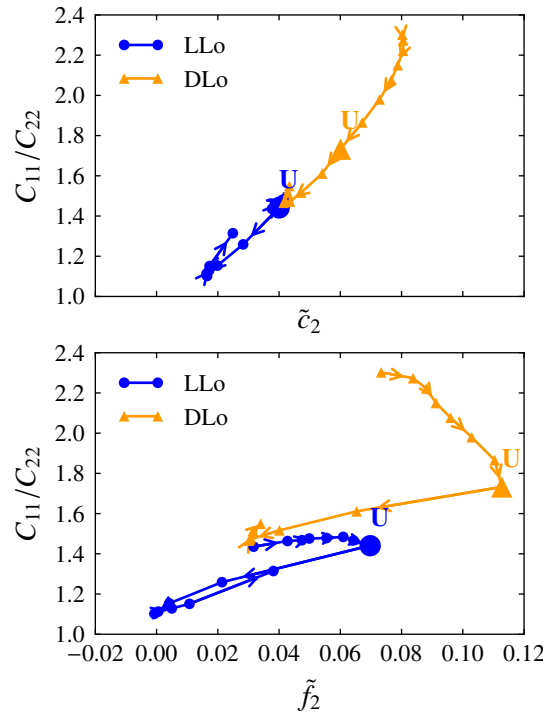
Figure 5.16: (top) Variations of the ratio C_{11}/C_{22} with $\tilde{c}_2$ and (bottom) $\tilde{f}_2$

glass beads using ultrasonic waves [Khidas and Jia, 2010] surprisingly showed agreement with the highly coordinated dense assemblies.

The moduli being confronted to data from real experiments on sand and beads assemblies, we attempted to correlate the measured moduli to structural parameters that are not accessible from experiments. Indeed, the moduli, if correlated to the micro-structure evolutions, can inversely provide information on the internal structure of specimen in real experiments. First, we investigate the performance of the classic voigt approximation to predict anisotropic moduli. In general, the prediction formulae are, as expected from previous studies, very poor estimates except for nearly isotropic or well coordinated states as well as dense configuration at high stress levels for longitudinal moduli. While moduli ratios are only accurately estimated for longitudinal moduli in mainly isotropic states. However, concerning the bulk modulus, accurate estimates are provided by both Voigt and Reuss approximations. This modulus was shown not to depend on the structure anisotropy and exhibits quite similar behavior to isotropic compression results.

The moduli was shown to depend, next to density and coordination number, on the fabric and force anisotropy. These anisotropies, as represented by the second order coefficients of Legendre polynomial expansions of force and contact distributions, have an important impact on the moduli at similar values of density and coordination number. Although investigations of moduli evolution with force and fabric anisotropies did not lead to explicit formulae, they clearly showed that the fabric anisotropy is the most determining root of elastic anisotropy.

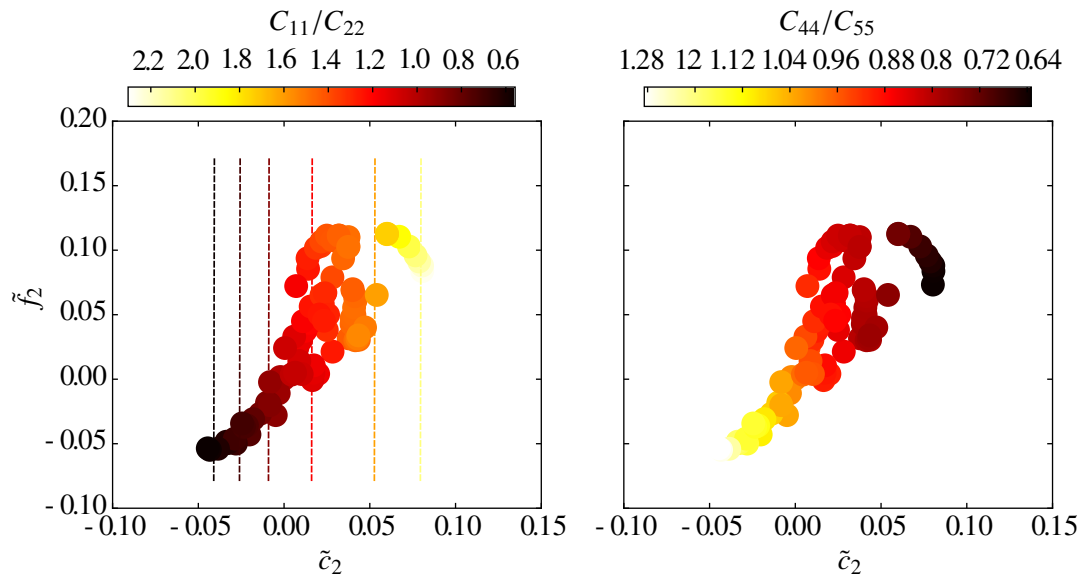Figure 5.17: (Left) Evolution of ratio C_{11}/C_{22} with $\tilde{c}_2$ and $\tilde{f}_2$. (Right) Evolution of ratio C_{44}/C_{55} with $\tilde{c}_2$ and $\tilde{f}_2$. The colors of dots give the values of the ratio with respect to the color map.

Conclusions and perspectives

Conclusions

The creep behavior observed in granular materials is still a widely unexplained phenomenon. The physical phenomena at its origin are suspected to govern the long term behavior of a wide class of civil engineering materials and geomaterials of practical interest, which motivates fundamental studies on this subject. It is expected that the detailed analysis of the microstructural evolution of granular materials at grain scale might provide new insights on this questions. This work aims to propose a framework combining experimental and numerical tools to study time-dependent, possibly fast phenomena such as creep.

The experimental part consists on combining microtomography with digital image correlation to measure the individual grains rigid body motions during experimental tests. However, for time-dependent behaviors such as creep, applying the classical correlation method to laboratory tomography in-situ experiments, would fail to catch the fast evolutions involved in the short-term behavior of creep. This is due to the fact that the acquisition of a tomographic image requires about one hour of scanning time, in usual laboratory conditions. In the early stages of creep, the sample might undergo significant evolutions during such a time laps, which would be impossible to capture. In the present thesis, we have proposed a new method named Discrete Digital Projection Correlation (D-DPC), which allows overcoming such limitation.

The method only requires a sparse sinogram (i.e. a small number of radiographic projections) of the deformed state, which is insufficient to carry out the full 3D reconstruction. Therefore, a model that generates digital projections from the reference reconstruction for any given set of grain rigid body motions was developed. The grain rigid body motions are then determined by minimizing the discrepancy between the generated digital projections and the acquired experimental projections of the deformed state.

Implementation details of the projection model are provided in this work. In particular, great concern was given to speeding up the computation of the digital projections, because it has a significant impact on the execution time of the minimization process. Algorithm-level and compile-level optimizations were considered next to parallelization.

In order to assess the performances of D-DPC, it was applied to an experiment where the displacements (global translation of the specimen) were priorly known. The results showed that the method

is capable of retrieving the grain displacements with only two projections with an accuracy of about 0.1 voxels for translations and 1° for rotations (comparable to the accuracy of earlier methodes making use of the full 3D images in the deformed state) Further assessments of the method errors were carried out. These assessments provided a quantification of the errors from different sources. An adequate model was developed to estimate the noise-induced errors. Other investigations of error sources showed that intrinsic errors might cause errors larger than the image noise-induced ones. Typically, errors in the order of 0.01 to 0.1 voxels in translations and 0.1° in rotation are to be expected. This analysis showed possible routes to overcome the current accuracy limitation of the proposed D-DPC method.

In a second part of the work, Discrete Elements Method (DEM) was used to numerically investigate the oedometric compression of a model material, consisting of an assembly of beads interacting by elastic and frictional forces. The study provided multiple results concerning the mechanical response and the evolution of the internal state during compression cycles. Though this DEM study does not directly address the microscopic origins of creep in granular materials, it provides a basis for the investigation of contact network instabilities and rearrangements that may originate the macroscopic creep if triggered by contact creep.

DEM simulations were used to investigate the macroscopic behavior of model granular materials under oedometric compression, in relation with the evolution of internal state variables. Moreover, this study provided correlations between the internal structural parameters, that are still difficult to measure on experiments, to macroscopic elastic moduli. Since the latter is being commonly measured in real experiments, these correlations constitute a qualitative assessment of the internal structure evolutions in experimental specimens.

In this study, simulations of quasi-static oedometric compression of glass bead assemblies (friction coefficient $\mu = 0.3$, Young modulus $E = 70$ GPa and Poisson ratio $v = 0.3$) were carried out. Different packing processes enabled the preparation of initial states varying in density, coordination number as well as force and fabric anisotropy. The assemblies were subjected to axial stresses ranging from 10 kPa to 31.6 MPa while still abiding by Hertz-Mindlin elastoplastic contact laws. The strain response in compression cycles was observed to be almost reversible unlike the reported behavior of sand in the literature. Such lack of irreversibility should be attributed to the absence of plasticity or damage in the contact model. Although the strain evolution is nearly reversible, the internal state of the material does evolve irreversibly. The irreversibility is observed in decreasing coordination numbers during compression cycles and in the variations of anisotropy. The coefficient K_0, representative of stress anisotropy, was not constant except for states which initially gain anisotropy at preparation phase. It was shown that the stress anisotropy could be accurately captured through simple statistical descriptors of the fabric and force distributions.

It was also shown that the response is anelastic, since the strains, predicted by elastic moduli measured along the compression cycle, showed important difference with actual strains. However, the elastic moduli accurately express the stress-strain behavior for small strain increments (about 10^{-5}) for which the anelastic contributions are negligible. Furthermore, it was shown that friction mobi-

lization has a more important impact on the anelastic response than contact network rearrangements. Even if the elastic moduli do not describe the macroscopic behavior, they can provide informations on the microstructural features of the anisotropic granular packings. Correlations between elastic moduli and internal structure parameters were investigated.

First, the measured moduli were confronted to experimental data in order to link the different numerically simulated initial states to experimental ones. Then, classical Voigt approximation (also called the Effective Medium Theory (EMT)) formulae were tested and their limits of applicability were identified. In particular, it was shown that such expressions provide acceptable estimates for nearly isotropic or well coordinated states or for longitudinal moduli in dense configurations at high stress levels, while moduli ratios were only accurately estimated for longitudinal moduli in mainly isotropic states. Finally, the elastic moduli were related to fabric and force anisotropy and it was shown that the elastic anisotropy is essentially correlated with the fabric anisotropy.

Perspectives

Improvements of D-DPC method

Further speeding up of the method implementation

As it was detailed in Sec. 2.7, a great care was taken in improving the implementation of the projection model in order to speed up the minimization process. However, for the minimization algorithm (Levenberg–Marquardt) an existing implementation was used. This implementation is not parallel and does not account for the Jacobian sparsity for matrix operations. Therefore, using a personal implementation would provide more control and allows a better optimization.

Improving the description of grain geometry

We saw in Sec. 3.3 that the discretization of the image produces errors in the generated digital projections. Therefore, using a better representation of grain geometry would enhance the method accuracy. The polygonal discretization as introduced in Sec.3.3, might be a good choice. However, it should be recalled that the geometric description of the grains comes from a first tomographic experiment, carried out on the sample in its initial state. How to get an accurate faceted description of the boundaries of the grains from this initial scan remains an open question. [Vlahinić et al., 2014] recently proposed an interesting approach based on level-sets to post-process the voxel-wise constant grey level reconstruction. A variant of this method, allowing for gray level variations inside the grains might be well worth investigating.

Integration over the ray beam

In Sec. 3.4, it was shown how considering the integration over ray beams in the projection model reduces the effect of the lumped beam assumption. However, integrating the intensity (exponential of projections) is very costly. [Gao, 2012] provided an extension of its algorithm to estimate the

intersection of voxels with surfaces (ray beams) rather than with lines (unique rays). This algorithm can be extended to 3D case, and allow a fast estimation of the integration of projections. Then, with adequate approximations, one could estimate the integration of intensities.

Improved versions of the D-DPC method based on the above suggestions might produce evaluations of grain motions with an accuracy significantly better than competing methods, still with much lower numbers of projections, consistent with the image-noise model presented in Sec. 3.2. Their practical application on realistic samples of granular materials with large numbers of grains (several ten thousands) would certainly require the use of massively parallel high performance computers. Such an innovative tool, combined with the fast acquisition of radiographic projections with low noise levels, which are now possible on synchrotron-based facilities, would certainly provide new insights on the micro-mechanical understanding of the time-dependent behavior of granular media, not only in the short term regime, where deformations are larger but fast, but also in the long term one, where they are lower and slower. Overall phenomenological behaviors such as logarithmic creep might then be explained by the observations of grain scale local motions and their statistical analysis.

About the DEM oedometric compression study

Studying the effect of the inertia number on structure perturbations

We have pointed out the fact that the equilibration phase of configurations results in a small numerical creep. During this phase, the strain rate, expressed in dimensionless form by the inertia number I, decreases. As I tends to get smaller the friction mobilization decreases indicating that the variations of I has an impact on the structure evolution. Therefore, it might be interesting to conduct a study with different values and variations of I to probe its effect on the behavior features like the resulted elastic domain.

Contact damage and plasticity

As it was observed in the numeric simulations of this work, the strain response is almost reversible. This behavior was attributed to the absence of damage or plasticity in the contact law. Therefore, comparing our simulation to further simulations, that take account of such phenomena, is interesting for better understanding of this result. Moreover, with adequate parameterization of the problem, the irreversibility can be quantified against some parameters of contact damage, contact plasticity or particle geometry. However, the identification of such parameters is still as difficult as the creep origin inverstigation.

Tri-axial compression

In the oedometric compression, the only controlled solicitation is the vertical stress (or strain). Therefore, a small range of stress anisotropy can be obtained depending on the internal structure of the assemblies. Other packing processes, than those used in this work, might help obtaining more variation of K_0. For instance, in tri-axial tests both vertical and horizontal stresses can be controlled,

and hence, specific initial stress anisotropy can be obtained. This would mainly allow to increase the diversity of the available measurements, allowing for more quantitative statistical correlations on the structural parameters.

Moreover, we can also study the behavior of the specimens under tri-axial compression. This may allow, for example, to study the elastic domain with respect to other moduli than those relating the stresses to the axial strain.

Future studies of creep

As mentioned in the motivations of this work, the study of creep is a main outlook of this study.

In the experimental part, D-DPC in its current state allows to measure individual grain displacements with accuracies comparable to the ones of other correlation techniques, while allowing to study time-dependent phenomena. Therefore, at this stage D-DPC is applicable to the short-term behavior of creep. Moreover, it was shown that the intrinsic errors are the most impacting on D-DPC accuracy. Therefore, future enhancements based on the error assessments may allow to achieve better accuracies, capable of measuring the small displacements involved in the long-term behavior of creep.

In the numerical part, the internal structure evolutions in the oedometric compression were systematically studied. The next step is to reproduce the phenomena at the origin of the onset of creep. For instance, the weakening of grains contact under constant load can be at the origin of the structure rearrangements. The difficulty of modeling such aging in contacts is the choice of adequate parametrization with physical roots.

Other disturbances of the structure may be external to the experiments such as ambient vibrations, grain dilation (due to temperature change, as example). Those instabilities may perturb the structure equilibrium and result in consecutive rearrangements. In this case, the logarithmic behavior of creep may be a consequence of the improvement of the structure stability triggered by the rearrangements themselves. Such type of perturbation can be readily studied in DEM by testing their effect on equilibrated states.

Finally, other mechanisms, inspired by in-situ experiments, can be simulated. The comparison of experimental and numerical results would provide a better understanding of creep.

Appendix A

Structure of stiffness matrix

We provide here additional information on the definition and structure of stiffness matrix $\underline{\mathbf{K}}$, as introduced in (5.3) and discussed in Ref. [Agnolin and Roux, 2007c]. Contact force $\mathbf{F}_{ij}$ transmitted from i to j is split into its normal and tangential components as $\mathbf{F}_{ij} = F_{ij}^N \mathbf{n}_{ij} + \mathbf{F}_{ij}^T$. Considering an equilibrium configuration with N_c force-carrying contacts, the static contact law relates the $3N_c$-dimensional contact force increment vector $\Delta \mathbf{f}$, formed with the values ΔF_{ij}^N, $\Delta \mathbf{F}_{ij}^T$ of the normal and tangential parts of all contact force increments, to relative displacements, gathered in $3N_c$-dimensional vector $\delta \mathbf{u}$ as

$$\Delta \mathbf{f} = \underline{\underline{\mathcal{K}}} \cdot \delta \mathbf{u}. \tag{A.1}$$

This defines the block diagonal *local stiffness matrix* $\underline{\underline{\mathcal{K}}}$, of dimensions $(3N_c \times 3N_c)$. $\underline{\underline{\mathcal{K}}}$ does not couple different contacts. The 3×3 block of $\underline{\underline{\mathcal{K}}}$ corresponding to contact i, j, $\underline{\underline{\mathcal{K}}}_{ij}$, provided friction is not fully mobilized reads:

$$\underline{\underline{\mathcal{K}}}_{ij}^E = \begin{bmatrix} K_N(h_{ij}) & 0 & 0 \\ 0 & K_T(h_{ij}) & 0 \\ 0 & 0 & K_T(h_{ij}). \end{bmatrix} \tag{A.2}$$

Stiffnesses $K_N(h_{ij})$ and $K_T(h_{ij})$ are given by (4.3) and (4.4). This simple form of $\underline{\underline{\mathcal{K}}}_{ij}$ is an approximation, relying on simplifications of the Hertz-Mindlin laws (see [Agnolin and Roux, 2007c]).

The *rigidity matrix* [Agnolin and Roux, 2007a], which should not be confused with the stiffness matrix, relates the relative displacements to the N_f degrees of freedom. Normal unit vector $\mathbf{n}_{ij}$ pointing from i to j (along the line joining centers for spheres), the relative displacement $\delta \mathbf{u}_{ij}$, for spherical grains with radii R_i, R_j writes

$$\delta \mathbf{u}_{ij} = \tilde{\mathbf{u}}_i + \underline{\theta}_i \times R_i \mathbf{n}_{ij} - \tilde{\mathbf{u}}_j + \underline{\theta}_j \times R_j \mathbf{n}_{ij} + \underline{\underline{\varepsilon}} \cdot \mathbf{r}_{ij}, \tag{A.3}$$

$\mathbf{r}_{ij}$ denoting the vector pointing from the center of the first sphere i to the nearest image (by the periodic translation group of the boundary conditions) of the center of the second one j. The normal part $\delta \mathbf{u}_{ij}^N$ of $\delta \mathbf{u}_{ij}$ is the increment of normal deflection h_{ij} in the contact.

The rigidity matrix $\underline{\underline{\mathbf{G}}}$ is $3N_c \times N_f$-dimensional, it is defined by the linear correspondence expressed by relation (A.3), which transforms $\mathbf{U}$ into the $3N_c$-dimensional vector of relative displacements at contacts $\delta\mathbf{u}$:

$$\delta\mathbf{u} = \underline{\underline{\mathbf{G}}} \cdot \mathbf{U} \tag{A.4}$$

The equilibrium equations – the statements that contact forces $\mathbf{f}$ balance load $\mathbf{F}^{\text{ext}}$ – can simply be written with the transposed rigidity matrix, as [Agnolin and Roux, 2007a]

$$\mathbf{F}^{\text{ext}} = {}^{\mathbf{T}}\underline{\underline{\mathbf{G}}} \cdot \mathbf{f}. \tag{A.5}$$

Stiffness matrix $\underline{\underline{\mathbf{K}}}$ results from Eqs. A.4, A.1 and A.5:

$$\underline{\underline{\mathbf{K}}} = {}^{\mathbf{T}}\underline{\underline{\mathbf{G}}} \cdot \underline{\underline{\mathcal{K}}} \cdot \underline{\underline{\mathbf{G}}} \tag{A.6}$$

Note that the symmetry and the positiveness of the stiffness matrix is immediately apparent in (A.6), given the diagonal form of $\underline{\underline{\mathcal{K}}}$ in (A.2), and the positive signs of stiffnesses K_N, K_T. In Ref. [Agnolin and Roux, 2007c], a correction to $\underline{\underline{\mathbf{K}}}$ is identified, which stems from the preexisting forces prior to application of stress increments. This correction, which is not symmetric in general, is however negligible as long as $\underline{\underline{\mathbf{K}}}$ is positive definite, which is equivalent to the non-existence of a non-trivial kernel of $\underline{\underline{\mathbf{G}}}$, i.e. "mechanism motions" or "floppy modes". Such free motions are absent [Agnolin and Roux, 2007a] in equilibrated packs of spherical balls, save for global translations of all grains in the periodic cell, and for (rare) two-coordinated balls. Global rigid-body translations are readily eliminated in matrix computations on assuming one grain to be elastically tied to a fixed "ground", and two-coordinated grains are also innocuous (see [Agnolin and Roux, 2007a, Agnolin and Roux, 2007c]).

Bibliography

[Agnolin and Roux, 2007a] Agnolin, I. and Roux, J.-N. (2007a). Internal states of model isotropic granular packings. I. Assembling process, geometry, and contact networks. *Phys. Rev. E*, 76(6):061302.

[Agnolin and Roux, 2007b] Agnolin, I. and Roux, J.-N. (2007b). Internal states of model isotropic granular packings. II. Compression and pressure cycles. *Phys. Rev. E*, 76(6):061303.

[Agnolin and Roux, 2007c] Agnolin, I. and Roux, J.-N. (2007c). Internal states of model isotropic granular packings. III. Elastic properties. *Phys. Rev. E*, 76(6):061304.

[Amiot et al., 2013] Amiot, F., Bornert, M., Doumalin, P., Dupré, J.-C., Fazzini, M., Orteu, J.-J., Poilâne, C., Robert, L., Rotinat, R., Toussaint, E., et al. (2013). Assessment of digital image correlation measurement accuracy in the ultimate error regime: main results of a collaborative benchmark. *Strain*, 49(6):483–496.

[Ando et al., 2012] Ando, E., Hall, S. A., Viggiani, G., Desrues, J., and Bésuelle, P. (2012). Grain-scale experimental investigation of localised deformation in sand: a discrete particle tracking approach. *Acta Geotechnica*, 7(1):1–13.

[Arthur and Menzies, 1972] Arthur, J. R. F. and Menzies, B. K. (1972). Inherent anisotropy in sand. *Géotechnique*, 22:115–128.

[Aste et al., 2005] Aste, T., Saadatfar, M., and Senden, T. J. (2005). Geometrical structure of disordered sphere packings. *Phys. Rev. E*, 71.

[Atman et al., 2005] Atman, A., Brunet, P., Geng, J., Reydellet, G., Combe, G., Claudin, P., Behringer, R., and Clément, E. (2005). Sensitivity of the stress response function to packing preparation. *J. Phys.: Condens. Matter*, 17:S2391–S2403.

[Atman et al., 2014] Atman, A. P. F., Claudin, P., Combe, G., and Martins, G. H. B. (2014). Mechanical properties of inclined frictional granular layers. *Granular Matter*, 16:193–201.

[Augustesen et al., 2004] Augustesen, A., Liingaard, M., and Lade, P. V. (2004). Evaluation of time-dependent behavior of soils. *International Journal of Geomechanics*, 4(3):137–156.

[Azéma et al., 2012] Azéma, E., Descantes, Y., Roquet, N., Roux, J.-N., and Chevoir, F. (2012). Discrete simulation of dense flows of polyhedral grains down a rough inclined plane. *Phys. Rev. E*, 86:031303.

[Azéma and Radjaï, 2014] Azéma, E. and Radjaï, F. (2014). Internal struture of inertial granular flows. *Phys. Rev. Lett.*, 112:078001.

[Azéma et al., 2013] Azéma, E., Radjaï, F., and Dubois, F. (2013). Packings of irregular polyhedral particles: Strength, structure, and effects of angularity. *Phys. Rev. E*, 87:062223.

[Balay et al., 2015] Balay, S., Abhyankar, S., Adams, M. F., Brown, J., Brune, P., Buschelman, K., Dalcin, L., Eijkhout, V., Gropp, W. D., Kaushik, D., Knepley, M. G., McInnes, L. C., Rupp, K., Smith, B. F., Zampini, S., and Zhang, H. (2015). PETSc users manual. Technical Report ANL-95/11 - Revision 3.6, Argonne National Laboratory.

[Balay et al., 1997] Balay, S., Gropp, W. D., McInnes, L. C., and Smith, B. F. (1997). Efficient management of parallelism in object-oriented numerical software libraries. In *Modern software tools for scientific computing*, pages 163–202. Springer.

[Bay et al., 1999] Bay, B. K., Smith, T. S., Fyhrie, D. P., and Saad, M. (1999). Digital volume correlation: three-dimensional strain mapping using x-ray tomography. *Experimental mechanics*, 39(3):217–226.

[Behnel et al., 2011] Behnel, S., Bradshaw, R., Citro, C., Dalcin, L., Seljebotn, D. S., and Smith, K. (2011). Cython: The best of both worlds. *Computing in Science & Engineering*, 13(2):31–39.

[Benahmed et al., 2004] Benahmed, N., Canou, J., and Dupla, J.-C. (2004). Structure initiale et propriétés de liquéfaction statique d'un sable. *Comptes-Rendus Académie des Sciences, Mécanique*, 332:887–894.

[Besnard et al., 2006] Besnard, G., Hild, F., and Roux, S. (2006). "finite-element" displacement fields analysis from digital images: application to portevin–le châtelier bands. *Experimental Mechanics*, 46(6):789–803.

[Beucher, 2001] Beucher, S. (2001). Geodesic reconstruction, saddle zones and hierarchical segmentation. *Image Anal Stereol*, 20(2):137–141.

[Beucher et al., 1992] Beucher, S. et al. (1992). The watershed transformation applied to image segmentation. *SCANNING MICROSCOPY-SUPPLEMENT-*, pages 299–299.

[Beucher and Lantuéjoul, 1979] Beucher, S. and Lantuéjoul, C. (1979). Use of watersheds in contour detection. In *International Workshop on Image Processing: Real-time Edge and Motion Detection/Estimation*, Rennes, France.

[Biarez and Hicher, 1993] Biarez, J. and Hicher, P.-Y. (1993). *Elementary Mechanics of Soil Behaviour*. A. A. Balkema, Rotterdam.

[Bornert et al., 2009] Bornert, M., Brémand, F., Doumalin, P., Dupré, J.-C., Fazzini, M., Grédiac, M., Hild, F., Mistou, S., Molimard, J., Orteu, J.-J., et al. (2009). Assessment of digital image correlation measurement errors: methodology and results. *Experimental mechanics*, 49(3):353–370.

[Bornert et al., 2004] Bornert, M., Chaix, J.-M., Doumalin, P., Dupré, J.-C., Fournel, T., Jeulin, D., Maire, E., Moreaud, M., and Moulinec, H. (2004). Mesure tridimensionnelle de champs cinématiques par imagerie volumique pour l'analyse des matériaux et des structures. *Instrumentation, Mesure, Métrologie*, 4(3-4):43–88.

[Bruchon, 2014] Bruchon, J.-F. (2014). *Investigation by means of X-ray computed tomography of capillary collapse in granular materials*. Theses, Université Paris-Est.

[Bruchon et al., 2013] Bruchon, J.-F., Pereira, J.-M., Vandamme, M., Lenoir, N., Delage, P., and Bornert, M. (2013). Full 3d investigation and characterisation of capillary collapse of a loose unsaturated sand using x-ray ct. *Granular Matter*, 15(6):783–800.

[Cardona and Geradin, 1988] Cardona, A. and Geradin, M. (1988). A beam finite element nonlinear theory with finite rotations. *International Journal for Numerical Methods in Engineering*, 26(11):2403–2438.

[Cavaretta et al., 2010] Cavaretta, I., Coop, M., and O'Sullivan, C. (2010). The influence of particle characteristics on the behaviour of coarse grained soils. *Géotechnique*, 60(6):413–423.

[Chambon and Crouzil, 2003] Chambon, S. and Crouzil, A. (2003). Dense matching using correlation: new measures that are robust near occlusions. In *Proceedings of British Machine Vision Conference (BMVC 2003)*, volume 42, pages 143–152.

[Chen et al., 1988a] Chen, Y.-C., Ishibashi, I., and Jenkins, J. T. (1988a). Dynamic shear modulus and fabric: part i, depositional and induced anisotropy. *Géotechnique*, 38(1):23–32.

[Chen et al., 1988b] Chen, Y.-C., Ishibashi, I., and Jenkins, J. T. (1988b). Dynamic shear modulus and fabric: part ii, stress reversal. *Géotechnique*, 38(1):33–37.

[Combe and Roux, 2011] Combe, G. and Roux, J.-N. (2011). Construction of Granular Assemblies under Static Loading. In [Radjaï and Dubois, 2011], chapter 6, pages 153–180.

[Danielsson, 1980] Danielsson, P.-E. (1980). Euclidean distance mapping. *Computer Graphics and Image Processing*, 14(3):227–248.

[di Benedetto et al., 2003] di Benedetto, H., Doanh, T., Geoffroy, H., and Sauzéat, C., editors (2003). *Deformation characteristics of geomaterials: Recent investigations and prospects*, Lisse. Swets and Zeitlinger.

[Donev et al., 2005] Donev, A., Torquato, S., and Stillinger, F. H. (2005). Pair correlation function characteristics of nearly jammed disordered and ordered hard-sphere solids. *Phys. Rev. E*, 71(1):011105.

[Duttine et al., 2007] Duttine, A., Di Benedetto, H., Pham Van Bang, D., and Ezaoui, A. (2007). Anisotropic small strain elastic properties of sands and mixture of sand-clay measured by dynamic and static methods. *Soils and Foundations*, 47(3):457–472.

[Elata and Berryman, 1996] Elata, D. and Berryman, J. G. (1996). Contact force-displacement laws and the mechanical behavior of random packs of identical spheres. *Mechanics of Materials*, 24:229–240.

[Emam et al., 2005] Emam, S., Roux, J.-N., Canou, J., Corfdir, A., and Dupla, J.-C. (2005). Granular packings assembled by rain deposition: an experimental and numerical study. pages 49–52, Leiden. Balkema.

[Estrada et al., 2011] Estrada, N., Azéma, E., Radjaï, F., and Taboada, A. (2011). Identification of rolling resistance as a shape parameter in sheared granular media. *Phys. Rev. E*, 84:011306.

[Ezaoui and di Benedetto, 2009] Ezaoui, A. and di Benedetto, H. (2009). Experimental measurements of the global anisotropic elastic behaviour of dry hostun sand during triaxial tests, and effect of sample preparation. *Géotechnique*, 59(7):621–635.

[Fazekas et al., 2007] Fazekas, S., Török, J., and Kertész, J. (2007). Critical packing in granular shear bands. *Phys. Rev. E*.

[Feldkamp et al., 1984] Feldkamp, L., Davis, L., and Kress, J. (1984). Practical cone-beam algorithm. *JOSA A*, 1(6):612–619.

[Feng and Yu, 1998] Feng, C. and Yu, A. (1998). Effect of liquid addition on the packing of mono-sized coarse spheres. *Powder technology*, 99(1):22–28.

[Fessler, 1996] Fessler, J. A. (1996). Mean and variance of implicitly defined biased estimators (such as penalized maximum likelihood): Applications to tomography. *IEEE Transactions on Image Processing*, 5(3):493–506.

[Gao, 2012] Gao, H. (2012). Fast parallel algorithms for the x-ray transform and its adjoint. *Medical physics*, 39(11):7110–7120.

[Gao and Wang, 2014] Gao, Y. and Wang, Y. H. (2014). Experimental and dem examinations of k0 in sand under different loading conditions. *ASCE Journal of Geotechnical and Geoenvironmental Engineering*, 140:04014012–1–04014012–11.

[Gay and da Silveira, 2004] Gay, C. and da Silveira, R. A. (2004). Anisotropic elastic theory of preloaded granular media. *Europhysics Letters*, 68:51–57.

[Gaye, 2015] Gaye, A. (2015). *Analyse multiéchelle des mécanismes de déformation du sel gemme par mesures de champs surfaciques et volumiques*. PhD thesis, Paris Est.

[Geoffroy et al., 2003] Geoffroy, H., di Benedetto, H., Duttine, A., and Sauzéat, C. (2003). Dynamic and cyclic loadings on sands: results and modelling for general stress-strain conditions. In di Benedetto, H., Doanh, T., Geoffroy, H., and Sauzéat, C., editors, *Deformation characteristics of geomaterials*, pages 353–363, Lisse. Swets and Zeitlinger.

[Gilabert et al., 2008] Gilabert, F. A., Roux, J.-N., and Castellanos, A. (2008). Computer simulation of model cohesive powders: Plastic consolidation, structural changes, and elasticity under isotropic loads. *Phys. Rev. E*, 78(1):031305.

[Goddard et al., 2010] Goddard, J. D., Jenkins, J. T., and Giovine, P., editors (2010). *IUTAM-ISIMM symposium on mathematical modeling and physical instances of granular flow*, volume 1227 of *AIP conference proceedings*. AIP.

[Gu et al., 2015] Gu, X., Hu, J., and Huang, M. (2015). K0 of granular soils: a particulate approach. *Granular Matter*, 17(6):703–715.

[Hall et al., 2010] Hall, S., Bornert, M., Desrues, J., Pannier, Y., Lenoir, N., Viggiani, G., and Bésuelle, P. (2010). Discrete and continuum analysis of localised deformation in sand using x-ray μct and volumetric digital image correlation. *Geotechnique*, 60(5):315–322.

[Hamilton, 1853] Hamilton, W. R. (1853). *Lectures on quaternions*.

[Hardin and Blandford, 1989] Hardin, B. O. and Blandford, G. E. (1989). Elasticity of particulate materials. *ASCE Journal of Geotechnical Engineering*, 115(6):788–805.

[Herrmann et al., 1998] Herrmann, H. J., Hovi, J.-P., and Luding, S., editors (1998). *Physics of Dry Granular Media*, Dordrecht. Balkema.

[Hicher, 1996] Hicher, P.-Y. (1996). Elastic properties of soils. *ASCE Journal of Geotechnical Engineering*, 122:641–648.

[Hild and Roux, 2006] Hild, F. and Roux, S. (2006). Digital image correlation: from displacement measurement to identification of elastic properties–a review. *Strain*, 42(2):69–80.

[Hoque and Tatsuoka, 1998] Hoque, E. and Tatsuoka, F. (1998). Anisotropy in elastic deformation of granular materials. *Soils and Foundations*, 38:163–179.

[Hutton and Osiecki, 1998] Hutton, B. F. and Osiecki, A. (1998). Correction of partial volume effects in myocardial spect. *Journal of Nuclear Cardiology*, 5(4):402–413.

[Ibrahimbegović et al., 1995] Ibrahimbegović, A., Frey, F., and Kožar, I. (1995). Computational aspects of vector-like parametrization of three-dimensional finite rotations. *International Journal for Numerical Methods in Engineering*, 38(21):3653–3673.

[Jacobs et al., 1998] Jacobs, F., Sundermann, E., De Sutter, B., Christiaens, M., and Lemahieu, I. (1998). A fast algorithm to calculate the exact radiological path through a pixel or voxel space. *CIT. Journal of computing and information technology*, 6(1):89–94.

[Jenkins et al., 2005] Jenkins, J. T., Johnson, D., La Ragione, L., and Makse, H. A. (2005). Fluctuations and the effective moduli of an isotropic, random aggregate of identical, frictionless spheres. *Journal of The Mechanics and Physics of Solids*, 53:197–225.

[Jenkins and La Ragione, 2001] Jenkins, J. T. and La Ragione, L. (2001). Particle spin in anisotropic granular materials. *International Journal of Solids and Structures*, 38:1063–1069.

[Johnson, 1985] Johnson, K. L. (1985). *Contact Mechanics*. Cambridge University Press.

[Kadau et al., 2003] Kadau, D., Bartels, G., Brendel, L., and Wolf, D. E. (2003). Contact dynamics simulations of compacting cohesive granular systems. *Phase Trans.*, 76:315–331.

[Kak and Slaney, 1988] Kak, A. C. and Slaney, M. (1988). *Principles of computerized tomographic imaging*. IEEE press.

[Karimpour and Lade, 2013] Karimpour, H. and Lade, P. V. (2013). Creep behavior in virginia beach sand. *Canadian Geotechnical Journal*, 50(11):1159–1178.

[Khalili et al., a] Khalili, M. H., Brisard, S., Bornert, M., Aimedieu, P., Pereira, J.-M., and Roux, J.-N. Discrete digital projections correlation: a reconstruction-free method to quantify local kinematics in granular media by x-ray tomography.

[Khalili et al., b] Khalili, M. H., Roux, J.-N., Pereira, J.-M., Brisard, S., and Bornert, M. Numerical simulation of one-dimensional compression of granular materials: Ii. elastic moduli, stresses and microstructure.

[Khalili et al., c] Khalili, M. H., Roux, J.-N., Pereira, J.-M., Brisard, S., and Bornert, M. A numerical study of one-dimensional compression of granular materials: I. stress-strain behavior, microstructure and irreversibility. Submitted to Phys. Rev. E.

[Khamseh et al., 2015] Khamseh, S., Roux, J.-N., and Chevoir, F. (2015). Flow of wet granular materials: a numerical study. *Phys. Rev. E*, 92:022201.

[Khidas and Jia, 2010] Khidas, Y. and Jia, X. (2010). Anisotropic nonlinear elasticity in a spherical bead pack: influence of the fabric anisotropy. *Phys. Rev. E*, 81:021303.

[Kruyt, 2014] Kruyt, N. P. (2014). Micromechanical study of elastic moduli of three-dimensional granular assemblies. *International Journal of Solids and Structures*, 51:2336–2344.

[Kruyt and Rothenburg, 2014] Kruyt, N. P. and Rothenburg, L. (2014). On micromechanical characteristics of the critical state of two-dimensional granular materials. *Acta Mechanica*, 225(8):2301 – 2318.

[Kuhn and Chang, 2006] Kuhn, M. R. and Chang, C. S. (2006). Stability, Bifurcation and Softening in Discrete Systems: A Conceptual Approach for Granular Materials. *International Journal of Solids and Structures*, 43:6026–6051.

[Kuwano and Jardine, 2002] Kuwano, R. and Jardine, R. J. (2002). On the applicability of cross-anisotropic elasticity to granular materials at very small strains. *Géotechnique*, 52:727–749.

[La Ragione and Jenkins, 2007] La Ragione, L. and Jenkins, J. T. (2007). The initial response of an idealized granular material. *Proceedings of the Royal Society A*, 463(2079):735–758.

[La Ragione and Magnanimo, 2012a] La Ragione, L. and Magnanimo, V. (2012a). Contact anisotropy and coordination number for a granular assembly: A comparison of distinct-element-method simulations and theory. *Phys. Rev. E*, page 031304.

[La Ragione and Magnanimo, 2012b] La Ragione, L. and Magnanimo, V. (2012b). Evolution of the effective moduli of an anisotropic, dense, granular material. *Granular Matter*, 14:749–757.

[Lade and Liu, 1998] Lade, P. V. and Liu, C.-T. (1998). Experimental study of drained creep behavior of sand. *Journal of Engineering Mechanics*, 124(8):912–920.

[Lam and Tatsuoka, 1988] Lam, W.-K. and Tatsuoka, F. (1988). Effects of initial anisotropic fabric and σ_2 on strength and deformation characteristics of soils. *Soils and Foundations*, 28:89–106.

[Leclerc et al., 2015] Leclerc, H., Roux, S., and Hild, F. (2015). Projection savings in CT-based digital volume correlation. *Experimental Mechanics*, 55(1):275–287.

[Lee et al., 2013] Lee, J., Tae, S. Y., Lee, D., and Lee, J. (2013). Assessment of k_0 correlation to strength for granular materials. *Soils and Foundations*, 53(4):584–595.

[Lemaître et al., 2009] Lemaître, A., Roux, J.-N., and Chevoir, F. (2009). What do dry granular flows tell us about dense non-brownian suspension rheology? *Rheologica Acta*, 48:925–942.

[Lenoir et al., 2007] Lenoir, N., Bornert, M., Desrues, J., Bésuelle, P., and Viggiani, G. (2007). Volumetric digital image correlation applied to x-ray microtomography images from triaxial compression tests on argillaceous rock. *Strain*, 43(3):193–205.

[Leung et al., 1997] Leung, C., Lee, F., and Yet, N. (1997). The role of particle breakage in pile creep in sand. *Canadian Geotechnical Journal*, 33(6):888–898.

[Lhuissier et al., 2012] Lhuissier, P., Scheel, M., Di Michiel, M., Boller, E., Adrien, J., Maire, E., Salvo, L., Blandin, J.-J., and Suery, M. (2012). Ultra fast tomography: New developments for 4d studies in material science. In De Graef, M., Friis Poulsen, H., Lewis, A., Simmons, J., and Spanos, G., editors, *1st International Conference on 3D Materials Science*, pages 203–208. John Wiley & Sons, Inc.

[Limodin et al., 2007] Limodin, N., Salvo, L., Suéry, M., and DiMichiel, M. (2007). In situ investigation by X-ray tomography of the overall and local microstructural changes occurring during partial remelting of an Al-15.8 wt.% Cu alloy. *Acta Materialia*, 55(9):3177–3191.

[Lopera Perez et al., 2015] Lopera Perez, J. C., Kwok, C. Y., O'Sullivan, C., Huang, X., and Hanley, K. J. (2015). Numerical study of one-dimensional compression in granular materials. *Géotechnique Letters*, 5:96–103.

[Lucas et al., 1981] Lucas, B. D., Kanade, T., et al. (1981). An iterative image registration technique with an application to stereo vision. In *IJCAI*, volume 81, pages 674–679.

[Mader et al., 2011] Mader, K., Marone, F., Hintermüller, C., Mikuljan, G., Isenegger, A., and Stampanoni, M. (2011). High-throughput full-automatic synchrotron-based tomographic microscopy. *Journal of Synchrotron Radiation*, 18(2):117–124.

[Magnanimo et al., 2008] Magnanimo, V., La Ragione, L., Jenkins, J. T., Wang, P., and Makse, H. A. (2008). Characterizing the shear and bulk moduli of an idealized granular material. *Europhys. Lett.*, 81:34006.

[Makse et al., 1999] Makse, H. A., Gland, N., Johnson, D., and Schwartz, L. (1999). Why effective medium theory fails in granular materials. *Phys. Rev. Lett.*, 83(24):5070–5073.

[Makse et al., 2000] Makse, H. A., Johnson, D. L., and Schwartz, L. M. (2000). Packing of compressible granular materials. *Phys. Rev. Lett.*, 84(18):4160–4163.

[McCool et al., 2012] McCool, M., Robison, A. D., and Reinders, J. (2012). *Structured Parallel Programming*. Morgan Kaufmann, 225 Wyman Street, Waltham, MA 02451, USA.

[McDowell, 2003] McDowell, G. (2003). Micromechanics of creep of granular materials. *Géotechnique*, 53(10):915–916.

[McNamara and Herrmann, 2006] McNamara, S. and Herrmann, H. J. (2006). Quasirigidity: some uniqueness issues. *Phys. Rev. E*, 74:061303.

[Miksic and Alava, 2013] Miksic, A. and Alava, M. J. (2013). Evolution of grain contacts in a granular sample under creep and stress relaxation. *Physical Review E*, 88(3):032207.

[Mitchell and Soga, 2005] Mitchell, J. and Soga, K. (2005). *Fundamentals of Soil Behavior*. Wiley.

[Moré, 1978] Moré, J. J. (1978). The levenberg-marquardt algorithm: implementation and theory. In *Numerical analysis*, pages 105–116. Springer.

[Morozov, 1984] Morozov, V. A. (1984). *Methods for Solving Incorrectly Posed Problems*. Springer-Verlag.

[Myers et al., 2015] Myers, G. R., Geleta, M., Kingston, A. M., Recur, B., and Sheppard, A. P. (2015). Bayesian approach to time-resolved tomography. *Optics express*, 23(15):20062–20074.

[Nakagawa and Luding, 2009] Nakagawa, M. and Luding, S., editors (2009). *Powders and Grains 2009*. American Institute of Physics.

[Oda, 1972] Oda, M. (1972). Initial fabrics and their relation to mechanical properties of granular materials. *Soils and Foundations*, 12:17–36.

[O'Hern et al., 2003] O'Hern, C., Silbert, L. E., Liu, A. J., and Nagel, S. R. (2003). Jamming at zero temperature and zero applied stress: The epitome of disorder. *Phys. Rev. E*, 68(1):011306.

[Okuchi and Tatsuoka, 1984] Okuchi, Y. and Tatsuoka, F. (1984). Some factors affecting k_0 values of sand measured in triaxial cell. *Soils and Foundations*, 24(3):52–68.

[Oliphant, 2012] Oliphant, T. (2012). Numba python bytecode to llvm translator. In *Proceedings of the Python for Scientific Computing Conference (SciPy)*.

[O'Sullivan, 2011] O'Sullivan, C. (2011). *Particulate discrete element modeling, a geomechanics perspective*. Spon Press, London.

[Otsu, 1975] Otsu, N. (1975). A threshold selection method from gray-level histograms. *Automatica*, 11(285-296):23–27.

[Pan et al., 2009] Pan, B., Qian, K., Xie, H., and Asundi, A. (2009). Two-dimensional digital image correlation for in-plane displacement and strain measurement: a review. *Measurement science and technology*, 20(6):062001.

[Pannier et al., 2010] Pannier, Y., Lenoir, N., and Bornert, M. (2010). Discrete volumetric digital image correlation for the investigation of granular type media at microscale: accuracy assessment. In *EPJ Web of Conferences*, volume 6, page 35003. EDP Sciences.

[Perona and Malik, 1990] Perona, P. and Malik, J. (1990). Scale-space and edge detection using anisotropic diffusion. *IEEE Transactions on pattern analysis and machine intelligence*, 12(7):629–639.

[Pestana and Whittle, 1998] Pestana, J. M. and Whittle, A. (1998). Time effects in the compression of sands. *Geotechnique*, 48(5).

[Peyneau and Roux, 2008a] Peyneau, P.-E. and Roux, J.-N. (2008a). Frictionless bead packs have macroscopic friction, but no dilatancy. *Phys. Rev. E*, 78:011307.

[Peyneau and Roux, 2008b] Peyneau, P.-E. and Roux, J.-N. (2008b). Solidlike behavior and anisotropy in rigid frictionless bead assemblies. *Phys. Rev. E*, 78:041307.

[Polyak, 1977] Polyak, B. (1977). Subgradient methods: A survey of soviet research. In *Nonsmooth optimization: Proceedings of the IIASA workshop March*, pages 5–30.

[Rad and Tumay, 1987] Rad, N. S. and Tumay, M. T. (1987). Factors affecting sand specimen preparation by raining. *ASTM Journal of Geotechnical Testing*, 10:31–37.

[Radjaï et al., 2012] Radjaï, F., Delenne, J.-Y., Azéma, E., and Roux, S. (2012). Fabric evolution and accessible geometrical states in granular materials. *Granular Matter*, 14:259–264.

[Radjaï and Dubois, 2011] Radjaï, F. and Dubois, F. (2011). *Discrete-element modeling of granular materials*. Wiley.

[Radjaï and Roux, 2004] Radjaï, F. and Roux, S. (2004). Contact dynamics study of 2d granular media : critical states and relevant internal variables. In Hinrichsen, H. and Wolf, D. E., editors, *The Physics of Granular Media*, pages 165–187, Berlin. Wiley-VCH.

[Radjaï et al., 2004] Radjaï, F., Troadec, H., and Roux, S. (2004). Basic features of granular plasticity. In Antony, S. J., Hoyle, W., and Ding, Y., editors, *Granular Materials: Fundamentals and Applications*, pages 157–183, Cambridge. Royal Society of Chemistry.

[Rannou et al., 2010] Rannou, J., Limodin, N., Réthoré, J., Gravouil, A., Ludwig, W., Baïetto-Dubourg, M.-C., Buffière, J.-Y., Combescure, A., Hild, F., and Roux, S. (2010). Three dimensional experimental and numerical multiscale analysis of a fatigue crack. *Computer methods in applied mechanics and engineering*, 199(21):1307–1325.

[Rodrigues, 1840] Rodrigues, O. (1840). Des lois géométriques qui régissent les déplacements d'un système solide dans l'espace, et de la variation des coordonnées provenant de ces déplacements considérés indépendamment des causes qui peuvent les produire. *Journal de Mathématiques Pures et Appliquées*, 5:380–440.

[Rothenburg and Kruyt, 2004] Rothenburg, L. and Kruyt, N. P. (2004). Critical state and evolution of coordination number in simulated granular materials. *International Journal of Solids and Structures*, 41(2):5763–5774.

[Roux, 2000] Roux, J.-N. (2000). Geometric origin of mechanical properties of granular materials. *Phys. Rev. E*, 61:6802–6836.

[Roux and Chevoir, 2011] Roux, J.-N. and Chevoir, F. (2011). Dimensional Analysis and Control Parameters. In [Radjaï and Dubois, 2011], chapter 8, pages 199–232.

[Roux and Combe, 2002] Roux, J.-N. and Combe, G. (2002). Quasistatic rheology and the origins of strain. *C. R. Physique*, 3:131–140.

[Roux and Combe, 2010] Roux, J.-N. and Combe, G. (2010). How granular materials deform in quasistatic conditions. In [Goddard et al., 2010], pages 260–270.

[Roux and Combe, 2011] Roux, J.-N. and Combe, G. (2011). Quasi-Static Methods. In [Radjaï and Dubois, 2011], chapter 3, pages 67–101.

[Roux and Hild, 2006] Roux, S. and Hild, F. (2006). Stress intensity factor measurements from digital image correlation: post-processing and integrated approaches. *International Journal of Fracture*, 140(1):141–157.

[Roux et al., 2002] Roux, S., Hild, F., and Berthaud, Y. (2002). Correlation image velocimetry: a spectral approach. *Applied optics*, 41(1):108–115.

[Roux et al., 2008] Roux, S., Hild, F., Viot, P., and Bernard, D. (2008). Three-dimensional image correlation from x-ray computed tomography of solid foam. *Composites Part A: Applied science and manufacturing*, 39(8):1253–1265.

[Saint-Cyr et al., 2012] Saint-Cyr, B., Szarf, K., Voivret, C., Azéma, E., Richefeu, V., Delenne, J.-Y., Combe, G., Nouguier-Lehon, C., Villard, P., Sornay, P., Chaze, M., and Radjaï, F. (2012). Particle shape dependence in 2d granular media. *Europhysics Letters*, 98(4):44008.

[Sanzeni et al., 2012] Sanzeni, A., Whittle, A. J., Germaine, J. T., and Colleselli, F. (2012). Compression and Creep of Venice Lagoon Sands. *J. Geotech. Geoenviron. Eng.*, 138:1266–1276.

[Schreier et al., 2000] Schreier, H. W., Braasch, J. R., and Sutton, M. A. (2000). Systematic errors in digital image correlation caused by intensity interpolation. *Optical engineering*, 39(11):2915–2921.

[Schreier and Sutton, 2002] Schreier, H. W. and Sutton, M. A. (2002). Systematic errors in digital image correlation due to undermatched subset shape functions. *Experimental Mechanics*, 42(3):303–310.

[Shepp and Vardi, 1982] Shepp, L. A. and Vardi, Y. (1982). Maximum likelihood reconstruction for emission tomography. *IEEE transactions on medical imaging*, 1(2):113–122.

[Shibuya et al., 1992] Shibuya, S., Tatsuoka, F., Teachavorasinskun, S., Kong, X.-J., Abe, F., Kim, Y.-S., and Park, C.-S. (1992). Elastic deformation properties of geomaterials. *Soils and Foundations*, 32:26–46.

[Siddon, 1984] Siddon, R. L. (1984). Fast calculation of the exact radiological path for a three-dimensional ct array. *Medical physics*, 12(2):252–255.

[Sidky et al., 2006] Sidky, E. Y., Kao, C.-M., and Pan, X. (2006). Accurate image reconstruction from few-views and limited-angle data in divergent-beam ct. *Journal of X-ray Science and Technology*, 14(2):119–139.

[Silbert et al., 2002] Silbert, L. E., Ertaş, D., Grest, G. S., Halsey, T. C., and Levine, D. (2002). Geometry of frictionless and frictional sphere packings. *Phys. Rev. E*, 65(3):031304.

[Smith, 2015] Smith, K. (2015). *Cython: A Guide for Python Programmers*. Sebastopol: O'Reilly.

[Somfai et al., 2007] Somfai, E., van Hecke, M., Ellenbroek, W. G., Shundyak, K., and van Saarloos, W. (2007). Critical and noncritical jamming of frictional grains. *Phys. Rev. E*, 75(2):020301.

[Song et al., 2008] Song, C., Wang, P., and Makse, H. A. (2008). A phase diagram for jammed matter. *Nature*, 453:629–632.

[Suiker and Fleck, 2004] Suiker, A. S. J. and Fleck, N. A. (2004). Frictional collapse of granular assemblies. *ASME Journal of Applied Mechanics*, 71:350–358.

[Sutton et al., 2008] Sutton, M., Yan, J., Tiwari, V., Schreier, H., and Orteu, J. (2008). The effect of out-of-plane motion on 2d and 3d digital image correlation measurements. *Optics and Lasers in Engineering*, 46(10):746–757.

[Sutton et al., 2009] Sutton, M. A., Orteu, J. J., and Schreier, H. (2009). *Image correlation for shape, motion and deformation measurements: basic concepts, theory and applications*. Springer Science & Business Media.

[Tariel, 2013] Tariel, V. (2013). *Population library*.

[Tatsuoka, 2001] Tatsuoka, F. (2001). Impacts on geotechnical engineering of several recent findings from laboratory stress-strain tests on geomaterials. In Correia, G. and Brandle, H., editors, *Geotechnics for roads, rail tracks and earth structures*, pages 69–140, Lisse. Balkema.

[Than et al., 2016] Than, V.-D., Khamseh, S., Tang, A. M., Pereira, J.-M., Chevoir, F., and Roux, J.-N. (2016). Basic mechanical properties of wet granular materials: A dem study. *ASCE Journal of Engineering Mechanics*.

[Thornton, 2000] Thornton, C. (2000). Numerical simulations of deviatoric shear deformation of granular media. *Géotechnique*, 50:43–53.

[Vlahinić et al., 2014] Vlahinić, I., Andò, E., Viggiani, G., and Andrade, J. E. (2014). Towards a more accurate characterization of granular media: extracting quantitative descriptors from tomographic images. *Granular Matter*, 16(1):9–21.

[Wagne et al., 2002] Wagne, B., Roux, S., and Hild, F. (2002). Spectral approach to displacement evaluation from image analysis. *The European Physical Journal Applied Physics*, 17(3):247–252.

[Walton, 1987] Walton, K. (1987). The effective elastic moduli of a random packing of spheres. *Journal of Mechanics and Physics of Solids*, 35:213–226.

[Wang et al., 2010] Wang, L., Heripre, E., El Outmani, S., Caldemaison, D., and Bornert, M. (2010). A simple experimental procedure to quantify image noise in the context of strain measurements at the microscale using DIC and SEM images. *EPJ Web of Conferences*, 6:40008.

[Wang et al., 2009] Wang, Y., Sutton, M., Bruck, H., and Schreier, H. (2009). Quantitative error assessment in pattern matching: effects of intensity pattern noise, interpolation, strain and image contrast on motion measurements. *Strain*, 45(2):160–178.

[Welker and McNamara, 2009] Welker, P. R. and McNamara, S. C. (2009). What triggers failure in frictional granular assemblies? *PRE*, 79:061305.

[Wolfe, 1975] Wolfe, P. (1975). A method of conjugate subgradients for minimizing nondifferentiable functions. In *Nondifferentiable optimization*, pages 145–173. Springer.

[Wood, 1990] Wood, D. M. (1990). *Soil Behaviour and Critical State Soil Mechanics*. Cambridge University Press.

[Wyart, 2006] Wyart, M. (2006). On the rigidity of amorphous solids. *Annales de Physique Fr.*, 30:1–96.

[Zhang and Makse, 2005] Zhang, H. P. and Makse, H. A. (2005). Jamming transitio in emulsions and granular materials. *Phys. Rev. E*, 72:011301.